Hot Compression Behaviour of Two-Phase Ti-6A1-4V: Experiments and State-Variable Modelling

Thesis

Hot Compression Behaviour of Two-Phase Ti-6Al-4V: Experiments and State-Variable Modelling

Mulyadi

Ph.D. The Open University 2007

Hot Compression Behaviour of Two-Phase Ti-6Al-4V: Experiments and State-Variable Modelling

Mulyadi **Ph.D.** **2007**

The Open University

EX12

RESEARCH SCHOOL

Library Authorisation Form

Please return this form to the Research School with the two bound copies of your thesis to be deposited with the University Library. All candidates should complete parts one and two of the form. Part three only applies to PhD candidates.

Part One: Candidates Details

Name: MULYADI PI: W4400406

Degree: DOCTOR OF PHILOSOPHY (PhD)

Thesis title: HOT COMPRESSION BEHAVIOUR OF TWO-PHASE Ti-6Al-4V: EXPERIMENTS AND STATE-VARIABLE MODELLING

Part Two: Open University Library Authorisation

I confirm that I am willing for my thesis to be made available to readers by The Open University Library, and that it may be photocopied, subject to the discretion of the Librarian.

Signed: ..... Date: 15th NOVEMBER 2007

Part Three: British Library Authorisation [PhD candidates only]

If you want a copy of your PhD thesis to be available on loan to the British Library Thesis Service as and when it is requested, you must sign a British Library Doctoral Thesis Agreement Form. Please return it to the Research School with this form. The British Library will publicise the details of your thesis and may request a copy on loan from the University Library. Information on the presentation of the thesis is given in the Agreement Form.

Please note the British Library have requested that theses should be printed on one side only to enable them to produce a clear microfilm. The Open University Library sends the fully bound copy of theses to the British Library.

The University has agreed that your participation in the British Library Thesis Service should be voluntary. Please tick either (a) or (b) to indicate your intentions.

(a) ☑ I am willing for The Open University to loan the British Library a copy of my thesis. A signed Agreement Form is attached

(b) ☐ I do not wish The Open University to loan the British Library a copy of my thesis.

Signed: ..... Date: 15th NOVEMBER 2007

Mulyadi
The Open University

Ph.D. Thesis
September 2007

Hot Compression Behaviour of Two-Phase Ti-6Al-4V: Experiments and State-Variable Modelling

ABSTRACT

The flow stress behaviour of two-phase Ti-6Al-4V and its individual α and β phases has been characterised during isothermal forging at temperatures of 850-1050°C and strain rates of 0.3-0.003/s. The influence of initial pre-form microstructure has also been investigated by heat-treating the as-received globular microstructure to produce an acicular β-transformed microstructure. It is found that flow stress behaviour exhibits a strong dependence on working temperature and imposed strain rate for the two-phase globular, two-phase acicular and single α-phase materials. However, for the single β-phase, steady state stress is found to be relatively constant with increasing temperature for the range of 925-975°C and strain rates of 0.3-0.003/s.

A pronounced discontinuous yielding phenomenon has been observed for globular Ti-6Al-4V at high temperature (≥900°C) and high strain rates (≥0.01/s). On the other hand, for acicular Ti-6Al-4V, flow stress curves reveal a broad peak stress level at low strains followed by moderate to extensive flow softening until a steady-state stress is reached. For the individual phases in Ti-6Al-4V, flow stresses of the single β-phase is found to be much lower than for the α-phase and most of flow stress curves of the β-phase are of a steady-state type with negligible flow softening. There is an indication of initial work hardening behaviour after the onset of plastic deformation at low strains for deformation of single α-phase at 925-950°C and 0.3/s, whilst a pronounced flow softening is exhibited particularly at 975°C and strain rates of 0.03-0.3/s.

A semi-empirical, history-dependent constitutive model for the prediction of the flow behaviour of Ti-6Al-4V which incorporates the temperature-dependent volume fraction and flow properties of the individual α and β phases is presented. It is found that a modified iso-strain approach can be employed in order to better predict the entire flow stress curve of acicular Ti-6Al-4V including the post-peak softening behaviour. This is achieved by introducing structural variable to represent the strain accumulation resulting from gross interaction mechanisms between the α and β phases during deformation.

The structural interaction variable has been linked with microstructure information from deformed cylindrical work-pieces, allowing derivation of a set of microstructure relationships. To provide the basis for more general process simulations, the modified iso-strain model has been implemented as a user-routine in DEFORM-2D finite element software and validated for an isothermal forging of a complex-shape double-truncated cone specimen. Excellent agreement was observed between the predicted forging load and the measured load-displacement data and trends in the evolved microstructure were also well-predicted.

ACKNOWLEDGEMENTS

I would like to express my sincere gratitude to my supervisors Dr Martin Rist, Prof. Lyndon Edwards and Dr Jeffery Brooks who have taught me a lot during my PhD. Without their continuous support, guidance and advice, it would not have been possible to complete this difficult task. From the deepest of my heart, I would like to thank you very much for all your help. Special thanks to Dr Jeffery Brooks and Dr Andrew Wilson for providing samples and discussions, including excursions to TIMET and QinetiQ during this project.

I would like to acknowledge The Open University for its financial support during my PhD. I would also like to thank all technical staff in the Department of Materials Engineering, especially to Mr Stan Hiller, Mr Pete Ledgard, Mr Gordon Imlach, Mr Ian Norman, Mr Tim Gough who have provided me a lot of technical assistantship. Special thanks are also for Ms Rehana Malik and Ms Debbie Derbyshire who have provided me support in University administration.

My grateful thanks are due to Mr Mark Endean as my third party monitor during my PhD. I have had useful discussions about PhD study including good tips for 'job searching'. My acknowledgements go to all students and researchers for their warm friendship, especially to M. Kashif Khan, Himanshu Lalvani, Moshiur Rahman, Joao Gomes, David Sefton, Mehmet Kartal, Olivier Zanellato, Shiv Sharma, Ashwin Rao and Dr David Liljedahl. My special thanks to Dr Supriyo Ganguly who gave me invaluable advice and discussion.

I entirely dedicate this work to my wife Elis Kartika and my son Ichsan Hilmy Mulyadi, who have been the greatest joy and pleasure in my life. Her continuous love and encouragement throughout my PhD has made me strong to face this life with its full of uncertainty. When I faced very difficult and stressful time during Tsunami disaster, when my beloved mum, sister and brother were gone forever and never to be found, she always stood beside and provided me with full of care and love. I also offer this work to my dad and sister for their blessings, love and good wishes. Without them, I would not have accomplished this big achievement in my life.

PREFACE

This thesis is submitted for the degree of Doctor of Philosophy of The Open University, United Kingdom. The work described in this thesis was carried out in the Department of Materials Engineering, Faculty of Mathematics, Computing and Technology, between October 2003 and September 2007, under the supervision of internal supervisors Dr Martin Rist, Prof. Lyndon Edwards and external supervisor Dr. Jeffery Brooks. It is an original work of the author except where clearly referenced. None of this work has been submitted for a degree or other qualification at this or any other university. Some of the results of this work have been published in academic journals and conference proceedings as listed below:

- Published in Journal

1. Mulyadi, M., Rist, M.A., Edwards, L., Brooks, J.W., *Parameter Optimisation in Constitutive Equations for Hot Forging*, Journal of Materials Processing Technology **177**(2006), pp 311-314, Elsevier.

- Presented in Conference and Published in Conference Proceedings

1. M. Mulyadi, M.A. Rist, L. Edwards, J.W. Brooks, A.F. Wilson, *A Hot Deformation Model for Two-Phase Titanium Alloys Based on An Internal Stress Approach*, The 11th World Conference on Titanium, Ti-2007, International Conference Hall in Kyoto, Japan, June 3-7, 2007.

2. M. Mulyadi, M.A. Rist, L. Edwards, J.W. Brooks, *Optimisation and Confidence Region Estimation of Constitutive Parameters in Equation for Hot Metal Deformation*. In: Proceedings of the 8th International European Scientific Association for Material Forming (ESAFORM) Conference, D. Banabic, ed.(2005), pp 61-64: Cluj-Napoca, Romania, April 27-29 ISBN: 9732711736.

Mulyadi

September 2007

Table of Contents

NOMENCLATURE

Symbol	Description
Roman	
$[Al]_{eq}$	Aluminium equivalent
$[Mo]_{eq}$	Molybdenum equivalent
2D	Two dimensional
3D	Three dimensional
a	Value of objective function $F(x)$ at kth iteration
A_i	Instantaneous cross-sectional area
A_o	Contact area
A	Material constant
a_1, a_2, a_3, a_4	Structural constants
AR	Aspect ratio of α-laths
b_1, b_2, b_3, b_4	Structural constants
C	Strain hardening coefficient
c_1, c_2, c_3, c_4	Structural constants
C_{int}	Scaling constant
C_p	Specific heat capacity
D_i	Instantaneous diameter of specimen
d	Dimensional space
$D_{(k)}$	Diagonal scaling matrix
D_0	Initial diameter of specimen
e	Emissivity
EDM	Electrical Discharge Machine
EDX	Energy Dispersive X-Ray
F	Load, external applied deformation force
f	Friction factor
f_α	Volume fraction of α-phase
f_β	Volume fraction of β-phase
$F(\bar{x})$	Objective function
FE	Finite Element

FEGSEM	Field Emission Gun Scanning Electron Microscopy
$f_j(\bar{x})$	Residue of experiment and model output
g	Jacobian gradient vector of first partial derivatives of $F(x)$
h_{th}	Heat transfer coefficient between environment - workpiece
H_{cone}	Height of double truncated cone
H_i	Instantaneous height
H	Hessian matrix of second partial derivatives
H_0	Initial height of work-piece/specimen
h_d	Interface heat transfer coefficient between dies and work-piece
H_j	Hessian matrix of each $f_j(x)$
I	Identity matrix
ID	Inside diameter
k_{th}	Thermal conductivity
K	Scaling constant
k	Number of iteration
k_{ys}	Shear yield stress of forging
LL	α-lath length
LVDT	Linear Variable Differential Transformer
LW	α-lath width
m	Strain rate sensitivity
M	Mass
$m_{(k)}(s)$	Quadratic approximation model of objective function
M_d	Deformation induce martensite temperature
m_f	Shear friction factor
MPT	Multi Purpose Testing
M_s	Martensite start temperature
MTS	Mechanical Testing System
n	Stress exponent
n_{ss}	Structure-stress exponent
OD	Outside diameter
$p_{(k)}$	Ratio indicating the agreement between the model function and the objective function at each step
PM	Powder Metallurgy
q	Structure sensitivity parameter

Q	Apparent activation energy
q_{int}	Structure sensitivity parameter for two-phase interaction mechanisms
Q_{int}	Apparent activation energy for the two-phase interaction mechanisms
$\dot{q}$	Heat flux per unit area at the free surface of the work-piece
r	Disk radius
R	Universal gas constant
s	Step change
S	Temperature sensitivity of the flow stress
SEM	Scanning Electron Microscopy
t_{cone}	Thickness of double truncated cone
T	Working/processing temperature (Kelvin)
t	Time
T_a	Ambient temperature
TC	Temperature in Celcius
T_d	Die temperature
T_s	Specimen temperature
T_{test}	Test temperature
u	Number of data points
w	Number of unknown parameters
V	Volume
V_i	Instantaneous die/crosshead velocity
$\dot{w}$	Heat dissipation rate
$\bar{x}$	Design variables
y_j	Experimental data
Z	Zener-Hollomon parameter
Z_{int}	Zener-Hollomon parameter for two-phase interaction mechanism

Greek

α	Hexagonal closed packed
α	Exponential damping constant relating structure and strain
α'	Hexagonal martensitic phase
α''	Orthorombic alpha phase
α_2	A finely dispersed ordered phase
α_c	Flow localisation parameter
α_{int}	Exponential damping constant relating structure and strain
α_p	Primary alpha phase
α_s	Secondary alpha phase
β	Body centred cubic
β	Exponential damping constant relating stress to strain
$\delta\varepsilon$	Incremental strain
$\delta\sigma$	Incremental stress
δt	Incremental time
δT	Incremental temperature
$\delta T_{adiabatic}$	Adiabatic temperature rise
δW	Incremental mechanical work
δE	Conductive heat loss
$\Delta\sigma$	Magnitude of flow softening
$\Delta\sigma_s$	Change in stress
$\Delta_{(k)}$	A positive scalar representing the size of the region over which the approximation can be 'trusted'
ΔH	Displacement
ΔID	Change of inside diameter
ε	True strain
$\dot{\varepsilon}$	True strain rate
ε_α	Strain in α-phase
ε_β	Strain in β-phase
$\varepsilon_{\alpha\beta}$	Strain in the two-phase $\alpha + \beta$ system
ε_i	Initial strain

φ	Confidence interval
γ	Flow softening index
γ'	Flow softening rate
λ	Generalised structure-related internal variable
λ_{ss}	Steady-state structure related variable (target value)
$(\lambda_o)_{\text{int}}$	Scaling constant
$(\lambda_{\text{ss}})_{\text{int}}$	Steady-state structural related variable related for two-phase interaction mechanisms
λ_i	Initial value of structure-related variable
λ_{int}	Structural related variable for two-phase interaction mechanisms
λ_o	Scaling constant
λ_{LM}	Damping parameter for Levenberg-Marquardt algorithm
μ	The coefficient of Coulomb friction
ρ	Density
σ_α	Stress evolution of the individual α-phase
σ_β	Stress evolution of the individual β-phase
σ	The uniaxial compressive stress
σ_{fric}	Friction-corrected flow stress
σ_i	Initial stress
σ_{is}	Initial target stress
σ_{it}	Instantaneous target stress
$\sigma_{\alpha\beta}$	Total stress of the two-phase α + β system
σ_n	Normal stress
σ_P	Peak stress
σ_{SB}	Stephan-Boltzmann constant
σ_{ss}	Steady-state stress
σ_t	Average flow stress
σ_j	Experimental stress
$\sigma_j(\bar{x})$	Stress value obtained from the model
τ_f	Tresca friction shear stress
τ	Frictional shear stress

Chapter 1

Introduction

In 1791 William Gregor the British mineralogist and chemist first discovered a new element of metal in the black magnetic sand ilmenite, and the metal was then called "titanium", which originated from the titans of Greek mythology as a symbol of power and strength [1]. Titanium ranks as the ninth most plentiful element and the fourth most abundant structural metal in the Earth's crust after aluminium, iron, and magnesium. Its unique inherent properties such as high strength-to-weight ratio, excellent corrosion resistance and moderate strength at high temperatures, make titanium an attractive metal for use in aerospace, chemical and general engineering as well as for biomedical applications. In particular, excellent stability of metallurgical structure at elevated temperatures, combined with superior creep resistance properties, has led to the application of titanium alloys in critical aero-engine parts such as turbine blades and discs in the low and intermediate sections of compressors.

A large number of technologically important titanium alloys consist of two phases (α-phase/hexagonal closed packed and β-phase/body centred cubic) either at service temperatures or at thermo-mechanical processing temperatures. Among two-phase α/β titanium alloys, Ti-6Al-4V is one of the most widely used in the aerospace industry because of its good combination of mechanical properties, and has been one of the most intensively developed and studied of the Ti alloys [2].

In order to shape Ti-6Al-4V into various final forged products, the alloy can undergo several thermo-mechanical processing operations. There are two major requirements related to thermo-mechanical processing of Ti-6Al-4V [3]:

(1) the production of final shapes through primary hot working operations above the β-transus temperature involving coarse ingot breakdown followed by secondary mill operations including hot forging, extrusion and rolling;

(2) the control of microstructure development during different stages of thermo-mechanical processing in order to optimise the final mechanical properties of the alloy.

Hot forging operations usually involve the imposition of non-uniform deformation rate and temperature paths to large plastic deformation, so that the alloy can undergo significant, often beneficial, internal microstructure evolution. As a two-phase α/β alloy system, Ti-6Al-4V shows complex deformation behaviour in the hot forging regime due to the interaction between each constituent. Because of an inherent temperature sensitivity, the internal microstructure, such as the volume fraction and morphology of each phase, evolves during hot forging. In addition, the kinetics of deformation are also highly dependent on working temperatures and applied strain rates during forming operations.

Knowledge of plastic flow behaviour is important for improving the efficiency of industrial hot forging and for control of the microstructure development during deformation. Therefore, it is beneficial to develop a constitutive model that can

characterise the flow stress behaviour and microstructure evolution under certain processing conditions. Proper modelling of the flow stress behaviour requires constitutive equations that can describe the evolution of strain or strain rate in terms of stress, working temperature, time and any suitable microstructure features. The constitutive equations should ideally incorporate some physical understanding of the deformation mechanisms that are likely to operate during forging. Such equations are usually semi-empirical and necessarily complex, often involving highly non-linear, power law or exponential relationships that incorporate a number of material-specific constants. Graphical methods are usually carried out in order to determine these material parameters from well-constrained laboratory-scale experiments, often reducing the problem to a linear relationship between two of the variables at a time, all others being assumed constant. Numerical optimisation methods are available which enable determination of all optimised parameters in a set of equations simultaneously, without resort to simplification of the model used.

Substantial modelling of plastic flow and microstructure development has been performed for single-phase materials including state variable descriptions of flow stress behaviour and the mechanisms of dynamic recrystallisation during hot working [4, 5]. On the other hand, less modelling work has been performed on two-phase alloy systems such as Ti-6Al-4V and the modelling of flow stress and microstructure development during forging of these materials has become one of the major challenges in modern materials science. In particular, there is a need to develop a predictive model that can describe the macroscopic high-temperature deformation behaviour of two phase alloy systems in terms of the hot deformation history of each constituent phase.

From this consideration, the technical objectives of this thesis are:

(i) to characterise the flow stress behaviour of both Ti-6Al-4V and its individual α and β phases at various temperatures by performing isothermal compression tests under constant strain-rate. The relationship between flow stress behaviour and initial pre-forming microstructure will also be investigated by heat treating the as-received globular microstructures to produce an acicular β-transformed microstructure.

(ii) to present a semi-empirical, history-dependent constitutive model for the prediction of the flow behaviour of Ti-6Al-4V which incorporates the temperature-dependent volume fraction and flow properties of the individual α and β phases and an embedded structural-related variable for microstructure prediction. In addition, a strain-rate-jump test will be used to assess the effectiveness of the model developed in simulating a sudden change of deformation path

(iii) to investigate the microstructure evolution of globular and acicular initial microstructures of the alloy under various processing conditions (temperature, strain and applied strain rate) and to employ the constitutive model developed to predict microstructure evolution within a non-uniform deformed work-piece.

1.1. Structure of thesis

Chapter 2 covers the metallurgy, microstructure and properties of α, α + β and β titanium alloys, and includes an overview of state variable modelling for hot forging.

Chapter 3 provides details of the experimental methodology used for this work. It covers material characterisation, procedures of isothermal compression testing, techniques of metallography and quantitative image analysis.

Chapter 4 details the experimental flow stress behaviour of Ti-6Al-4V and its individual α and β phase alloys during isothermal compression testing. Temperature and strain-rate sensitivities of steady-state stress are investigated.

Chapter 5 is concerned with modelling the forging behaviour of Ti-6Al-4V. State-variable constitutive equations are employed to model the entire flow stress behaviour of Ti-6Al-4V and its individual phases. The model is incorporated into finite element model code in order to analyse state variable distribution within the deformed work-piece. A validation of the model is discussed.

Chapter 6 illustrates the microstructure evolution of Ti-6Al-4V with different initial microstructures (globular α and acicular α morphologies). Microstructural measurements under different processing conditions are also described and related to state-variable evolution.

Chapter 7 includes conclusions of the investigation carried out in this dissertation and suggestions for further work.

Chapter 2

Structure Properties and Processing of Titanium Alloys

2.1. Introduction

Since first developed in the 1940s, titanium and titanium alloys have become technologically important alternative materials to steel, aluminium and nickel base super alloys [6]. Their moderate density of about 4.5gcm^{-3}, which lies in between aluminium (2.7gcm^{-3}) and steel (7.8gcm^{-3}), combined with a relatively high yield strength at elevated temperatures and excellent corrosion resistance, has stimulated aerospace industries to explore further application of these alloys for critical aero-engine components, for example, turbine blades and compressor discs [7].

Hot forging, casting and powder metallurgy are usually employed to manufacture titanium products into various shapes. Among these processing routes, hot forging is the most applied manufacturing process due to its capability to induce favourable microstructures.

The combination of plastic deformation and heat treatment applied during forging has enabled this processing method to generate a large variety of final microstructures in titanium alloys. Using thorough knowledge of forge processing windows, and strict process control, reproducible microstructures and mechanical properties of products are possible. The selection of optimum working temperatures and other forging parameters is necessary to obtain beneficial changes in the

morphology of the α and β phases that in turn dictate the final mechanical properties and other characteristics of the alloy [6].

It is important to have a comprehensive knowledge of the physical and mechanical metallurgy of titanium alloys in order to understand the relationship between processing parameters and microstructure evolution. This chapter covers the physical metallurgy and the forging applications of titanium alloys, including their microstructure development during various heat treatments.

2.2. Structure and properties of titanium and titanium alloys

2.2.1. Crystal structure

Like other metals, titanium can crystallize in different crystal structures. The complete transformation from one into another crystal structure is defined as an allotropic transformation. Titanium and its alloys crystallize at low temperatures in a hexagonal closed packed structure (α phase). At high temperatures, a body-centred cubic (β phase) remains stable up to the melting point (~1670°C) [8]. Figure 2.1 schematically illustrates the crystal structures of titanium at the atomic level.

The temperature at which the transformation takes place is called the transus temperature. The β-transus temperature for pure titanium is 882±2°C [9]. The existence of this allotropic transformation and the corresponding β-transus temperature offers the prospect of having alloys with α, β or mixed α/β microstructures and the possibility of using thermo-mechanical processing to extend

further the large variety of microstructure morphologies which influence the mechanical properties of titanium alloys.

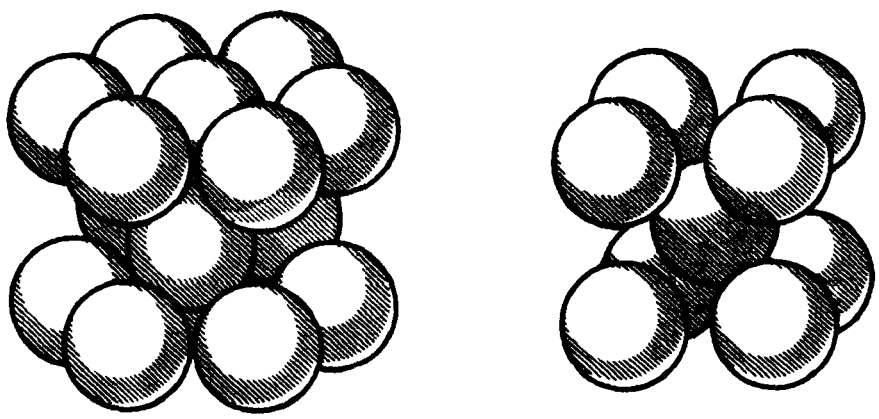

Figure 2.1: Crystal structure of α (hcp) and β (bcc) phase at the atomic level [8].

2.2.2 Effect of alloying elements

As a transition metal categorised in the periodic system chart, titanium with atomic number of 22 and atomic weight of 47.90 has an incomplete shell in its electronic structure which enables the formation of solid solutions with most substitutional elements having a size factor within ± 20%. Reaction between titanium and its alloys with some interstitial elements including the gases oxygen, hydrogen and nitrogen can occur at temperatures well below the respective melting points. In general, titanium is a highly reactive metal that may form solid solutions and compounds having metallic, covalent or ionic bonding with other elements [7]. The number of electrons per atom of the alloying element (or the group number) has an important effect in stabilising either the α or β phase in titanium alloys. Alloying elements with electron/atom ratios of less than 4 stabilise the α-phase, elements with a ratio of 4 have a neutral effect, and elements with ratios greater than 4 stabilise the β-phase [7]. Depending on their interaction with titanium, the elements listed in the periodic systems chart can be classified into 4 main categories, namely [10]:

i). *Continuous solid-solution-forming elements with α or β titanium*: zirconium and hafnium have an outer-shell electronic configuration similar to that of titanium. The structure is also isomorphic to titanium. Thus the phase diagrams with these elements, shown in Fig. 2.2.a, display typical continuous α and β solid solutions. Fig 2.2.b illustrates the effect of alloying elements like vanadium, niobium, tantalum, and molybdenum on the phase diagrams of titanium. These alloying elements are isomorphic to β-titanium and have limited solubility in the α phase. The reaction of titanium with these elements can form a continuous solid solution with the β allotrope of titanium.

ii). *Limited solid-solution-forming elements with α and β titanium*: chromium, manganese, iron, cobalt, nickel and copper undergo eutectoid transformation and lower the β transus. By increasing the group number, the maximum solubility in β titanium decreases and eutectoid temperature increases. The phase diagram of titanium with these elements is summarised in Fig 2.2.c. On the other hand, aluminium, gallium, and indium show a peritectoid reaction and raise the β transus. These elements have higher solubility in α titanium. The phase diagram describing the effect of these alloying elements to titanium alloys is illustrated in Fig. 2.2.d.

iii). *Ionic and covalent compound-forming elements*: flourine, chlorine, bromine, iodine, sulphur, selenium, tellurium, and phosphorous form ionic and covalent compounds with titanium. These elements are not classified into solid solutions in α or β titanium.

iv). *Elements not interacting with titanium*: apart from beryllium, which has limited solubility in β titanium, no other alkali or alkaline earth metal interacts with titanium.

Boron, carbon, oxygen, nitrogen, and hydrogen form interstitial solid solutions because of the different size between the atoms of titanium and these elements. The solubility of these elements varies within α and β titanium. On the order of few 100 ppm of non-metallic elements are typically present as the impurities during manufacturing processes of titanium alloys.

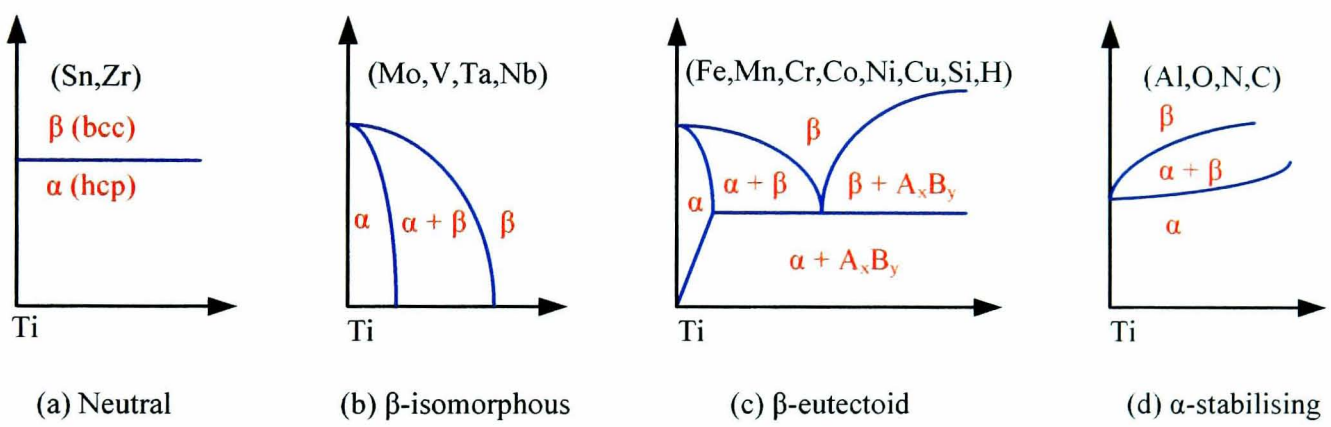

Figure 2.2: The effect of alloying elements on phase diagrams of titanium alloys.

2.2.3 Classification of titanium alloys

The alloying elements of titanium as explained in §2.2.2 can be classified as α-stabilisers, β-stabilisers or neutral, depending on their effect on the β-transus temperature. The α-stabilisers act to raise the β-transus temperature, thus extending the α-phase regime to higher temperatures and enabling development of a two-phase α + β regime. Aluminium is the most important element for stabilising the α-phase.

Interstitial elements like oxygen, nitrogen, and carbon also have stabilising effects on the α-phase. On the other hand, β-stabilisers depress the β-transus temperatures and are categorised as β-isomorphous or β-eutectic elements. Mo, V and Ta are the most important β-isomorphous alloying elements due to their high solubility in titanium. Of the β-eutectic elements, low volume fractions of Fe, Mn, Cr, Co, Ni, Cu, Si and H added to titanium can lead to the formation of intermetallic compounds. Neutral alloying elements like Sn and Zr have little effect on the β-transus temperature. However, these neutral elements contribute to strengthening of the α phase [1].

A three dimensional phase diagram, which consists of two-phase diagrams with α- and β-stabilising elements, is schematically outlined in Fig 2.3. According to this phase diagram, titanium alloys can be classified into three main groups designated α, α+β and β, with further subdivision into near-α and meta-stable β alloys. The individual alloy classes are discussed in the next section below.

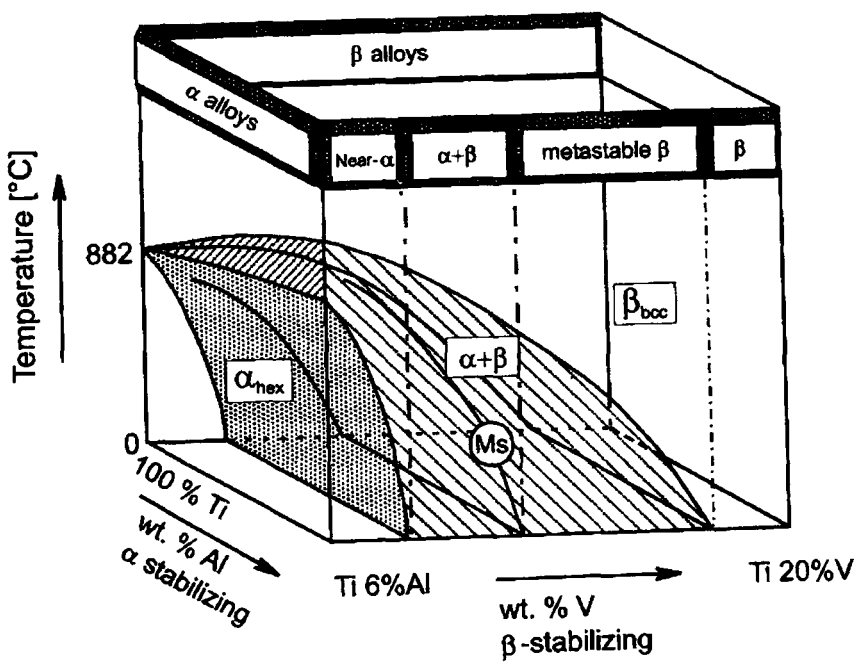

Figure 2.3: Schematic of three-dimensional phase diagram of titanium alloys [1].

2.2.3.1. α-alloys

Essentially, the α-alloys contain all α microstructure, so that, the β phase (stable or meta-stable) cannot be retained at room temperature. Even if the α-alloys are annealed in the α + β phase regime, it is still impossible to produce the β phase since its composition lies to the left of the M_s (martensite start temperature) line at room temperature as shown in Fig 2.3 [11].

The α-alloys include commercially pure titanium (CP-Ti). Among CP-Ti groups, several grades exist depending on the oxygen and iron content. Oxygen and nitrogen cause interstitial hardening and are normally present as impurities. To obtain a specific range of strength levels ranging from 240MPa to 740MPa, the level of oxygen is carefully controlled in several grades of commercial-purity CP-Ti alloys. Among all grades of CP titanium, Grade 1 shows the lowest level of strength and excellent cold formability. Therefore, it is generally used for applications that require excellent corrosion resistance with only low strength, for example, cladding alloys for steel reactors and sheet metal for explosive claddings. Grade 2, with tensile strength ranging from 390MPa to 540MPa is the most widely used CP titanium grade. Grade 3, with a higher strength level, is exclusively used for pressure vessel applications. The highest strength grade 4 (up to 740MPa) is mostly used for mountings and fittings; hot working at 300°C is required for shaping this grade into complex parts [1].

Examples of CP titanium are [12]:

(1) CP Ti grade 1: Ti-0.5Fe-0.4O-0.05N-0.08C-0.015H

(2) CP Ti grade 2: Ti-0.25Fe-0.2O-0.03N-0.08C-0.015H

(3) CP Ti grade 3: Ti-0.03Fe-0.2O-0.05N-0.08C-0.015H

(4) CP Ti grade 4: Ti-0.2Fe-0.15O-0.08C-0.015H

Alpha alloys contain α-stabilising elements such as aluminium and oxygen and/or neutral elements like tin and zirconium. These alloying elements produce solid solution hardening and increase tensile strength from 35MPa up to 70MPa for each percent increment of the added element. However, the amount of α-stabilizing elements alloyed to titanium must be limited to 9% of the so-called 'aluminium equivalent' to avoid embrittlement effects that occurs due to an ordering reaction. The ordering reaction, particularly in binary Ti-Al alloys, can lead to the formation of a finely dispersed ordered phase (α_2) at elevated temperature. The α_2 phase has a coherent crystal lattice with the α phase over a wide temperature range. Aluminium equivalent is determined empirically from the composition by summing the weight percentage as follows [7]:

$$[Al]_{eq} = Al + \frac{1}{3}Sn + \frac{1}{6}Zr + 10(O + C + 2N) \qquad \text{(Eq.2.1)}$$

The α-alloys have a single phase, retaining hcp crystal structure at room temperature. These alloys are among the most difficult titanium alloys to forge as their hcp lattice structure causes them to exhibit a significant rate of strain hardening behaviour. However, these alloys display good ductility down to very low temperatures and

consequently their tensile strength is relatively low. Their high thermal stability leads to reasonable creep resistance and toughness. The α-alloys are not heat treatable for modifying their mechanical properties, but are easy to weld. The most commonly used α-alloy is the ternary composition Ti-5Al-2.5Sn. As one of the oldest developed titanium alloys, Ti-5Al-2.5Sn has gained wide acceptance for cryogenic applications, such as a material for hydrogen tanks and pressure vessels [3].

The mechanical properties of α-alloys are relatively insensitive to microstructure. However, morphologies of the α phase can be obtained in three different forms [7]:

a. Equi-axed grains (see Fig. 2.4.a) with relatively small size can be formed when the alloys are hot worked and annealed in the α-phase field. Because of the low temperatures involved, grains are inhibited from excessive growth and grain boundaries are pinned by the impurities that are usually present in the alloys.

b. Hexagonal martensitic phase α′, can be produced by quenching from the β-phase field, as shown in Fig. 2.4.b, in which the prior β-grains are still clearly visible. The α′ is produced by a massive transformation which contains a high density of dislocations and little or no twinning. The structure of α′ comprises colonies of laths or plates separated by low angle boundaries. The hardening effect of this structure is negligible due to the large size of the prior β-grains and the absence of supersaturation of the substitutional alloying atoms.

c. Widmanstatten plates as illustrated in Fig. 2.4.c, can be produced by slow cooling from the β-phase field. For high purity alloys, this microstructure is referred to as serrated α, whereas, if β-stabilising elements/impurities such as hydrogen are present, the α-plates may produce a 'basket weave' effect. (Fig. 2.4.d).

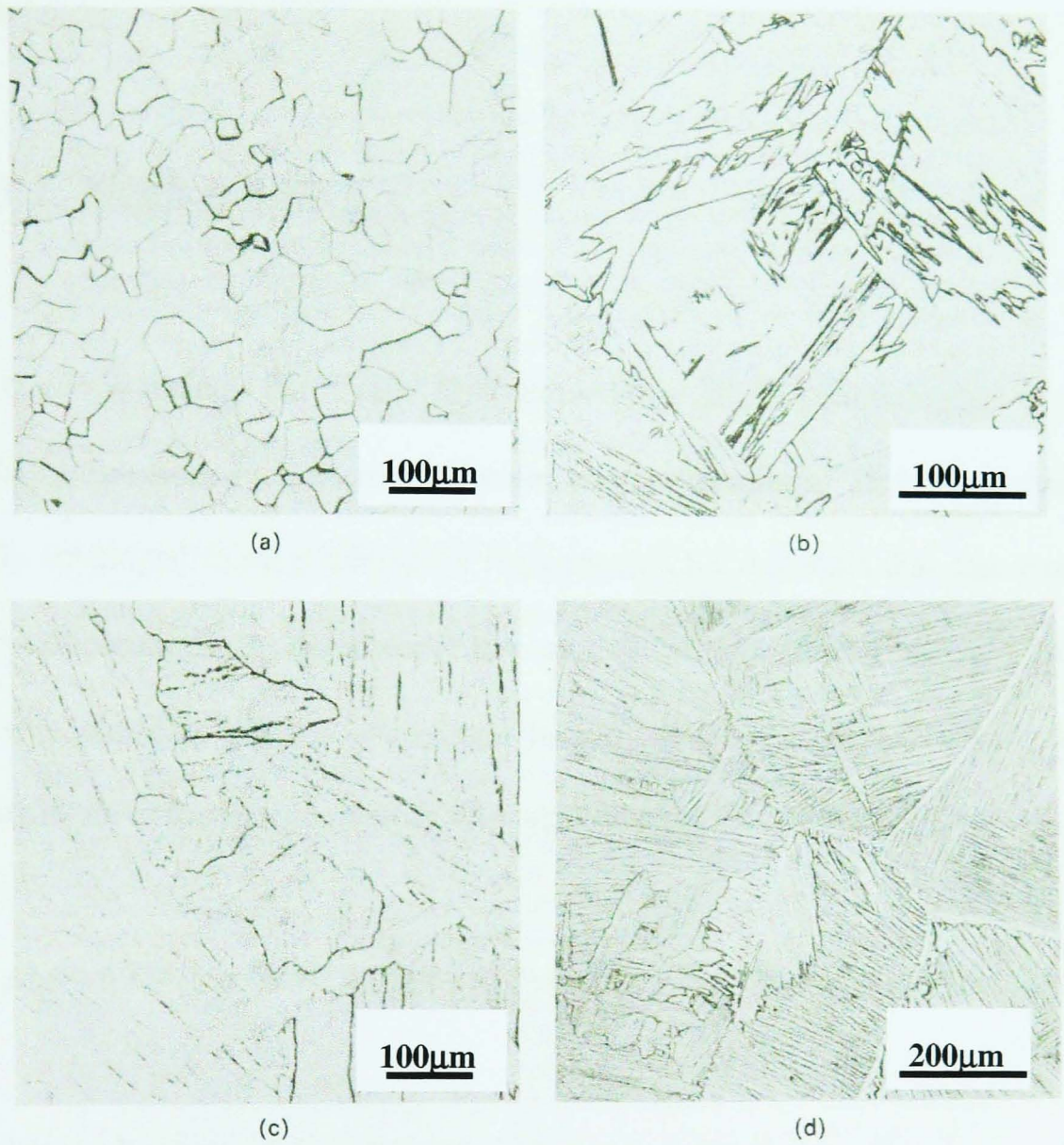

Figure 2.4: Microstructure of CP Titanium: a). equi-axed grains of α annealed at 700°C for 1 hr; x100 b). Martensitic α′ quenched from β-phase field; x150 c). Widmanstatten plates of α air cooled from the β-phase field; x100 d). A basket weave structure of Widmanstatten plates of the α-phase delineated by small amounts of the β-phase; near-α alloy IMI 685 air-cooled from the β-phase field; x75 [7].

α-alloys which have been cooled from the β-phase field show a lower level of tensile strength, room temperature fatigue resistance and ductility compared to alloys having an equi-axed type microstructure. However, the characteristic microstructure obtained from β-phase cooling exhibits a higher level of fracture toughness and creep resistance. The morphology of the grain (size and shape) and the structure of grain boundaries of titanium alloys are important in determining their bulk mechanical properties.

2.2.3.2. Near-α alloys

Near α-alloys include the classic high-temperature alloys containing up to 2% β-stabilising elements such as molybdenum and/or vanadium. This alloy class was initially developed to meet aerospace requirements for materials that can operate at higher temperatures in the compressor section of gas turbine engines. The β-stabilising elements alloyed are related to the 'molybdenum equivalent', defined empirically from the composition of alloying elements (in %wt) by [7]:

$$[Mo]_{eq}=Mo+0.6V+0.44W+0.28Nb+0.22Ta+1.25Cr+1.25\ Ni+1.7Co+2.5Fe \quad \text{(Eq.2.2)}$$

β-stabilising elements are intentionally added to broaden the α + β temperature field so that these alloys can be hot worked within the α + β and β phase fields. The final microstructure of these alloys are primarily α-phase containing small amounts of retained meta-stable β produced by cooling as solute enrichment can occur on passing through the α + β field [11]. By alloying with β-stabilising elements, the

forgeability of near-α alloys can be improved. In addition, the alloys can combine excellent creep resistance from the α-phase with higher strength properties from the α + β microstructure. Because of this beneficial property combination, this alloy class has been the most widely used commercial high temperature Ti alloy in aero-engine applications, where the upper operating temperature is in the range 500-550°C. Near α-alloys also show higher tensile strength at room temperature than the α-alloys and have superior creep resistance to all the titanium alloys at temperatures above 400°C. The improvement in strength and creep resistance is mainly due to the formation of a martensitic structure α′ (produced by quenching from β phase field) and the manipulation of α/α′ phase during heat treatment.

Most of the near-α alpha alloys are hot worked and heat-treated in the α + β phase field in order to retain the primary α phase. Near-α alloys included in this group are Ti-8Al-1Mo-1V (Ti-8-1-1), Ti-6Al-2Sn-4Zr-2Mo-0.1Si, Ti-11Sn-2.25Al-5Zr-1Mo-0.2Si (IMI 679) [3].

To obtain the maximum creep strength properties, the alloys are solution treated at a temperature at which the volume fraction of the α and β phases is approximately equal. They are then air cooled to obtain equi-axed grains of primary α and Widmanstatten α which forms by nucleation and growth from β-phase as shown in Figure 2.5.a. If the cooling rate is faster, then the β-phase will transform into a martensitic α′ structure that leads to some increase in tensile strength. However, this typical martensitic α′ structure will reduce the creep resistance properties at the upper end of the temperature range (>450°C). In order to enhance creep properties,

the alloys are normally subject to a stabilising heat treatment at temperatures ranging from 500 up to 590°C.

Ti-8Al-1Mo-1V was the first near α-alloy specially developed for high temperature applications. The alloy had a lower density plus good weldability and forgeability due to a high percentage of β-stabilising elements. However, the percentage of aluminium equivalent content in excess of 9% has led to problems of instability, loss of ductility and stress corrosion due to the ordering reaction of α_2 formation after long term service at high temperature [1].

The next generation alloy, Ti-6-2-4-2, was developed by TIMET and has a lower content of aluminium equivalent. In the 1970s, RMI modified the alloying elements of Ti-6-2-4-2 by introducing a small amount of Si. The addition of up to 0.1% Si could significantly increase the strength and creep resistance behaviour of these alloys. Hereafter, the alloy was known as Ti-6-2-4-2-S. At high temperatures, silicon would dissolve in the α-phase and precipitate as silicides that can pin mobile dislocations from climb and glide, which in turn inhibits deformation from taking place. For this reason, all new high temperature titanium alloys have been alloyed with up to 0.5% of Si. The first commercially available near-α alloy containing Si was IMI 679 developed by IMI in the United Kingdom.

Some of the near-α alpha alloys are also hot worked and heat-treated in the β phase field in order to improve creep resistance performance. Hot working carried out in the β-phase field has the advantage of reducing the forging load required because of the higher temperature involved and due to the easier deformation of the β phase.

The near-α alloys included in this group are Ti-6Al-5Zr-0.5Mo-0.25Si (IMI 685), Ti-5.5Al-3.5Sn-3Zr-0.25Mo-1Nb-0.3Si (IMI 829), and Ti-6Al-2.75Sn-4Zr-0.4Mo-0.45Si (Ti-1100) [3].

IMI 685 was the first alloy used in the β-annealed condition due to the superior creep performance obtained from this microstructure. Laths of martensitic α′ (as shown in Figure 2.5.b) are produced by rapid quenching of the alloy from 1050°C. Residual stress induced by quenching can be reduced by aging at temperatures ranging from 500-550°C. The aging treatment can also cause some strengthening because the martensitic α′ produced from quenching transforms into laths of α bounded by a fine dispersion of particles. From electron diffraction studies, these fine particles have been identified as either body centre cubic, originating from β-phase titanium, or face centre cubic. Fine particles of β-phase are produced by globularisation of alpha laths but little is known of the other phase except that it contains titanium, molybdenum and silicon. If aging is performed at higher temperatures, e.g. 850°C, softening behaviour will occur and $(Ti, Zr)_5Si_3$ will precipitate on dislocation networks in the boundaries between the α-laths as shown in Figure 2.5.c [7].

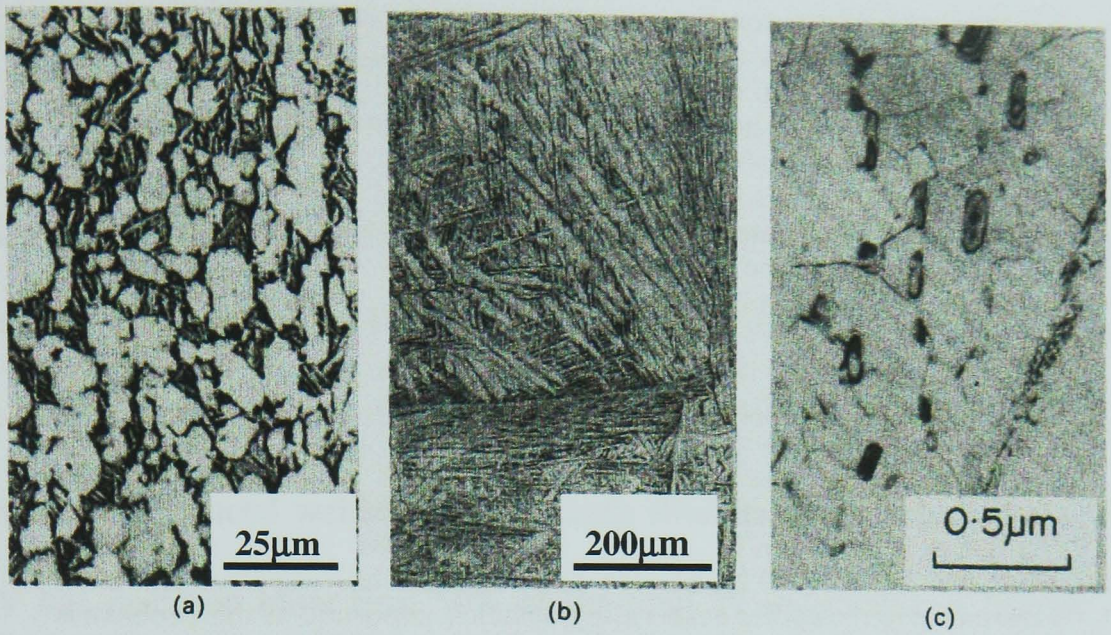

Figure 2.5: a). Microstructure of IMI 679 air-cooled from the α + β phase field showing primary (white) and Widmanstatten α; x500. b). IMI 685 oil-quenched from the β-phase field showing laths of the martensitic α′-phase delineated by the β-phase; x75. c). Microstructure of IMI 685 quenched from the β-phase field and aged at 850°C illustrating particles of the phase $(TiZr)_5Si_3$; x30000 [7].

IMI 685 exhibits high creep resistance within the temperature range 450 to 520°C.

The creep properties can be maximised by transforming the microstructure into a basket weave type morphology. This type of microstructure is obtained by applying intermediate quenching with rates of 1 to 10°C/s from the β-phase field.

The follow up near-α alloy, Ti-5.5Al-3.5Sn-3Zr-0.25Mo-1Nb-0.3Si designated as IMI 829, was developed to improve high creep resistance properties up to 600°C. Compared to the earlier near-α alloys, IMI 829 exhibit superior oxidation resistance which has enabled this alloy to be used in long term service at high temperatures.

The most advanced conventional high temperature near-α alloy today is the American TIMETAL 834, initially developed in the UK, which can withstand high service temperatures close to 600°C if long-term oxidation protection is provided [1].

2.2.3.3. α + β alloys

Ti-6Al-4V (IMI 318) was initially developed at the Illinois Institute of Technology in the United States in the early 1950s. The alloy was developed in order to improve the tensile strength and forgeability over previous α-alloys. Although α + β alloys exhibit slightly reduced weldability and creep strength properties above 400°C, Ti-6Al-4V has made up more than 50% of the total Ti alloy sales in Europe and the United States [7].

The α + β alloys mostly contain α-stabilising elements to strengthen the α phase, as well as 4-6 % of β-stabilising elements to retain some β phase on quenching from the β and α + β phase fields. Such a proportion of α and β-stabilising elements produces a broad α + β phase field region down to room temperature. In addition, the β-stabilising elements contribute solid solution strengthening of the β-phase, although these effects are relatively small. By subsequent tempering or ageing treatments, the tensile strength properties of the alloys can be improved, exceeding 1400MPa at room temperature [7].

The final microstructure of α + β alloys which have a phase diagram of the β-isomorphous type (Figure 2.2.b) is sensitive to heat treatments employed, i.e., whether the alloy is slow-cooled from the β-phase (β-annealed) or from the α + β phase (mill-annealed). For the β-phase annealed, the α-phase usually transforms into Widmanstatten laths in a β-matrix while the β-phase possibly transforms into martensitic α′ structure, depending on the cooling rate applied. A basket-weave

structure, as shown in Figure 2.6.a, is the typical microstructure obtained if slow cooling rates are employed. In general, the rate of cooling is important in determining the morphology of the Widmanstatten laths. On the other hand, the typical microstructure produced by cooling from the $\alpha + \beta$ phase field (mill-annealed) is an equi-axed structure consisting of primary α and β-transformed grains as displayed in Figure 2.6.b. The structure of β-transformed material (the Widmanstatten laths) is shown in Figure 2.6.c taken by the transmission electron microscope. In addition, mill-annealing, usually performed at 700°C, can relieve residual stresses produced during manufacturing processes. Subsequent hot working and annealing cycles can be carried out to modify grain sizes, whilst the volume fraction of primary α is determined based on the lever rule.

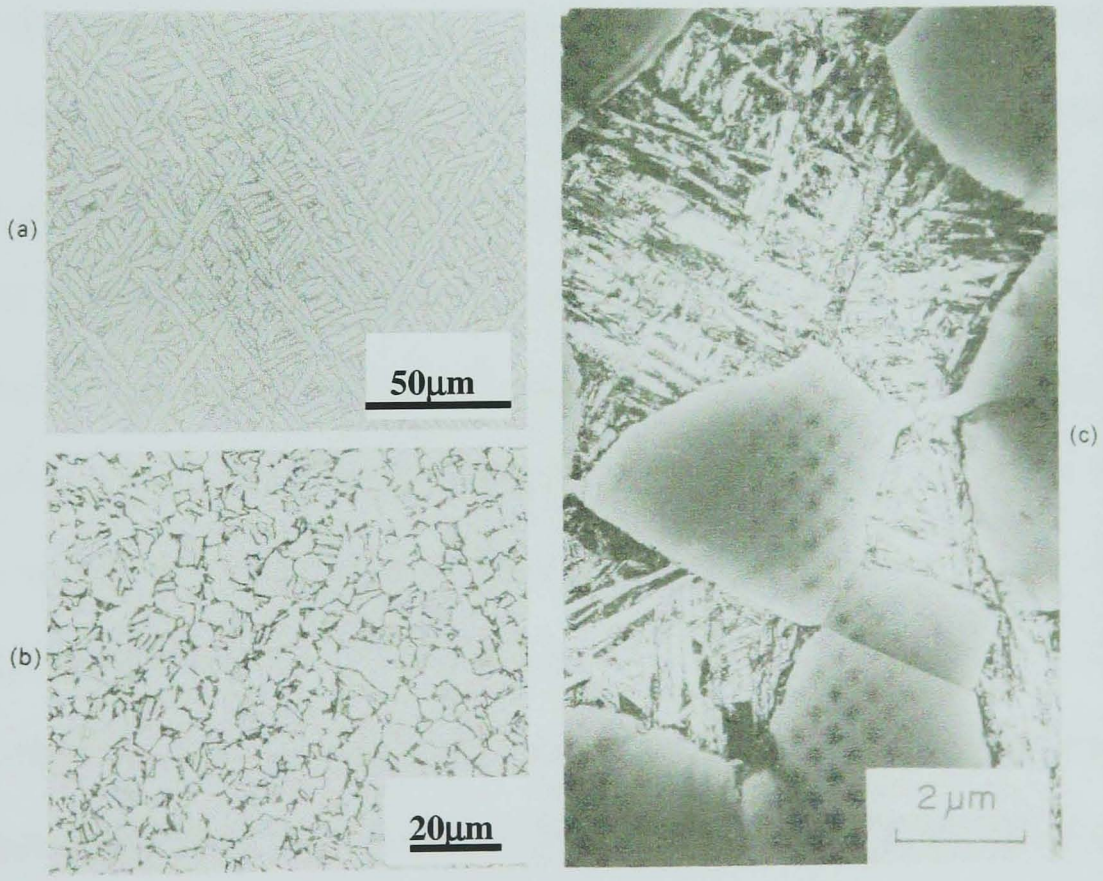

Figure 2.6: Microstructure of Ti-6Al-4V: a). Basket weave structure of Widmanstatten α-laths within a β matrix slowly cooled from the β-phase field; x320 b). Equi-axed grains of α and transformed β (Widmanstatten α) mill-annealed at 700°C; x500 c). TEM micrograph of the structure of Widmanstatten α in (b) x7500 [7].

In the β-eutectoid alloys, e.g., Ti-230, a lamellar eutectoid of α and a compound of Ti_2Cu is produced by cooling from the β-phase field at very slow rates. Due to the embrittlement caused by the phases produced, the β-eutectoid alloys have not become commercially available for engineering applications. Whilst Ti_2Cu is particularly useful for strengthening Ti-230, some other alloys use other precipitate strengthening mechanisms.

Among the α + β alloys, the annealed condition alloys are mostly used for engineering applications. The microstructure and the mechanical properties of these alloys are highly influenced by prior forging history. The alloys forged in the α + β phase field, which have an equi-axed type of microstructure, are found to be more ductile, whilst fracture toughness and fatigue strength properties are much higher for the β-forged and annealed alloys. For fully β-heat treated alloys, it demonstrates superior low cycle fatigue strength properties, but exhibits poor strength properties for high cycle fatigue. The excellent fatigue performance of β-annealed alloys is associated with the fact that cracks can only propagate at a slower rate through the microstructure consisting of acicular Widmanstatten laths of the hard α-phase, with the possible occurrence of crack branching. For applications that require higher strength, various α + β alloys have been developed to meet the requirement such as Ti-6Al-6V-2Zr-0.7Fe-0.7Cu (Ti-662), Ti-4Al-4Sn-4Mo-0.5Si (IMI 551), Ti-6Al-2Sn-4Zr-6Mo and Corona-5 (Ti-4.5Al-5Mo-1.5Cr). These alloys were mostly used for aircraft engine mounting brackets and undercarriage components. Other α + β alloys, like Ti-6-2-2-2-2, Ti-55-24-S or Ti-17, were particularly developed for high temperature applications in gas turbine engines up to 400°C [1].

2.2.3.4. Near-β alloys

Near-β or meta-stable β alloys are defined as titanium alloys containing about 10-15% of β-stabilising elements (as the minimum limit of composition to retain β-phase) in order to suppress the martensitic start transformation (M_s) down to room temperature [13]. This means that the alloys can retain the β-phase by avoiding the β-phase transformation into a martensitic (α′) structure following rapid quenching. However, the β-phase can still be transformed into α′ by mechanical working carried out above room temperature. This phenomenon occurs because the near-β alloys have a certain temperature at which deformation-induced martensite starts to form (M_d), and this usually lies above room temperature [11, 14]. The retained β-phase is called meta-stable due to the fact that it still can precipitate the α-phase during aging treatment at subtransus temperatures [15].

The complex microstructure of near-β alloys has been a key factor for designers when optimising mechanical properties to promote higher strength and higher toughness. The meta-stable alloys having both properties, e.g., Ti-10V-2Fe-3Al (Ti 10-2-3) were first commercialised between 1969 and 1978. In general, the near-β alloys have been successfully used for industrial applications but with some limitations due to their relatively high specific weight, modest weldability, poor oxidation and complex microstructure [1].

2.2.3.5. β-alloys

The addition of 30% of β-stabilising elements to titanium allows retention of a fully stable 100% β-phase at room temperature. The beta stability can be related by the molybdenum equivalent as a parameter that quantifies the combination of the effects of the various β-stabilising elements [16]. A content value of 10% of β-stabilising elements is the minimum limit to produce stable β-phase. The fully β-alloys offer superior cold forgeability due to their body centre cubic structure. At lower temperatures (~ 800°C), the alloys can undergo recrystallisation to produce a finer and defect-free β grain structure upon hot deformation [11]. These alloys can also be strengthened up to 1400MPa by age hardening. The high concentration of β stabilising elements gives an advantage in increasing hardenability through heat treatment. However, it also causes ingot segregation problems and increases the overall density so that some alloys are found to have relative densities in excess of 5 [7].

Thermo-mechanical processing of the β-alloys consists of a hot working operation followed by heat treatment. For the leaner beta alloys, the final step of the hot working is performed in the α + β phase field whilst for the richer beta alloys, the hot working step is preferably carried out in the β-phase field. The heat treatment steps consist of a solution treatment carried out at subtransus or supertransus temperatures followed by quenching and subsequent aging treatment. Supertransus solution treatment produces coarse β microstructure whilst the precipitation of primary α (α_p) occurs from the solution treatment carried out at temperatures slightly below the β

transus. During this subtransus solution treatment, the chosen temperature determines the volume faction of α_p. On the other hand, hot working operations (e.g. forging and rolling) are intentionally performed to change the morphology of α_p from needle-like into globular shape. Again, the volume fraction and the size of the secondary α (α_s) are also controlled by aging temperature, time and solution treatment temperature [17]. The α_s can contribute significant strengthening effects to the β alloys. At lower temperatures ranging from 400 to 600°C, the α_s can precipitate in a homogeneous structure in lean beta alloys like Ti-10-2-3, or be inhomogeneous in richer β-alloys such as Ti-3Al-8V-6Cr-4Mo-4Zr (BETA C).

Cold working is usually carried out to homogenise distribution of the α_s [18]. Examples of β-alloys are the American Ti-8Mo-8V-2Fe-3Al (Ti 8823), Ti-11.5Mo-6Zr-4.5Sn (Beta III) and Ti-15V-3Cr-3Sn-3Al (Ti 15-3-3-3). These alloys can exhibit higher strength levels by a combination of solid solution hardening and age hardening, and have been used for aircraft sheet and casting parts, fasteners and springs [19].

2.2.4 Microstructure of titanium alloys

Due to the allotropic and phase transformations, titanium alloys can exhibit a large variety of microstructures depending on alloy chemistry and thermo-mechanical treatments. The latter consist of complex sequential processes like solution heat treatment, deformation, and aging as schematically illustrated in Figure 2.7. The morphological evolution of the α and β phases due to metallurgical processes like

recrsytallisation, globularisation/spheroidisation etc. has led to more variations of microstructure produced [13].

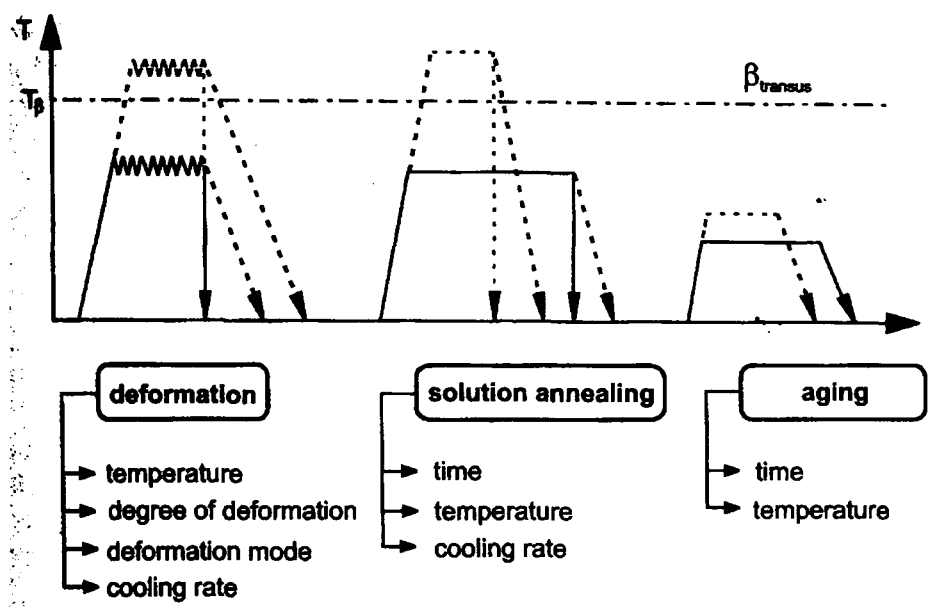

Figure 2.7: Schematic of thermo-mechanical processing of titanium alloys [1].

There are two microstructures resulting from extreme arrangements of the α and β phases, i.e., acicular/lamellar and globular/equi-axed microstructures [12]. The acicular microstructures are produced upon cooling from the β phase field through nucleation of α phase at grain boundaries, and then growth into the prior β grains. On the other hand, globular microstructures are the result of a recrystallisation processes, where the alloys have been hot worked in the α + β field to introduce sufficient hot work into the material. Both types of structure can have a fine and a coarse arrangement of each phase depending on cooling rates.

A schematic pseudobinary phase diagram of Ti-6Al-4V shown in Figure 2.8 can be used to illustrate the microstructure development of titanium alloys. In this case, the β-transus is the key temperature for separating the single β-phase and the two-phase

$\alpha + \beta$ fields. The evolution of an acicular microstructure obtained upon cooling from the β-phase field can be classified depending on cooling rate [1]:

a. On slow cooling (e.g. furnace cooling) from super-transus temperatures, β-phase transforms into Widmanstatten α phase by nucleation and growth (as shown in Figure 2.8.a) resulting in pure lamellar microstructures. Small amounts of β-phase might be retained depending on concentration of alloying elements. The presence of β-phase can be increased as the alloying elements are increased.

b. On rapid quenching (e.g. water quenching) from supertransus temperature, β-phase transforms into martensitic α' (hcp) resulting in a very fine needle-like microstructure (as shown in Figure 2.8.b) or orthorhombic α'' in the alloys which have a higher proportion of β-stabilising elements.

Upon cooling from sub-transus temperature ($\alpha + \beta$ phase field), the development of acicular/lamellar microstructures can be classified as:

a. On slow cooling from sub-transus temperature, small amounts of β-phase are retained surrounding the coarse and light coloured α lamellae as shown in Figure 2.8.c and e.
b. On rapid cooling from sub-transus temperature and above the martensitic start temperature (M_s), β-phase transforms into martensite as shown in Figure 2.8.d. The microstructure that results from rapid cooling from a temperature lower than M_s is shown in Figure 2.8.f. Here, martensite is no longer obtained and the volume fraction of the β-phase is further decreased.

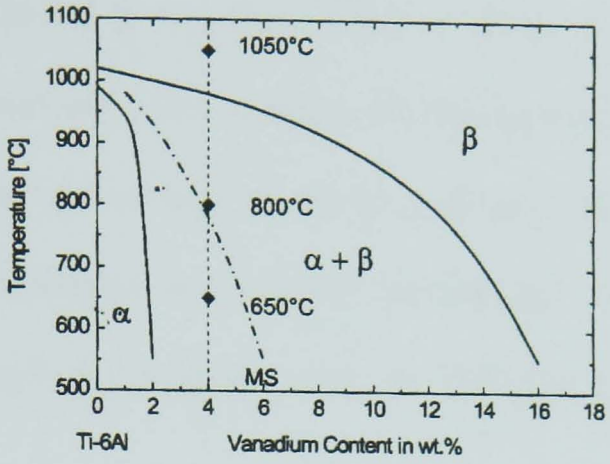

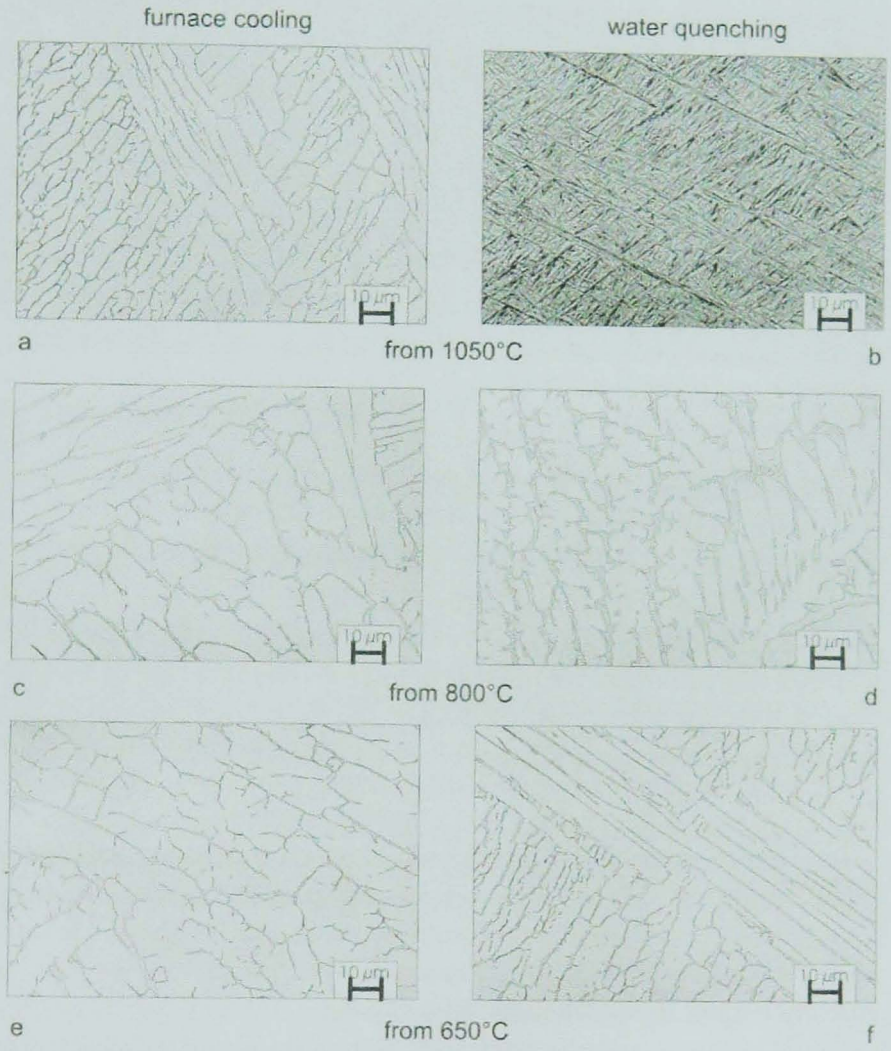

Figure 2.8: A schematic pseudo-binary phase diagram of Ti-6Al-4V; microstructure obtained after slow cooling (50°C/hr) and water quenching from β and α + β phase fields [1].

For globular microstructures, the evolution of microstructure upon subsequent solution heat treatment in the $\alpha + \beta$ phase fields is shown in Figure 2.9.a. As the annealing treatment is prolonged, the globular microstructures coarsen as shown in Figure 2.9.b. Sub-transus solution heat treatment produces a bimodal microstructure with a combination of globular and acicular morphology consisting of globular primary α within an acicular $\alpha + \beta$ matrix, as shown in Figure 2.9.c and d.

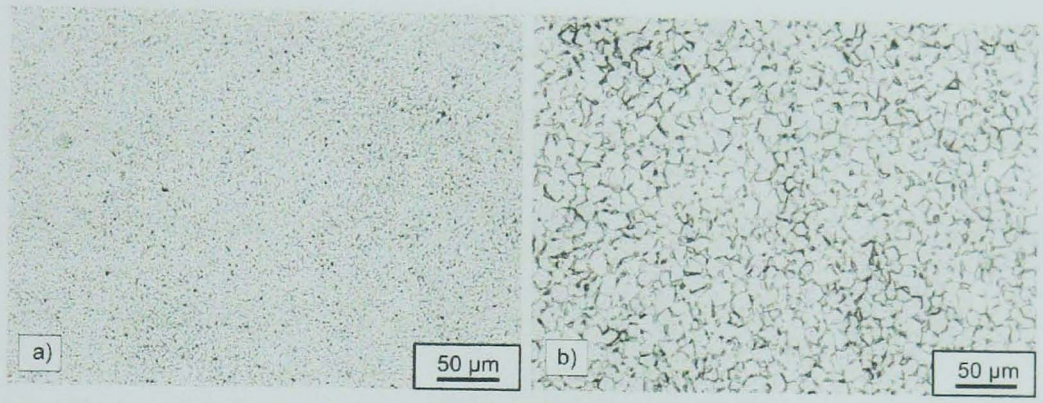

Figure 2.9: Globular microstructures of Ti-6Al-4V: a). fine; b). coarse; c). and d). bimodal microstructures (optical and transmission electron micrograph) [1].

2.2.5 Properties of titanium alloys

The mechanical and physical properties of titanium alloys are strongly influenced by the volume fraction, the morphology and the inherent properties of the α and β phases. Compared with bcc β phase, the anisotropic hcp α phase shows limited plastic deformability, lower ductility, higher strain hardening, higher creep resistance

and lower diffusion rate. The differences of properties of the three main classes of titanium alloys can be summarised as follows [1]:

a. α alloys have a lower density than β alloys since the β alloys usually contain heavy elements such as Mo or V.

b. α alloys as a single phase exhibit only moderate strength whilst the $\alpha + \beta$ and β alloys can be age-hardened to a high and very high level of strength respectively.

c. β alloys show lower ductility due to their higher strength levels. Ductility is affected by microstructure. Without age hardening, β alloys exhibit relatively similar ductility to α and $\alpha + \beta$ alloys. By applying β-heat treatment, β alloys can exhibit very high ductility.

d. α alloys have superior creep resistance behaviour due to the limitation of atomic diffusion and deformability in the hcp crystal lattice. For lamellar and bimodal microstructures with a discontinuous β distribution, good creep resistance is also displayed.

e. α alloys show excellent corrosion resistance due to their higher affinity for oxygen to form a dense oxide layer (TiO_2) on the surface.

f. α and $\alpha + \beta$ alloys show higher weldability than β alloys particularly when the β alloys are age hardened to higher strength. However, for high strength $\alpha + \beta$ alloys, it is extremely difficult to weld.

g. Due to their limited deformability and strain hardening behaviour, α and $\alpha + \beta$ alloys can only be forged at elevated temperatures. Consequently, α and $\alpha + \beta$ alloys show more limited cold forgeability than β alloys.

In addition, the mechanical properties of titanium alloys are also affected by morphology, e.g. the shape of the α phase in α + β alloys [20]. Fine equi-axed microstructures exhibit higher fatigue strength, higher ductility, better ability to retard crack initiation and are a requirement for superplastic forming. On the other hand, coarse lamellar microstructures show higher fracture toughness as well as a superior resistance to creep and fatigue crack growth. Interfaces between α and β phases in lamellar and equi-axed structures are usually preferred sites for void nucleation during tensile loading. Voids can grow on both lamellar and equi-axed structures along the path of the interface between α and β phases. However, in lamellar structures, voids reach a critical size for fracture at lower strains compared to equi-axed structures, where hard α phases act as crack stoppers. Thus, the lamellar structures have lower ductility than equi-axed ones. A well-balanced combination of these mechanical properties can be achieved from mixed microstructures of equi-axed primary α within lamellar β phase, that is, bimodal microstructures.

2.3 Forging of titanium alloys

Thermo-mechanical treatment of raw titanium is an important process that must be carefully performed in order to achieve high quality forged products. The starting microstructures of titanium alloys are affected by this treatment and thermo-mechanical processing can be tailored to obtain a required final microstructure which in turn can dictate the mechanical properties for suitable applications.

The processing routes necessary to produce forging stocks of titanium involve a number of processes such as mixing of titanium sponge and alloying elements,

pressing into briquette shapes and welding to form electrodes for subsequent double or triple vacuum arc-remelting as shown in Figure 2.10. The cylindrical cast ingots produced are then radial or hand forged into billet and bar forms. Alternate forging steps are performed at subtransus and super-transus temperatures in order to break up the coarse ingot structure into fine equi-axed microstructures. The final step is usually carried out by die forging in the $\alpha + \beta$ field.

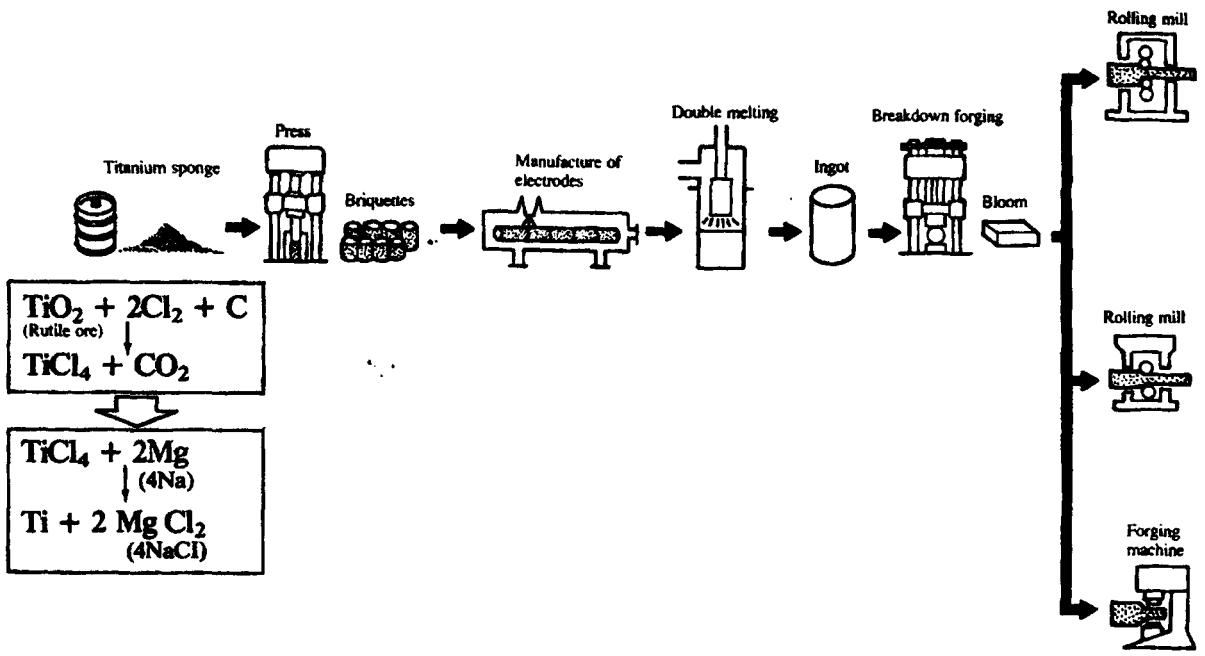

Figure 2.10: Processing routes of forging stock production of titanium alloys [21].

Further principal processing of the forging stock can be classified as [22]: (i) conventional (α/β) forging, in which the forging is performed below the beta transus; and (ii) β forging, in which the deformation of the alloy is conducted above the beta transus. However, there are possible combinations on these approaches in order to achieve desired final forging microstructure and mechanical properties depending on service requirements. The morphology of the α-phase are often modified by combinations of forging and heat treatment during the conventional (α/β) forging of the α and $\alpha+\beta$ alloys. On the other hand, fully stabilised β-alloys are typically forged above the beta transus since the manipulation of the α-phase by varying forging parameters is less prevalent [23].

The characteristic of each forging can be summarised as (Figure 2.11) [6]:

a. α/β forging

- The forging temperatures are usually 30°C to 100°C below the β transus temperature. The required temperature is high enough to avoid cracking problems when the alloys are forged at high strain rate.
- The heating time during deformation has to be carefully controlled to avoid overheating of the microstructure above the β transus temperature.
- The amount of deformation and strain rate applied have to be controlled in order to produce an equi-axed (globular) primary α morphology resulting from recrsytallisation and globularisation. Air cooling after forging is usually sufficient to maintain the final desired microstructures.

b. β forging

- The forging has to be carried out before the β/α transformation takes place (due to its greater sensitivity to deformation conditions).
- The soaking time prior to forging must be controlled to avoid excessive grain growth and hydrogen pick-up.
- The degree of deformation and cooling rate after β forging have to be controlled to avoid undesired microstructure development, such as decoration of grain boundaries with α phase.

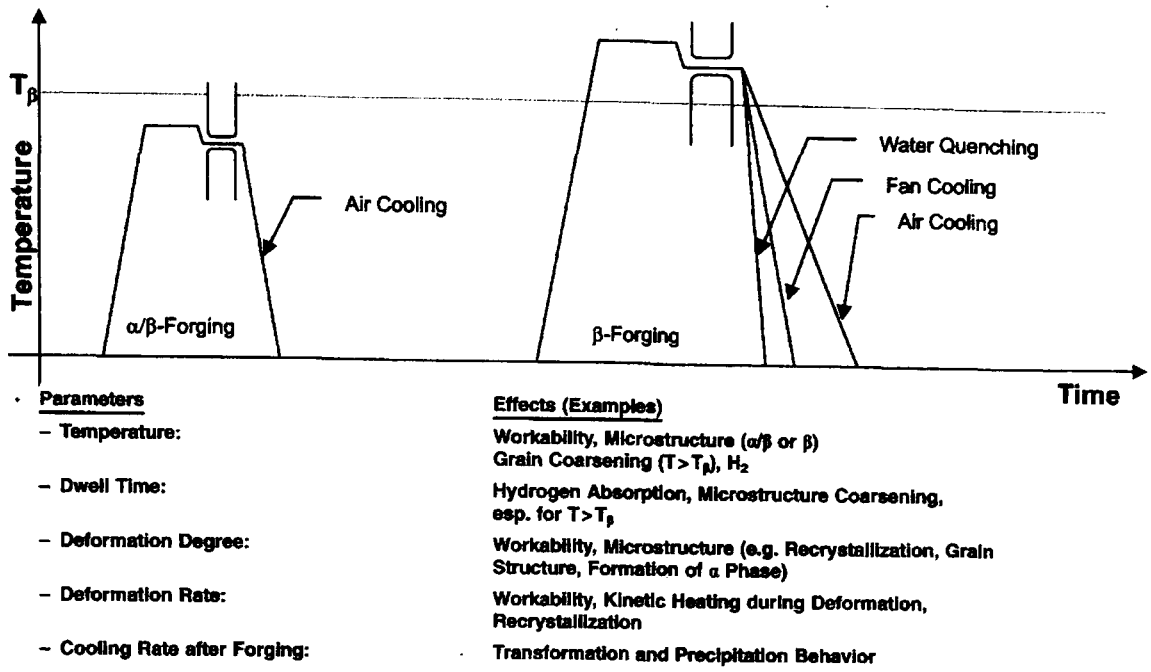

Figure 2.11: Important parameters affecting forging of titanium alloys [6].

Typical heat treatment, as shown in Figure 2.12, consists of β and α/β solution treatments to obtain various morphologies of α phase. The β solution treatment can produce lamellar or Widmanstatten α lath structure which has higher fracture toughness and lower ductility. On the other hand, the α/β solution treatment leads to the formation of bimodal microstructures consisting of equi-axed primary α within a β transformed matrix. The volume fraction of the primary α is controlled by the solution treatment temperature whilst the colony size of the lamellar structure obtained from β transformation is determined by the cooling rate. To increase the alloy's strength, a subsequent stress relief annealing or an aging treatment can be performed. However, the temperature for this treatment should be carefully selected, treatment at a too high temperature would not result in a higher gain in strength.

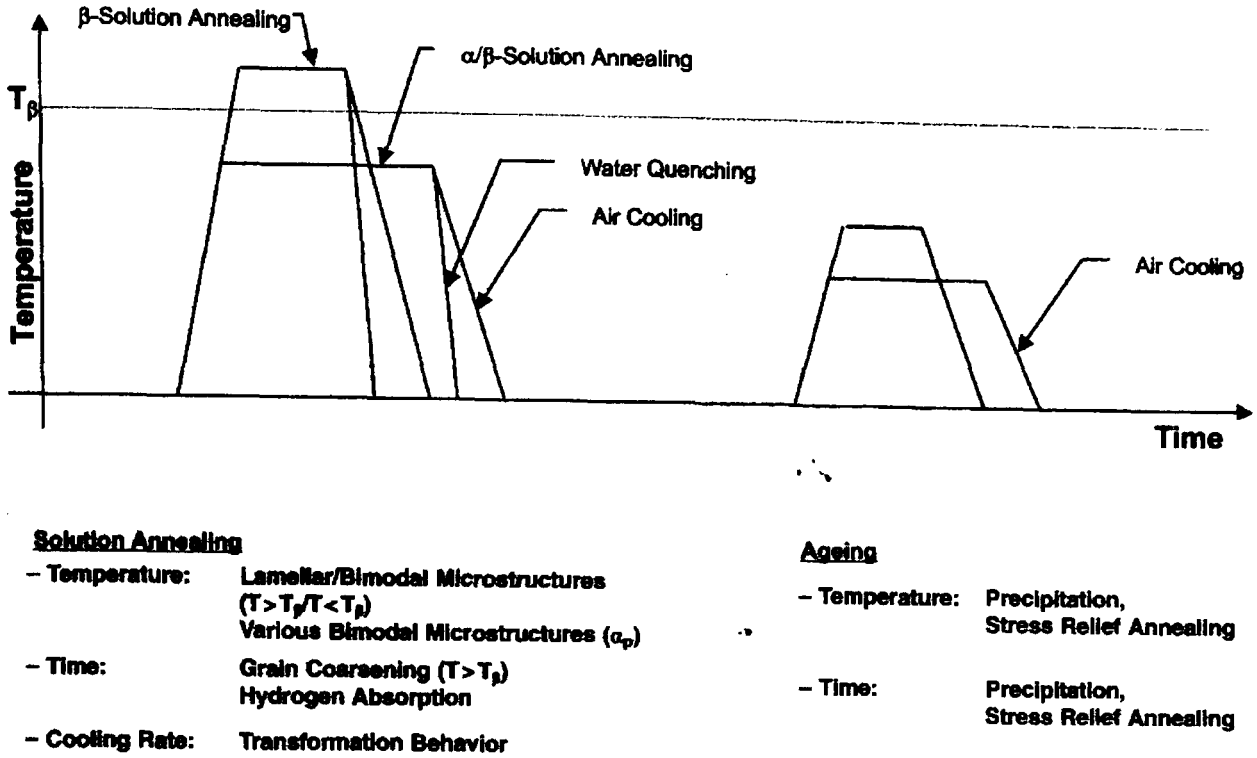

Figure 2.12: Scheme of heat treatment of titanium alloys [6].

2.4 Simulation and modelling of isothermal forging of titanium alloys

2.4.1 Advantages of isothermal forging

In conventional forging, dies are pre-heated to a temperature of about 315 to 425°C to reduce the die chilling effect in which heat is conducted from the hot work-piece to the cold dies [24]. Die chilling can affect the forging characteristic and the quality of the forged products. A decrease of working temperature due to die chilling can increase the flow stress of titanium alloys drastically and alter the overall flow behaviour, which in turn may cause defects/cracks in the forged products.

In order to avoid die chilling, it is necessary to perform isothermal forging where the dies and the work-piece are maintained at about the same temperature. Special dies and lubricants are required which can operate at the high working temperatures. Due

to tight process controls, isothermal forging has enabled near-net shape forming of complex components from alloys with very narrow processing windows. Thus, isothermal forging has been adopted by forge masters as a very cost effective route for the manufacture of critical components made from expensive materials [25]. The potential advantages obtained from isothermal forging are [24]:

a. Elimination of die chilling allows the production of forged materials having closer geometric tolerances compared to conventional forging. This in turn can save on input material and production costs.

b. Forging with a slow ram speed, e.g. using a hydraulic press, can be employed without having to consider the heat loss due to die chilling. Lowering the speed of the ram reduces the applied strain rate which in turn reduces the forging load. The lower pressure required enables forging of larger sizes of material.

However, isothermal forging requires [23]: (i) special dies from expensive materials that can withstand high temperature; (ii) a heating system controller that can maintain uniform and constant temperature; (iii) special high temperature lubricant acting as thermal insulators; (iv) high temperature coating or inert atmosphere conditions to protect from oxidation.

2.4.2 Workability of metals

Several mechanical tests and modelling techniques have been developed in order to simulate and to optimise forging processes. Generally, the tests and techniques utilised for designing a forging process aim to achieve good quality final products in

terms of microstructure uniformity, grain size and grain flow characteristics and simultaneously to optimise forging parameters (load and production cost).

Workability of a metal is regarded as one of the major design considerations in a forging process. Workability can be defined as a complex property describing the relative ease with which a metal can be shaped by plastic deformation. The workability of a metal can be evaluated by measurement of the metal resistance to deformation and by determination of the largest possible plastic deformation that can be achieved without fracture [26]. Hence, the workability of a metal is completely described by its flow stress as a function of strain, strain rate, temperature, its failure behaviour and its metallurgical transformations.

A number of laboratory simulation tests have been developed in order to assess the workability of a material. The primary tests include compression, tension, torsion and bending. Among these tests, the compression or "upset" test has been primarily developed and used to investigate the workability of a metal. The advantage of the compression test is due to its capability in achieving large amounts of plastic deformation without introducing the problems of necking as occurs in tension. In this thesis, hot upset tests were used to evaluate the material workability at elevated temperature in order to simulate isothermal forging.

2.4.3 Simulation of isothermal forging by hot upset testing

Parameters for forging processes are usually determined based on prior experience with similar alloys. If the parameters derived produce good quality forged products,

usually there is no additional attempt to optimise the forging process. However, in practice this is often not the case and production equipment and personnel are required to perform an optimisation study, hence increasing the cost of processing.

A laboratory-scale simulation of the forging process is often a cost-effective means of obtaining processing parameters. A simulation can be carried out by deforming relatively small amounts of material under carefully controlled processing conditions. The deformation parameters and the results produced can be related to the commercial isothermal forging process through constitutive analytical equations. In addition, the parameters and the data generated can be utilised as input for process modelling performed by computer simulation, e.g. finite element analysis. Primary input variables in isothermal forging simulations are the working temperature and strain rate. The strain depends on the process being simulated and the amount of deformation occurring in the process. One of the most useful output variables is flow stress, as a measure of metal workability in response to an applied deformation [27]. Uni-axial compression of cylindrical specimens is one of the standard tests by which the flow stress of a metal can be measured accurately and reproducibly.

2.4.4 Modelling of isothermal forging of titanium alloys

The continuing development of computer simulation and numerical modelling has driven the state of the art in recent forge processing. Process modelling enables significant reductions in the cost of the design and the analysis of hot forging operations by rapidly implementing the simulation of the process before any actual trial runs [25]. In order to properly apply process modelling techniques, there is a

need for constitutive equations that can describe the flow stress behaviour of a metal during isothermal forging. The constitutive model derived is usually based on certain physical principles such as:

a. Plastic deformation caused by mobile dislocation motion, which is inherently strain rate dependent. The rate effects are due to thermal activation of various flow processes, and thus plastic flow stress is also temperature dependent [28].

b. The instantaneous response of a material to deformation, which depends on the current state of the material. The current state caused by prior deformation history of a material can be represented by a small number of macroscopic internal variables [29].

The appropriate internal variables and their evolution equations are usually expressed as complex relationships between forging process parameters and are not easily identifiable.

2.4.4.1. Finite element modelling

One of the most important achievements in analysis and simulation of forging processes has been the development and application of the finite element (FE) method [30-32]. The major advantage of using the FE method is its capability to generalise various boundary value problems with little restriction on work-piece geometry by implementing a proper discretisation procedure. In practice, forging processes consist of several operational steps in order to shape the billet into complex desired shapes by using special dies or tools. The FE method permits simulation and

analysis of all these steps for prediction of the instantaneous velocities, strain rates, strains, stresses and temperatures within the deforming metal.

Rigid-plastic and rigid-viscoplastic are common assumptions used by FE analysis for forging simulations. These assumptions imply that the flow stress is a function of strain, strain rate and temperature by neglecting the elastic response of the material. In addition, the distribution of residual stresses is usually not of major concern. The assumptions offer the advantages of reducing the effort and computer time required for simulating metal flow, and predicting stress, strain, strain rate, velocities and temperatures with high accuracy [33]. The inputs of FE simulation for forging process include three different parameter sets [25]:

a. Geometric parameters represent the geometry of the billet material and the dies.
b. Process parameters include the forging equipment, the temperature, the interfacial friction condition, and the transfer and dwell times during all forging steps.
c. Material parameters such as the flow stress of the work-piece, and the thermal properties of the work-piece and dies for heat transfer simulation.

The outputs generated from a forging simulation include:

a. The metal flow behaviour that is important in predicting defects that might occur during forging.
b. The local stress, strain, strain rate and temperature distributions that are required for quality control.
c. The process parameters required for equipment selection, necessary to check the control and consistency of the forging operation.

Chapter 3

Experimental Methodology

As part of this thesis hot isothermal compression tests were carried out on α/β Ti-6Al-4V samples, and on single-phase samples alloyed to reproduce the individual α and β phases present in the two-phase material. The procedures and methodology associated with the testing and metallurgical examination of these samples are detailed in this chapter.

3.1 Characterisation of testing materials

3.1.1 α + β titanium alloy Ti-6Al-4V

The two phase α + β titanium alloy Ti-6Al-4V was supplied by QinetiQ Ltd (Farnborough, UK) and produced by TIMET UK Ltd (Birmingham, UK) as a round bar of 40.18mm diameter. The chemical compositions of the alloying elements quantified from wet chemical analysis (in weight percent) are listed in Table 3.1.

Table 3.1. **Wet chemical analysis of Ti-6Al-4V (in weight percent).**

Ti	Al	V	Fe	C	O	H	N
89.29	6.48	3.99	0.22	0.023	0.158	0.005	0.002

The material was produced by using a standard grade double vacuum arc remelted TIMETAL 6-4 ingot. The ingot was then β hot-forged to reduce its size down to an intermediate rectangular section by using an open die forging press. This forging operation was performed in a number of steps and followed by re-heats. The rectangular section was further cut into multiple pieces and β hot-rolled down to an intermediate square section. After further cutting operations, the material was α + β hot-rolled to reduce its size down to the final product [34].

3.1.2 α- and β-phase alloys in Ti-6Al-4V

TIMET UK Ltd (Birmingham, UK) also provided alloys consisting wholly of the α and β phases found in Ti-6Al-4V at various temperatures 900, 925, 950 and 975°C, relevant to hot forging. The alloys were supplied as bars with lengths of about 70mm and nominal 15x15mm square sections. The α and β phase compositions were formulated, blended and melted by a technique known as button melting (because the first melt ingot has a button-like shape). The button-shaped ingots were forged above their β-transus temperature to obtain the rectangular shape. The square ingots were then preheated at temperatures of 890°C (alloys with nominal temperatures of 900 and 925°C) and 930°C (alloys with nominal temperatures of 950 and 975°C) followed by rolling to the final section size of 15x15mm. Reheat was performed between subsequent rolling to prevent crack initiation. The final bars were heated to their respective temperatures for 30 minutes followed by air cooling in order to release residual strains that arise during rolling.

The chemical compositions of the water quenched α and β alloys determined using SEM/EDX, Wet Chemical and Inert Gas Fusion measurement techniques are listed in Table 3.2. The β transus temperatures were calculated by using TIMET's proprietary β relationship data.

Table 3.2. **Chemical compositions of α and β phase alloys with their calculated β transus temperatures (in weight percent).**

Temperature (°C)	Single α-phase alloys compositions					Calculated β-transus (°C)
	Al	V	Fe	O	N	
900	7.3	1.67	0.03	0.27	0.045	1084
925	7.78	1.46	0.075	0.24	0.035	1079
950	7.55	1.8	0.044	0.22	0.035	1066
975	7.46	1.58	0.109	0.22	0.025	1061
Single β-phase alloys compositions						
900	5.61	7.29	0.41	0.06	0.04	923.8
925	5.97	5.56	0.31	0.07	0.03	948
950	6.14	5.13	0.37	0.095	0.03	962.1
975	6.64	4.56	0.2	0.165	0.045	1007

3.2 Experimental procedures

3.2.1 Work-piece geometry

Cylindrical specimens for hot compression tests were wire machined from the supplied materials by a FANUC ROBOCUT α-O*i*B Electrical Discharge Machine which is available in the Department of Materials Engineering, at The Open University. The specimen geometry for this purpose is shown in Figure 3.1. The aspect ratio of the specimen, which is defined as the ratio of the original height to the original diameter, is 1.5. This value is widely used and recommended for hot

compression testing [35]. The advantage of using a long thin test-piece is to minimise the effects of friction and die chilling, because most of the specimen volume is unaffected by the dead-metal zones at the platens. However, buckling can occur if the test-piece aspect ratio higher than 2 [27].

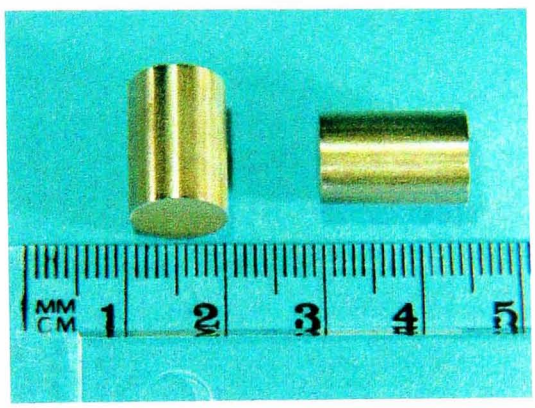

(a)

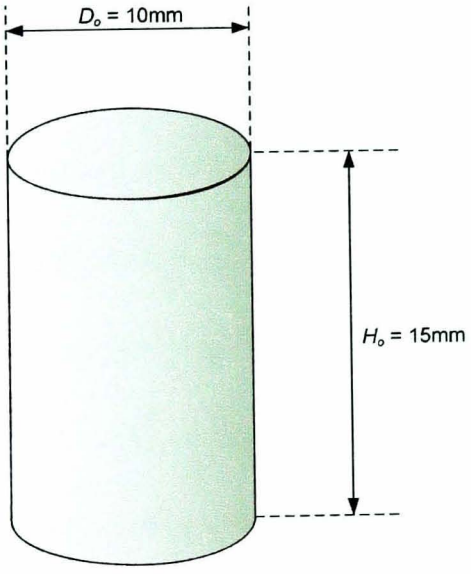

(b)

Figure 3.1: Illustration of (a) photograph and (b) detailed geometry size of uni-axial cylindrical work-pieces employed for hot compression tests.

In addition, a double-truncated cone specimen, as illustrated in Figure 3.2, was also employed in this study. The aim of using this geometry was to validate and assess the effectiveness of constitutive models, developed in predicting applied load and microstructure evolution during isothermal forging, when applied to a complex-geometry work-piece.

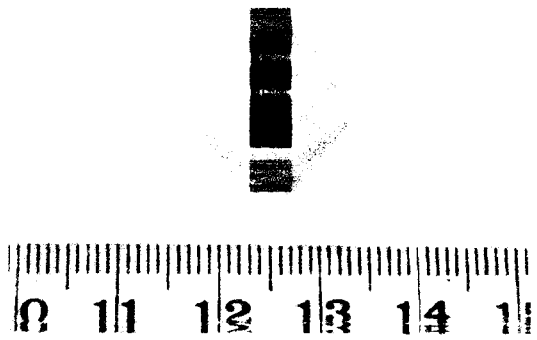

Figure 3.2: A double-truncated cone work-piece exploited for isothermal forging.

This type of specimen was initially devised by Erman and Kuhn in order to extend the range of surface strains available toward the vertical, tensile strain axis [36]. The specimen was artificially pre-bulged by machining a taper on a cylinder. By applying compression load, lateral spread of interior material expands the rim circumferentially while little axial compression is applied to the rim. Each combination of height, H_{cone}, and thickness, t_{cone}, gives a different ratio of tensile to compressive strain. Detailed geometry of the specimen used here is schematically displayed in Figure 3.3.

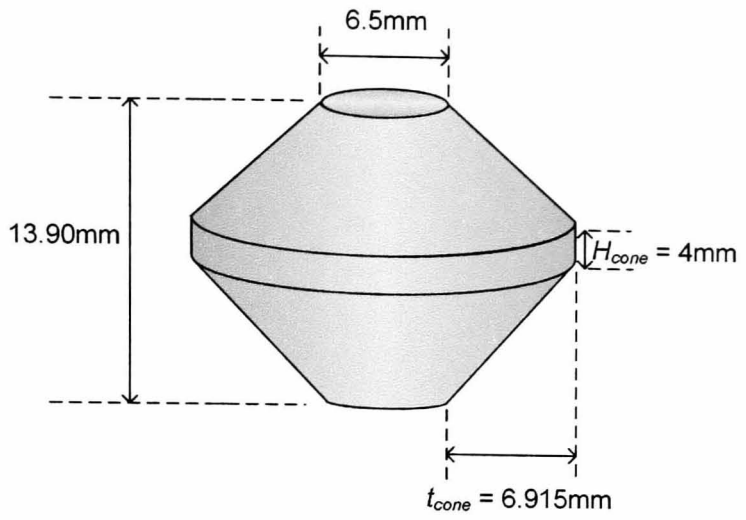

Figure 3.3: A double-truncated cone work-piece exploited for this study.

3.2.2 Mechanical testing apparatus

Hot compression tests were carried out by using a computer-controlled servo-hydraulic MTS 100kN machine coupled with an Instron Severn Furnaces Ltd Radiant Furnace model RHS1856A (see Fig 3.4). The system is illustrated schematically in Fig. 3.5. The furnace is designed as an air cooled 1100°C radiant furnace for general load train heating [37]. Twelve infrared tungsten halogen lamps (240V/1000W each) were used as the heat source, surrounding both the platens and the specimen. Multi Purpose Testing (MPT) software produced by the MTS Corporation was used to control the machine for performing the tests under constant true strain rates up to 0.3/s.

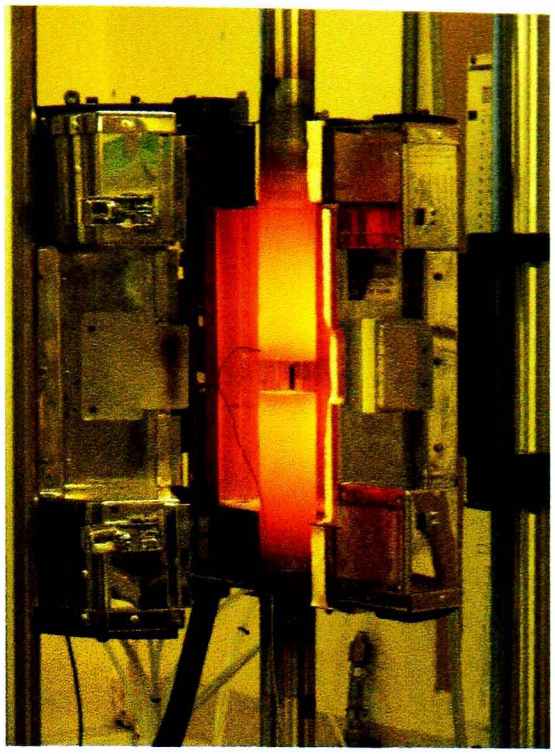

Figure 3.4: MTS testing machine and the furnace for uni-axial hot compression testing.

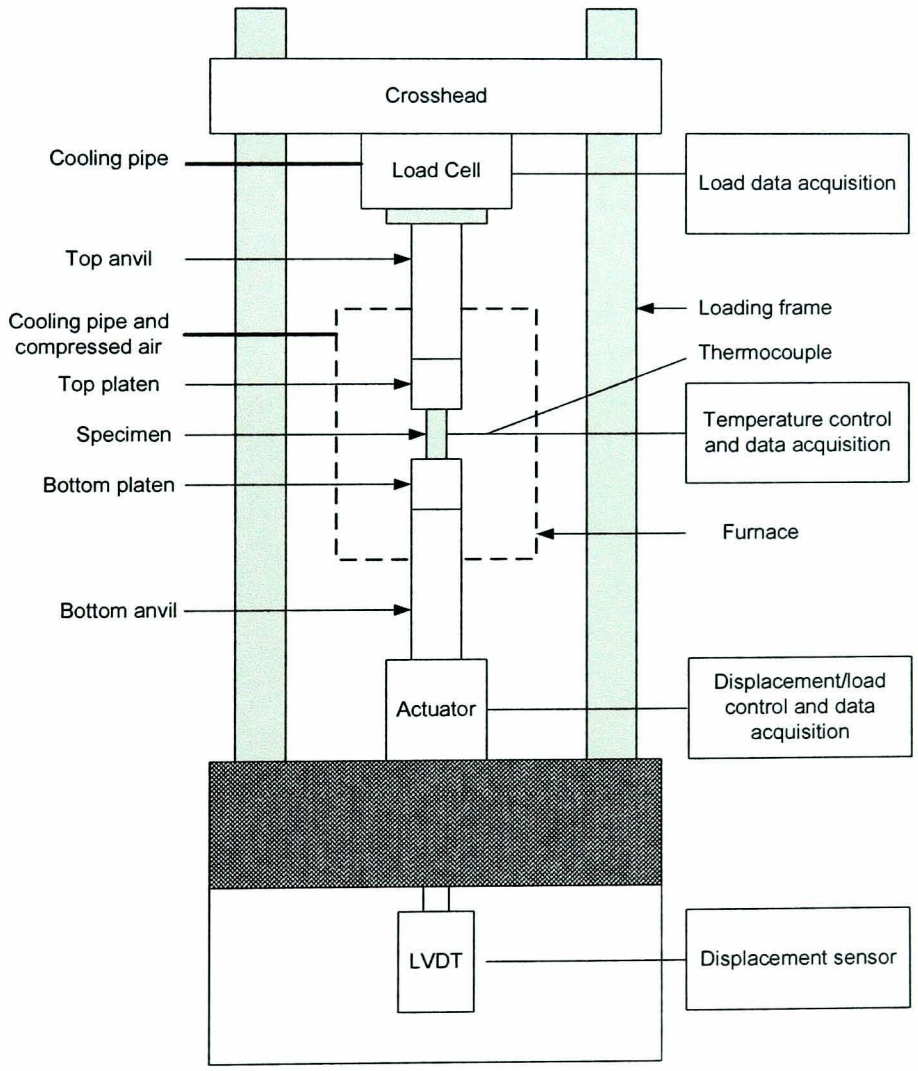

Figure 3.5: Schematic of hot compression-testing system.

The load measured by the 100kN load cell and the displacement measured by the linear variable differential transformer (LVDT) can be logged at given sampling frequencies using the software for conversion into true stress-true strain curves. The conversion was performed using the standard method assuming constant volume and uniform deformation. Directionally-solidified MAR M-247 was used for the platens, EDM-machined to a diameter of 50mm. Anvils were manufactured from PM-1000, a Ni-Cr superalloy dispersion-strengthened with yttrium oxide.

Isothermal conditions were maintained by using a Eurotherm 8-segment programmable controller model 2408 (Figure 3.6) which takes its control input from a specimen-contacting R-type thermocouple. For protection, an independent Eurotherm 2132 was also added as a temperature alarm. The maximum heating rate that could be achieved is 1°C/s [38].

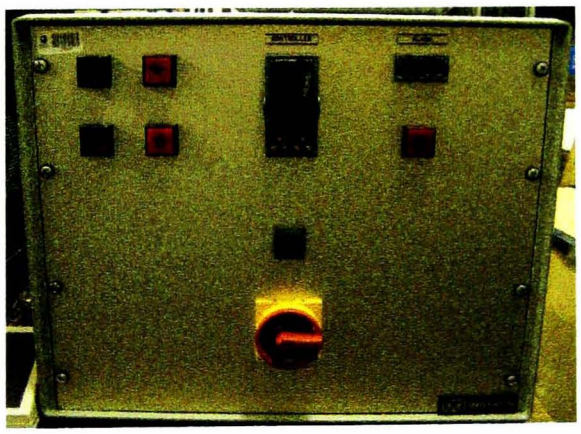

Figure 3.6: Eurotherm 8-segment temperature programmable controller model 2408.

3.2.3 Hot compression testing

Specimens were coated with the glass lubricant Acheson Deltaglaze FB-412 for lubrication and environmental protection prior to heating. Acheson boron nitride DAG-5710 in water was applied over the top of the glass lubricant coated to specimens, and also on the surface of the lower and upper platens. The boron nitride lubricant was utilised in order to minimise the specimen-platen interfacial friction and hence to reduce the specimen barrelling. In addition, it was used to help separate the dies from the specimen, i.e., as a parting agent. The calibration of the specimen temperature was performed by using a dummy test piece with the same geometry. Three K-type thermocouples were embedded within small holes of 0.5mm diameter and 5mm depth at the mid-height and also 3.75mm from its ends. As an example, a result of temperature measurement during calibration is given in Fig 3.7.

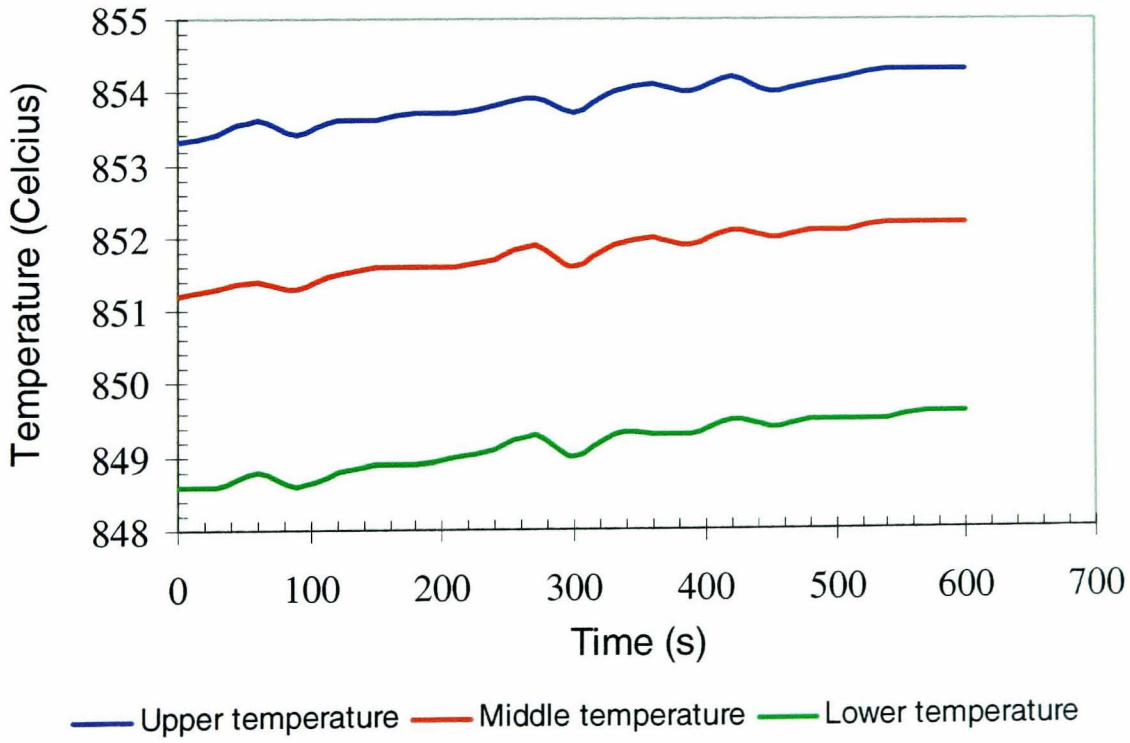

Figure 3.7: A measurement result during temperature calibration at 850°C.

From Figure 3.7, it can be seen that the test-piece temperature at all positions was relatively stable to within variation ±1°C. The temperature variation from point to point within the test-piece and the deviation from the specified test temperature were found to be in the range ±1-3°C. The temperature variation within the test-piece is well within the recommended range for measurement good practice in hot compression testing (±4°C) [35]. Although for temperature sensitive material such as titanium, temperature control should be better than ±2°C.

During testing, a control R-type thermocouple was attached to the middle of the specimen to monitor its surface temperature, and two K-type thermocouples were inserted into the upper and lower platens. Prior to forging, a small compressive load of 100N was applied under load control and the specimen was heated at a rate 1°C/s and then soaked for 10 minutes at the equilibrium test temperature. Load control was chosen to enable adjustment of the position of the lower platen in order to compensate for thermal expansion of the entire loading system. Next, the specimens were forged under fixed true strain rate control to a true strain of 1 and were water-quenched as soon as possible with a typical time delay of between 5 – 15 seconds. In all cases, the forging axis was parallel to the specimen height. Some specimens were also heated up without applying deformation, soaked for 10 minutes at test temperatures and then water quenched. These undeformed microstructures were then used as references in order to investigate the microstructure evolution of deformed specimens at different strain rates.

3.2.4 Determination of flow stress by hot upset test

Typical data obtained from the compression testing are the load F, which is recorded by a load cell, and displacement ΔH, which is defined as the distance the crosshead has travelled from the starting point of the test as measured using an LVDT or extensometer. The true stress is defined as the load F divided by the instantaneous cross-sectional area of the cylinder with diameter D_i. For a homogeneous upsetting test, a uni-axial cylinder with initial height H_o is forged to instantaneous height H_i resulting in the expansion of initial diameter D_o following the law of volume conservation:

$$D_o^2 H_o = D_i^2 H_i \qquad \text{(Eq. 3.1.1)}$$

Assuming frictionless conditions, the uni-axial compressive stress (flow stress), σ, associated with external applied deformation force F is calculated by:

$$\sigma = \frac{F}{A_i} = \frac{4F}{\pi D_i^2} = \frac{4F}{\pi D_o^2 H_o} \qquad \text{(Eq. 3.1.2)}$$

On the other hand, the true strain in a compression test can be calculated as a function of the instantaneous height H_i of the cylinder by:

$$\varepsilon = \ln\left(\frac{H_i}{H_o}\right) = \ln\left(\frac{H_o - \Delta H}{H_o}\right) = \ln\left(1 - \frac{\Delta H}{H_o}\right) \qquad \text{(Eq. 3.1.3)}$$

The true strain rate $\dot{\varepsilon}$ during compression testing can be expressed in terms of the instantaneous crosshead velocity V_i and the instantaneous height H_i given by:

$$\dot{\varepsilon} = \frac{d\varepsilon}{dt} = \frac{d(\ln H_i / H_o)}{dt} = \frac{1}{H_i}\frac{dH_i}{dt} = \frac{V_i}{H_i} \qquad \text{(Eq. 3.1.4)}$$

As H_i decreases, in order to maintain the constant true strain rate during the test, a servo-hydraulic machine can be employed to reduce the velocity of the moving ram continuously based on the above equation.

The effect of strain rate on the flow stress of a material can be described by its strain-rate sensitivity, *m*. The strain rate sensitivity quantifies the increase in stress required to cause a certain increase in plastic strain rate $\dot{\varepsilon}$ at a given level of plastic strain ε and temperature T:

$$m = \left(\frac{\Delta \log \sigma}{\Delta \log \dot{\varepsilon}}\right)_{\varepsilon,T} = \left(\frac{\log(\sigma_2 / \sigma_1)}{\log(\dot{\varepsilon}_2 / \dot{\varepsilon}_1)}\right) \qquad \text{(Eq. 3.1.5)}$$

3.2.5 Determination of interfacial friction

During forging operations, the flow of metal is caused by the load transferred from the dies to the forged material. The frictional conditions at the interface of the die and work-piece greatly influence the flow of metal including formation of surface and internal defects and stresses on the dies. The interfacial friction is controlled by using the appropriate lubricant for a specific application [39]. In order to assess the

performance of the lubricant and to predict forming pressure or load, it is important to quantify the interfacial friction in terms of a coefficient or a factor [40, 41]. The frictional shear stress τ, is calculated by:

$$\tau = \mu\sigma_n \quad \text{or} \quad \tau = f\sigma = \frac{m_f}{\sqrt{3}}\sigma \qquad \text{(Eq. 3.1.6)}$$

where m_f lies between 0 (frictionless condition) and 1 (sticking condition). The above equation indicates that the frictional shear stress τ, is proportional to the normal stress σ_n, acting at the interface and on the friction coefficient μ. In addition, the shear stress is also dependent on the flow stress of the material σ, and the friction factor f, or the shear factor m_f. Lubricity, as represented by the friction factor f, or the shear factor m_f, is commonly measured by using the ring test [40]. The ring test is a method for assessing the interfacial friction condition by deforming a flat ring-shape specimen to a known axial reduction. The geometry changes in the inside diameter (ID) and in the outside diameter (OD) of the deformed ring are greatly dependent on the friction condition at the die-ring interface. Hence, the change in the inside diameter can be used as a sensitive means for assessing the interface friction. If the die-ring interface is frictionless, the ring would deform in a similar manner to a solid disk, with each material element flowing outward radially at a rate proportional to its distance from the centre. As deformation proceeds, the ID of the ring is decreased when the friction is large, and the ID is increased when the friction is low.

The ring test is a simple method since there is no requirement to know the amount of load for deforming the ring. In order to obtain the friction factor, the ID of the deformed ring must be compared with the values predicted by using various friction factors, f or friction coefficients, μ. Several investigations have been performed for this purpose [40, 42, 43]. Theoretical calibration curves have been developed by measuring the geometry change of the rings deformed at various friction coefficients, μ. The results are plotted in the form of theoretical calibration curves. In determining the value of the friction coefficient μ and the shear factor m_f for a certain condition, the measured dimensions (reduction in height and change in internal diameter) are placed on the suitable calibration curve.

For the current study, ring compression tests were performed by deforming as-received Ti-6Al-4V ring specimens which posses the ratio of the outside diameter (OD): inside diameter (ID): height (H_o) of 6:3:2. The geometry of the ring specimens used in this study is illustrated in Figure 3.8.

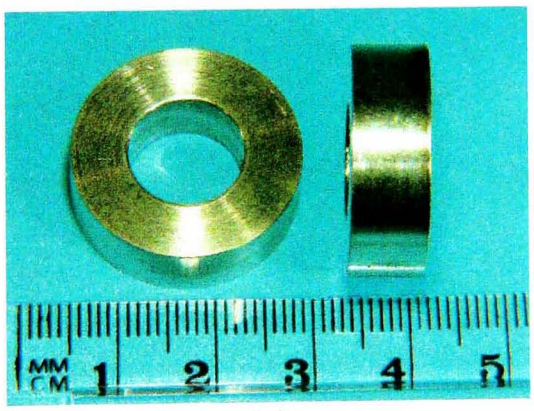

(a)

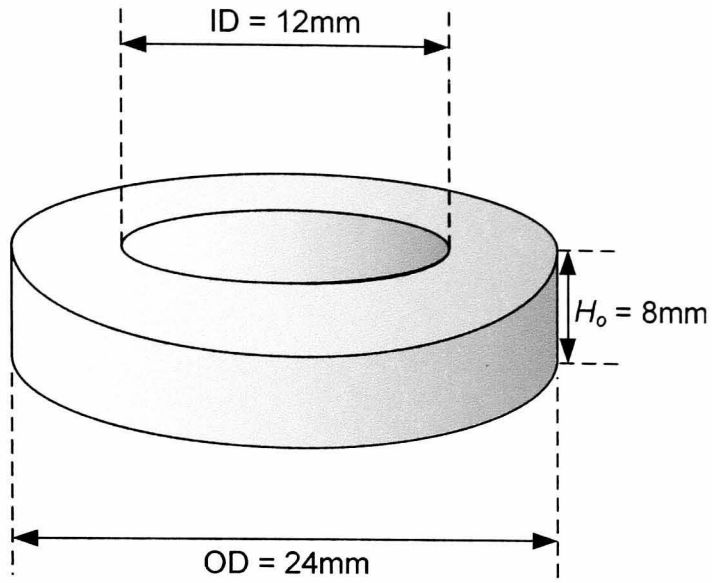

(b)

Figure 3.8: (a). Actual specimens and (b) geometry scheme for ring specimens used in this study.

Ring specimens were compressed to a true strain 1 at various strain rates and test temperatures used during the general testing programme. The change of inside diameter, ΔID (at the mid-height) and the height reduction, ΔH were measured from six points along the perimeter and then the average values were taken. By doing so, a plot of the percent height reduction vs the percent change of inside diameter can be produced to estimate the friction coefficient, μ. The friction coefficients associated with the test temperatures and strain rates were determined by means of superimposing the generated plot onto the calibration curves (Figure 3.9) for different friction conditions investigated by Cockroft's experiment [40, 44, 45].

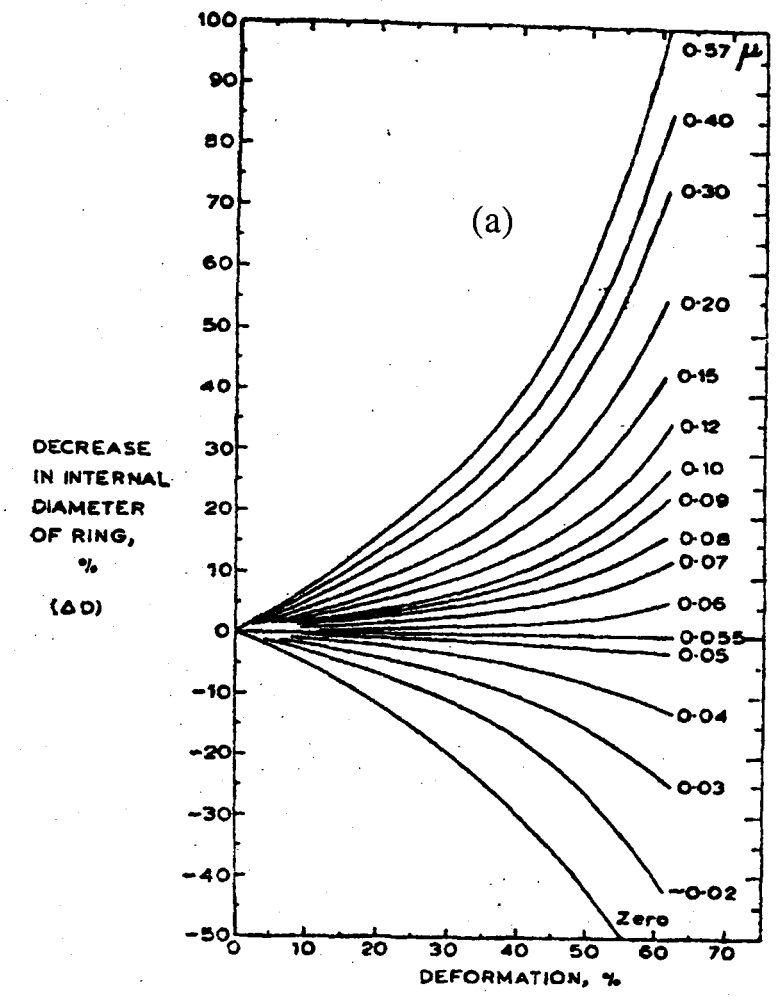

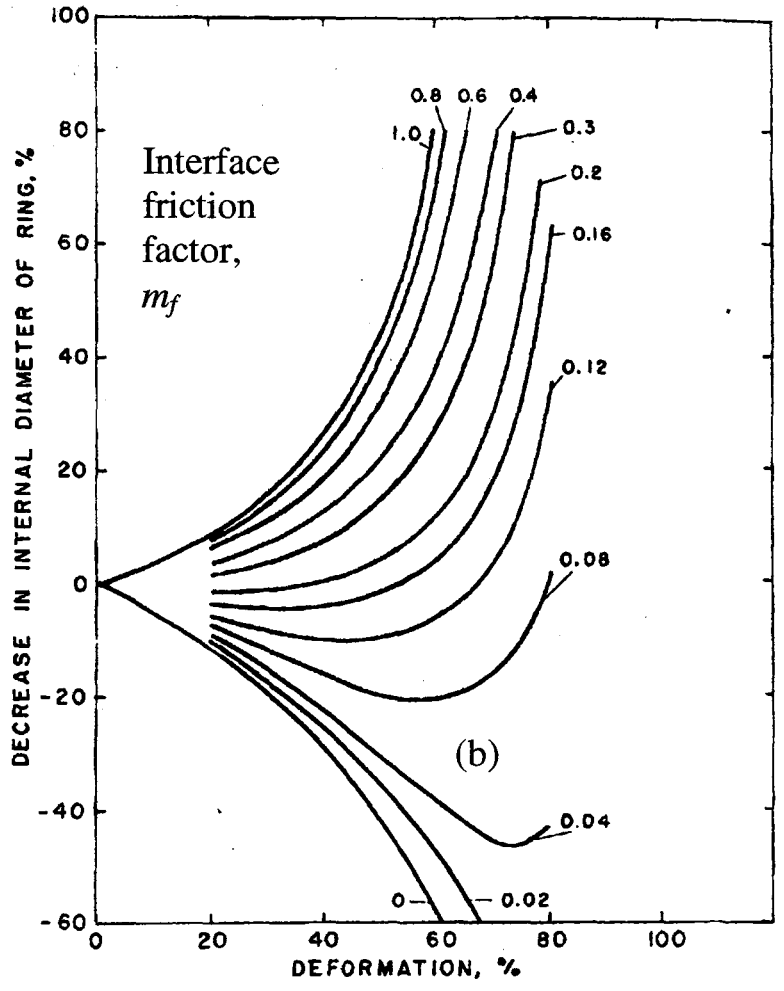

Figure 3.9: Theoretical calibration curves for upsetting rings having OD:ID:thickness ratios of 6:3:2 at various values of (a) friction coefficient, μ and (b) shear factor, m_f [40, 44].

3.2.6 Effect of initial microstructure

In this study, the as-received material Ti-6Al-4V with globular initial microstructure, as shown in Figure 3.10.a, was heat-treated by holding at a sub-transus temperature of 950°C for 10 minutes, then heating to a super-transus temperature of 1050°C and soaking for 2 minutes, followed by water quenching. The heat-treated specimens, characterised by acicular microstructure (Figure 3.10.b), were compressed at elevated temperatures in order to investigate the effect of initial microstructure on the flow stress behaviour.

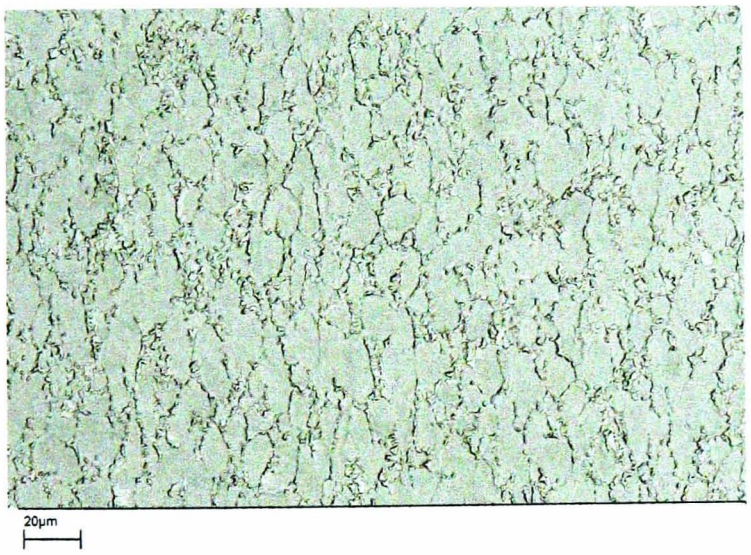

(a)

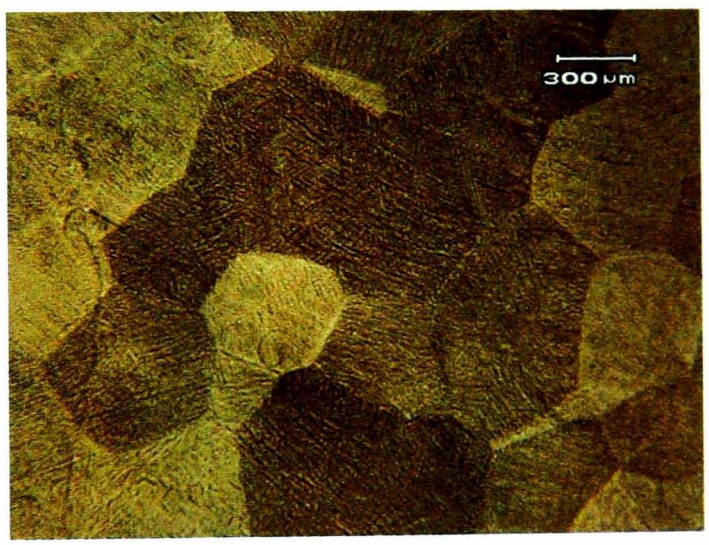

(b)

Figure 3.10: Microstructures of (a) as-received and (b) heat treated Ti-6Al-4V used for this study.

3.2.7 Interrupted testing

To investigate the effect of deformation/strain on microstructure evolution, a series of compression tests were carried out at 950°C and interrupted at various strain levels of 0.03, 0.1, 0.2, 0.5 and 1.0 (for as received Ti-6Al-4V) and 0.04, 0.1, 0.5 and 1 (for

heat treated Ti-6Al-4V). The deformed specimens were water quenched immediately upon cessation of the tests, in order to 'freeze' the evolved microstructure at the temperature. Microstructures developed prior to test were also captured for comparison purposes.

3.2.8 Strain rate jump testing

To further supplement the overall testing programme, strain rate jump tests were carried out at 950°C in order to simulate the instantaneous changes in strain rate that might occur during actual forge processing, and also to validate the constitutive modelling being developed.

In summary, the test matrix in Table 3.3 shows all the isothermal compression tests carried out for this study.

Table 3.3 **Matrix of hot isothermal compression tests at various temperatures and true strain rates applied for (a) interrupted, (b) stain rate jump and (c) uninterrupted tests**

(a)

Specimen Geometry	**Interrupted test**	**Temperature (°C)**	**Strain Rate (s^{-1})**
Cylinder	As-received Ti-6Al-4V	950	0.01
	Heat-treated Ti-6Al-4V	950	0.01

(b)

Specimen Geometry	**Strain-rate jump test**	**Temperature (°C)**	**Strain Rate (s^{-1})**
Cylinder	Heat-treated Ti-6Al-4V	950	$0.3 \rightarrow 0.03$

(c)

Specimen Geometry	Uninterrupted Test	Temperature (°C)	Strain Rate (s^{-1})
Cylinder	As-received Ti-6Al-4V	850	0.3, 0.1, 0.03, 0.01, 0.003
		900	0.3, 0.1, 0.03, 0.01, 0.003
		950	0.3, 0.1, 0.03, 0.01, 0.003
		1000	0.3, 0.1, 0.03, 0.01, 0.003
		1050	0.3, 0.1, 0.03, 0.01, 0.003
	Heat-treated Ti-6Al-4V	925	0.3, 0.03, 0.003
		950	0.3, 0.03, 0.003
		975	0.3, 0.03, 0.003
	Single α–phase alloys	925	0.3, 0.03, 0.003
		950	0.3, 0.03, 0.003
		975	0.3, 0.03, 0.003
	Single β-phase alloys	900	0.3, 0.03, 0.003
		925	0.3, 0.03, 0.003
		950	0.3, 0.03, 0.003
		975	0.3, 0.03, 0.003
Ring	As-received Ti-6Al-4V	850	0.3, 0.003
		900	0.3, 0.03
		925	0.3, 0.003
		950	0.3, 0.003
		975	0.3, 0.003
		1000	0.3
		1050	0.3
Double-truncated cone	Heat-treated Ti-6Al-4V	950	0.01

3.3 Processing of flow stress data

3.3.1 Effect of machine compliance

The flow stress curves derived from experiment were corrected for machine compliance at different test temperatures. The load-displacement curves produced were corrected by subtracting the deformation of loading system (i.e. the elastic component of the entire system of servo-actuator, platens and load cell) from the displacement measured by LVDT. The compliance calibration was conducted by applying the maximum load obtained during the test at the temperature of interest with the top and bottom platens in direct contact. The measured displacement obtained from this test indicates the deformation of the entire system as a function of the applied load.

3.3.2 Effect of the interfacial friction

It is important to take account of the interfacial friction effect that occurs between the test piece and the platens. By considering slab analysis of the homogeneous compression of a flat circular disk, the friction-corrected flow stress, σ_{fric} is calculated from the average deformation pressure by the following equation [46]:

$$\sigma_{fric} = \frac{2\sigma}{\left(\frac{\mu r}{h}\right)^2 \cdot \left(e^{2\mu r/h} - 2\frac{\mu r}{h} - 1\right)} \qquad \text{(Eq. 3.1.7)}$$

where σ is the average deformation pressure or experimental flow stress, μ the coefficient of Coulomb friction, r the radius, and h the instantaneous height. This approach was employed by assuming that the barrelling is not present at the edges of the disk and the thickness is small enough so that the axial compressive stress is constant through the thickness.

3.3.3 Effect of deformation heating

It is generally assumed that only 3 to 5% of the mechanical work of plastic deformation remains in the material as stored energy [27]. The remaining portion is transformed into heat that can affect the specimen temperature during testing. At slow strain rates, the rate of heat generated is usually very small and will escape through the platens and to the environment. The heat will be conducted away during the long time periods of the test so that the deformation process can be assumed to be isothermal. However, at very high strain rate, there is not enough time for the heat loss and the specimen temperature will be increased. In order to obtain the flow stress at constant temperature and high strain rate, it is necessary to make a correction for the effect of the deformation heating. For a uni-axial cylinder with volume V, the incremental mechanical work done δW (in Joules) can be calculated from the area under the stress-strain curve:

$$\delta W = V.\sigma_t.\delta\varepsilon \qquad \text{(Eq. 3.1.8)}$$

where σ_t is the average flow stress for the incremental strain, $\delta\varepsilon$.

The conductive heat loss δE at a contact area A_o between the platens and the work-piece for one time increment δt can be estimated by the expression:

$$\delta E = h.\delta t.2A_o(T_s - T_d) \qquad \text{(Eq. 3.1.9)}$$

where h is the heat transfer coefficient ($Wm^{-2}K^{-1}$), T_s is the temperature of the specimen and T_d is the temperature of the die. The remaining energy is the difference between the mechanical work and the conductive heat loss, and is converted to the adiabatic temperature rise $\delta T_{adiabatic}$ in the work-piece which can be calculated as:

$$\delta T_{adiabatic} = \frac{\delta W - \delta E}{C_p.M} \qquad \text{(Eq. 3.2.1)}$$

where C_p is the specific heat capacity ($JKg^{-1}K^{-1}$) and M is the mass (kg). Knowing the adiabatic temperature rise, we can estimate the correction that must be subtracted to the uncorrected stress. By plotting the uncorrected flow stress versus the corrected temperature (T_{test}-$\delta T_{adiabatic}$) at various strain rates, we can obtain the slope of this plot as the temperature sensitivity which can then be used to calculate the change in stress caused by the temperature rise:

$$\Delta\sigma_s = \delta T_{adiabatic} \cdot \left.\frac{\delta\sigma}{\delta T}\right|_{\varepsilon,\dot{\varepsilon}} \qquad \text{(Eq. 3.2.2)}$$

Finally, the deformation-heating corrected flow stress curve is obtained by adding the stress difference from Equation 3.1.5 to the uncorrected flow stress.

3.4 Metallography and Quantitative Image Analysis

3.4.1 Metallographic procedures

The main difficulty in preparing titanium for metallographic analysis is its extreme ductility, which make this material prone to mechanical deformation and scratching [47]. In order to overcome this problem, a specific metallographic preparation routine is required during cutting, grinding and polishing. In this study, suitable metallographic procedures were developed, as summarised in Table 3.4 and 3.5. The first step was to section specimens through the centre parallel to the forging axis by using a silicon carbide cut-off wheel. The sectioned specimens were then mounted into conductive Bakelite moulding powder for scanning electron microscope observation. The subsequent procedure was to grind specimens with silicon carbide papers with grit sizes varying from 220-2500. These plane grinding steps were then followed by three polishing steps on a hard surface, using MD-Nap clothes produced by Struers [48]. Diamond paste suspensions of 6 and 3μm were used as abrasive material during polishing. The final polishing step was a chemical-mechanical polishing with a mixture of colloidal silica (OP-S) and 30% hydrogen peroxide. During chemical-mechanical polishing, the titanium surface continuously reacted with the hydrogen peroxide. Colloidal silica suspension was used to remove the reaction product during polishing. Due to this reaction, the polished surface was free of scratches and mechanical deformation. These procedures were proven to give reproducible results of a flat, scratch-free and mirror-like quality surface. Finally, the polished specimens were immersed for about 10 seconds in an etchant to further aid microstructure characterisation. Chemical compositions of the etchant used consisted of 0.5ml HF, 5ml lactic acid and 94.5cc distilled water [34].

Table 3.4 **Grinding Step**

Step	**Plane Grinding**	**Fine Grinding 1**	**Fine Grinding 2**	**Fine Grinding 3**	**Fine Grinding 4**
Surface	Si-C paper #220	Si-C paper #500	Si-C paper, #800	Si-C paper, #1200	Si-C paper, #2500
Lubricant	Water	Water	Water	Water	Water
rpm	300	250	250	250	250
Force (lbs)	15	10	10	10	10
Time (min)	10	5	5	5	5

Table 3.5 **Polishing Step**

Step	**Fine Polishing 1**	**Fine Polishing 2**	**Fine Grinding 3**
Surface	MD-Nap	MD-Nap	MD-Nap
Suspension	Diamond paste 6 µm	Diamond paste 3 µm	OP-S + H_2O_2 (90ml OP-S + 10ml H_2O_2 30%)
Lubricant	Struers-DP Red/blue Lubricant	Struers-DP Red/blue lubricant	Struers-DP Red/blue lubricant
Rpm	150	150	150
Force (N)	30	30	30
Time (min)	10	5	5

3.4.2 Optical and scanning electron microscopy

A field emission scanning electron microscope (FEGSEM) Zeiss Supra ™ 55VP was utilised to carry out microstructure analysis by using backscattered electron imaging mode with an operating voltage of 10kV. In backscattered micrographs, the α-phase appears darker because of its lower atomic number and the β-phase appears white. In addition, optical micrographs were captured using the Reichart MeF3 inverted metallurgical microscope coupled with a Olympus DP12 digital camera in bright field mode.

3.4.3 Quantitative image analysis

Backscattered images of microstructures were analysed using the quantitative image analysis software ImageJ [49] and ImageTool [50]. ImageJ software was used to quantify the volume fraction of primary α-phase, whilst ImageTool was used to determine area, length, width, perimeter, orientation and aspect ratio of the primary α-phase. Backscattered micrographs obtained from the SEM were in gray scale, hence further threshold procedures were still required in order to convert these into binary images. By doing so, gray shades that existed in both the α and β-phases were removed and contrast between the phases were enhanced. However, because of the complexity of the microstructures, hand painting of the primary α was necessary using an electronic graphical tablet. Finally, the backscattered images were fully converted to binary-type images (the α-phase is shown black and the β-phase is shown white as depicted in Figure 3.11), and were ready to be further quantified by the image analysis software.

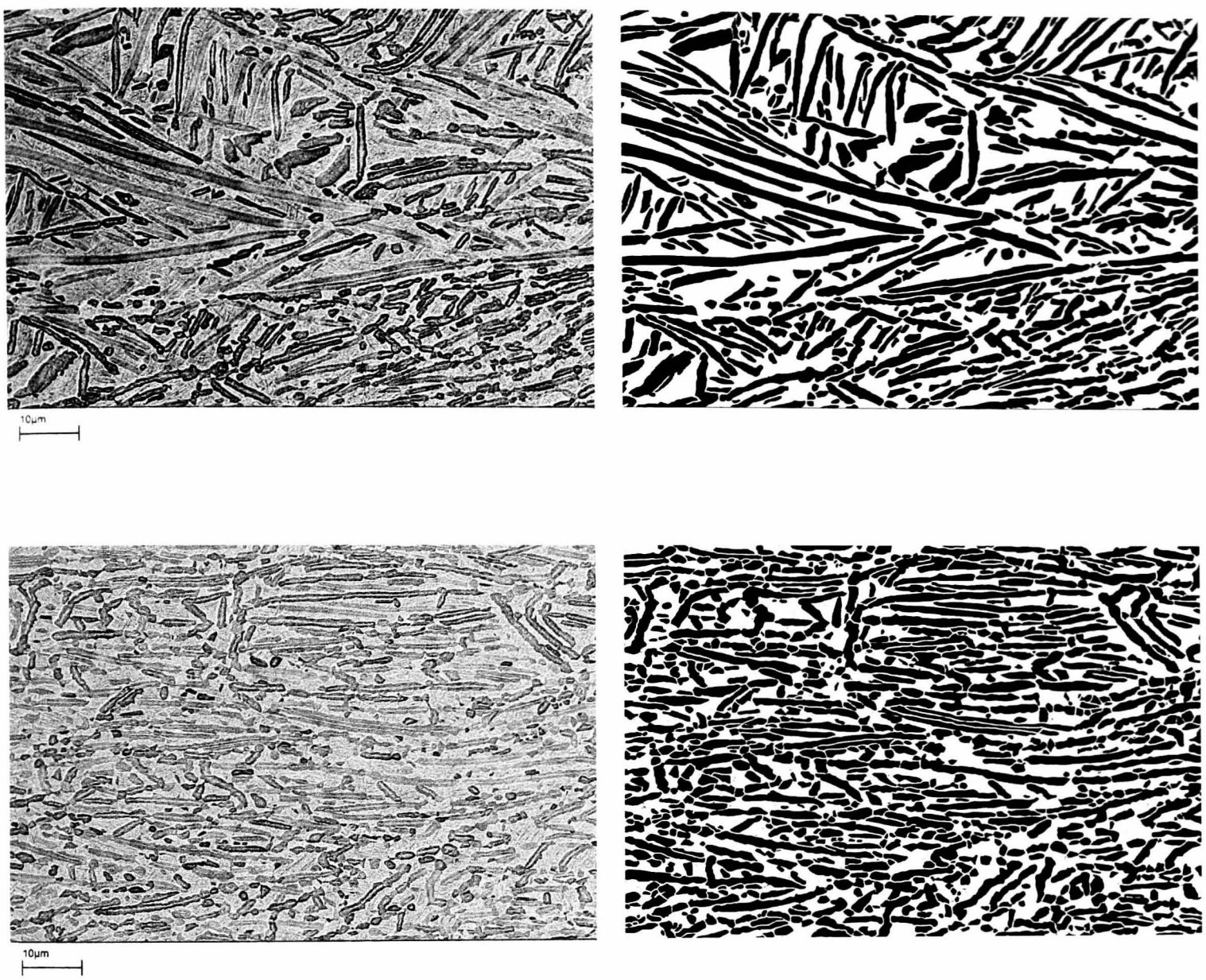

(a) Backscattered images (b) Processed images

Figure 3.11: Illustration of image processing: (a) original backscattered images (b) processed threshold images.

Chapter 4

Flow Stress Behaviour of Ti-6Al-4V during Isothermal Compression

In this chapter, experimental results related to the isothermal flow stress behaviour of the as-received and β-heat-treated two-phase Ti-6Al-4V, and its single-phase constituents are presented. Measurement results from a series of ring compression tests are also presented in order to examine interfacial conditions at various temperatures and strain rates. Techniques for correcting the raw flow stress data in terms of machine compliance, friction and deformation heating are discussed. The influences of processing parameters, *i.e.* working temperature and imposed strain rate, on flow stress behaviour are investigated and analysed using Arrhenius-type power law equations.

4.1 Flow stress correction

4.1.1 Compliance correction of flow stress

Deformation of the loading frame system was assessed at different test temperatures in order to correct the flow stress curves obtained from the hot compression tests. The displacement-load curves of the loading system obtained are displayed in Figure 4.1. Deformation of the specimen was determined by subtracting the loading frame deformation from the total displacement measured by the LVDT. This indirect technique for displacement measurement is permitted since the resolution of the LVDT is relatively high (In theory, the resolution of LVDT is infinite. The only

limitation is due to the ability of the associated electronic equipment to sense the change in output of the LVDT, and this is better than 10μm in our system)

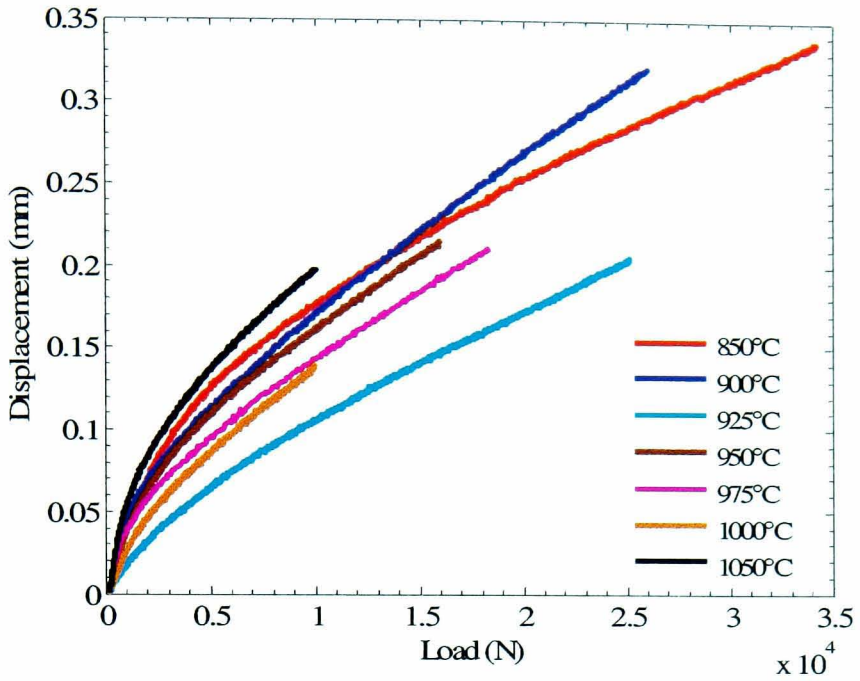

Figure 4.1: Displacement-load curves of the loading frame for all test temperatures.

The effect of the machine deformation correction on the flow stress of Ti-6Al-4V with globular (as-received) initial microstructure during isothermal compression at 850°C and 0.3/s is presented in Fig. 4.2. The compliance-corrected data shows a higher stiffness compared to the raw data.

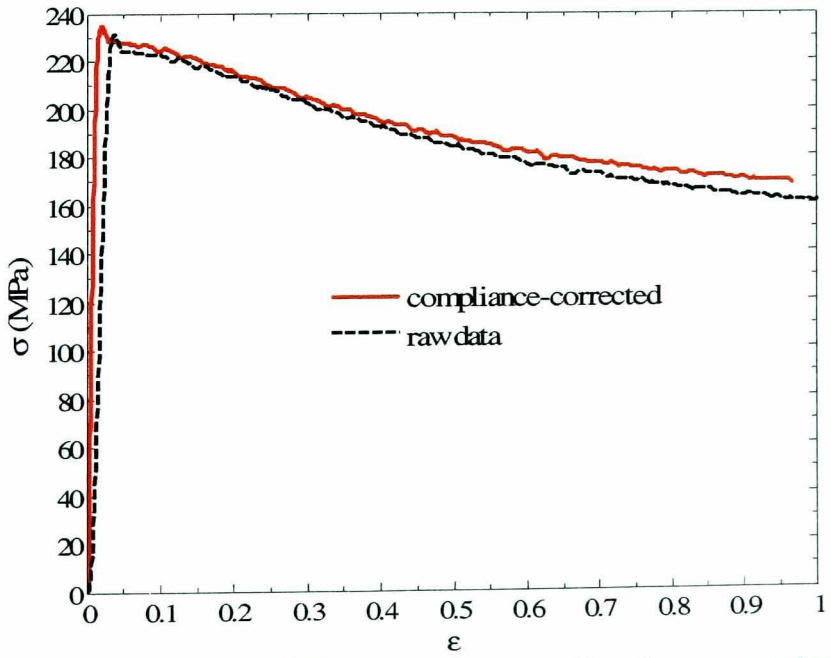

Figure 4.2: Compliance corrected flow stress curve for the as-received Ti-6Al-4V at 850°C and 0.3/s.

4.1.2 Friction correction of flow stress

The interfacial friction condition between the test-piece and the platens was examined by conducting ring compression tests at various test temperatures. As an example, Figure 4.3 shows a comparison between undeformed and deformed ring specimens under different temperatures at a strain rate of 0.3/s. Measurements of ΔID (the inside diameter change) and ΔH (the height reduction change) were superimposed on the calibration curves produced from Cockroft's experiment [40]. Figure 4.4 illustrates the measurement results of the ring compression test obtained when using Acheson Boron nitride DAG 5710 mixed in water as a lubricant. The measurement results are also tabulated in Table 4.1. It can be seen that the estimated friction coefficients μ were relatively low (between 0.03-0.1) confirming that the lubricant system used during this study can minimise the friction effectively.

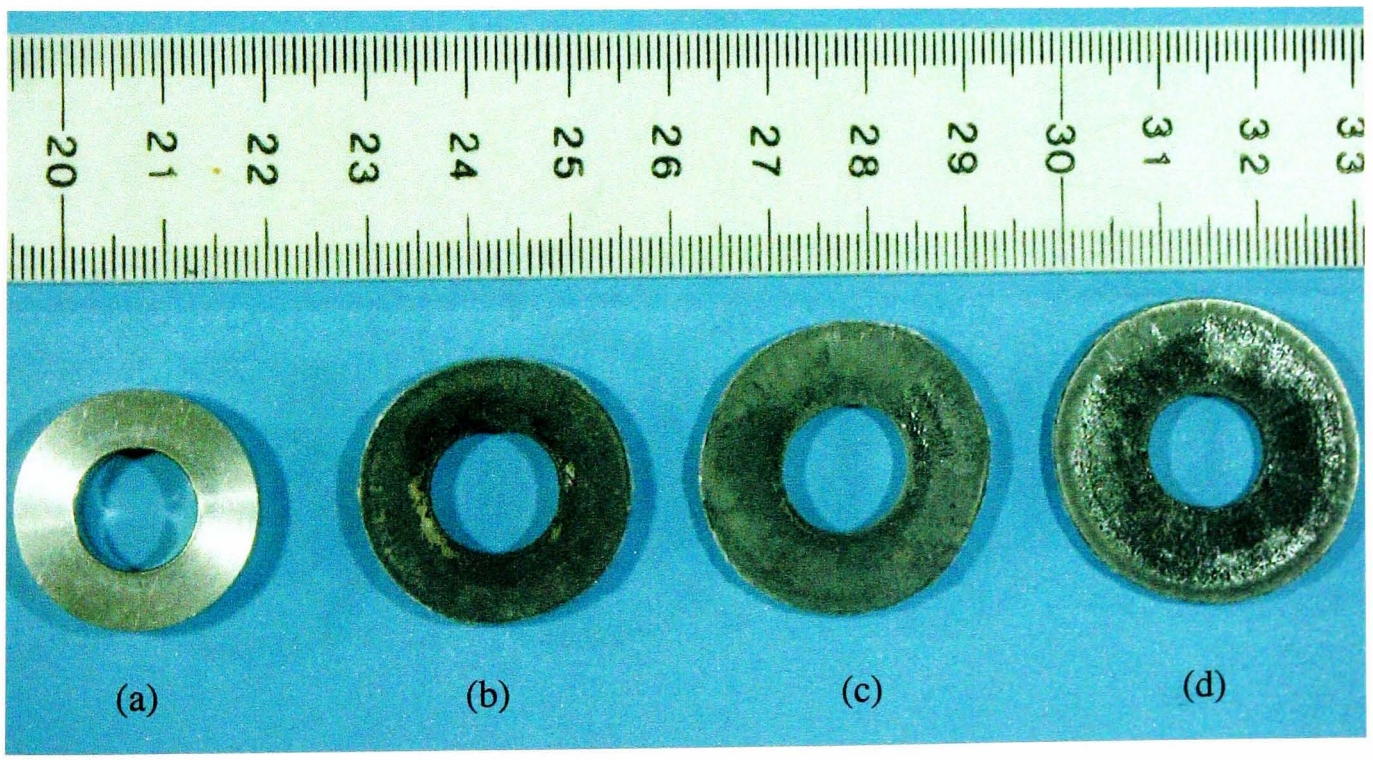

Figure 4.3: Illustration of (a) an original and deformed ring specimens under conditions of (b) 850°C, 0.3/s (c) 900°C, 0.3/s (d) 950°C, and 0.3/s.

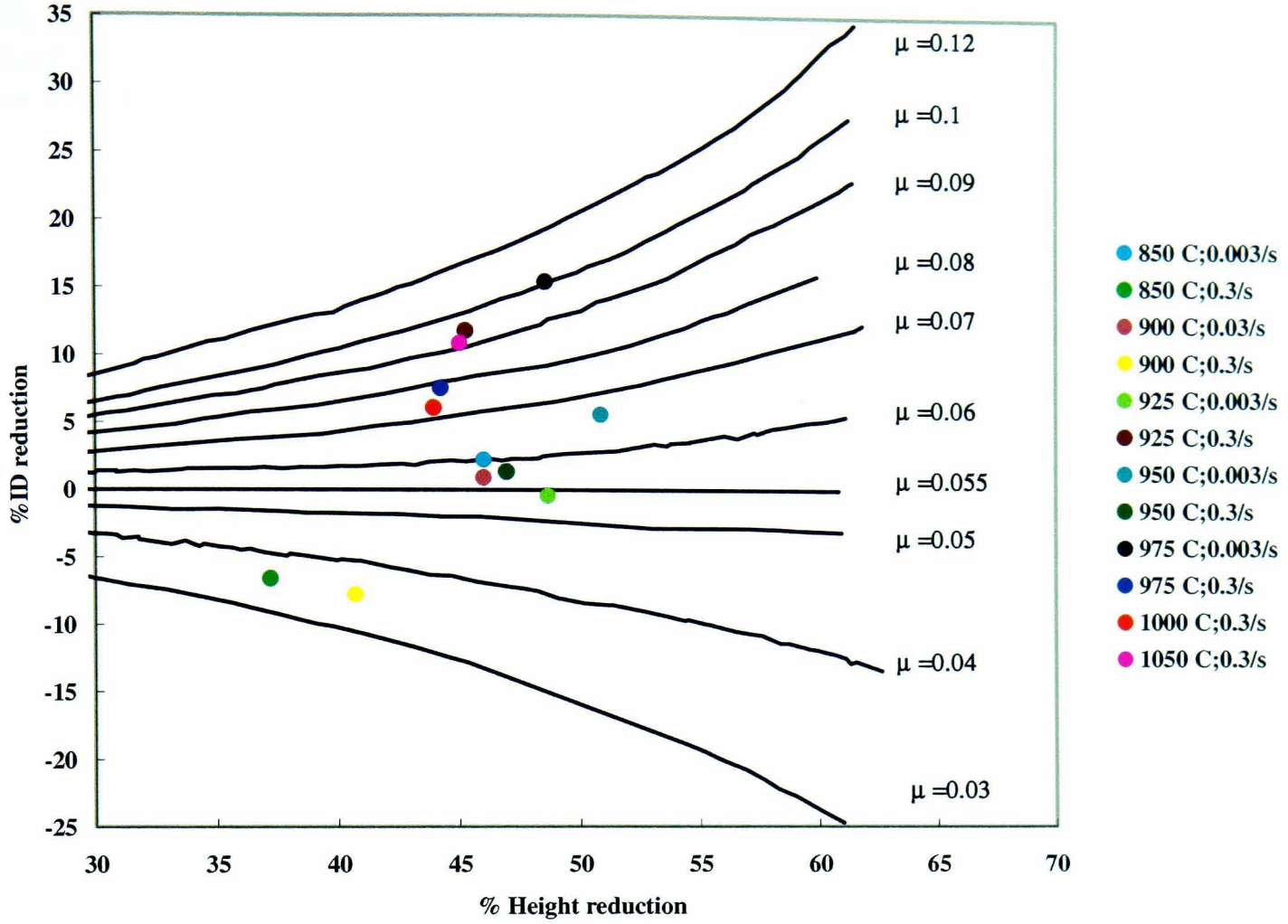

(a)

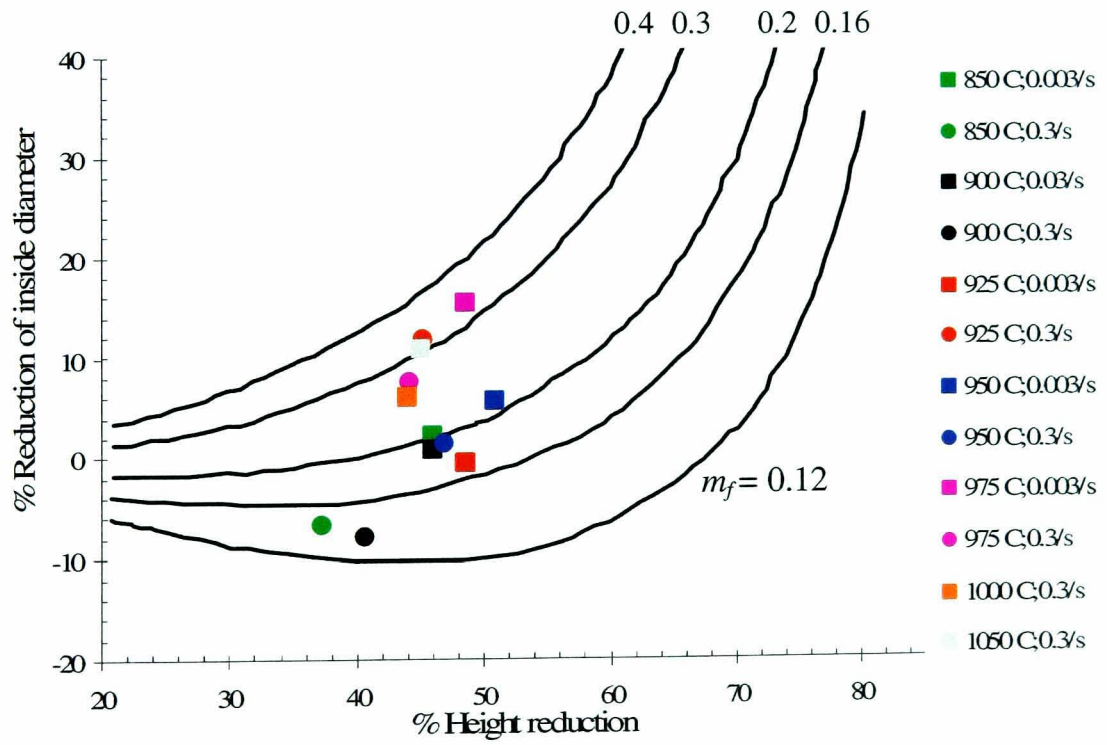

(b)

Figure 4.4: Comparison of experimental measurements with the calibration curves at various temperature/strain rate conditions for different values of (a) friction coefficient, μ and (b) friction factor, m_f.

Table 4.1. **Measurement results of ring compression tests and associated friction coefficient, μ and friction factor m_f, at various fixed strain rates and temperatures.**

T (°C)	$\dot{\varepsilon}$ (1/s)	%ΔH	%ΔID	μ	m_f
850	0.003	46	2.2	0.06	0.2
850	0.3	37.2	-6.6	0.035	0.15
900	0.03	46	0.9	0.057	0.2
900	0.3	40.7	-7.8	0.035	0.14
925	0.003	48.7	-0.4	0.055	0.17
925	0.3	45.3	11.8	0.095	0.32
950	0.003	50.9	5.6	0.068	0.22
950	0.3	47	1.3	0.057	0.19
975	0.003	48.6	15.4	0.1	0.32
975	0.3	44.2	7.5	0.08	0.28
1000	0.3	43.9	6.1	0.074	0.26
1050	0.3	45	10.8	0.091	0.3

Figure 4.5 shows the temperature-dependence of μ and m_f at strain rates of 0.3 and 0.003/s. It can be seen that, with increasing working temperature, interfacial friction between the dies and work-pieces increases slightly, as indicated by higher values of both μ and m_f at higher temperature. This tendency may be attributed to the inherent properties of glass lubricant used. As temperature increases, glass viscosity decreases and it starts to flow as non-viscous fluid, which in turn reducing its effectiveness as lubricant.

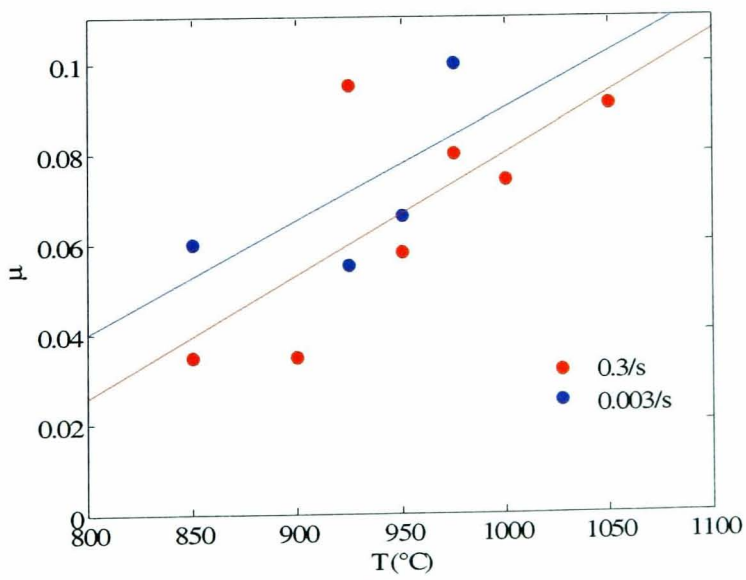

(a)

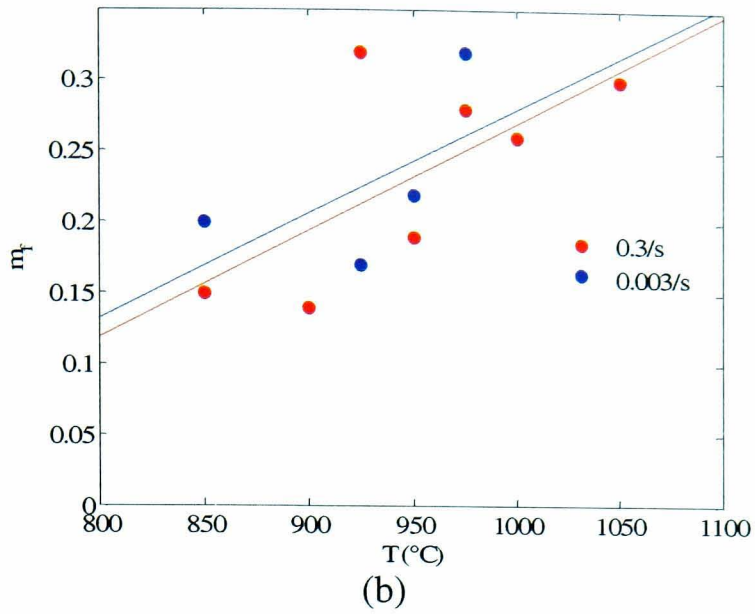

(b)

Figure 4.5: Correlation between (a) μ and (b) m_f obtained from ring tests with testing temperatures.

A comparison between undeformed and deformed cylindrical test pieces under various strain rates at temperature of 850°C is shown in Figure. 4.6.

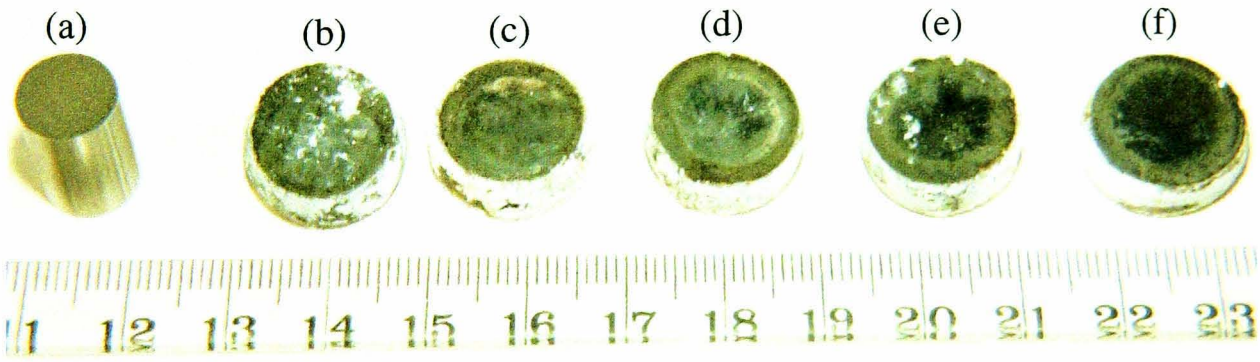

Figure 4.6: Photograph of (a) undeformed and deformed cylindrical specimens at 850°C under strain rates of (b) 0.3, (c) 0.1, (d) 0.03, (e) 0.01 and (f) 0.003/s.

The effects of the friction correction on the flow stress curve of Ti-6Al-4V with globular initial microstructure at 850°C and 0.3/s is illustrated in Figure. 4.7. The friction-corrected flow stress shows only a slight difference when compared to the compliance-corrected flow stress, due to the low interfacial friction coefficient.

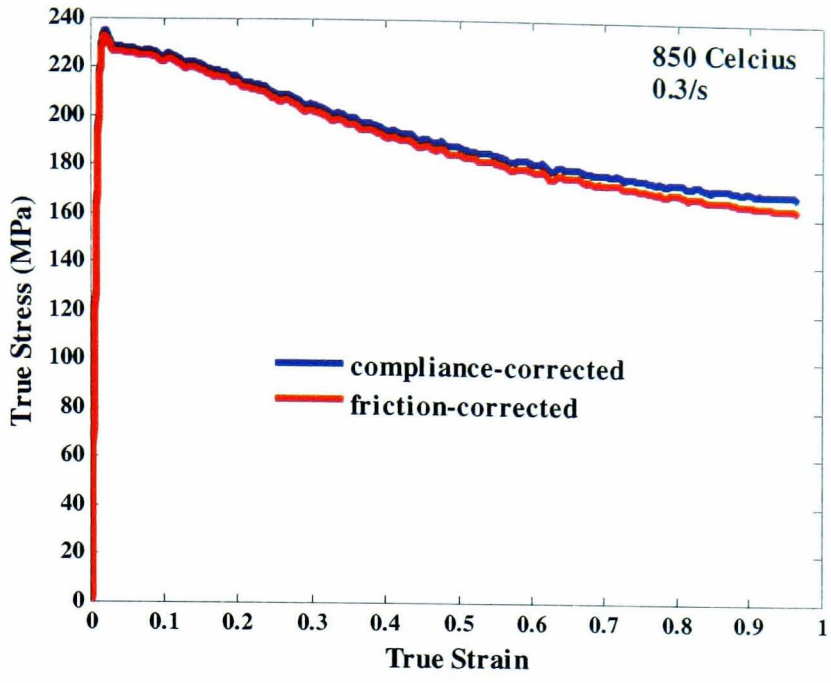

Figure 4.7: Comparison of compliance-corrected with the friction-corrected flow stress curve at 850°C and 0.3/s for globular initial microstructure.

4.1.3 Adiabatic-heating correction of flow stress

Figure 4.8 shows the effect of the adiabatic-friction and compliance-correction to the flow stress curve of Ti-6Al-4V with globular initial microstructure at 850°C and 0.3/s. The adiabatic heating caused by rapid deformation rate can disrupt the isothermal condition by raising the work-piece temperature, leading to a reduction in flow stress. For this reason, the adiabatic heating correction has a marked effect in reducing flow stress softening, at least at higher deformation rates. Any remaining flow stress softening must be the result of microstructure change. Flow stress curves presented in the following sections are the adiabatic-friction and compliance-corrected curves.

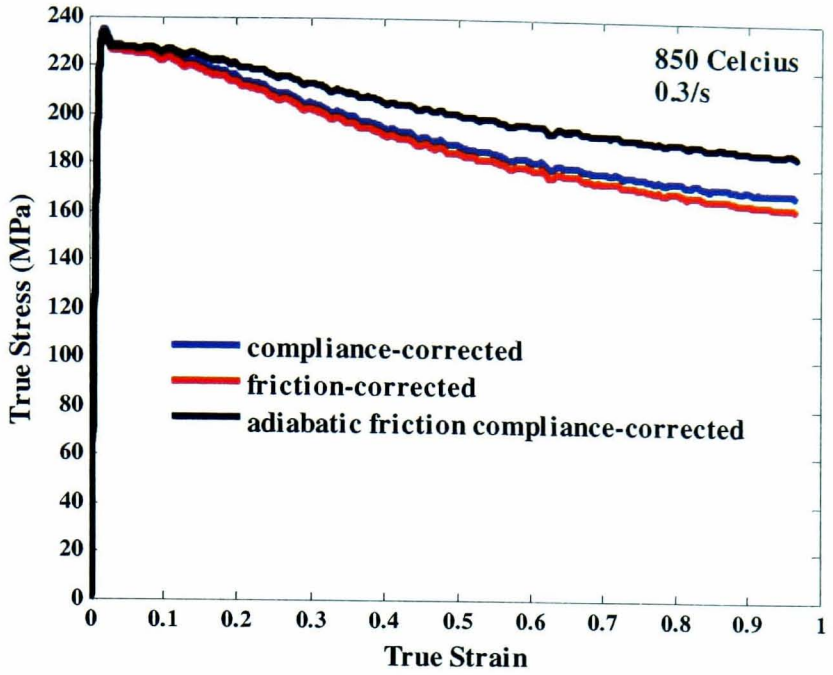

Figure 4.8: Effects of adiabatic correction on the flow stress curve at 850°C and 0.3/s for globular initial microstructure.

4.1.4 Errors in flow stress measurements

Errors in flow stress measurements need to be quantified in order to ensure repeatability of measurement results. A series of hot compression tests has been performed on the same materials at the same processing conditions ($\dot{\varepsilon}$, ε, T) to assess the level of variation between each independent measurement. Errors in flow stress results can be determined based on peak (σ_p) and steady state stress (σ_{ss}) from multiple measurements. Peak stress (σ_p) is the maximum stress whilst the steady-state stress (σ_{ss}) is the minimum stress attained during hot deformation.

For example, the standard deviation calculated for repeated uninterrupted testing of globular Ti-6Al-4V deformed at 850°C and 0.1/s is 1.6MPa for a peak stress average of 201.8MPa (an error in peak stress of 0.8%) and 2.5MPa for a steady-state flow stress average of 145.8MPa (an error in steady-state stress of 1.7%), as illustrated in Figure 4.9.a. The quantified errors are well within an acceptable range based on

Measurement Good Practice Guide [35], indicating a high reliability of experimental results produced from the strictly controlled testing conditions. In addition, the strain-rate jump test shown in Fig.4.9.b clearly demonstrates the consistency of testing.

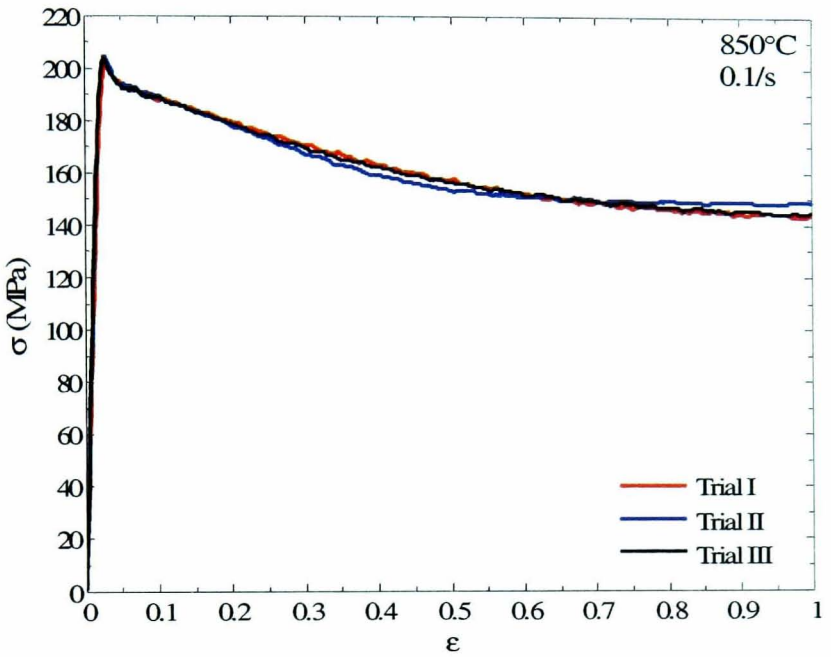

(a)

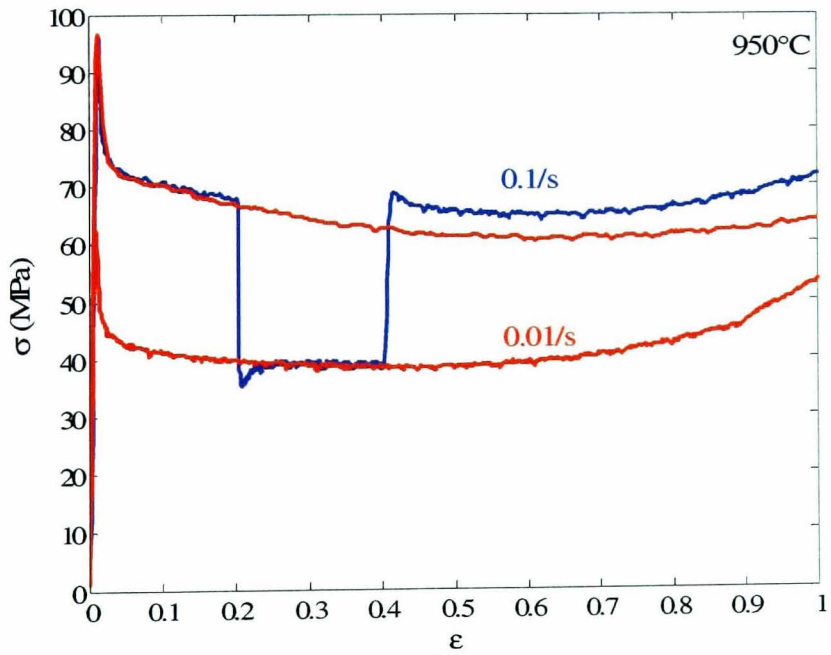

(b)

Figure 4.9: Experimental results from repeated hot compression tests of (a) globular Ti-6Al-4V at 850°C; 0.1/s; (b) strain rate jump tests for globular Ti-6Al-4V at 950°C and 0.1/s $\rightarrow$ 0.01/s $\rightarrow$0.1/s.

4.2 Flow stress behaviour of Ti-6Al-4V with globular initial microstructure

4.2.1 Flow stress behaviour in the two-phase $\alpha + \beta$ field

The flow stress curves derived from isothermal testing of Ti-6Al-4V with globular initial microstructures at sub-transus temperatures of 850, 900 and 950°C are presented in Figure. 4.10. It can be seen that the flow stress curves exhibit a strong dependence on temperature and strain rate. Thus, the flow stress behaviour of the as-received Ti-6Al-4V can be considered to be governed by thermally activated processes. At a given temperature, flow stress increases as strain rate increases, and at a given strain rate, flow stress decreases as temperature increases, at all strains. At higher strain rates (>0.01/s), the flow stress curves show peak stresses at low strains followed by flow softening towards a steady state stress. For these tests, an abrupt stress-drop phenomenon was observed which was more pronounced at higher sub-transus temperatures. At slower strain rates (<0.01/s) and lower temperatures, the flow stress curves were of steady state type with no pronounced peak.

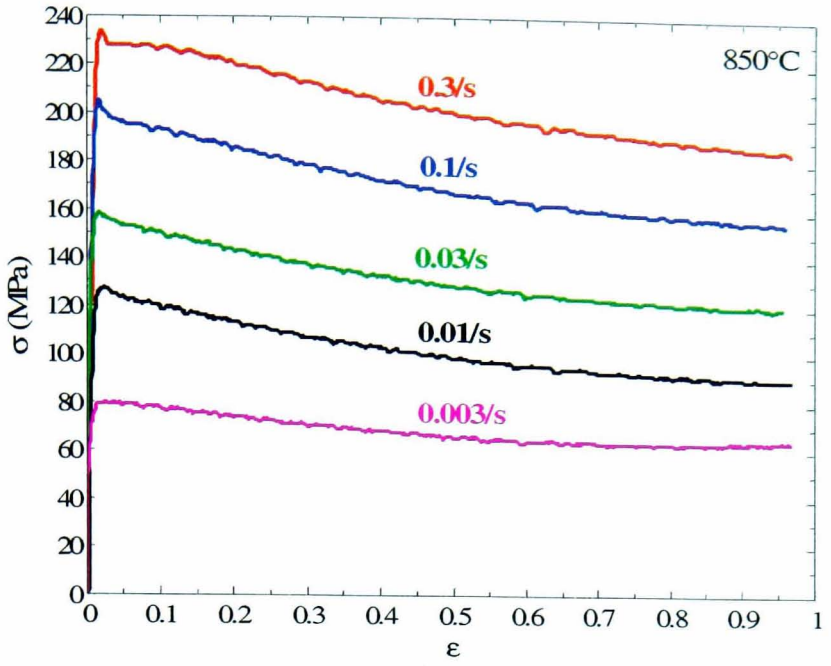

Figure 4.10: Flow stress curves of Ti-6Al-4V with globular initial microstructure at sub-transus temperatures of (a) 850, (b) 900 and (c) 950°C.

4.2.2 Flow stress behaviour in the single β-phase field

The flow stress curves of Ti-6Al-4V with globular initial microstructure at super-transus temperatures are summarised in Figure 4.11. It is obvious that most of the flow stress curves reveal a sharp yield drop (discontinuous yielding) followed by near steady-state deformation.

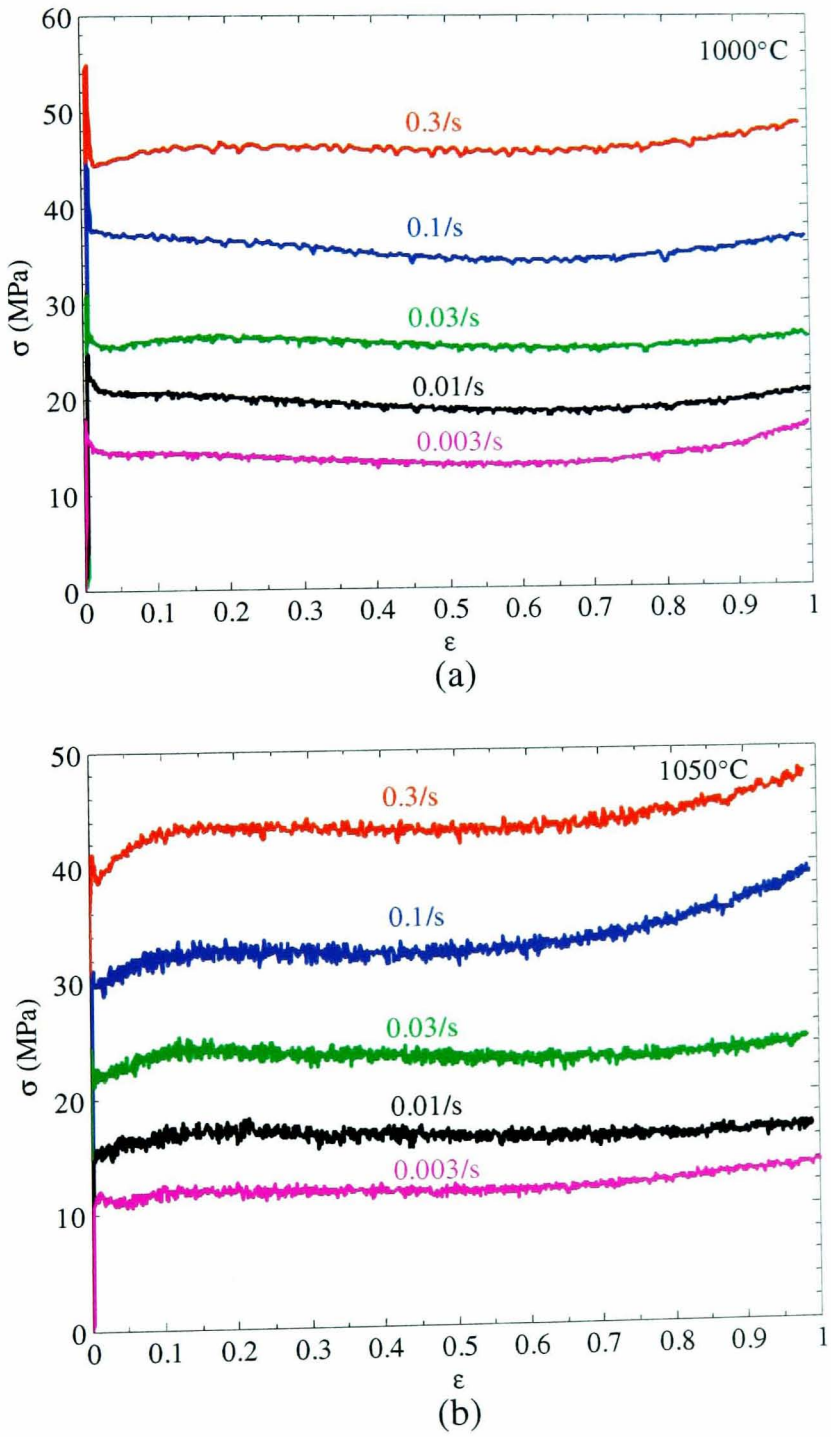

Figure 4.11: Flow stress curves of Ti-6Al-4V with globular initial microstructure at super-transus temperatures of (a) 1000 and (b) 1050°C.

Hot deformation in the beta phase field is typical of that for materials undergoing dynamic recovery in which the rate of hardening by generation of dislocations is balanced by the rate of softening due to dislocation annihilation, thus resulting in the constant flow stress deformation [15]. Higher steady-state stresses occurred at higher strain rates and lower deformation temperatures as shown in Figure 4.11.

4.2.3 Discontinuous yielding behaviour

As observed in Figures 4.10 and 4.11, a discontinuous yield drop was exhibited in the flow stress curves of as-received Ti-6Al-4V. The discontinuous yielding phenomenon has been found for a range of materials including those having a body-centred cubic crystal structure [51, 52]. Although a yield drop is not exhibited in pure β-Ti, discontinuous yielding has been observed in a large number of β-Ti alloys such as Ti-10V-2Fe-3Al, Ti-15V-3Cr-3Sn-3Al, Ti-3Al-8V-6Cr-4Mo-4Zr [51, 53] and has been attributed to mobile dislocation generation [54]. This phenomenon can be explained by using two theories, *i.e.* the static and the dynamic deformation theories [55]. The static theory involves dislocation locking and unlocking. The initial yielding is related to the break-away of dislocations from a solute atom environment. The dislocations are pinned by the solute atoms and these dislocations will break away from their locking points when subject to sufficiently high stress, thus generating a higher density of mobile dislocations that eventually leads to an abrupt yield stress drop. Hence, the yield point can be considered as an indicator of the applied stress required in order to loosen dislocations from their pinning points [56]. The dynamic theory relates to the rapid generation of new mobile dislocations from grain boundary sources upon pre-straining. Thus, dislocation density is

suddenly increased, followed by dislocation motion and multiplication which in turn leads to deformation proceeding from the grain boundary region inward [15, 57]. These two theories rely upon the same foundation which is the initial mobile dislocation inside the material is low prior to deformation. It has also been observed that the discontinuous yielding depends on the composition [55]. As the solute content increases, the stress drop at the yield point is increased.

4.2.4 Effect of imposed strain rate

The flow stress data can be analysed by using a traditional method where the flow stress is considered to have a power law dependence on the imposed strain rate [58]. The flow stress, σ can be related to strain rate, $\dot{\varepsilon}$ as:

$$\sigma = C\dot{\varepsilon}^m \qquad \text{(Eq. 4.1.1)}$$

where C is the strain-hardening coefficient and m is a strain rate sensitivity parameter. Strain rate sensitivity quantifies the effect of strain rate on the flow stress of a certain material. It gives a measure of the stress increase required to generate a certain increase in plastic strain-rate at a given level of plastic strain and a given temperature [27]. The strain-rate sensitivity can be derived based on Equation 4.1.1 using a log-log plot of the steady state stress, σ_{ss} against the imposed strain rate at various temperatures, as illustrated in Figure 4.12. It can be seen that the constant temperature behaviour can be fitted linearly, which is generally observed in high temperature materials. The strain rate sensitivity values can be estimated from the gradients of these curves [59]. The relationship between stress and strain rate

indicates that, as strain rates increases, the material increasingly hardens due to the increased rate of dislocation generation which in turn increases dislocation density. Since the rate of dislocation annihilation depends on the dislocation density [28], recovery mechanisms such as climb and cross-slip would be faster at higher imposed strain rate.

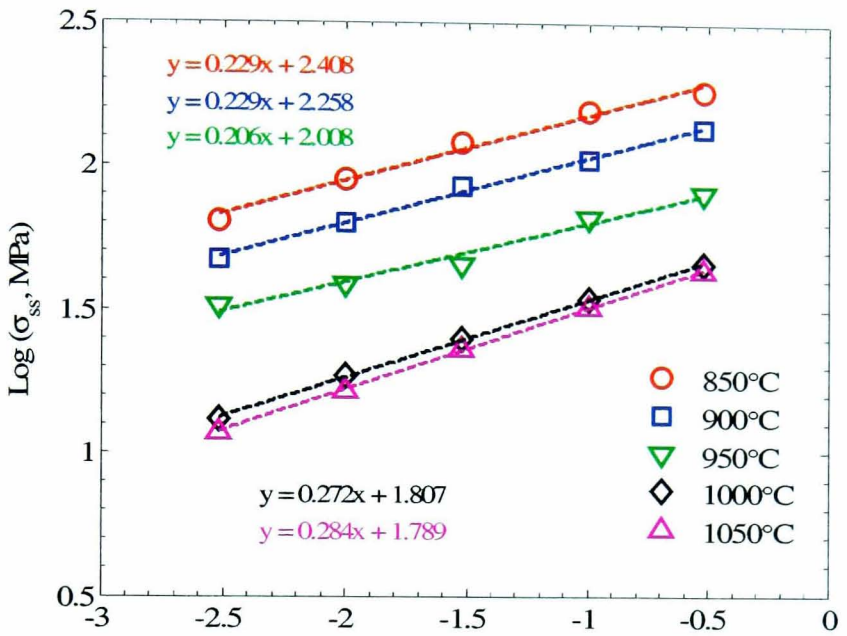

Figure 4.12: The variation of steady-state stress, σ_{ss} with strain rate, $\dot{\varepsilon}$ at subtransus and supertransus temperature for the Ti-6Al-4V with globular initial microstructure.

The variation of strain rate sensitivity m for as-received Ti-6Al-4V with globular initial microstructure at temperatures ranging from 850-1050°C is illustrated in Fig. 4.13. The maximum m-value is obtained above the β-transus temperature whilst the minimum m-value is achieved near the sub-transus temperature. The strain rate sensitivities obtained for this study were in the range from 0.20-0.29.

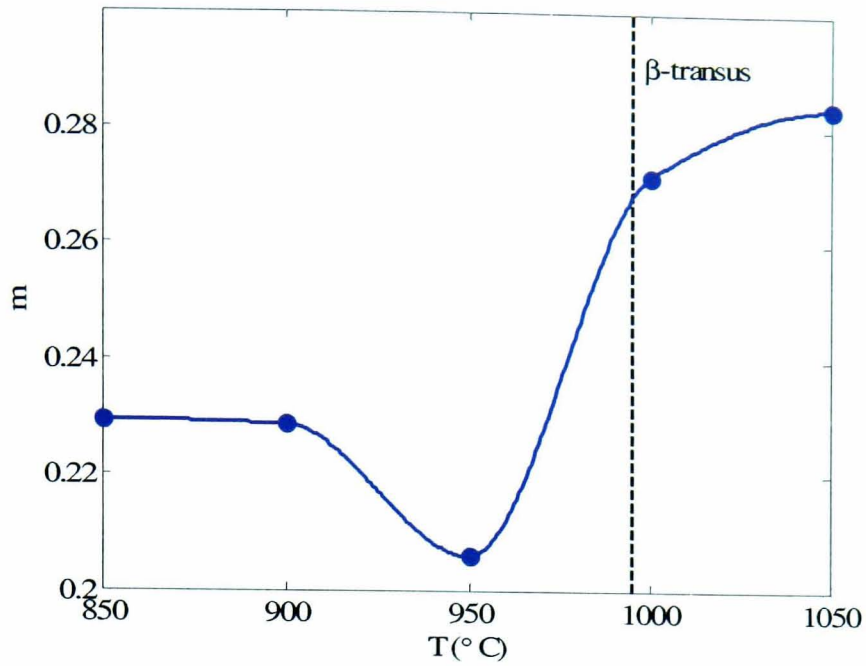

Figure 4.13: The variation of strain rate sensitivity *m* with temperature for the Ti-6Al-4V with globular initial microstructure, derived using steady state flow stress.

4.2.5 Effect of working temperature

The effect of working temperature on the flow stress behaviour for the as-received Ti-6Al-4V was evaluated at various constant strain rates in more detail by plotting the steady state stress against temperature, as shown in Figure 4.14. It can be seen that hot deformation occurring in the two phase $\alpha + \beta$ field is strongly dependent on temperature. Flow stresses were found to be much higher in the $\alpha + \beta$ field, indicating that plastic deformation becomes more difficult in this region. On the other hand, the temperature sensitivity of the flow stresses was relatively weak in the β field as indicated by the plateau above the β transus. This behaviour is in agreement with the results reported by Seetharaman for Ti-6Al-4V [58] and Semiatin for Ti-6Al-2Sn-4Zr-2Mo alloy [60]. Hence, hot working in this higher temperature regime may give an advantage in reducing the load required and thus providing better formability. The transition in the temperature sensitivity below the β transus may then be attributed to the change of volume fraction of the α and β phases and to the different deformation characteristics of the individual phases.

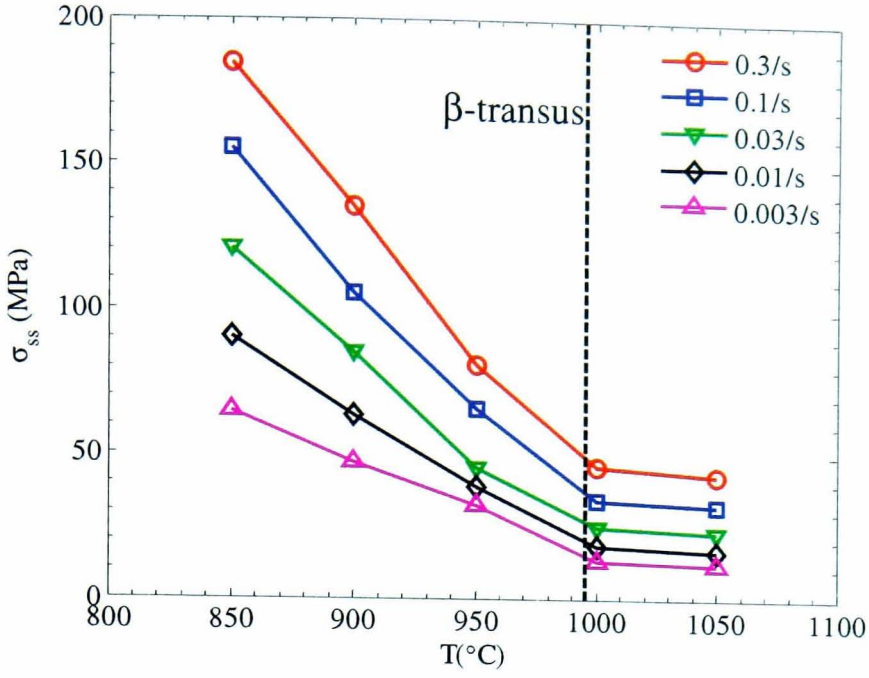

Figure 4.14: Temperature dependence of the steady-state flow stress below and above the β-transus for the Ti-6Al-4V with globular initial microstructure.

In the lower α + β phase field, the ratio of α is much higher than β, and α as a major constituent dominates the overall flow stress behaviour of two-phase Ti-6Al-4V. As temperature increases beyond the β-transus, α transforms into a continuous β phase that begins to dominate the total flow stress. In the single β-phase field, the flow stresses show a weak temperature dependence that reflects the deformation characteristic of this dominant constituent. According to Flower, the temperature sensitivity of flow stress for α and β phases is diffusion-rate dependent [11]. At temperatures where diffusion is slow, deformation of both alpha and beta exhibits high temperature sensitivity. On the other hand, at temperatures where rapid diffusion contributes to the deformation processes, a low temperature sensitivity of flow stresses is observed. However, for the β phase, the transition from higher to lower temperature sensitivity in flow stress occurs at a much lower absolute temperature than for the α phase. Therefore, deformation occurring in the two-phase α+β field should still be dominated by the deformation characteristics of the α phase. Quantitatively, the temperature sensitivity of the flow stress at constant strain rate, $\dot{\varepsilon}$

and strain ε can be defined as a non-dimensional parameter, S defined by [61]:

$$S = \frac{1}{T}\left[\frac{\partial(\log\sigma)}{\partial(1/T)}\right]_{\dot{\varepsilon},\varepsilon} \qquad \text{(Eq. 4.1.2)}$$

where σ is stress (MPa) and T is the working temperature (Kelvin). Based on the above equation, the temperature sensitivity of flow stress can be evaluated at various strain rates by plotting logarithmic values of steady state stress σ_{ss} against $1/T$, as illustrated in Figure 4.15. Then, S is obtained by dividing the slope of each curve by the test temperature. From Figure 4.16, it can be seen that the temperature sensitivity of flow stress increases with decreasing temperature at constant strain rate.

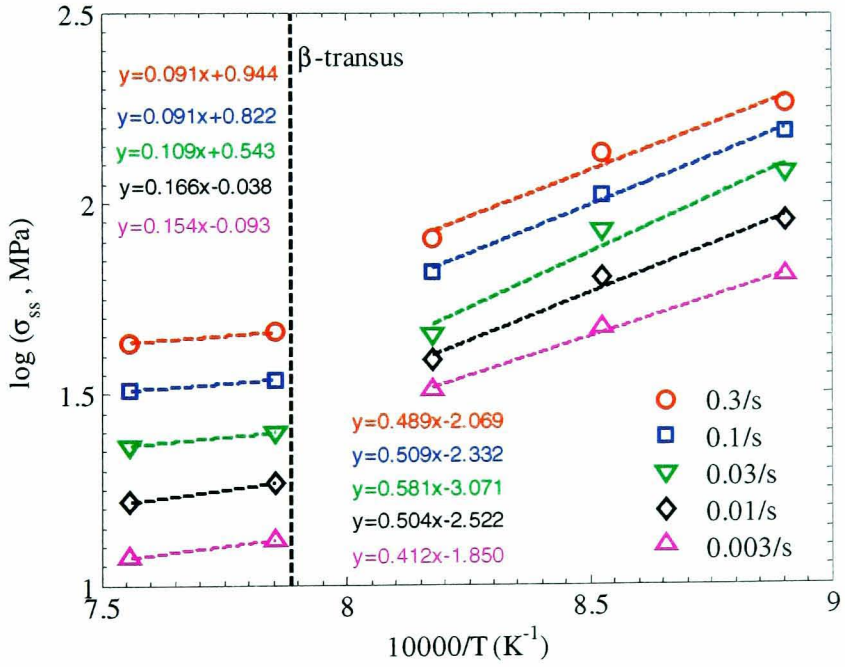

Figure 4.15: A plot of log (σ_{ss}) versus reciprocal temperature at various strain rates for Ti-6Al-4V with globular initial microstructure.

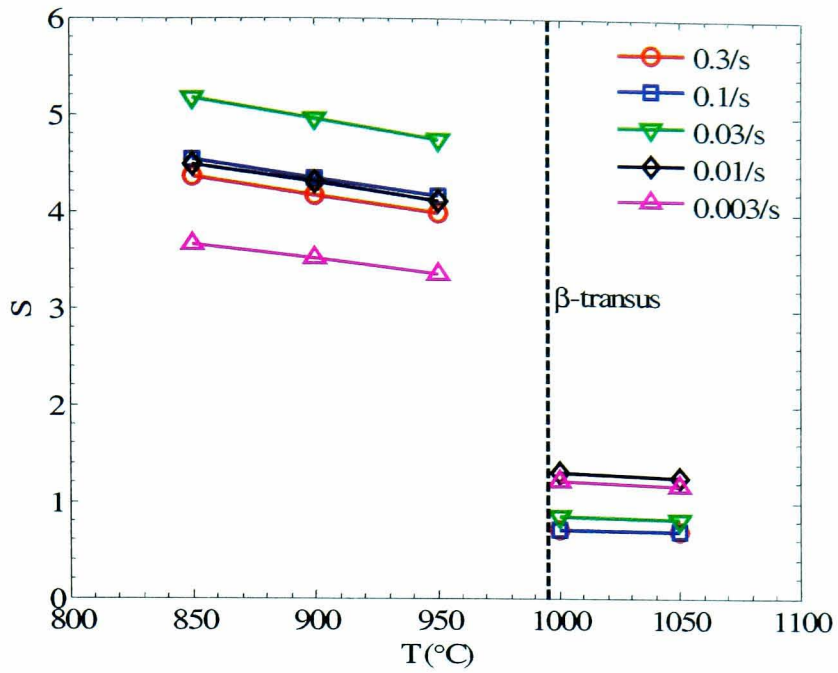

Figure 4.16: The variation in temperature sensitivity, *S*, as a function of temperature at various strain rates for Ti-6Al-4V with globular initial microstructure.

In order to understand the rate controlling process during hot deformation, an attempt has been made to estimate the apparent activation energy for the deformation mechanisms by using an empirical power-law equation that relates the steady-state flow stress to temperature and strain rate [62-64]:

$$\dot{\varepsilon} = A\sigma^n \exp\left(\frac{-Q}{RT}\right) \qquad \text{(Eq. 4.1.3)}$$

where A is a constant, Q is an apparent activation energy, R is the universal gas constant and n is the stress exponent. The latter can be determined from the inverse of the slopes of the curves in Figure 4.12. In the $\alpha + \beta$ field, the stress exponent n is estimated to be 4.3 for the strain rate range 0.003 – 0.3/s. In the single β-phase field, the estimated stress exponent n is 3.6.

Based on the equation 4.1.3, the apparent activation energy, Q can be determined by using an Arrhenius plot, which is constructed by plotting logarithmic values of

steady state stress, σ_{ss} against reciprocal of temperature, $1/T$ (Kelvin), as shown in Fig. 4.17.

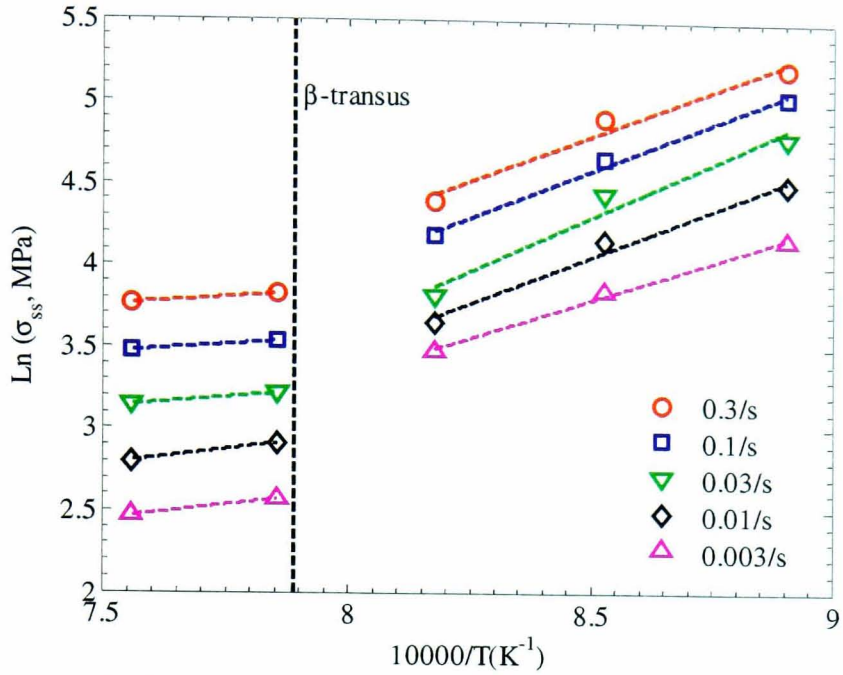

Figure 4.17: The variation of steady-state stress with inverse of temperature for sub-transus deformation of Ti-6Al-4V with globular initial microstructure.

Q can be calculated from the slopes of the curves by using the expression:

$$Q = Rn\left[\frac{\partial \ln \sigma_{ss}}{\partial(1/T)}\right]_{\dot{\varepsilon}} = \frac{R}{m}\left[\frac{\partial \ln \sigma_{ss}}{\partial(1/T)}\right]_{\dot{\varepsilon}} \quad \text{where } n = 1/m \qquad \text{(Eq. 4.1.4)}$$

The estimated activation energy Q for subtransus deformation is 409kJ/mol, which is much higher than that for self diffusion in α-titanium (150kJ/mol) [65]. This result is in agreement with previous work which reports that for hot deformation within α + β region, activation energies obtained are usually much higher than that for self-diffusion and are in the range 310-720kJ/mol [11, 66, 67]. The large Q value suggests that the operative dynamic restoration process during sub-transus deformation is a complex combination of various deformation mechanisms, due to the temperature dependence of volume fraction of the individual phase and the

difference between the flow stresses of the hard α and soft β phases [68]. On the other hand, the activation energy Q obtained for supertransus deformation is estimated here to be 84kJ/mol, which is comparable to that for self diffusion in the β phase (153kJ/mol) [53]. Because both plots in Figure 4.12 & 4.17 can be fitted linearly, it is useful to relate σ_{ss} with the Zener-Hollomon parameter Z, which is defined as [69]:

$$Z = \dot{\varepsilon} \exp\left(\frac{Q}{RT}\right) \qquad \text{(Eq. 4.1.5)}$$

where the Zener-Hollomon parameter combines the effects of the two important process variables $\dot{\varepsilon}$ and T for hot deformation. For doing this correlation, both n and Q are assumed constant within the range of working temperature and imposed strain rates. Due to the different activation energy values for the α+β and β regions (409 and 84kJ/mol respectively), the analysis was separated into two linear regions, as shown in Figure 4.18. The relationships between σ_{ss} and Z were found to be:

$$\begin{aligned} \sigma_{ss} &= 0.012Z^{0.227} \; ; 850 \le T \le 950°C \; ; 0.003 \le \dot{\varepsilon} \le 0.3s^{-1} \\ \sigma_{ss} &= 7.142Z^{0.278} \; ; 1000 \le T \le 1050°C; 0.003 \le \dot{\varepsilon} \le 0.3s^{-1} \end{aligned} \qquad \text{(Eq. 4.1.6)}$$

These results suggest that the power-law creep equation used is valid in predicting steady state stress, σ_{ss} for the as-received Ti-6Al-4V within these regimes.

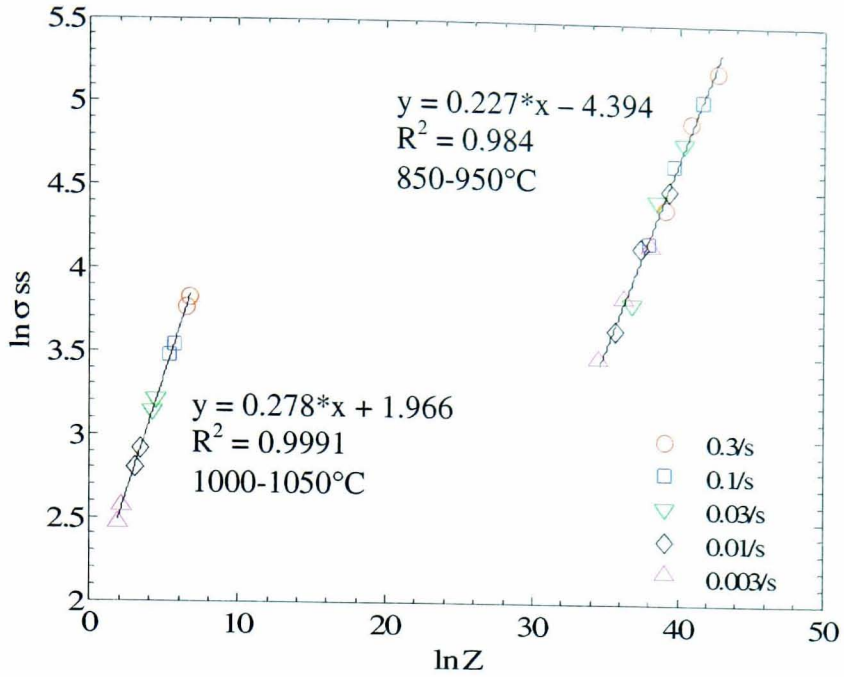

Figure 4.18: A log-log plot of steady state stress against Zener-Hollomon parameter for deformation in the $\alpha + \beta$ and β-phase fields for Ti-6Al-4V with globular initial microstructure.

4.3 Flow stress behaviour of Ti-6Al-4V with acicular initial microstructure

4.3.1 General behaviour

Typical corrected flow stress curves for Ti-6Al-4V with acicular initial microstructure obtained from hot compression tests at various constant strain rates are summarised in Fig 4.19. All flow stress curves reveal the characteristic features of strong initial strain hardening, a broad peak at low strains followed by moderate to extensive flow softening beyond the peak stress until a steady state stress is reached. These results are in agreement with previous studies on the hot deformation of Ti-6Al-4V with an acicular structure [70, 71]. There is no indication of the discontinuous yielding behaviour observed in the globular microstructure, indicating that the initial microstructure has a profound effect on the shape of the flow stress curves during hot deformation.

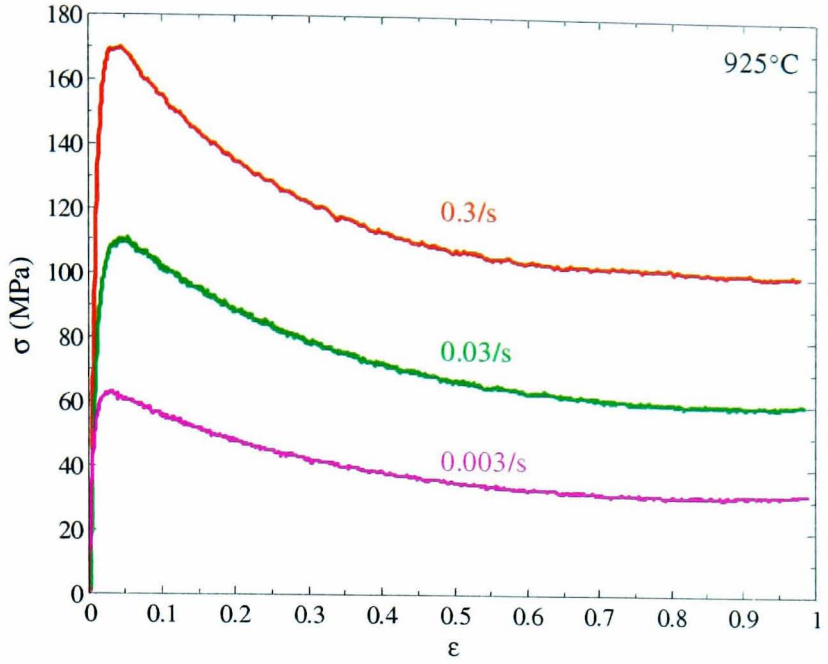

(a)

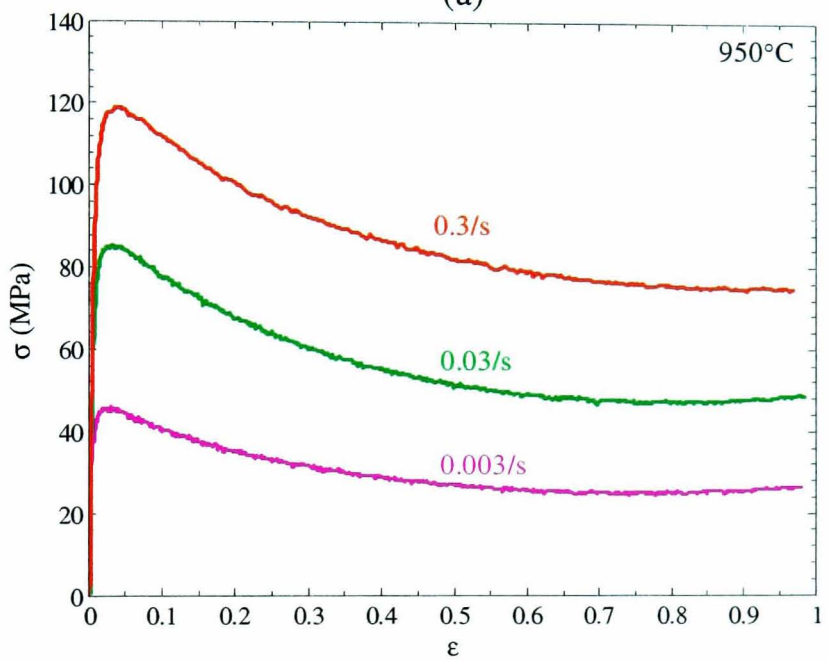

(b)

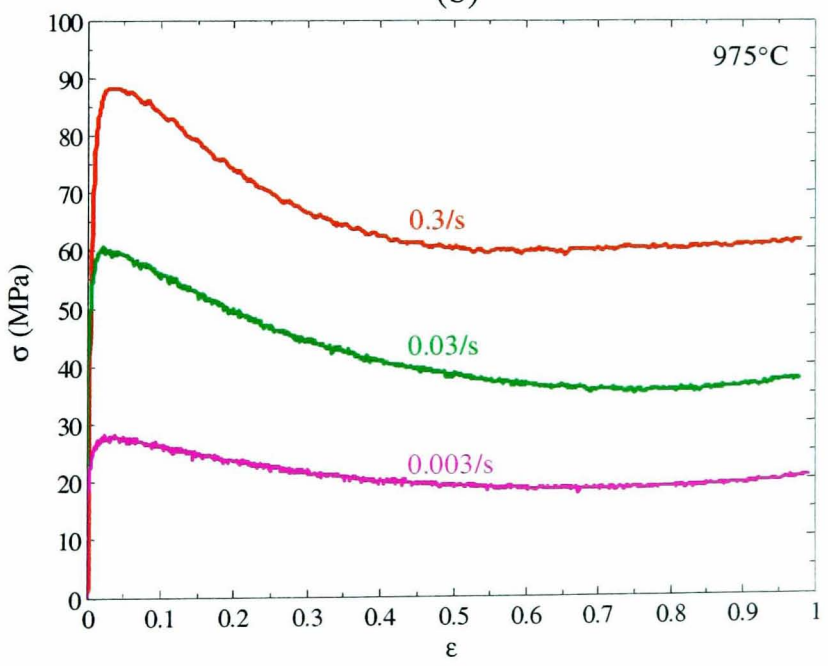

(c)

Figure 4.19: Flow stress curves of Ti-6Al-4V with acicular initial microstructure at temperatures of (a) 925, (b) 950 and (c) 975°C.

4.3.2 Effect of strain rate

The variation of flow stress with strain rate at various temperatures for the β-heat treated acicular Ti-6Al-4V is illustrated in Fig. 4.20.

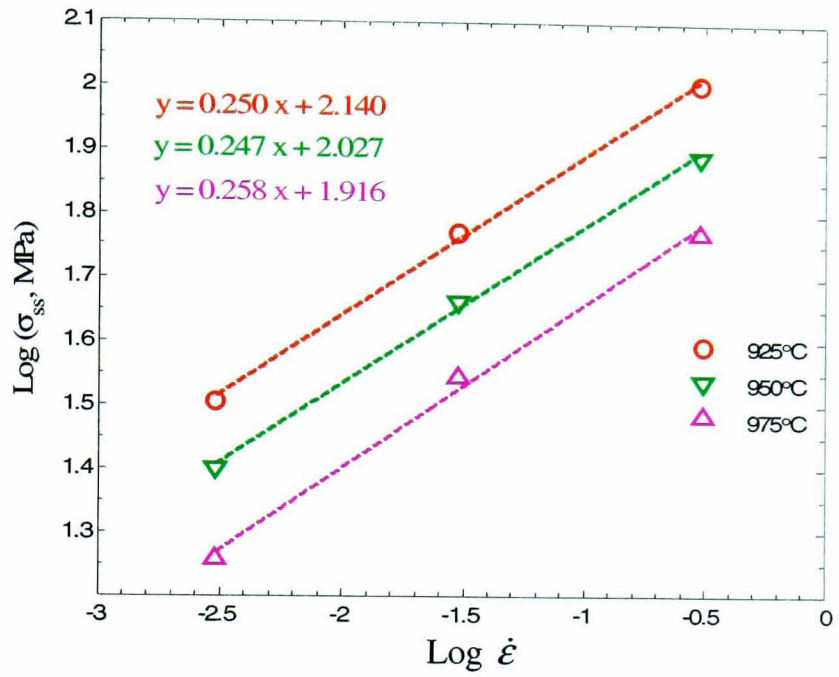

Figure 4.20: The variation of steady-state stress with strain rate for Ti-6Al-4V with acicular initial microstructure.

It is clear that the log σ_{ss} vs log $\dot{\varepsilon}$ plot can be fitted linearly for all the working temperatures. Similar behaviour has been observed for as-received Ti-6Al-4V where σ_{ss} increases with increasing the imposed strain rates. The variation of strain rate sensitivity, m estimated from the slopes of these curves lies in the range 0.24-0.26 for temperature regimes of 925-975°C, and again indicates that plastic deformation is non diffusion-driven type and controlled by coupled dislocation glide/climb (m = 0.23-0.27) [52, 72, 73].

4.3.3 Effect of working temperature

Figure 4.21 shows the variation of the steady state stresses, σ_{ss} with working temperature at constant strain rates of 0.003-0.3/s for the acicular Ti-6Al-4V.

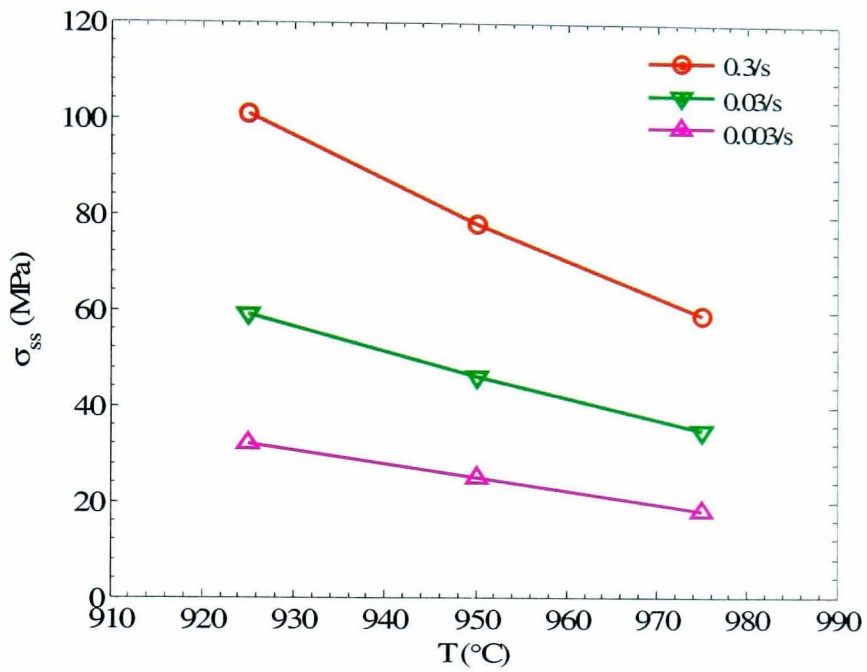

Figure 4.21: Temperature dependence of the steady-state stresses σ_{ss} for the Ti-6Al-4V with acicular initial microstructure.

It can be seen that σ_{ss} decreases markedly with increasing temperature, especially for a strain rate of 0.3/s, which indicates that the material has a high temperature sensitivity under these conditions. A strong temperature dependence of flow stress indicates that the overall deformation is dominated by the α-phase, which possesses a characteristically high temperature sensitivity. The variation of temperature sensitivity of flow stress, S with temperature can be seen from Figure 4.22, and was found to be in the range of 5.4-6.2 for all imposed strain rates.

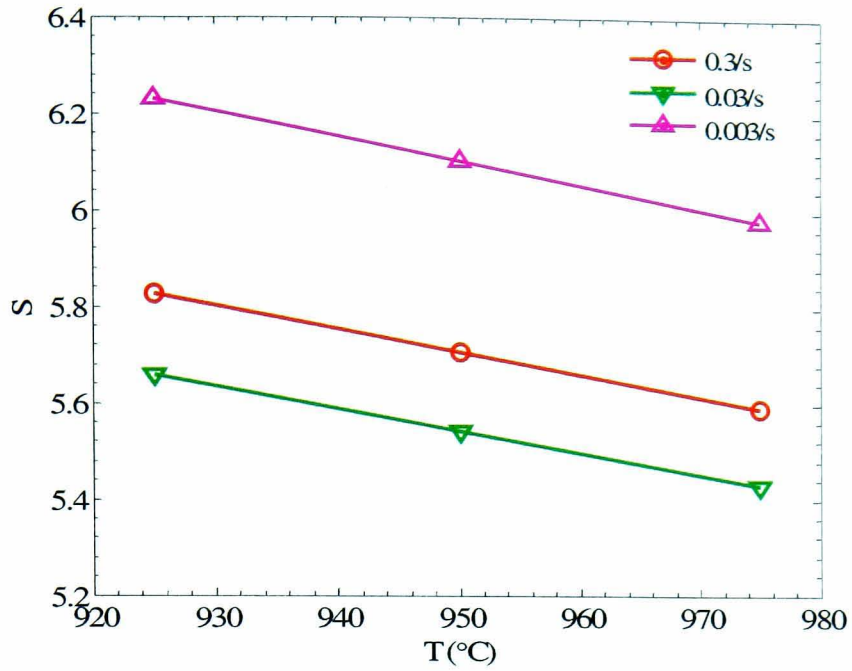

Figure 4.22: The variation in temperature sensitivity, *S*, as a function of reciprocal temperature at various constant strain rates for the Ti-6Al-4V with acicular initial microstructure.

An Arrhenius plot showing the variation of steady state stress with inverse of temperature on a semi-log scale is presented in Fig. 4.23.

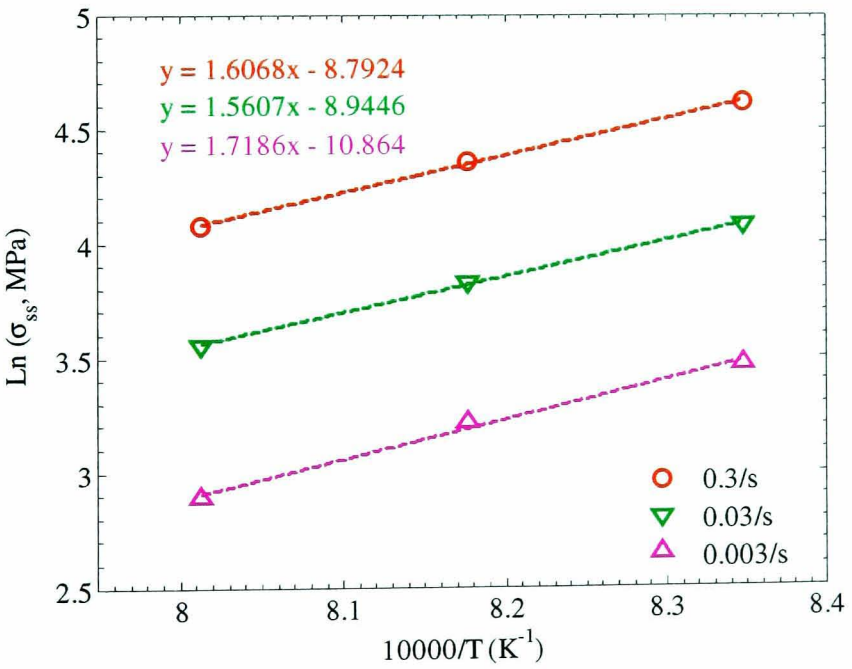

Figure 4.23: The Arrhenius plot used to show the variation of steady-state stress with inverse of temperature for Ti-6Al-4V with acicular initial microstructure.

The linear fits to the data are almost parallel suggesting that similar deformation mechanisms operate for all strain rates. The apparent activation energy, Q derived by using Equation 4.1.4, was found to be 538kJ/mol. This value is comparable to a previous finding (522kJ/mol) reported by Sheppard and Norley [74]. The high value of Q in this case may be attributed to the occurrence of dynamic globularisation of α laths into equi-axed morphology.

Figure 4.24 shows a log-log plot of σ_{ss} vs Z for all test conditions. It can be seen that σ_{ss} varies linearly with increasing Z, indicating that the power-law relationship is valid for predicting σ_{ss} during deformation at 925-975°C under strain rates of 0.003-0.3/s, such that:

$$\sigma_{ss} = 1.769.10^{-4}.Z^{0.252} \qquad \text{(Eq. 4.1.7)}$$

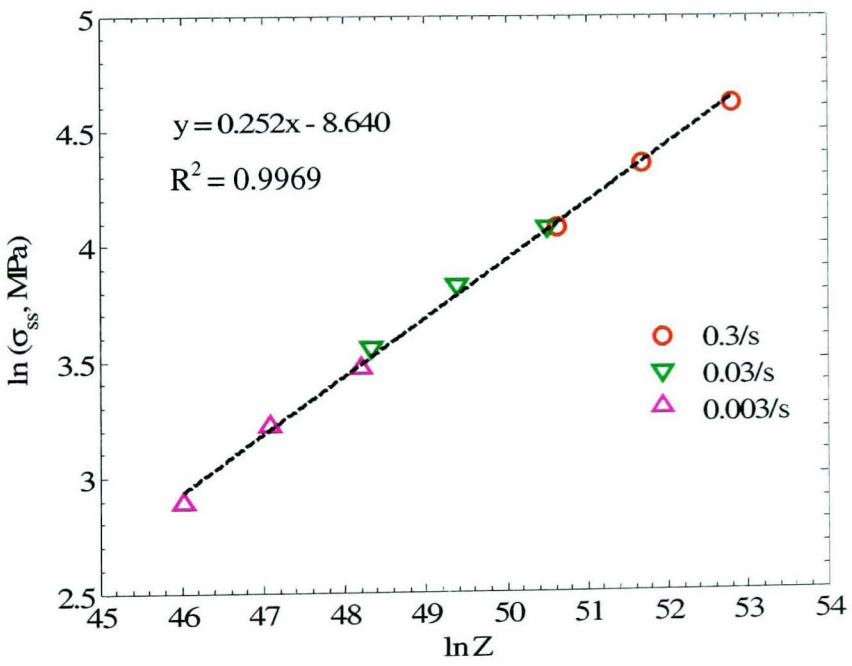

Figure 4.24: A log-log plot of steady state stress against Zener-Hollomon parameter for deformation of acicular Ti-6Al-4V at 925-975°C and 0.003-0.3/s.

4.3.4 Flow softening behaviour

As outlined previously, a flow-softening phenomenon is observed for all testing conditions. Since the flow stress curves presented here were corrected for adiabatic heating, a possible source of flow softening is related to morphological changes in the α-phase during deformation. According to Seetharaman and Semiatin [75], the pronounced gradual flow softening that occurs in the acicular morphology is mainly governed by two mechanisms, namely: microbuckling and dynamic globularisation of the lath structure. During the onset of peak stress at very low strain, α laths start to undergo deformation. This process involves translamellar shear within α laths which are oriented parallel and perpendicular to the forging direction. With increasing strain, the α lath structure evolves by bending, kinking or buckling which in turn orient the laths into preferred directions, i.e, parallel to the metal flow resulting in a net reduction of the flow stress. The second possible mechanism responsible for flow softening is related to the size and volume fraction of the dynamically globularised α structure. Since at low strain, the volume fraction of globularised α is small, flow softening is mainly controlled by microbuckling. With increasing strain, the globularised fraction is increased which in turn dominates the flow softening. Chapter 6 will discuss the microstructure evolution of β-heat treated acicular Ti-6Al-4V in detail.

Another mechanism that might be responsible for flow softening is a change of crystallographic texture [76]. Texture influences may arise as a result of the specific slip systems activated in the α and β-phases and interface sliding as a function of colony orientation. Based on polycrystalline plasticity calculations for the hexagonal

α-phase, both basal and prism slip show a tendency to increase texture hardening during compression of acicular materials. On the other hand, pyramidal slip does contribute to texture softening during compression.

The magnitude of flow softening $\Delta\sigma$ was quantified by calculating the difference between the peak stress, σ_p and the steady state stress, σ_{ss} at all conditions, as illustrated in Figure 4.25. It can be seen that $\Delta\sigma$ decreases linearly with increasing working temperature. In contrast, at a given temperature, $\Delta\sigma$ decreases with decreasing imposed strain rate.

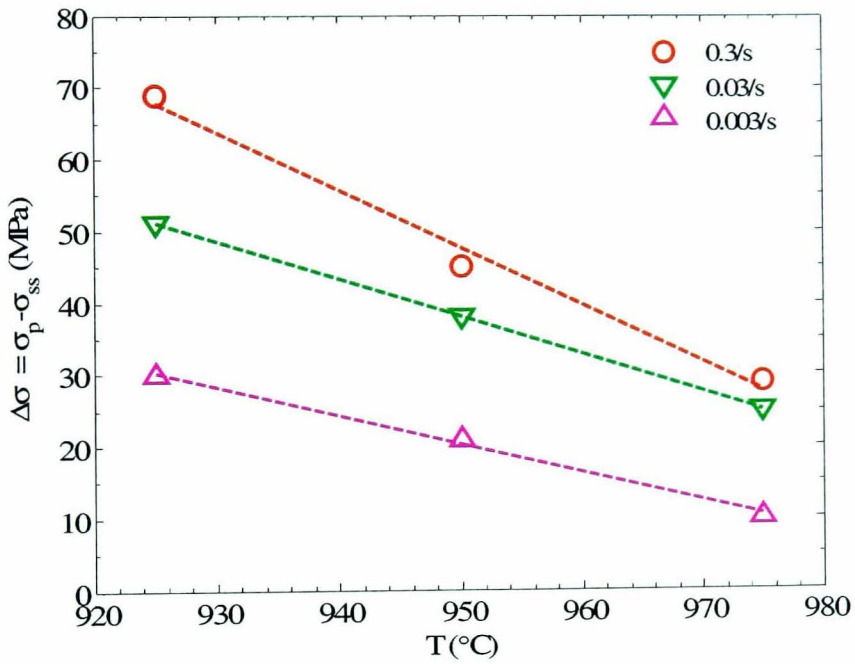

Figure 4.25: The variation of the flow softening during hot deformation of Ti-6Al-4V with acicular initial microstructure.

Table 4.1 lists the amount of microstructure-related flow softening quantified by using a relative difference between the peak stress, σ_p and steady state stress, σ_{ss}, given as [77]:

$$\gamma = \left.\frac{\sigma_p - \sigma_{ss}}{\sigma_p}\right|_{\dot{\varepsilon},T} \qquad \text{(Eq. 4.1.8)}$$

The flow softening index exhibited a strong temperature dependency, where γ values decrease with increasing working temperature. The higher γ values at lower temperatures may be attributed to the fact that the volume fraction of α-phase is much higher. Since a greater quantity of α transforms into β-phase with increasing temperature, the rate of flow softening at higher temperature ought to be reduced since deformation of the β-phase is characterised by an absence of flow softening. Similar behaviour has been observed in previous studies [77, 78]. On the other hand, it appears that the dependence of the flow-softening index, γ, on the imposed strain rates is relatively weak.

Table 4.1. Flow softening index, γ, for Ti-6Al-4V with acicular initial microstructure deformed at 925-975°C under constant strain rates of 0.003-0.3/s.

Temperature (°C)	**Flow softening index, γ**		
	0.3/s	**0.03/s**	**0.003/s**
925	0.41	0.46	0.48
950	0.37	0.45	0.46
975	0.33	0.42	0.36

Closer examination of the flow stress curves in Figure 4.19 reveals that the rate of flow softening varies with strain. In order to quantify the flow softening rate with respect to strain, another useful parameter, γ', can be determined by using an expression of the form [79]:

$$\gamma' = \frac{1}{\sigma}\left(\frac{\partial \sigma}{\partial \varepsilon}\right) = \frac{\partial \ln \sigma}{\partial \varepsilon} \qquad \text{(Eq. 4.1.9)}$$

For example, the result showing the variation of flow softening rate, γ', with strain, ε, during deformation at 925°C and 0.3/s is presented in Figure 4.26. It can be seen that the flow-softening rate varies with the highest rate occurring at low strain. The maximum softening rate (2.142) occurred at a strain of 0.07.

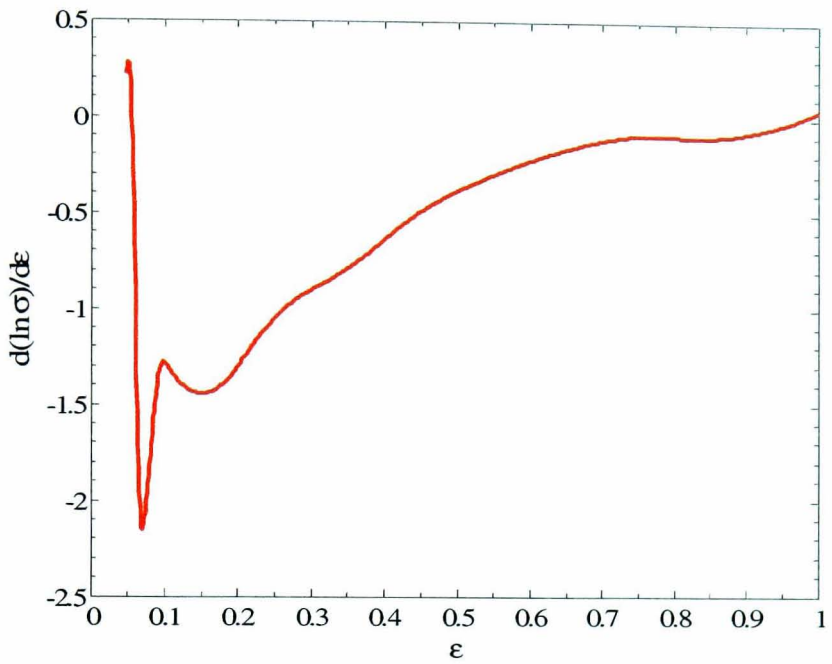

Figure 4.26: The variation of flow softening rate during hot deformation of Ti-6Al-4V with an acicular starting microstructure at 925°C and 0.3/s.

Flow softening or negative strain hardening can cause flow localisation during hot compression regardless of the effects of die chilling or high friction [61]. With knowledge of m and γ', it is possible to detect and predict if there is any indication of flow instability (flow localisation and shear banding) during hot deformation. The indicator is assigned as a flow parameter α_c, defined as [60, 80]:

$$\alpha_c = -\left(\frac{\gamma' - 1}{m}\right) \qquad \text{(Eq. 4.2.1)}$$

and non-uniform flow in compression is considered to occur when the flow parameter, α_c exceeds 5. Table 4.2 lists the values of α_c determined at true strain of 1

(the approximate steady state condition). It was found that all α_c values are lower than 5, indicating the likely absence of flow localisation during hot deformation. These predictions are in good agreement with the macroscopic profiles of deformed specimens shown in Figure 4.27 which display no indication of shear banding or flow localisation.

Table 4.2. Flow localisation parameter α_c at true strain of 1 for hot deformation of Ti-6Al-4V with an acicular starting microstructure at 925-975°C under strain rates of 0.003-0.3/s.

Temperature (°C)	**Flow localisation parameter, α_c**		
	0.3/s	**0.03/s**	**0.003/s**
925	3.83	3.15	4.46
950	4.04	2.73	1.66
975	3.95	2.09	1.97

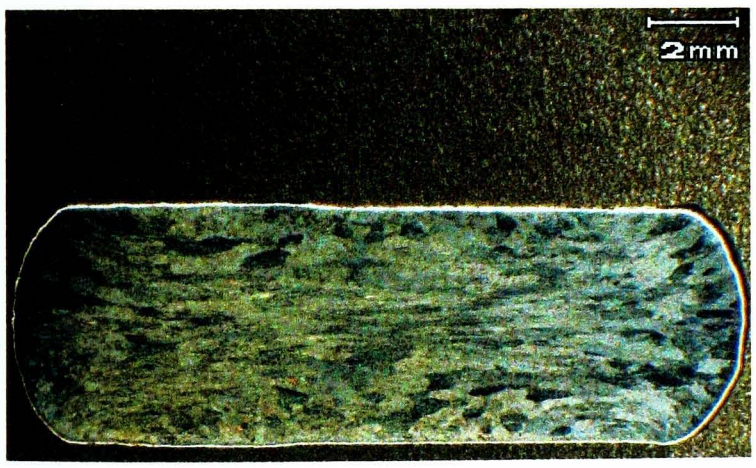

(a) 925°C;0.3/s

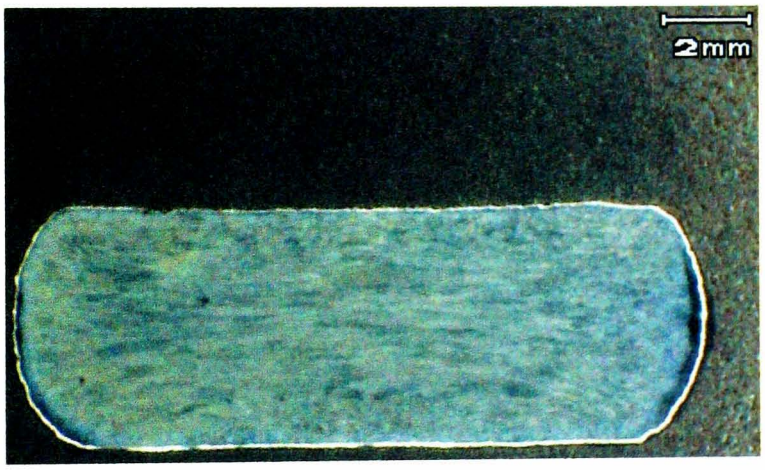

(b) 950°C;0.3/s

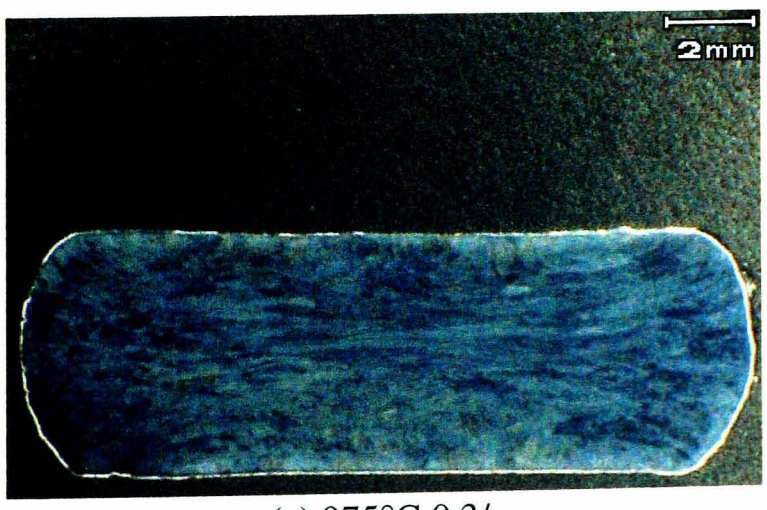

(c) 975°C;0.3/s

Figure 4.27: The transverse cross-sections of cylindrical specimens of acicular Ti-6Al-4V deformed to true strain of 1.

4.4 Flow stress behaviour of the single α and β-phase compositions in Ti-6Al-4V

4.4.1 General behaviour

Typical flow stress curves obtained for the single α-phase in Ti-6Al-4V are summarised in Fig. 4.28. The figure shows that the flow stress of the single α-phase alloys increases with strain rate and decreases with temperature. It is apparent that at lower temperatures (925 and 950°C) and higher strain rate (0.3/s), the flow stress curves exhibit initial work hardening behaviour after the onset of plastic deformation at strains of ~0.02. Following a peak stress there is a gradual decay to a steady-state condition. Higher peak stresses are observed at higher strain rates and lower temperatures. The flow softening effect is most pronounced at 975°C, whereas at higher strain rates, the flow stress curves only exhibit flow softening without significant work hardening behaviour.

On the other hand, a different type of flow stress behaviour is exhibited for single β-phase in Ti-6Al-4V, as shown in Figure 4.29. As expected, for a given set of conditions, the flow stress of single β-phase is much lower than that for the α-phase due to the fundamental deformation characteristics of the bcc crystal structure. Although in general most of the stress-strain curves of the β-phase are of the steady-state type, those at strain rates of 0.3 and 0.03/s and temperatures of 925, 950 and 975°C, show an initial peak stress followed by slight flow softening. However, the flow softening exhibited in the single β-phase is relatively negligible compared to that for the single α-phase material.

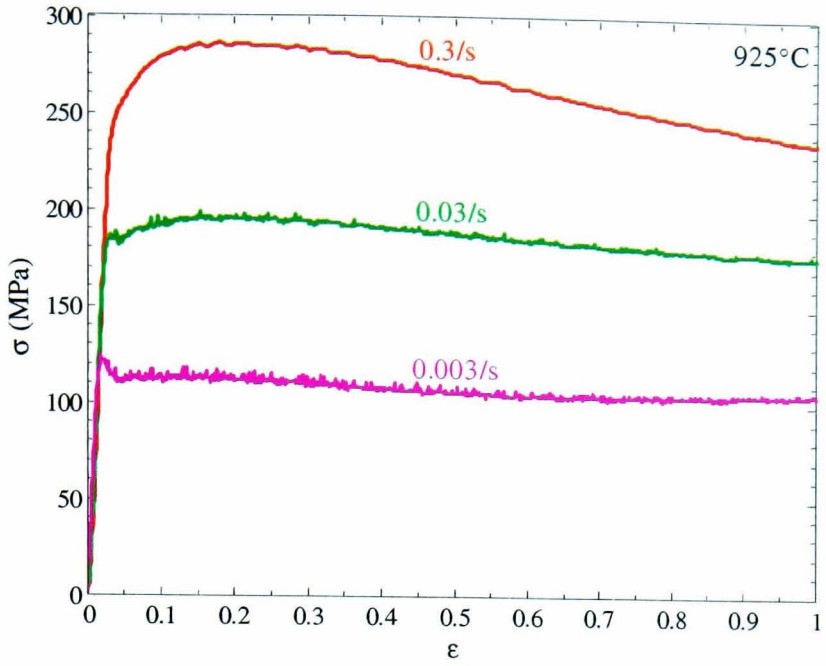

(a)

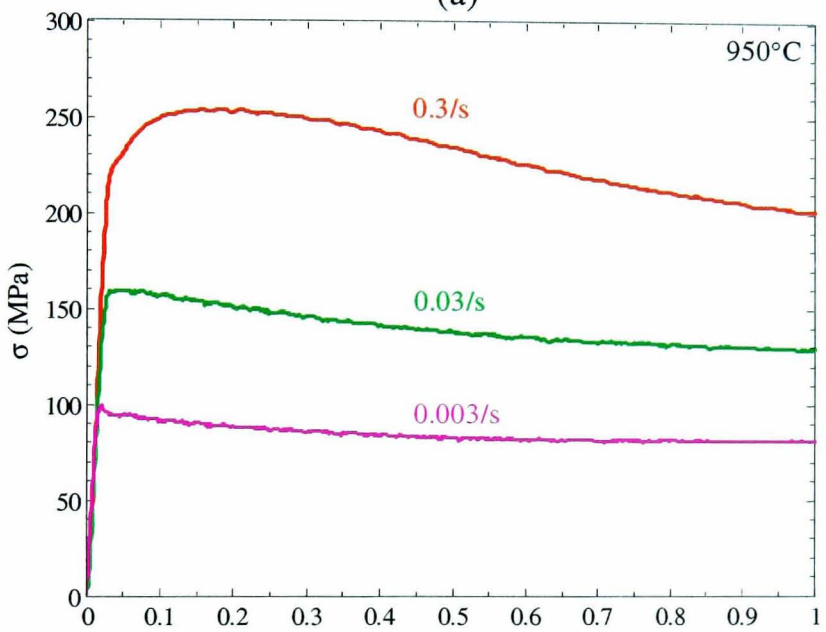

(b)

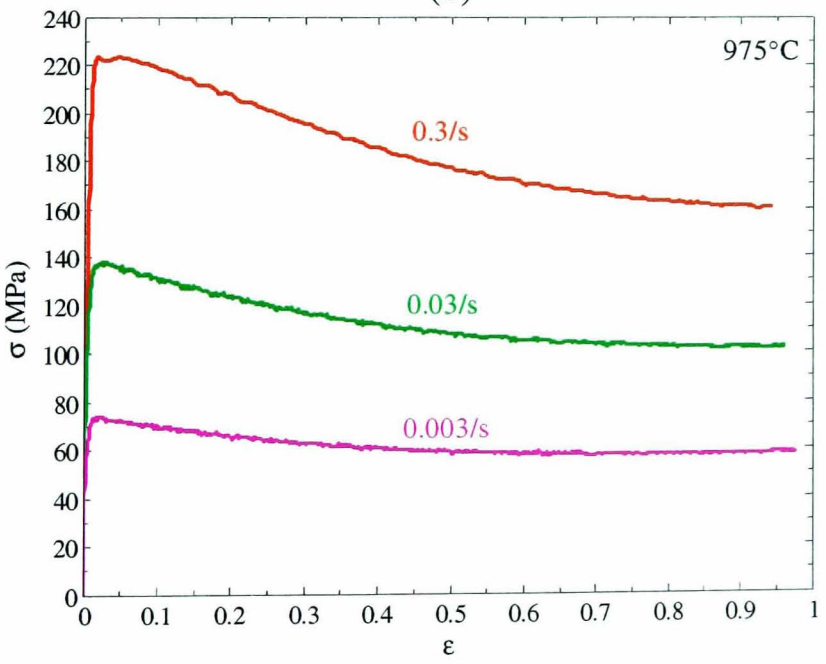

(c)

Figure 4.28: Flow stress curves of single α-phase in Ti-6Al-4V at temperatures of (a) 925, (b) 950 and (c) 975°C.

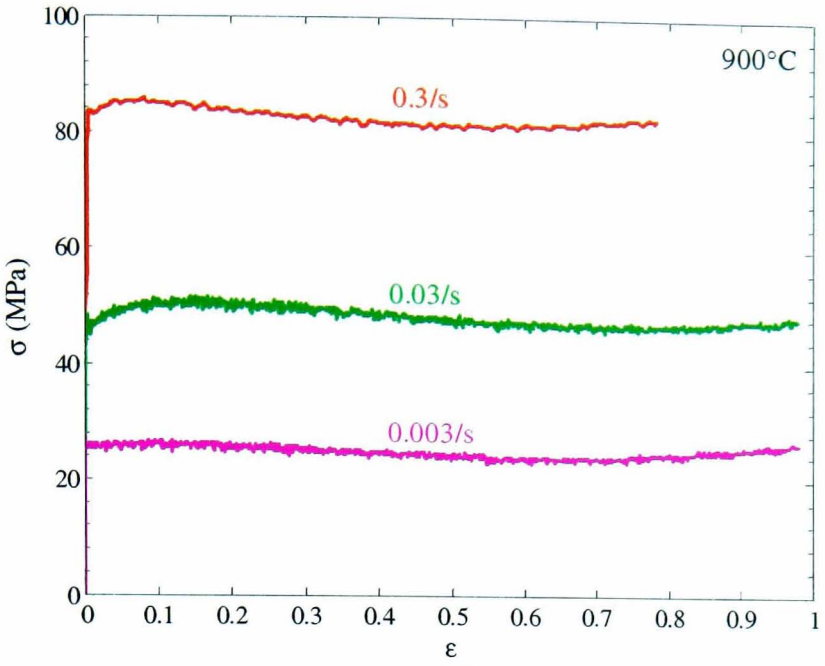
900°C
0.3/s
0.03/s
0.003/s
σ (MPa)
ε
0
20
40
60
80
100
0.1
0.2
0.3
0.4
0.5
0.6
0.7
0.8
0.9
1

(a)

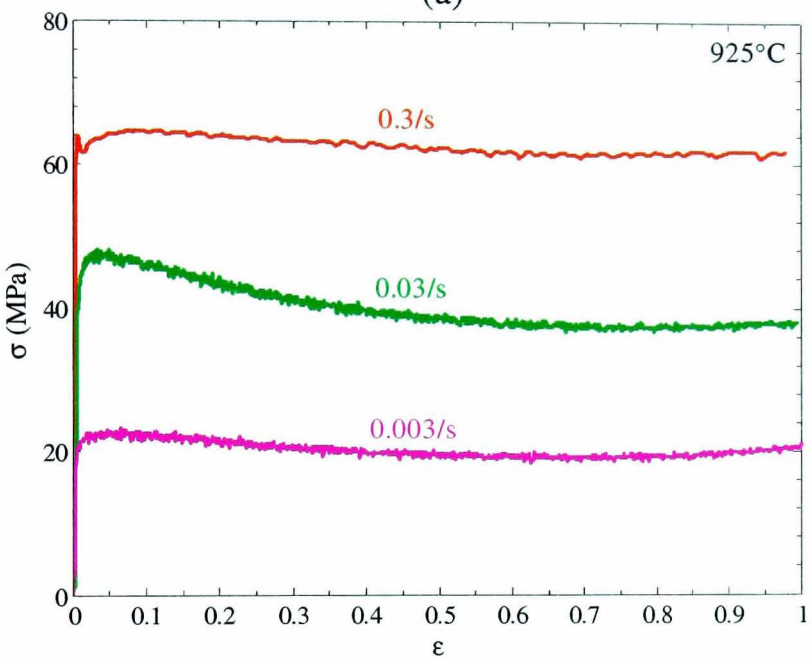
925°C
0.3/s
0.03/s
0.003/s
σ (MPa)
ε
0
20
40
60
80
0.1
0.2
0.3
0.4
0.5
0.6
0.7
0.8
0.9
1

(b)

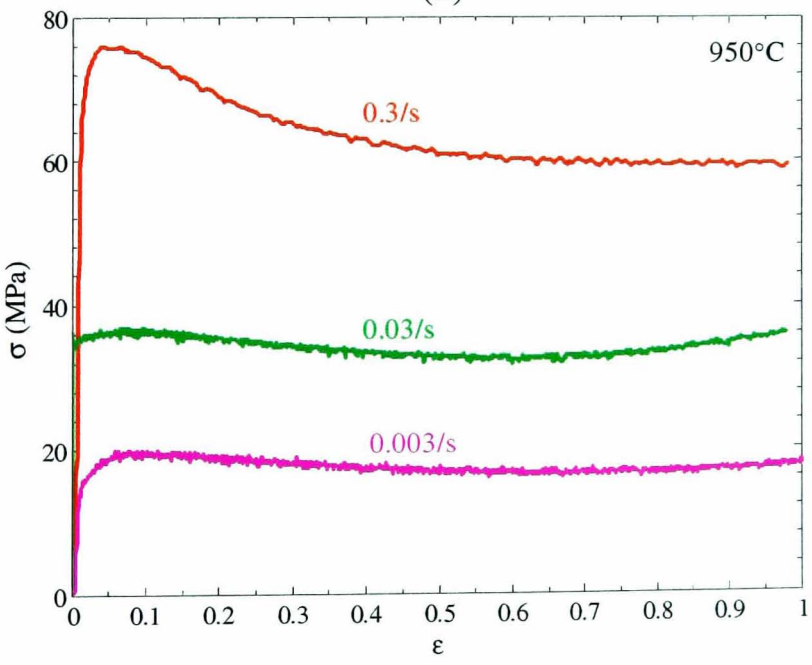
950°C
0.3/s
0.03/s
0.003/s
σ (MPa)
ε
0
20
40
60
80
0.1
0.2
0.3
0.4
0.5
0.6
0.7
0.8
0.9
1

(c)

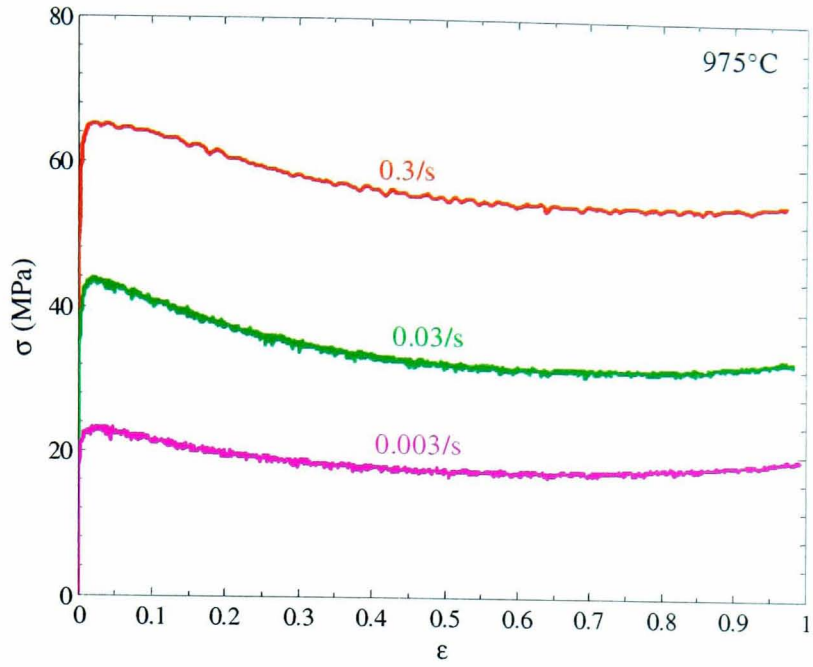

(d)

Figure 4.29: Flow stress curves of single β-phase in Ti-6Al-4V at temperatures of (a) 900, (b) 925, (c) 950 and (d) 975°C.

4.4.2 Effect of strain rate

The dependence of σ_{ss} on the imposed strain rate for both α and β-phase in Ti-6Al-4V at various temperatures can be represented in a log-log plot, as shown in Figure 4.30. It is obvious that σ_{ss} for the α-phase is much higher than for the β-phase at a given temperature and strain rate, indicating that the α-phase is much more resistant to plastic deformation due to the nature of its hcp crystal structure. It can be seen that σ_{ss} linearly increases with increasing strain rate for both the α and β-phases. The variation of strain rate sensitivity, m estimated from the slopes linear fits to these data lies in the range 0.19-0.21 for the α-phase and 0.25-0.26 for the β-phase. These m-values are comparable to those typical of deformation mechanisms controlled by dislocation glide (or climb-limited) processes characteristic of power law creep (m = 0.23-0.27) [52, 72, 73, 81].

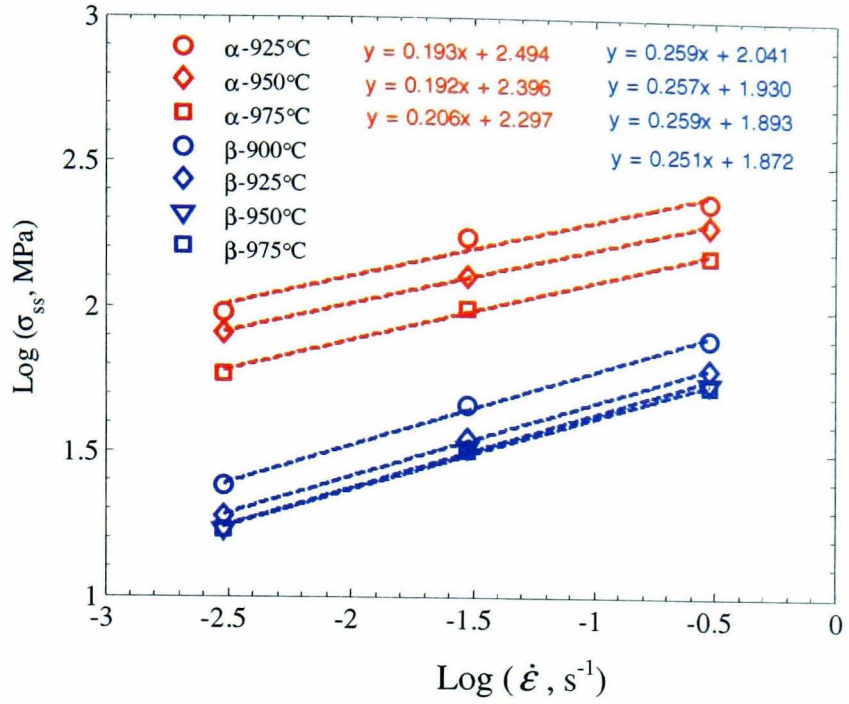

Figure 4.30: The variation of steady-state stress, σ_{ss} with strain rate, $\dot{\varepsilon}$ for single α and β-phases in Ti-6Al-4V.

4.4.3 Effect of working temperature

An illustration of the variation of steady state stress, σ_{ss} with working temperature for single α and β-phase in Ti-6Al-4V can be seen from Figure 4.31. It is clear that the α-phase exhibits a stronger temperature dependence of σ_{ss} at a given strain rate, where σ_{ss} drops steeply with increasing working temperature. In contrast, σ_{ss} for the β-phase is relatively constant with increasing temperature, particularly within the range of 925-975°C. To support this observation, the quantified temperature sensitivity of σ_{ss} for both α and β-phases is shown in Figure 4.32. At a given temperature and strain rate, the value of S is much higher for the α-phase than for the β-phase. It is found that S lies within the range 4.5-6.5 for the α-phase and 2-3 for the β-phase.

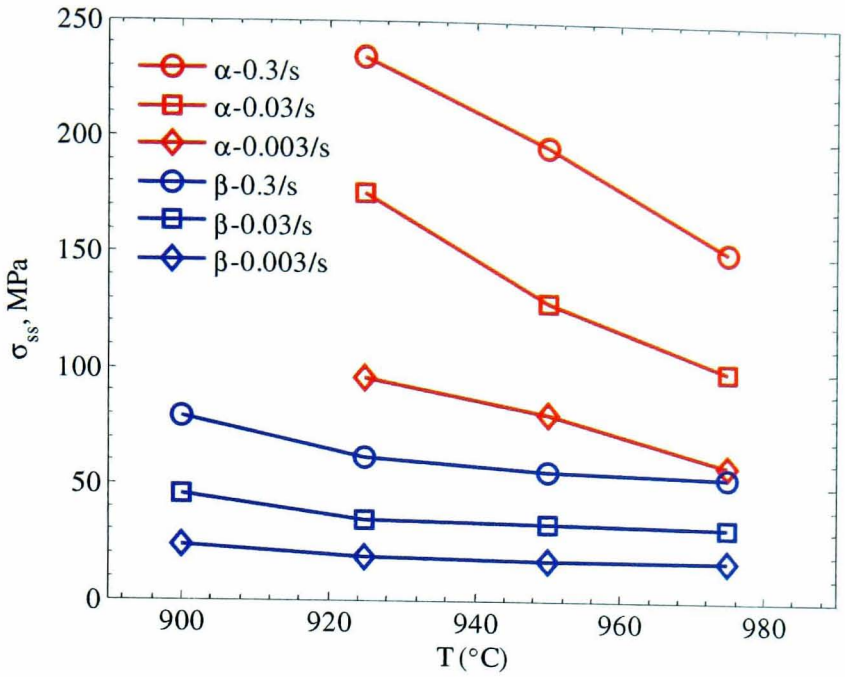

Figure 4.31: Temperature dependence of the steady-state flow stress for the single α and β-phases in Ti-6Al-4V.

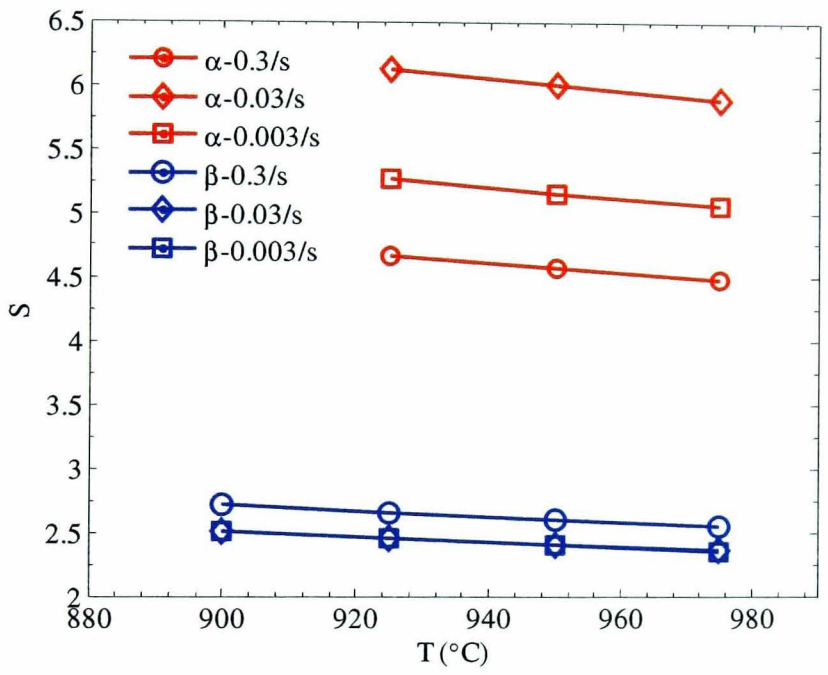

Figure 4.32: The variation of temperature sensitivity, *S,* with working temperature at various constant strain rates for the single α and β-phases in Ti-6Al-4V.

Figure 4.33 shows an Arrhenius plot of σ_{ss} *versus* reciprocal temperature for both α and β-phase compositions. It can be seen that the data varies linearly and the almost parallel slopes within each phase indicate similar operative deformation mechanisms over the range of temperatures and strain rates examined. The activation energy Q estimated from these curves is 623kJ/mol for the α-phase, which is significantly

higher than that for self diffusion in α-titanium (150kJ/mol) [65]. For the β-phase, Q is found to be 225.6kJ/mol, which is also higher than that for self diffusion in the pure β titanium (153kJ/mol) [53]. It should be emphasized that both the single α and β-phase alloys tested here are not pure α-Ti and β-Ti, but consists of various alloying elements with certain compositions depending on pre-determined temperatures so that the crystal structures of the alloys are entirely hcp (α-phase) and bcc (β-phase). For this reason, the higher Q values for the α and β-phases may be attributed to complex dislocation-solute atom interactions.

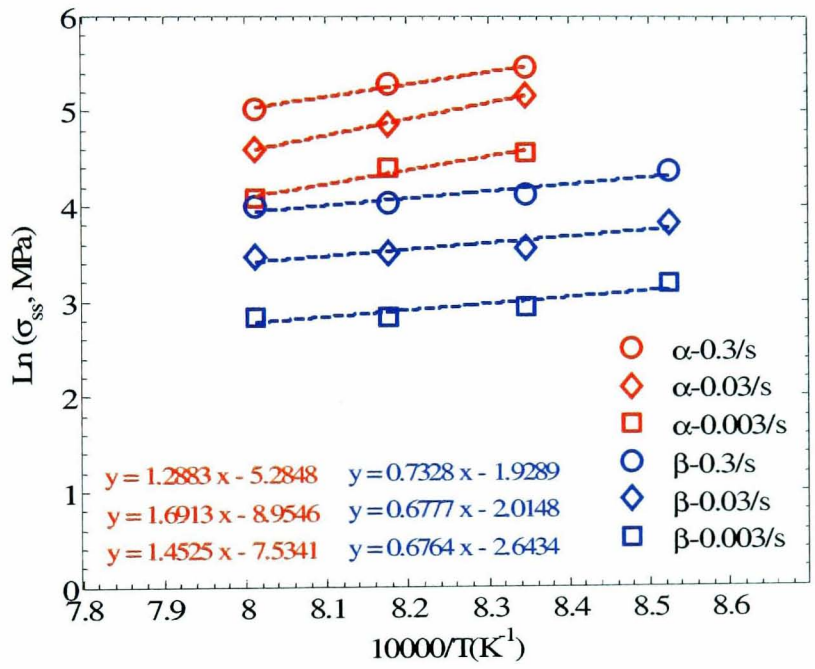

Figure 4.33: Arrhenius plot showing the variation of steady-state stress with inverse temperature for the single α and β-phases in Ti-6Al-4V.

Figure 4.34 shows a log-log plot of σ_{ss} vs Z for the single α and β-phase alloys. It can be seen that a power-law relationship is valid in characterising the data, where σ_{ss} can be expressed as:

Single α-phase: $$\sigma_{ss} = 1.41.10^{-3}.Z^{0.197} \quad \text{(Eq. 4.2.2)}$$

Single β-phase: $$\sigma_{ss} = 3.613.10^{-4}.Z^{0.1963} \quad \text{(Eq. 4.2.3)}$$

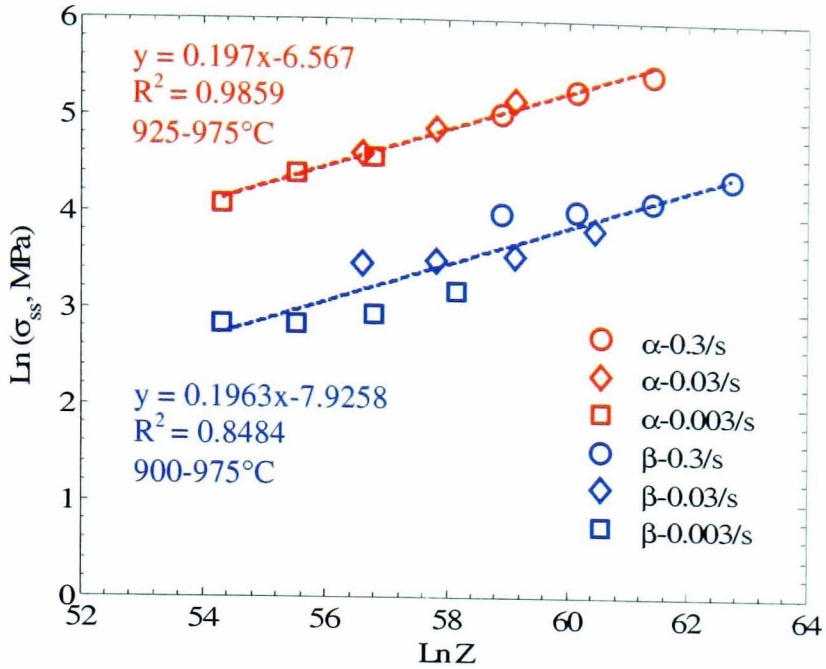

Figure 4.34: A log-log plot of σ_{ss} vs Z for the single α and β-phases in Ti-6Al-4V deformed at 900-975°C and 0.003-0.3/s.

4.5 Summary of results

Isothermal forging of Ti-6Al-4V with globular and acicular initial microstructures, and of the single α and β-phases in Ti-6Al-4V, was performed in the temperature range 850-1050°C at strain rates of 0.003-0.3/s with the following results:

(a) For the as-received Ti-6Al-4V with globular initial microstructure:

- Flow stress curves exhibit a strong dependence on working temperatures and imposed strain rates. With increasing temperature, flow stress decreases. In contrast, flow stress increases as the imposed strain rate increases.
- At strain rates higher than 0.01/s, flow stress curves derived during subtransus deformation showed peak stresses followed by flow softening towards a steady-state stress. On the other hand, at strain rates lower than 0.01/s, steady-state type behaviour was observed. For supertransus deformation, flow curves generally reveal a sharp yield drop followed by steady-state type deformation at strain rates of 0.003-0.3/s.

- A pronounced discontinuous yielding phenomenon was observed particularly during hot deformation at higher temperature (≥900°C) and higher strain rates (≥0.01/s).
- The strain rate sensitivities for the as-received Ti-6Al-4V were estimated to be within the range 0.21-0.23 and 0.27-0.28 for subtransus and supertransus deformation respectively.
- The apparent activation energies derived from Arrhenius plots were found to be 409 and 84kJ/mol for deformation in the two-phase $\alpha + \beta$ and single-phase β fields respectively.

(b) For the β-heat treated Ti-6Al-4V with acicular initial microstructure:

- All flow stress curves reveal a broad peak stress level at low strains followed by moderate to extensive flow softening until a steady-state stress is reached. The flow stress curves exhibit strong temperature dependence for deformation in the temperature range 925-975°C and at strain rates of 0.003-0.3/s.
- The strain rate sensitivity was obtained to be within the range 0.24-0.26.
- The estimated apparent activation energy was found to be 538kJ/mol based on an Arrhenius plot.

(c) For the single α and β-phase in Ti-6Al-4V:

- Flow stress of single α-phase increases with increasing imposed strain rate and decreasing working temperature. At 925-950°C and 0.3/s, there is an indication of initial work hardening behaviour after the onset of plastic deformation at low strains. At 975°C, a pronounced flow softening is exhibited particularly at strain rates of 0.03-0.3/s.

- Flow stress of the single β-phase was found to be much lower than for the α-phase reflecting the fundamental deformation characteristic of the bcc crystal structure. In general, most of flow stress curves of the β-phase were of the steady-state type with little flow softening observed at strain rates of 0.03-0.3/s in the temperature range 925-975°C. In contrast to the single α-phase, the steady state stress for the β-phase was relatively constant with increasing temperature, particularly within the range of 925-975°C.
- The strain rate sensitivities for the single α and single β-phase alloys were found to be within the ranges of 0.19-0.21 and 0.25-0.26, respectively, and comparable to those found for deformation mechanisms controlled by dislocation glide or climb-limited processes, characteristic of power law creep.
- The apparent activation energy for deformation was found to be 623kJ/mol and 225kJ/mol for the single α and β-phases, respectively. The higher values of Q than those for self-diffusion suggests complex dislocation interactions between the alloying elements.

The steady-state analysis presented in the chapter is useful in quantifying and characterising material behaviour for comparative purposes. However, the power-law creep equation is unable to model the entire flow stress curves of Ti-6Al-4V obtained during hot deformation, and in particular cannot be used to simulate the phenomenon of flow softening or any associated microstructural evolution. In the next chapter, the flow stress of Ti-6Al-4V with acicular initial microstructure will be further analysed using an internal state-variable model. Such an approach has advantages for modelling the entire flow stress behaviour (not only limited to σ_{ss}) and has greater flexibility in accounting for the flow softening and microstructural changes that occur during hot forging.

Chapter 5

Modelling and Finite Element Simulation of Isothermal Forging of Ti-6Al-4V

The forming of metals at elevated temperature, e.g., by extruding, forging and rolling, involves the imposition of non-uniform deformation rate and temperature paths to large strains, so that the material undergoes significant, often beneficial, microstructure change. Proper modelling of the deformation behaviour therefore requires constitutive equations that describe the evolution of strain (or strain rate) in terms of stress, temperature and suitable internal microstructure variables. Such formulations are usually semi-empirical and necessarily complex, often involving highly non-linear, power law or exponential relationships that incorporate a number of material-specific constants. The conventional approach has been to determine these material parameters from well-constrained laboratory experiments, often using graphical methods to reduce the problem to a linear relationship between two of the variables at a time, all others being assumed constant. However, there is an increasing trend towards the use of numerical optimisation methods that seek to find all the parameters in a set of equations simultaneously, without resort to simplification of the model used.

In this chapter, constitutive equations used for modelling hot forging of Ti-6Al-4V are presented. The flow stress curves for such two-phase titanium alloys are somewhat unusual in that they exhibit significant post-peak softening at high deformation rates. The constitutive model used here takes account of combined flow hardening and softening by assigning the weighted sum of deformation mechanisms

to a single internal state variable. This approach has already proved successful in modelling the deformation behaviour of several intermetallic compounds such as TiAl, Ti_3Al, Ni_3Al, NiAl [82-85], and conventional Ti alloys such as IMI-834, Ti-6246, Ti-10-2-3 [86].

The results from several numerical techniques for parameter optimisation in the constitutive equations will be compared. Numerical optimisation methods work by iteratively altering model parameter values in order to minimise the difference between prediction and experimental results, as computed through an 'objective function'. Careful selection of the most appropriate optimisation method and initial parameter starting point is necessary, otherwise convergence to a global minimum is unlikely to be achieved, and poor parameter estimation will result. A scheme for computing the confidence interval of each optimised parameter is also applied to such equations for the first time.

In addition, since there is a need to develop a predictive model that takes account of the deformation history and the two-phase nature of the material, this chapter will also outline the applicability of a semi-empirical, history-dependent constitutive model which takes account of the flow properties of each phase, and of temperature-dependent changes in phase volume fractions, to model the flow behaviour of two-phase Ti-6Al-4V.

5.1 Single internal state-variable model for hot deformation of Ti-6Al-4V

During plastic deformation of most metallic materials, the flow stress behaviour is highly non-linear due to plastic instabilities such as strain softening or hardening [87]. Constitutive equations are mathematical expressions that describe stress in terms of the strain, strain rate and temperature, as required for computer modelling of flow stress behaviour [88]. The general form of the constitutive equation for hot deformation processing is:

$$\sigma = f(\varepsilon, \dot{\varepsilon}, T) \qquad \text{(Eq. 5.1.1)}$$

where σ is the flow stress, ε is the true strain, $\dot{\varepsilon}$ is true strain rate, and T is the processing temperature. One of the oldest and most useful equations for modelling the steady-state flow stress is [89, 90]:

$$Z = A\sigma^{1/m} \qquad \text{(Eq. 5.1.2)}$$

where A is a material constant, m is strain rate sensitivity, and Z, the Zener-Hollomon parameter. Limitations of the constitutive model expressed by equation 5.1.2 are the absence of any embedded microstructural parameters describing the microstructure evolution that can be related to processing parameters during hot deformation, and the inability to model the entire flow stress curve since only steady- state stress behaviour is accounted for.

For these reasons, an alternative constitutive model, which takes account of internal gross structural evolution will be employed for this study in order to obtain an improved analysis of hot deformation behaviour.

Hot deformation behaviour of two-phase titanium alloys is characterised by the onset of peak stress at low strain, followed by a gradual decay to a steady-state stress. The steady-state level occurs due to a balance between work hardening and flow softening mechanisms and, at this stage, only minor internal microstructure evolution occurs. The constitutive model proposed by Bate and Brooks [67, 91, 92] is based on the concept of a steady or 'target' state for characterising overall deformation behaviour. The model assumes that dynamic recovery processes alone are responsible for softening and that the flow stress evolves towards an equilibrium steady state (target) condition in an exponential manner:

$$\frac{\partial \sigma}{\partial \varepsilon} = \beta(\sigma_{it} - \sigma) \qquad \text{(Eq. 5.1.3)}$$

where β is an exponential damping constant relating stress to strain and σ_{it} is the instantaneous target stress. A corresponding target structural state is also assumed to exist and a generalised structure-related variable, λ is introduced to take account of gross changes of internal state during deformation. Again assuming that λ evolves towards a target value, λ_{ss} in a manner analogous to equation (5.1.3):

$$\frac{\partial \lambda}{\partial \varepsilon} = \alpha(\lambda_{ss} - \lambda) \qquad \text{(Eq. 5.1.4)}$$

where α is an exponential damping constant relating structure and strain. The expected dependence of λ_{ss} on strain rate and temperature can be accounted for using a power law function of the Zener-Hollomon parameter, Z:

$$\lambda_{ss} = \lambda_o Z^q \qquad \text{(Eq. 5.1.5)}$$

where λ_o is a scaling constant and q is a structure sensitivity parameter. The magnitude of λ_{ss} is defined as a comparison between the initial target stress, σ_{is} and steady state stress, σ_{ss}. The initial target stress, σ_{is} is obtained by back extrapolation of the original stress-strain curve to strain, ε equal to 0. The instantaneous target stress, σ_{it} is expected to depend on strain rate, temperature and microstructure so that the internal variable λ can be used together with Z to determine the evolution of σ_{it} using a simple power law:

$$\sigma_{it} = K\lambda^{n_{ss}} Z^m \qquad \text{(Eq. 5.1.6)}$$

where K is a scaling constant, m is the strain-rate sensitivity, and n_{ss} is the structure-stress exponent (commonly unity so that structure behaves like stress). Figure 5.1.a illustrates the definitions of σ_{is}, σ_{it} and σ_{ss} schematically. Constitutive behaviour of materials undergoing hot forging is usually explored using a series of fixed strain-rate compression experiments on small-scale work-pieces under nominally isothermal conditions. Integration of Equations 5.1.3 and 5.1.4 over constant strain rate and temperature, with the initial condition that at $\varepsilon_i = 0$, $\sigma_i = 0$ and $\lambda_i = 1$ produces

$$\sigma = \sigma_{it}(1-\exp(-\beta\varepsilon)) \qquad \text{(Eq. 5.1.7)}$$

$$\lambda = \lambda_{ss} + (1-\lambda_{ss})\exp(-\alpha\varepsilon) \qquad \text{(Eq. 5.1.8)}$$

The model predicts a flow stress curve with an upper yield point that decays to a steady-state value at large strain, reflecting the evolution of the internal state variable, λ as illustrated in Figure 5.1.b.

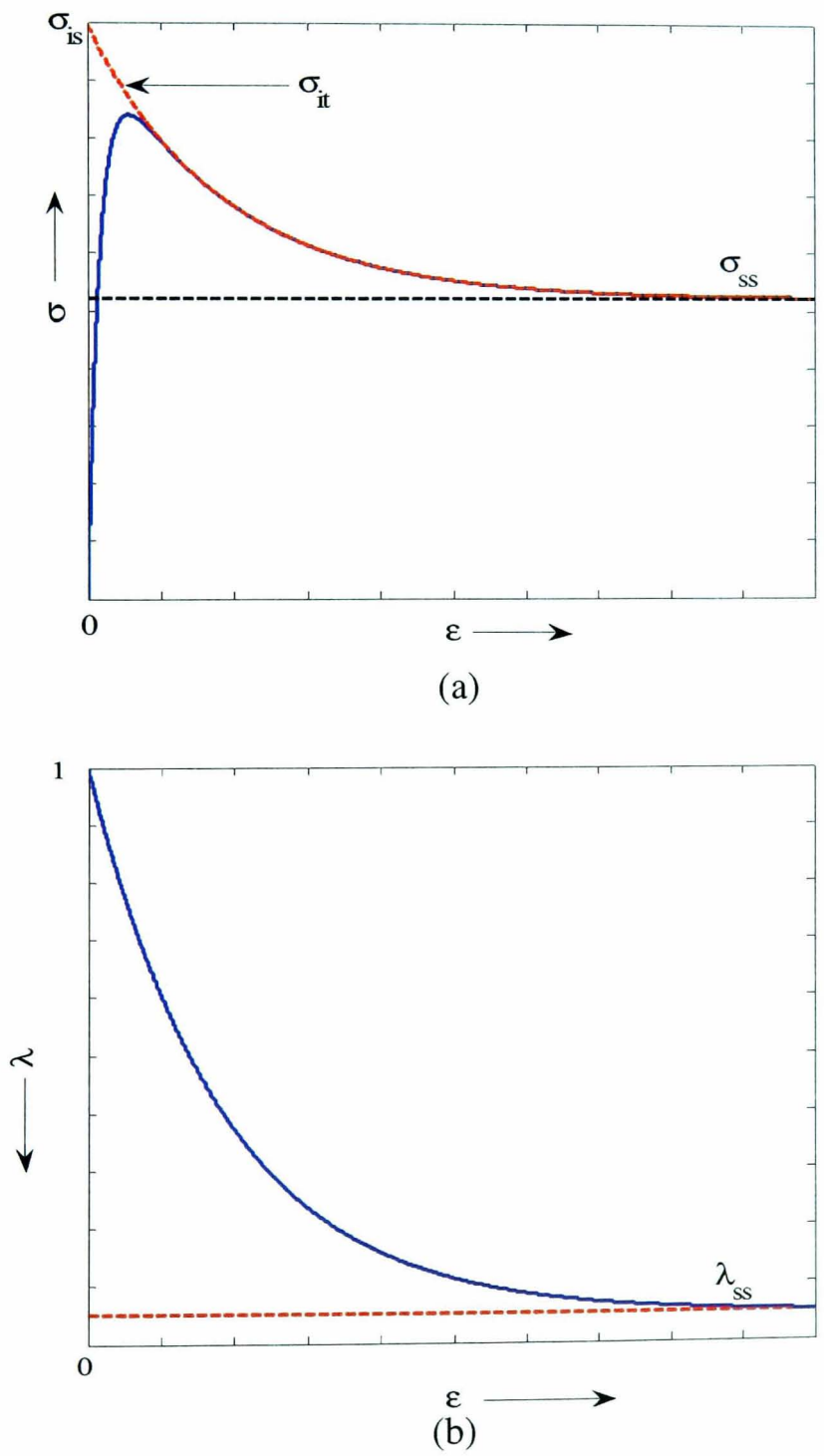

Figure 5.1: Evolution of (a) stress, σ, and (b) internal state-variable, λ, with strain, ε, as predicted by the constitutive model.

It is clear that the constitutive model is based on a chain of two exponential relationships describing the evolution of target stress and structure toward a steady state condition. Typical of non-linear constitutive equations describing high temperature deformation, the model incorporates several material parameters: K, λ_o, Q, m, q, α and β, all of which need to be determined from experimental flow stress data. It can be seen that the model has advantages for modelling the flow stress behaviour of Ti-6Al-4V because of its great flexibility in accounting for the flow softening that occurs during hot forging, and also because of its incorporation of an internal state variable, λ that can be used to predict microstructure evolution. Hereafter, equations 5.1.3 - 5.1.8 will be referred as the λ-model.

5.2 Determination of material constants

In order to use numerical optimisation to determine the best values for the material constants in the λ-model, initial parameter values need to be supplied as a starting point. These can be determined based on experimental data by using a combination of graphical and analytical methods.

5.2.1 Determination of starting values

The flow stress data were first analysed using conventional methods to obtain 'as-calculated' starting values for the parameters in the constitutive model. From the curves of initial and steady state stress vs temperature presented in Fig. 5.2., the activation energy was estimated by interpolating the value of temperature at a set of

arbitrary constant stresses. The temperature values obtained were then used to plot the Arrhenius curve shown in Figure 5.3, and a value for Q/R was obtained as the average of all curve gradients based on initial and steady state stress. The mean activation energy (Q) evaluated in this way was 566kJ/mol.

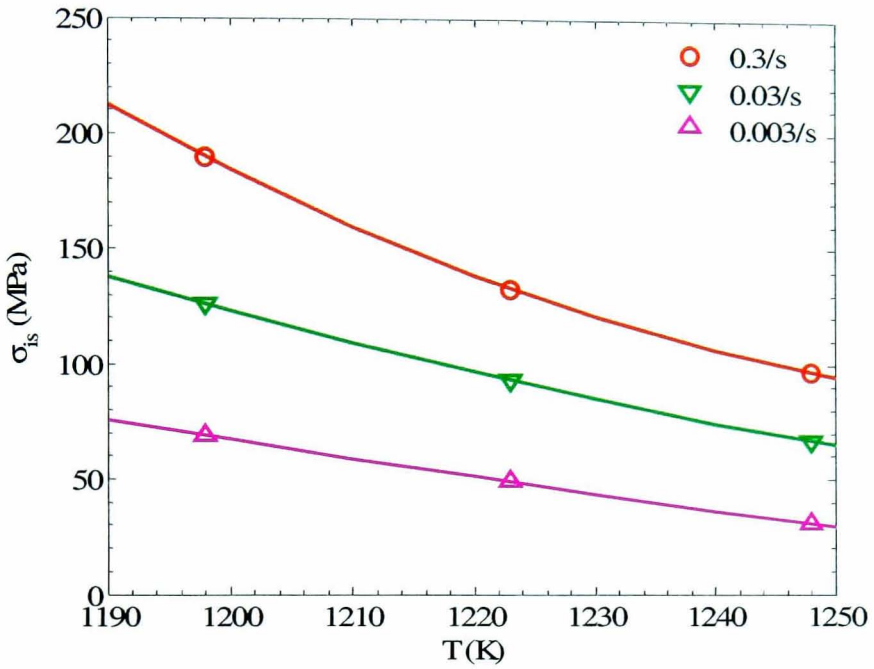

(a)

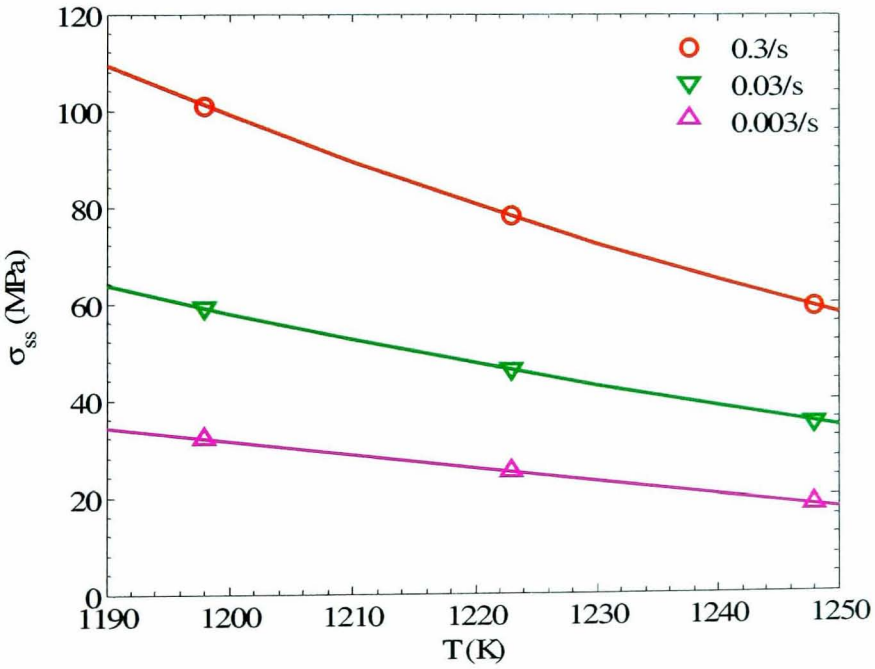

(b)

Figure 5.2: Temperature sensitivity of (a) initial target stress and (b) steady-state stress of Ti-6Al-4V with acicular initial microstructure.

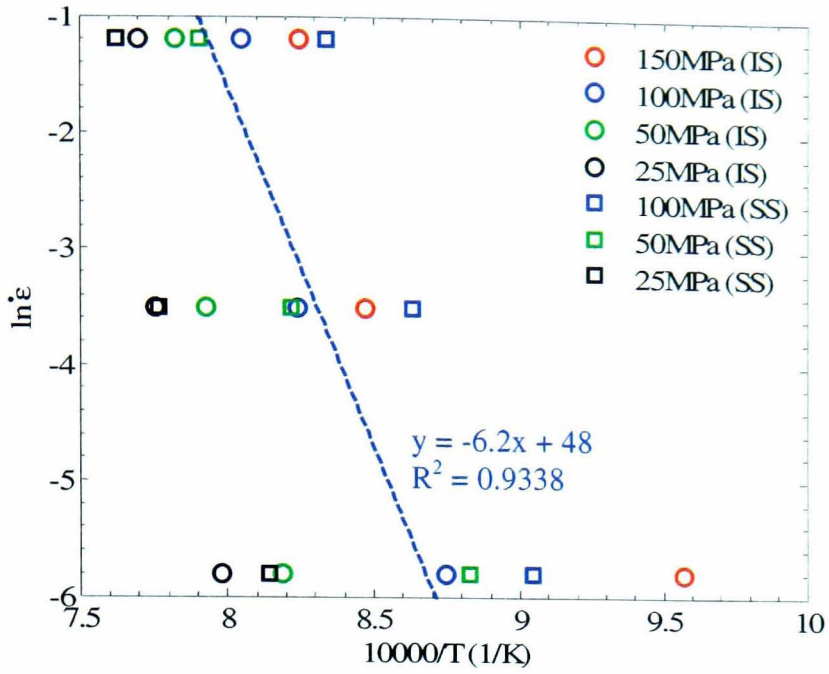

Figure 5.3: Arrhenius plot of ln (strain rate) vs 1/temperature for both initial and steady state stress of heat-treated Ti-6Al-4V.

The activation energy derived was then used to calculate the temperature compensated strain rate, Z, in order to obtain the strain rate sensitivity, m and structure sensitivity, q according to equations 5.1.6 and 5.1.5 respectively. The strain rate sensitivity derivation at steady state, σ_{ss} and initial stress, σ_{is} is presented in Figure 5.4.

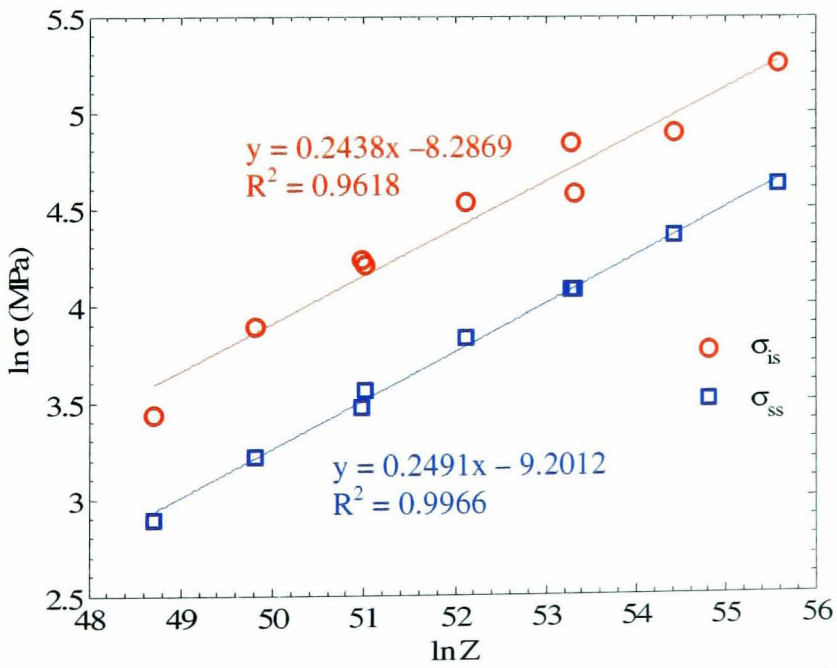

Figure 5.4: The strain rate sensitivity curve for acicular Ti-6Al-4V.

A log-log plot of the internal variable λ_{ss} against Z is presented in Figure 5.5. The plot allows the gradient q and intercept λ_o to be determined, and then λ_{ss} can be derived from:

$$\frac{\sigma_{ss}}{\sigma_i} = \frac{KZ^m \lambda_{ss}^n}{KZ^m \lambda_i^n} = \lambda_{ss} \qquad \text{(Eq. 5.1.9)}$$

since $n = 1$ and $\lambda_i = 1$

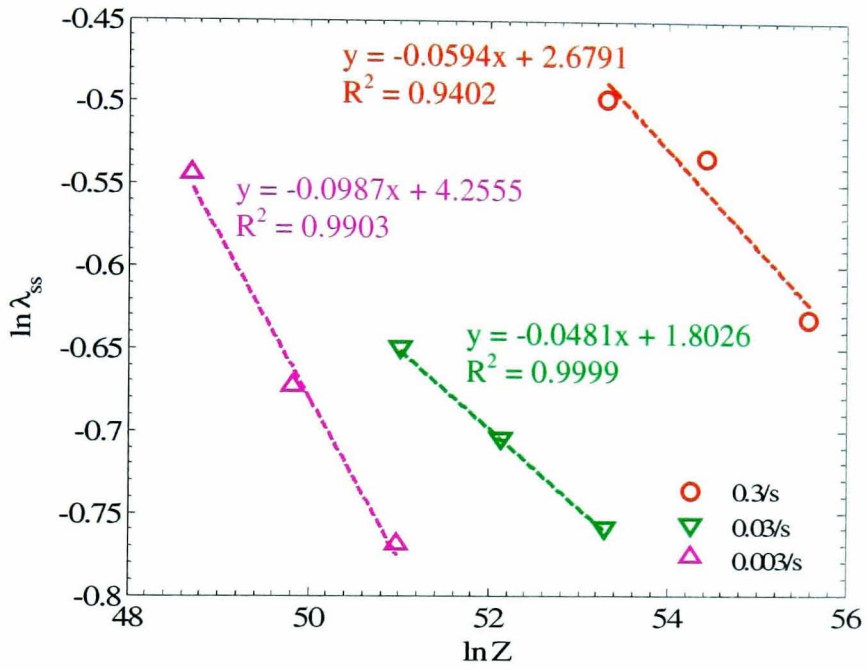

Figure 5.5: The structure sensitivity curve for heat-treated Ti-6Al-4V.

The remaining parameter K, can be determined by substituting the steady-state condition, $\sigma_{it} = \sigma_{ss}$ and $\lambda = \lambda_{ss}$, into equation 5.1.6 to yield:

$$\sigma_{ss} = K\lambda_o Z^{m+q} \qquad \text{(Eq. 5.2.0)}$$

Finally, α and β were assigned arbitrary positive real values. A summary of initial values for the constitutive parameters derived in this way is presented in Table 5.1.

Table 5.1. **Constitutive parameters for β-heat treated Ti-6Al-4V**

K	λ_o	m	q	n	Q (kJ/mol)	α	β
1.390e-4	30.376	0.246	-0.069	1	565.676	5	50

In the following sections, the above constitutive data will be used as a starting point for an optimisation algorithm in order to refine the fit between model and experiment.

5.2.2 Optimisation of material constants

During numerical optimisation unknown design variables $\bar{x} = [x_1 x_2 x_3 ... x_w]$ are sought by fitting model results to experimental data y_j (j = 1, 2, 3, …, u), where w and u are the number of unknown parameters and data points respectively [93]. Such parameter optimisation is best carried out using an objective function that computes the least squares difference between experimental data and modelled output i.e.

$$F(\bar{x}) = \sum_{j=1}^{u} (\sigma_j - \sigma_j(\bar{x}))^2 \qquad \text{(Eq. 5.2.1)}$$

where σ_j is the experimental stress and $\sigma_j(\bar{x})$ is the stress value obtained from the model. Due to the unavailability of an exact solution for the above non-linear function, the minimisation must be achieved iteratively by adjusting the unknown parameters in the model equations. There are a number of procedures available for the minimisation of Equation 5.2.1. These range from methods that make use of the functional value alone during the iterative process, to those that compute first and second order derivatives to expedite optimisation. The higher order 'gradient'

methods are computationally more expensive and can be unstable. In all cases, the iterative algorithm is set to terminate when the computed value of Equation 5.2.1 reaches a pre-determined condition. Individual algorithms used for the multidimensional non-linear optimisation are described below.

5.2.2.1. Nelder-Mead Direct Search (Simplex Algorithm)

The Nelder-Mead direct search method is one of a number of techniques that are defined as hill climbing methods [94]. The algorithm follows a path toward an optimum by evaluating an objective function at several points rather than by calculating derivatives. The substantial element is a geometric figure called a simplex that is defined as a set of $d + 1$ points in d-dimensional space. For instance, in the case of $d = 2$, the figure is an equilateral triangle. The simplex can move, shrink and expand toward a minimum. To find the minimum value of the objective function, the simplex method searches the parameter space using an initial simplex and the function is then evaluated at each of the vertices. The point associated with the highest value of the objective function is replaced by a point with a lower value to form a new simplex. To determine the location of this new point, the worst point is reflected through the centroid of the other two points. If the function evaluated at the new point does not reduce the value, then the new point is generated by contraction toward the centroid. If neither of these approaches finds a point with lower value, then the entire simplex is contracted towards the point having the lowest value. This iterative process is continued until convergence to a minimum is found. Figure 5.6 illustrates the basic moves involved within the algorithm.

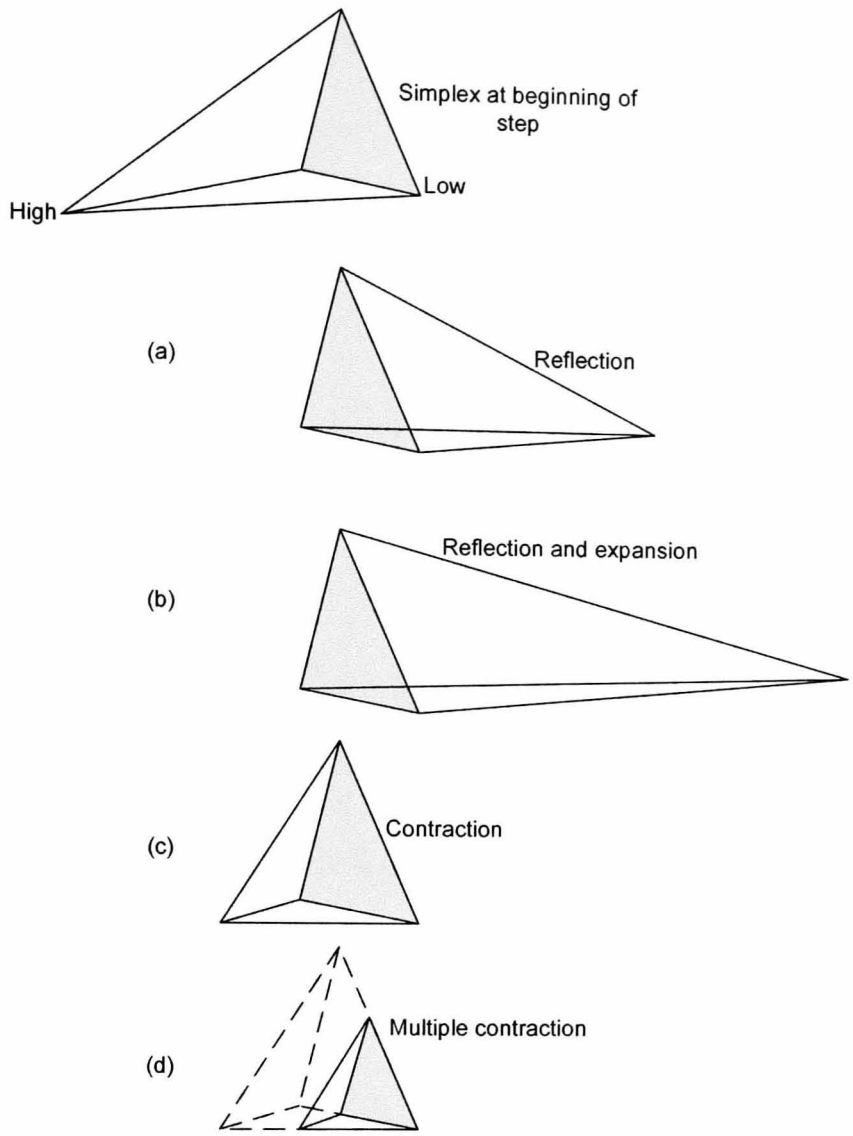

Figure 5.6: Illustration of the outcomes for a step in the Nelder-Mead simplex method. As an example, in the initial step, the simplex is a tetrahedron (top). At the end of the step, the simplex is transformed by performing (a) a reflection away from the high point, (b) a reflection and expansion away from the high point, (c) a contraction along one dimension from the high point, or (d) a contraction along all dimensions towards the low point [95].

5.2.2.2. Trust Region Newton Method

A large class of algorithms, collectively called Newton methods, make use of gradient information to minimise a function of several variables. A quadratic approximation is used to model a step change, s, in objective function $F(\bar{x})$. At the kth iteration the model function is given by:

$$m_{(k)}(s) = a + g_{(k)}^{T} s + \frac{1}{2} s^{T} H_{(k)} s \qquad \text{(Eq. 5.2.2)}$$

where $g = \nabla F(\bar{x})$ is the Jacobian gradient vector of first partial derivatives of $F(\bar{x})$. $H = \nabla^2 F(\bar{x})$ is the Hessian matrix of second partial derivatives, and $a = F(\bar{x}_k)$. At its minimum Equation 5.2.2 becomes $s_{(k)}=H_{(k)}^{-1}g_{(k)}$ and step $s_{(k)}$ leads directly to the minimum of the model function, but not necessarily of the real function. A key aspect of gradient methods is the correct choice of step size: the quadratic approximation is not valid if step s is too large. Trust region methods place a restriction on the size of the step such that $\|D_{(k)}.s\| \leq \Delta_{(k)}$ where $D_{(k)}$ is a diagonal scaling matrix and $\Delta_{(k)}$ is a positive scalar representing the size of the region over which the approximation can be 'trusted'. The magnitude of $\Delta_{(k)}$ is based on the agreement between the model function and the objective function at each step, as measured by the ratio:

$$p_{(k)} = \frac{f(\bar{x}_{(k)}) - f(\bar{x}_{(k)} + s_{(k)})}{f(\bar{x}_{(k)}) - m_{(k)}(s_{(k)})} \qquad \text{(Eq. 5.2.3)}$$

If $p_{(k)} \approx 1$ there is good agreement and the trust region can be expanded for the next iteration; if $p_{(k)}$ is close to zero or negative the trust region must be made smaller. In this study, the bounds of design variables were fixed within the range:

$0 < K < 10$, $0 < \lambda_o < 10$, $0 < Q < 900e3$, $0 < m < 1$, $-1 < q < 1$, $0 < \alpha < 100$, $0 < \beta < 200$.

5.2.2.3. The Levenberg-Marquardt Algorithm

Levenberg has modified the Newton algorithm for updating the step change by introducing a damping parameter λ_{LM}, given as $s_{(k)}=(H_{(k)}+\lambda_{LM}I)^{-1}g_{(k)}$ where I is the identity matrix [96].

However, this rule poses a disadvantage, that is, for a large value of λ_{LM}, the calculated $H_{(k)}$ is never used. Marquardt has overcome this problem by replacing I with the diagonal of the Hessian, defined as: $s_{(k)}=(H_{(k)}+\lambda_{LM}.\text{diag}H_{(k)})^{-1}g_{(k)}$. The damping parameter λ_{LM} is manipulated directly for each iteration in order to control the magnitude and the direction of the search step $s_{(k)}$.

When $F(\bar{x})$ can be minimised rapidly, a small value of λ_{LM} can be used to bring the algorithm closer to the Newton method above. In contrast, if $F(\bar{x})$ is not sufficiently reduced, a higher value of λ_{LM} takes the algorithm closer to the gradient descent direction. When $s_{(k)}$ has reached predefined limits, the iteration is terminated and the optimised solution is obtained based on the last $s_{(k)}$. In this study, similar bounds of design variables to the previous section have been used, that is:

$0< K <10,\ 0 <\lambda_o <10,\ 0 < Q <900e3,\ 0 < m < 1,\ -1 < q < 1,\ 0 < \alpha < 100,\ 0 < \beta < 200.$

5.2.3 Approximation of confidence intervals for least-squares solutions

In all cases, parameter confidence intervals can be calculated from the Hessian, H of $F(\bar{x})$ at the solution. The least-squares problem of Equation 5.2.1 can then be rewritten as:

$$F(\bar{x}) = \sum_{j=1}^{u} f_j^2(\bar{x}) \quad ; \qquad f_j(\bar{x}) = (\sigma_j - \sigma_j(\bar{x})) \qquad \text{(Eq. 5.2.4)}$$

$$H = 2(g^T g + \sum_{j=1}^{u} f_j(\bar{x}) H_j) \qquad \text{(Eq. 5.2.5)}$$

where H_j is the Hessian matrix of each $f_j(\bar{x})$. In the neighbourhood of the solution, $\|f(\bar{x})\|$ is often small compared to $\|g^T g\|$. In such cases, H is sufficiently approximated by $H \approx 2g^{\mathrm{T}}g$. Therefore, the computation of the Hessian matrix can be avoided. The Jacobian, g is returned by all the comprehensive least-squares routines and, in addition, a routine is available in the NAG Fortran Library to estimate variances of the parameters following the use of most of the nonlinear least-squares routines [97]. An unbiased estimate of the variance of the ith parameter x_i is

$$\operatorname{var} x_i = \frac{2F(\bar{x})}{u-w} diag(H)^{-1} \qquad \text{(Eq. 5.2.6)}$$

If x_i^* is the true solution, then the $100(1-\varphi)\%$ confidence interval on x_i is

$$x_i - \sqrt{\operatorname{var} x_i}\, t_{(1-\varphi/2,u-w)} < x_i^* < x_i + \sqrt{\operatorname{var} x_i}\, t_{(1-\varphi/2,u-w)} \qquad \text{(Eq. 5.2.7)}$$

where $t_{(1-\varphi/2,\ u-w)}$ is the $100(1-\varphi)/2$ percentage point of the t-distribution with u-w degrees of freedom.

5.2.4 Optimised material constants

In order to compare the performance of the above optimisation algorithms, it is useful to evaluate certain performance criteria, *i.e.*:

a. the effectiveness and degree of fit as represented by the value of the objective function at the optimised minimum.

b. the efficiency and rapidity of convergence as represented by the number of iterations and function evaluations required to reach the optimised value.

Table 5.2 lists optimised material constants of the λ-model obtained by the algorithms mentioned above when modelling the flow stress behaviour of acicular Ti-6Al-4V deformed within the strain rate range 0.003-0.3/s at temperatures of 925-975°C. It was found that Nelder-Mead is the most efficient algorithm in obtaining the minimum value of $F(\bar{x})$ because it requires less function evaluations and iterations; it also attained the lowest objective function value. The efficiency of the Nelder-Mead method is enhanced by the fact that the algorithm only evaluates an objective function value at several points rather than calculating derivatives. This approach reduces the time needed for computation. Note that the Levenberg-Marquardt and Trust Region Newton methods also reached acceptable minima but required many more iterations.

Table 5.2. **Optimised material constants of the λ-model for Ti-6Al-4V with acicular initial microstructure deformed in the temperature range 925-975°C at strain rates of 0.003-0.3/s.**

Material Constants	Nelder-Mead	Trust Region Newton	Levenberg Marquardt
K	2.010e-4 ± 1.654e-4	2.031e-4 ± 1.670e-4	2.029e-4 ± 1.669e-4
λ_o	9.296e-2 ± 1.134e-1	9.299e-2 ± 1.134e-1	9.299e-2 ± 1.133e-1
m	2.024e-1 ± 9.596e-3	2.024e-1 ± 9.598e-3	2.024e-1 ± 9.598e-3
q	2.534e-2 ± 1.837e-2	2.537e-2 ± 1.838e-2	2.537e-2 ± 1.838e-2
Q (kJ/mol)	691.517 ± 41.323	690.800 ± 41.294	690.800 ± 41.298
α	5.397 ± 1.181	5.397 ± 1.181	5.397 ± 1.181
β	5.924e1 ± 6.425	5.924e1 ± 6.425	5.924e1 ± 6.425
$F(\bar{x})$	4979.976	4980.012	4980.005
Iterations	5726	33750	29205
Function Evaluations	8690	360088	283680

Figure 5.7 summarises the λ-model prediction for Ti-6Al-4V with acicular initial microstructure after the initial values of material constants were optimised by the Nelder-Mead method. It is clear that the modelled output and the experimental data are in very good agreement. From Table 5.2, it can be seen that the estimated activation energy Q is still high, which indicates that the operative dynamic restoration processes are probably a combination of various complex deformation mechanisms between each phase constituent.

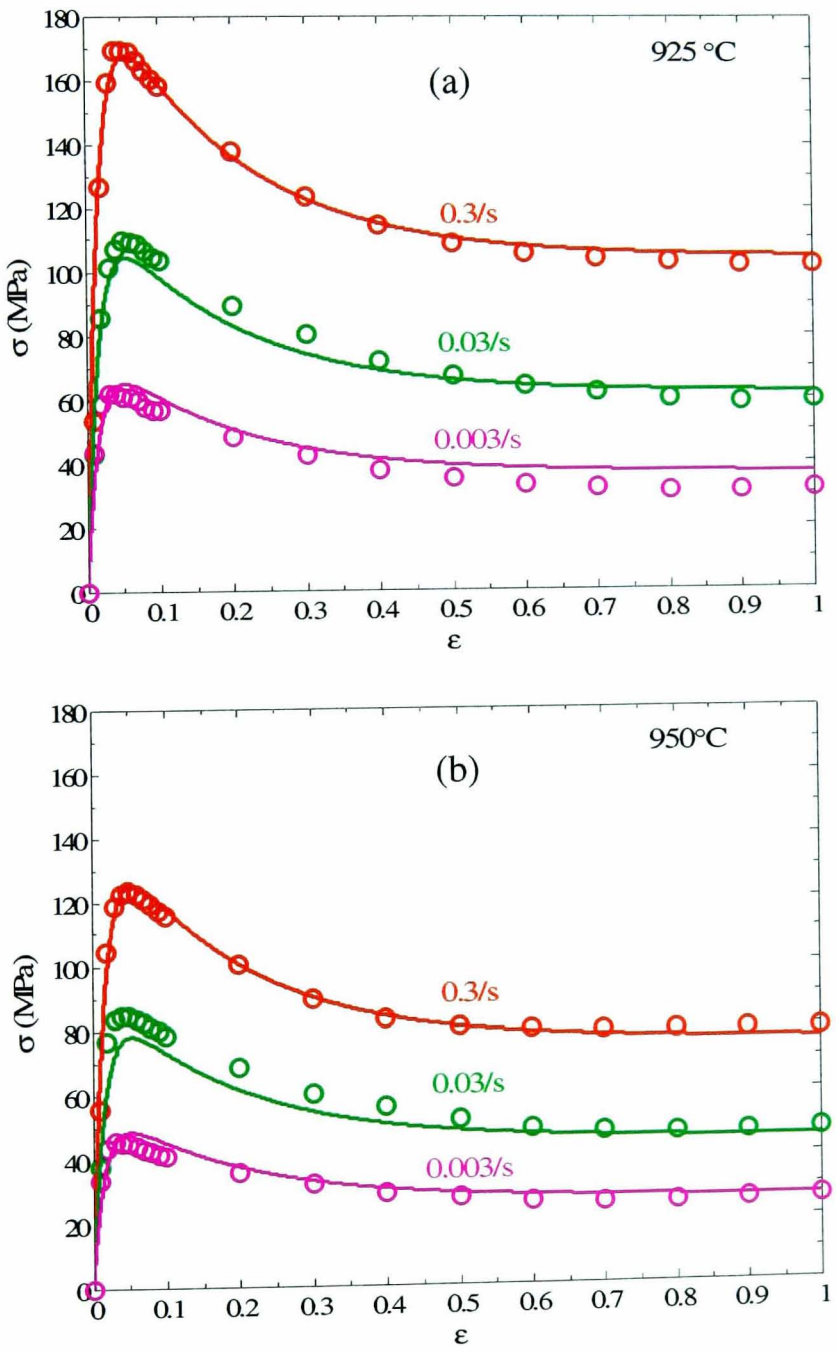

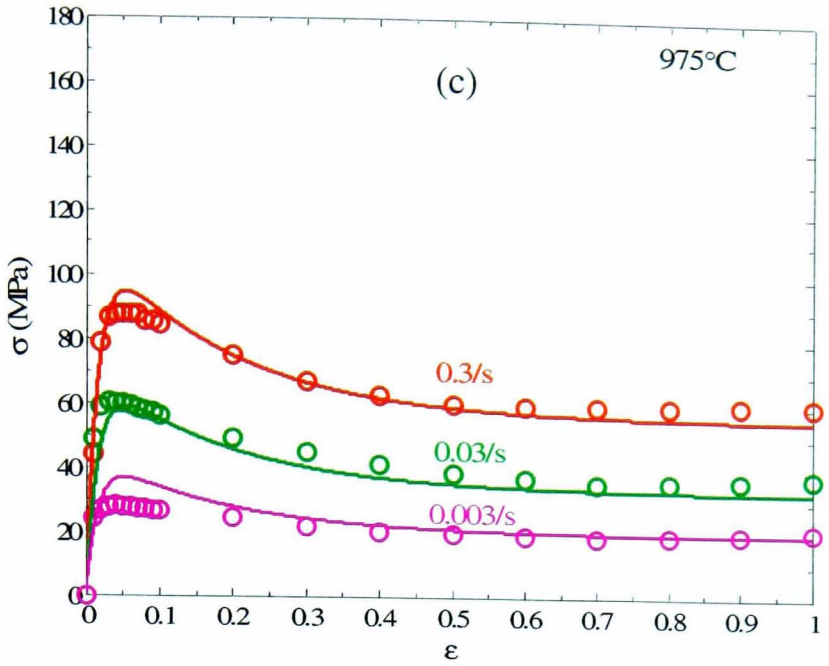

Figure 5.7: The λ-model fitted to flow stress behaviour of acicular Ti-6Al-4V deformed at strain rates of 0.003-0.3/s and temperatures (a) 925, (b) 950 and (c) 975°C. Circle: experimental data; line: the λ-model prediction.

5.3 Modified iso-strain model for hot deformation of two-phase $\alpha+\beta$ Ti-6Al-4V based on an internal state-variable approach

Although the flow stress behaviour of β-heat-treated acicular Ti-6Al-4V can be predicted adequately by using the single λ-model, as illustrated in Figure 5.7, it is important to establish a predictive model that can distinguish the deformation history of each phase constituent. An understanding of the deformation of individual phases would be especially beneficial in improving quantitative descriptions of hot flow behaviour in two-phase $\alpha + \beta$ titanium alloys generally.

Briottet *et al* [68] have employed several methods for modelling the flow stress of the aggregate of two-phase alloy systems by considering the deformation of individual phases based on uniform strain rate (Taylor or iso-strain approach), uniform stress (Sachs or iso-stress approach), and on a 'self-consistent' approach extended to power-law materials where stresses and strain rates are allowed to be

non-uniform within each phase. Semiatin *et al* [98] has also used a modified 'self-consistent' approach and incorporated the temperature variation of the α and β-phase composition and volume fraction in order to predict the flow stress behaviour of two-phase Ti-6Al-4V. In this work, the strain-rate sensitivity of the individual phases was assumed to be equal since an analytical solution [99] was only available for that particular case. Additionally, Semiatin *et al* approximated the flow stress behaviour of the individual α and β-phases by using steady-state power-law equations. In fact, the strain rate sensitivities for the single α and β-phases are known to be different, and their flow stress behaviour is more complex than can be satisfactorily modelled in this way – see experimental results and analysis presented in Chapter 4. The same approach has also recently been used by Vo *et al* for flow stress prediction of near-α IMI834 during hot working [100]. The common feature of all these studies is that they are only really effective in predicting peak stresses of the respective alloys. In addition, the absence of any structural-related variable within the approach, and the complexity of implementing such models within finite element analysis, means they have limited capability in predicting microstructure development during hot deformation.

In the current study, a new approach will be employed for modelling the full flow stress behaviour of two-phase Ti-6Al-4V. The method incorporates a more accurate quantitative description of flow stress for each phase, the temperature-dependence of the volume fraction of each phase, and an embedded independent structural-related variable. Thus, this method is expected to predict more accurately the full flow stress behaviour of the two-phase material, with an additional beneficial capability in predicting microstructure development during hot forging.

In the following sections, the λ-model is used to simulate the flow behaviour of the individual α and β phases in $\alpha+\beta$ titanium alloy Ti-6Al-4V. The optimised single-phase equations are then used to predict the flow stress of bulk two-phase Ti-6Al-4V with an acicular alpha initial microstructure by incorporating the temperature-dependent changes in phase volume fractions and gross interaction mechanisms between the α and β phases.

5.3.1 Constitutive modelling of α and β-phases in Ti-6Al-4V

Variation of the initial and steady state stress with respect to temperature during hot deformation of the individual α and β-phases in Ti-6Al-4V is illustrated in Figure 5.8. Initial and steady-state stress data were primarily used to estimate material constants within the constitutive model. Constitutive parameters for modelling flow stress behaviour of the single α and β-phases in Ti-6Al-4V were determined by using a combination of graphical, analytical and numerical optimisation methods as described in Section 5.2. Optimised material parameters in the λ-model are given in Table 5.3.

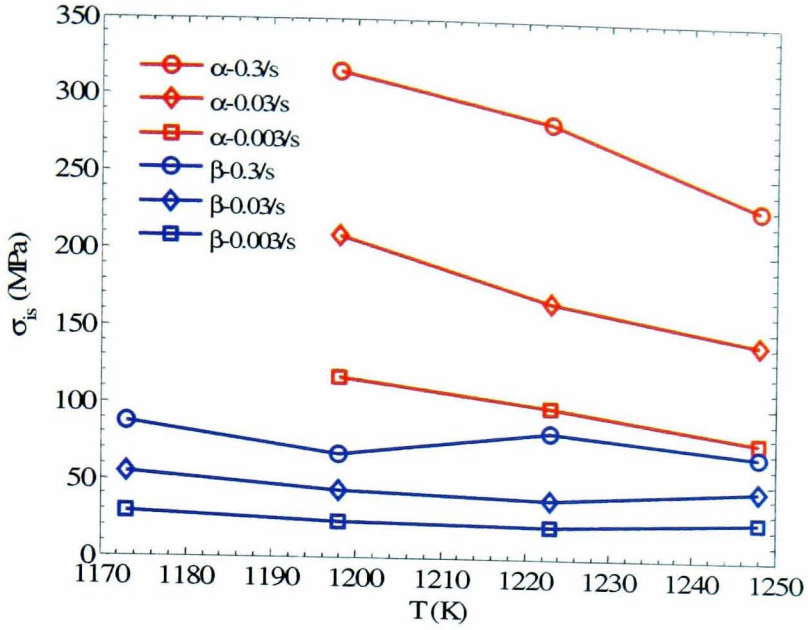

(a)

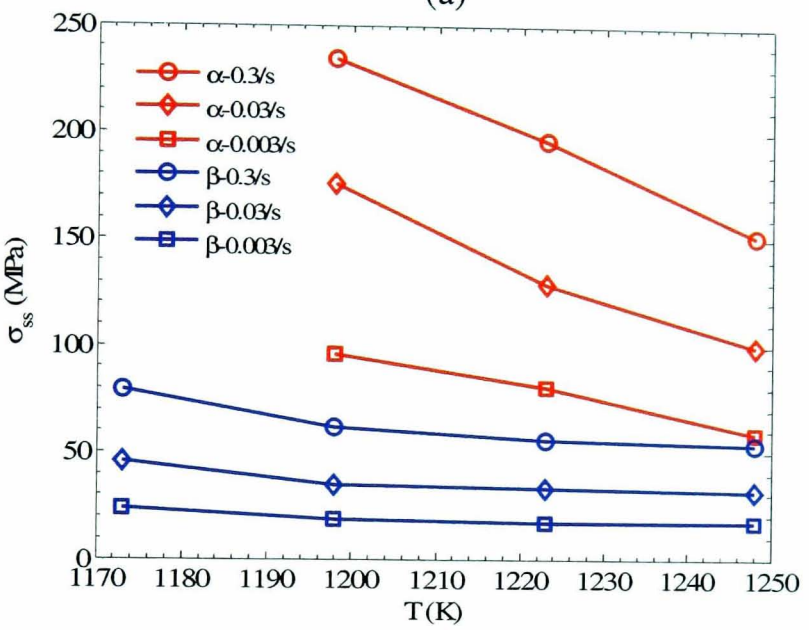

(b)

Figure 5.8: Variation of (a) initial and (b) steady state stress with temperatures for single α and β-phases in Ti-6Al-4V.

Table 5.3. **Optimised material constants in the λ-model for α and β-phases in Ti-6Al-4V deformed at temperatures of 900-975°C at strain rates of 0.003-0.3/s.**

Material Constants	Single α-phase	Single β-phase
K	0.0705 ± 0.0044	5.30 ± 0.29
λ_o	1.49 ± 0.08	0.840 ± 0.043
m	0.218 ± 0.070	0.259 ± 0.044
q	-0.018 ± 0.169	0.001 ± 0.099
Q (kJ/mol)	394.00 ± 77.72	115.00 ± 89.573
α	1.31 ± 0.33	3.79 ± 1.68
β	53.50 ± 5.05	110.00 ± 15.35

The activation energy Q obtained for the single α-phase is about 394kJ/mol, which is again much higher than that for self diffusion in α-titanium (150kJ/mol) [65], on the other hand, Q for the β-phase was found to be 115kJ/mol which is slightly lower than that for self-diffusion in the pure β titanium alloys (153kJ/mol) [53]. These discrepancies may be attributed to the single α and β-phase alloys tested not being true α and β titanium alloys (the alloying constituents of the materials used here vary with temperature). Figures 5.9 and 5.10 summarise the λ-model predictions for the flow stress of the single α and β-phase materials. Qualitatively, the model provides a reasonable representation of the flow stress behaviour of the single-phase alloys.

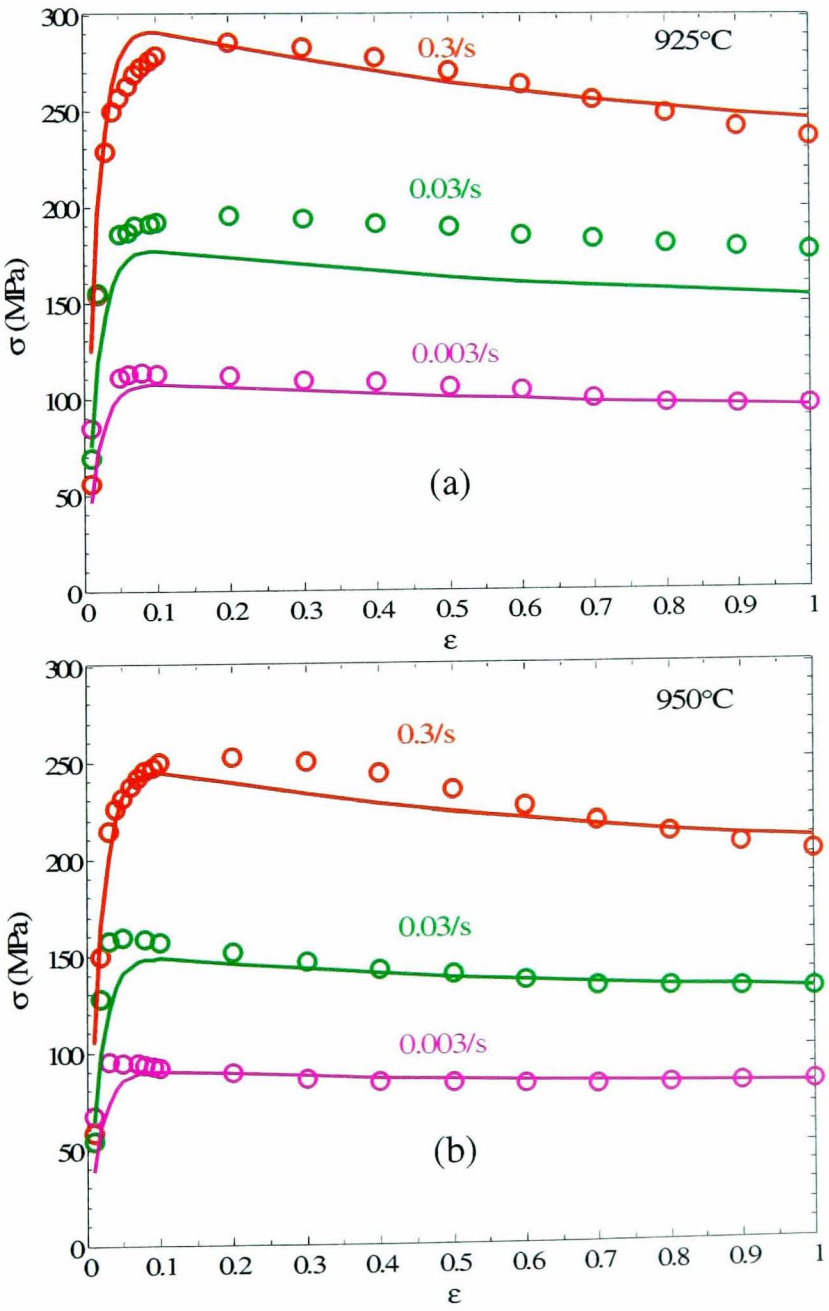

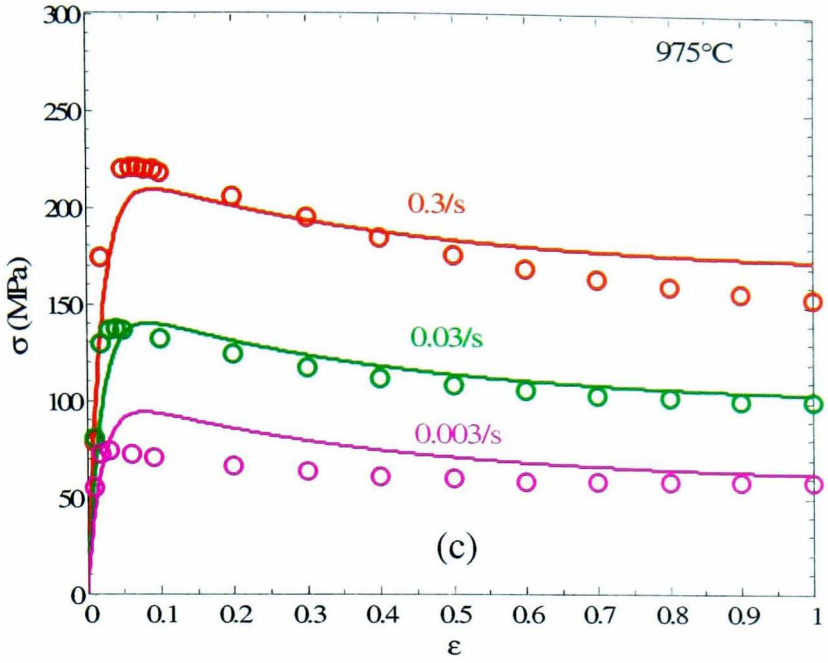

Figure 5.9: The λ-model prediction for flow stress behaviour of single α-phase in Ti-6Al-4V deformed at strain rates of 0.003-0.3/s and temperatures (a) 925, (b) 950 and (c) 975°C. Circle: experimental data; line: the λ-model prediction.

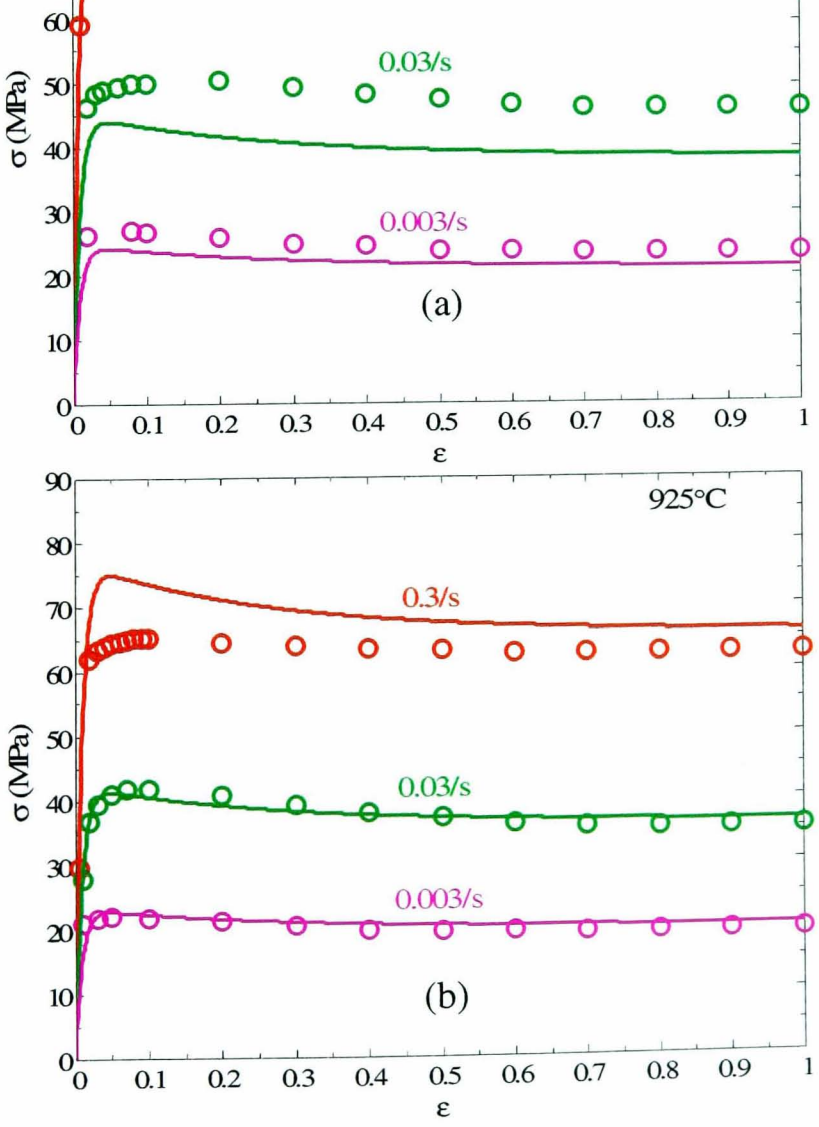

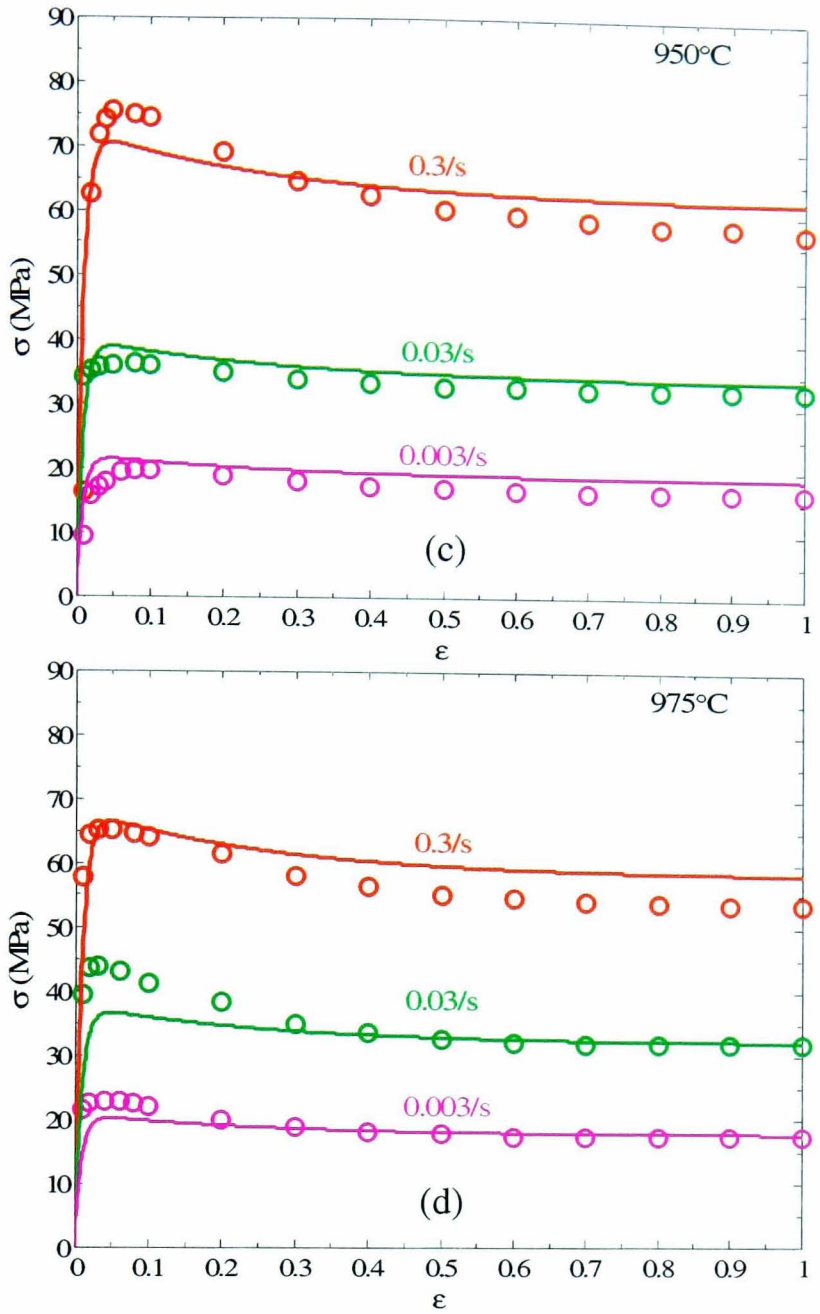

Figure 5.10: The λ-model prediction for flow stress behaviour of single β-phase in Ti-6Al-4V deformed at strain rates of 0.003-0.3/s and temperatures (a) 900, (b) 925, (c) 950 and (d) 975°C. Circle: experimental data; line: the λ-model prediction.

5.3.2 Constitutive modelling of two-phase Ti-6Al-4V

The flow stress behaviour of Ti-6Al-4V (with an acicular alpha microstructure) deformed in the α+β phase field can be modelled by using the iso-strain (Taylor) assumption for which the strain in the individual phases (α and β) is equal to that in the two-phase alloys, $\varepsilon_\alpha = \varepsilon_\beta = \varepsilon_{\alpha\beta}$. The flow properties of the two-phase alloy will depend upon the relative contributions of the single α and β-phases to the overall deformation. The flow stress of each phase is weighted by its temperature-dependent

volume fraction in order to determine the total stress response of the bulk α+β Ti-6Al-4V. Assuming strain compatibility within each phase, the total deformation of the two-phase material can be defined using the rule of mixtures:

$$\sigma_{\alpha\beta} = f_\alpha \sigma_\alpha + f_\beta \sigma_\beta \qquad \text{(Eq. 5.3.1)}$$

where f_α and f_β are equal to the volume fractions of α and β-phases; σ_α and σ_β are the stress evolution of the individual α and β-phases based on the λ-model respectively. The empirical equation relating the volume fraction of the α and β-phases to the temperature was derived by using experimental data to determine the β-approach curve (discussed in more detailed in Chapter 6), given by:

$$\begin{aligned} f_\beta &= (1.26\times10^{-3}.TC^2 - 1.91.TC + 743)/100 \\ f_\alpha &= 1 - f_\beta \end{aligned} \qquad \text{(Eq. 5.3.2)}$$

where TC is temperature in Celcius. Figure 5.11 illustrates the comparison between the flow stresses predicted by this method and the experimental data of two-phase acicular Ti-6Al-4V deformed at strain rates of 0.3-0.003/s and temperatures 925, 950 and 975°C. It can be seen that the peak stress of the alloy can be estimated by using an iso-strain model, however, the flow stress softening is poorly predicted due to the absence of post-peak interaction mechanisms embedded within the model (Eq. 5.3.1).

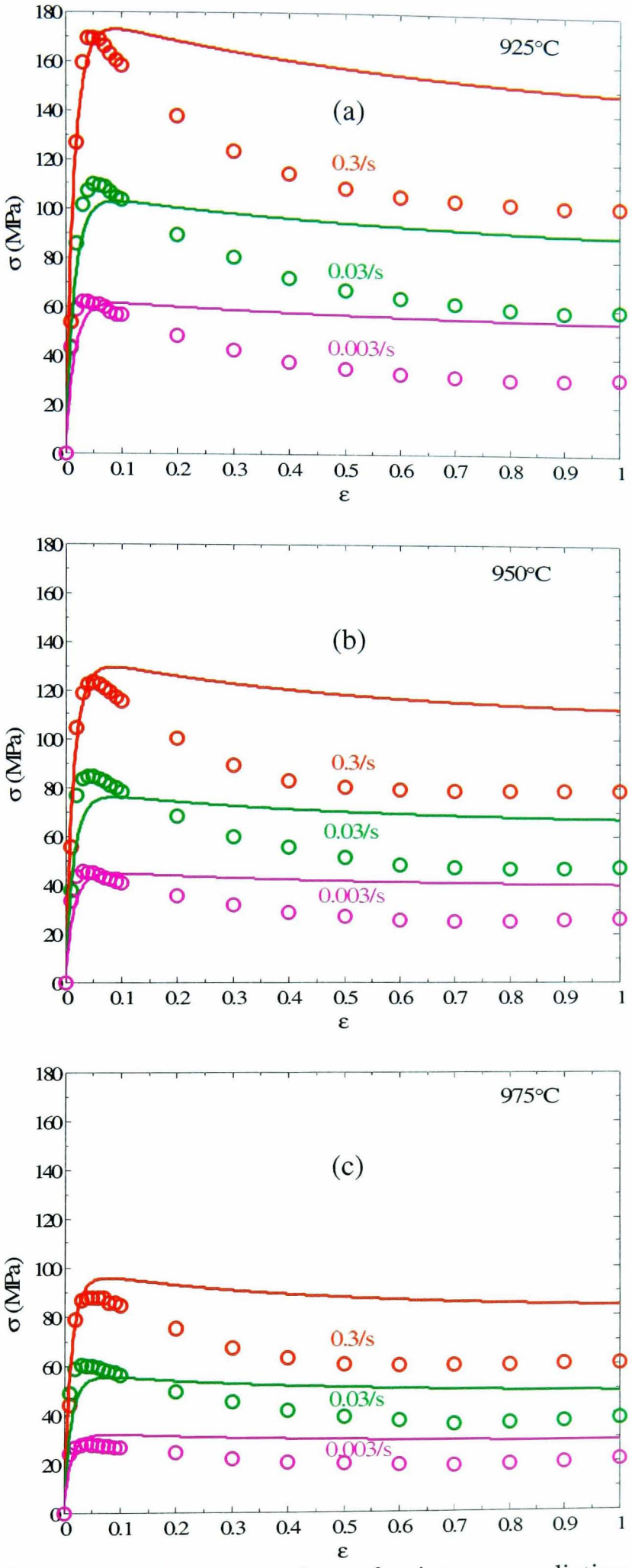

Figure 5.11: Comparison between a law of mixtures prediction (Eq. 5.3.3) and experimental flow stress of acicular Ti-6Al-4V deformed at strain rates of 0.003-0.3/s and temperatures (a) 925, (b) 950 and (c) 975°C. Circle: experimental data; line: the λ-model prediction.

In order to better predict the post-peak softening behaviour, a modification to Equation 5.3.1 has been made by incorporating a further structural-related variable that represents the strain accumulation resulting from interaction between phases during deformation. The modified iso-strain model can be re-written as:

$$\sigma_{\alpha\beta} = (f_\alpha \sigma_\alpha + f_\beta \sigma_\beta).C_{\text{int}}.\lambda_{\text{int}} \qquad \text{(Eq. 5.3.3)}$$

where C_{int} is a scaling constant and λ_{int} is a structural variable related to the interaction between phases. As λ_{int} also evolves towards a target condition, the evolution of λ_{int} can be described in a similar way to the evolution of the structural parameter with respect to strain, as given in Equation 5.1.4. Thus, λ_{int} can be defined as:

$$\frac{\partial \lambda_{\text{int}}}{\partial \varepsilon} = \alpha_{\text{int}}((\lambda_{ss})_{\text{int}} - \lambda_{\text{int}}) \qquad \text{(Eq. 5.3.4)}$$

where α_{int} is an exponential damping constant relating structure and strain. The strain rate and temperature-dependence of $(\lambda_{ss})_{\text{int}}$ can be formulated in a manner analogous to Equation 5.1.5, and defined as a power law function of the Zener-Hollomon parameter, Z_{int}:

$$(\lambda_{ss})_{\text{int}} = (\lambda_o)_{\text{int}} Z_{\text{int}}^q \qquad \text{(Eq. 5.3.5)}$$

$$Z_{\text{int}} = \dot{\varepsilon} \exp\left(\frac{Q_{\text{int}}}{RT}\right)$$

where $(\lambda_o)_{int}$ is a scaling constant, q_{int} is a structure sensitivity parameter and Q_{int} is the apparent activation energy for the two-phase interaction mechanism. Again, integration of Equation 5.3.4 over constant strain rate and temperature, with the initial condition that at $\varepsilon = 0$, the value of $\lambda_{int} = 1$ yields

$$\lambda_{int} = (\lambda_{ss})_{int} + (1 - (\lambda_{ss})_{int}) \exp(-\alpha_{int} \varepsilon) \qquad \text{(Eq. 5.3.6)}$$

The optimised constitutive parameters derived from the fitting of model Equations 5.3.3-6 to flow stress behaviour of two-phase acicular Ti-6Al-4V are listed in Table 5.4. Stress-strain predictions of the modified iso-strain model in the temperature range 900-975°C at strain rates of 0.003-0.3/s are illustrated in Figure 5.12. It is obvious that the modified iso-strain can predict the post-peak flow softening, indicating that the addition of structural related variable is effective in accounting for the interaction between α and β phases during deformation.

Table 5.4. **Material constants of the modified iso-strain model for acicular Ti-6Al-4V deformed at temperatures of 925-975°C at strain rates of 0.003-0.3/s**

C_{int}	$(\lambda_o)_{int}$	q_{int}	Q_{int} (kJ/mol)	α_{int}
1.08 ± 0.03	1.19± 2.40	-0.06 ± 0.02	142 ± 34.17	3.99 ± 1.18

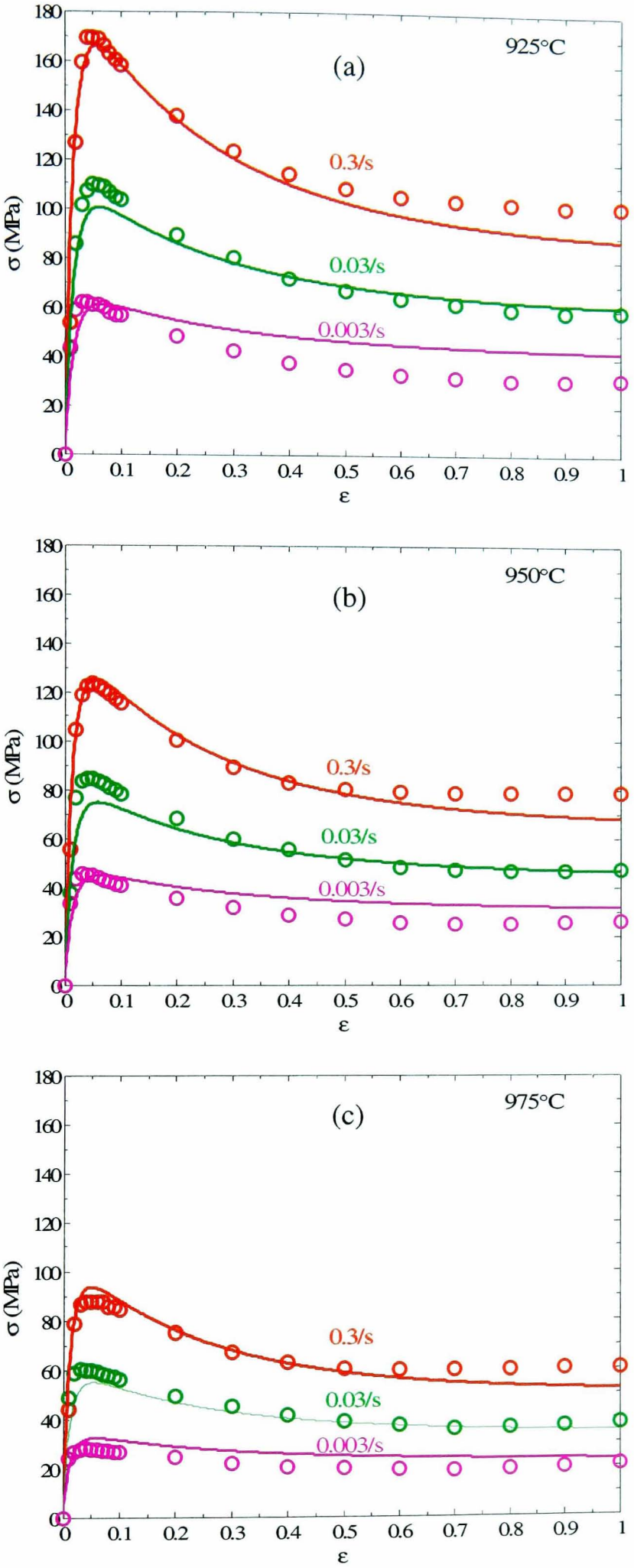

Figure 5.12: Comparison between a modified iso-strain prediction (Eq. 5.3.3-6) and experimental flow stress of acicular Ti-6Al-4V deformed at strain rates of 0.003-0.3/s and temperatures (a) 925, (b) 950 and (c) 975°C. Circle: data; line: model.

A key advantage of using internal state variables in constitutive models is their inherent capability to store the history of any final internal microstructural state, hence sudden changes of loading and temperature path can be accounted for. To demonstrate the predictive capability of the modified iso-strain model (Equations 5.3.3 to 5.3.6), a strain-rate jump test was performed at temperature 950°C with an instantaneous change in strain rate from 0.3 to 0.03/s at true strain of 0.2, and a further jump from 0.03 to 0.3/s at a strain of 0.4. Figure 5.13 compares the experimental and predicted strain-rate jump behaviour for acicular two-phase α+β Ti-6Al-4V at 950°C.

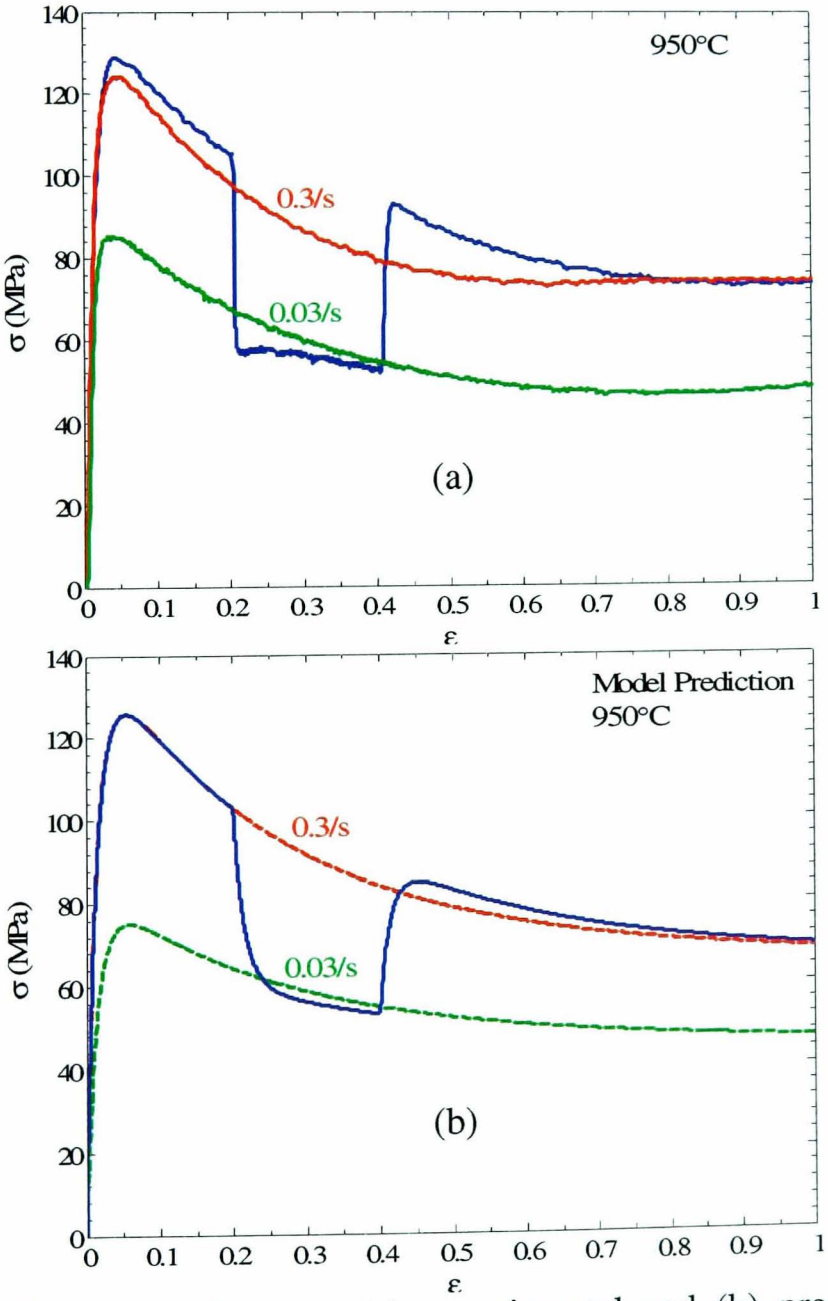

Figure 5.13: Comparison between (a) experimental and (b) predicted strain-rate jump flow stress for heat-treated two-phase α/β Ti-6Al-4V at 950°C.

From Figure 5.13, it can be seen that the model is able to predict the sudden change of imposed strain rate and to capture the tendency of undershoot and overshoot during the strain-rate jump test.

5.4 2D-finite element simulation of isothermal forging of two-phase Ti-6Al-4V

This section describes the simulation of isothermal forging of cylindrical and double-truncated cone specimens using the commercial finite element software DEFORM-2D version 8.1. The software is specially developed for hot and cold forging simulations by Batelle Columbus Laboratories and supported by Scientific Forming Technologies Co [101]. DEFORM-2D has the advantage of very stable remeshing capabilities, and the user is able to easily modify the input data [102].

The finite element method (FEM) is a powerful tool for analyzing metal forming processes due to its capability in producing detailed deformation information during simulated thermo-mechanical loading. In addition, FEM enables a large variety of problems to be solved by changing the model geometry and process parameters. With recent advanced development in finite element software and the availability of more powerful computers, commercial FE code allows the forging process to be simulated while predicting the distribution of stress, strain, temperature and structural variables within the work-piece simultaneously. Various thermo-mechanical parameter values and boundary conditions are required for finite element analysis of forging processes. In particular, it is necessary to characterize the bulk material properties of the work-piece, its initial conditions, the conditions at its free surfaces, and also at the die interface. The goal of this study was to evaluate the

strain, temperature and structural variable profile within both simple and complex specimen geometries, i.e. cylindrical and double-truncated cone work-pieces under rigid plastic analyses.

5.4.1 Pre-processing

For hot forging simulations, the finite-element pre-processor requires various input data. This includes material geometry (initial work-piece and dies), a constitutive model describing the flow stress behaviour of the work-piece, mechanical and thermal properties of materials, the interfacial friction condition between the dies and work-piece, and heat transfer properties between work-piece and dies.

5.4.1.1. Geometry and mesh

Geometries of the initial cylindrical work-piece and the dies used for FE simulation in this study are illustrated in Figure 5.14. The work-piece consisted of 2106 nodes and 2002 quadrilateral elements. The dies are considered as rigid bodies while the work-piece material is regarded as plastic. This assumption is reasonable since the dies are made from nickel-based alloy [103].

The geometry in a finite element model is represented by a mesh of non-overlapping elements. The cylindrical section is symmetric about the centre line which means that only one-half needs to be modelled. Nodal displacement within the work-piece was constrained by the contact boundary conditions imposed by the master surfaces. The bottom die was assigned as the primary die that moves upward in the *y* direction and

was constrained in the lateral x direction. The stationary top die was constrained in both directions.

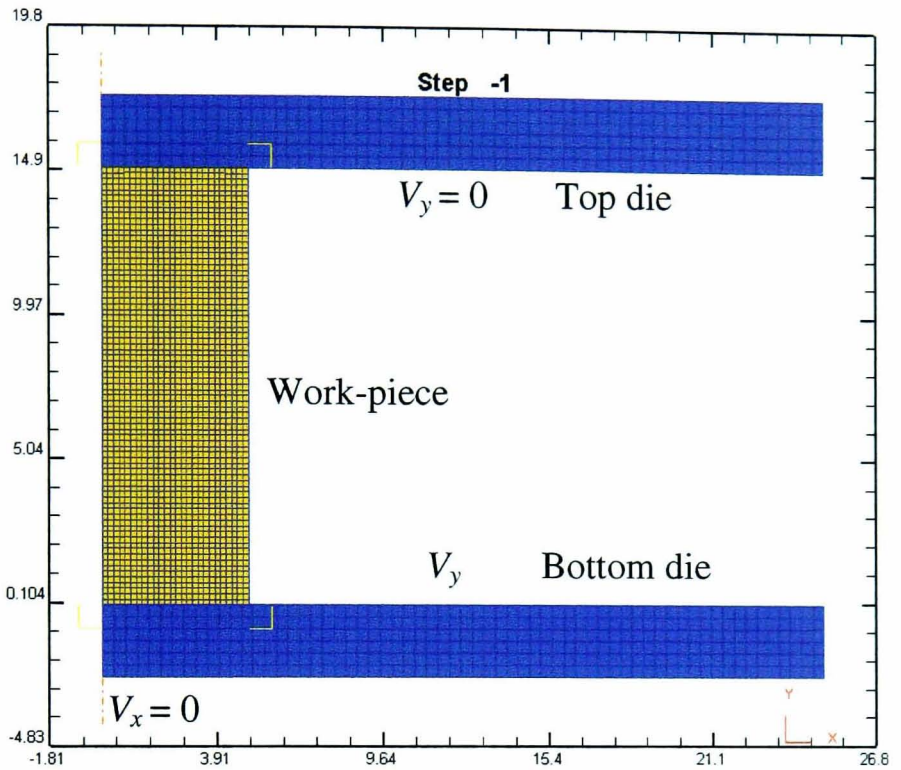

Figure 5.14: Axi-symmetrical finite element model of a uniaxial cylinder.

The movement of the bottom die was simulated by maintaining a constant true strain rate to simulate the actual isothermal upset test. This was implemented via a user-routine in which the speed of the ram was changed instantaneously as an exponential decay given by:

$$V_i = \dot{\varepsilon} H_0 \exp(-\dot{\varepsilon} t) \qquad \text{(Eq. 5.4.1)}$$

where V_i is the instantaneous die velocity (mm/s), $\dot{\varepsilon}$ the strain rate (s^{-1}), H_o the initial height of the work-piece (mm), and t the time (s). The simulation of forging was divided into a number of small incremental steps, typically 200 steps.

5.4.1.2. Material properties

The flow stress behaviour of the work-piece is described based on the constitutive two-phase model as given in Equations 5.3.3-6. The model was implemented into a user-routine written using Absoft Pro Fortran Version 7.0 [104]. The work-pieces are regarded as deformable plastic material, while the dies were treated as rigid material. Thermal properties of the dies and work-piece are required to simulate heat transfer and adiabatic heating effects, mainly for deformation at high strain rates. In DEFORM, heat flux within the work-piece is modelled using Fourier's law for heat conduction, given by:

$$\rho C_p \frac{dT_s}{dt} = \nabla(k_{th} \nabla T_s) + \dot{w} \qquad \text{(Eq. 5.4.2)}$$

where ρ is the density, C_p the specific heat capacity, k_{th} the thermal conductivity, t the time and $\dot{w}$ the heat dissipation rate. The heat flux per unit area at the free surface of the work-piece consists of conduction and convection process, evaluated with a heat transfer coefficient and radiation, evaluated using the Stephan-Boltzmann constant, defined as:

$$\dot{q} = h_{th}(T_a - T_s) + e\sigma_{SB}(T_a^4 - T_s^4) \qquad \text{(Eq. 5.4.3)}$$

where h_{th} is the heat transfer coefficient, T_a the ambient temperature, e the emissivity and σ_{SB} the Stephan-Boltzmann constant. Heat flux per unit area between die and work-piece was modeled using a further heat transfer coefficient:

$$\dot{q} = h_d (T_d - T_s) \qquad \text{(Eq. 5.4.4)}$$

where h_d is the interface heat transfer coefficient, T_s the work-piece temperature and T_d the die temperature. Since the analyses were carried out under nominally isothermal conditions, all the nodes of the work-piece and the dies were assigned uniform temperature prior to simulation. The thermal data required for forging simulations of cylindrical and double truncated cone specimens of Ti-6Al-4V are summarised in Table 5.5, and were obtained from various sources. Specific heat capacity C_p (J/kg/°C) and thermal conductivity k_{th} (W/m/°C) for Ti-6Al-4V were derived as functions of temperature TC (°C) [105]:

$$C_P = 5.322.10^2 + 3.097.10^{-1} TC - 2.823.10^{-4} TC^2 + 5.468.10^{-7} TC^3 \qquad \text{(Eq. 5.4.5)}$$

$$k_{th} = 10^{-5} TC^2 + 0.0098 TC + 6.3992 \qquad \text{(Eq. 5.4.6)}$$

Table 5.5. **Thermal properties for forging simulation of Ti-6Al-4V**

Thermal Property	**Symbol**	**Value**	**Units**	**Reference**
Density	ρ	4420	Kg/m^3	[106]
Environment - work-piece heat transfer coefficient	h_{th}	0.01	N/sec/mm/°C	[101]
Dies-work-piece interfacial heat transfer coefficient	h_d	4	N/sec/mm/°C	[107]
Work-piece emissivity	e	0.287	-	[108]

5.4.1.3. Interfacial friction factor

Finite element analysis uses a coefficient or factor to calculate interfacial friction stresses. For bulk forming analysis, constant shear friction (*Tresca* friction) is generally applied at the die-work-piece interface [109]. In the constant-shear friction model, the product of a friction factor and the shear define the interfacial shear stress at the die-work-piece interface, given by:

$$\tau_f = m_f . k_{ys} \qquad \text{(Eq. 5.4.7)}$$

where m_f is the friction factor and k_{ys} the shear yield stress of the forging. The values of friction factor m_f used for the finite element simulations were determined based on the calibration curves described in Chapter 3 (Figure 4.4.b and Table 4.1).

5.4.2 Simulation results of isothermal forging of uniaxial cylindrical specimen

Isothermal forging simulations of uniaxial cylindrical specimens were carried out at various strain rates and temperatures. Simulations of tests performed at 950°C and 0.3 and 0.01/s were analysed and compared in order to investigate the effect of strain rate on the strain, stress, temperature and structural variable distribution within the cylindrical work-piece.

5.4.2.1. Distribution of effective plastic strain

Figure 5.15 illustrates the distribution of local effective strain at bulk strains of 0.5 and 1.0 for isothermal forging of the cylindrical work-piece at 950°C and strain rates of 0.3 and 0.01/s.

After 0.5 bulk strain, it can be seen that the local strain is distributed non-uniformly within the work-piece, with the central region undergoing the most intense deformation. After further deformation, ε = 1.0, the central area of more intense plastic deformation becomes narrower and suppressed along the radial line of the deformed work-piece. In addition, it is also observed that the maximum local strain occurs at the corners that are close to the folding edges (barrelling edges). The profile of local effective strain is not greatly affected by imposed strain rate during deformation.

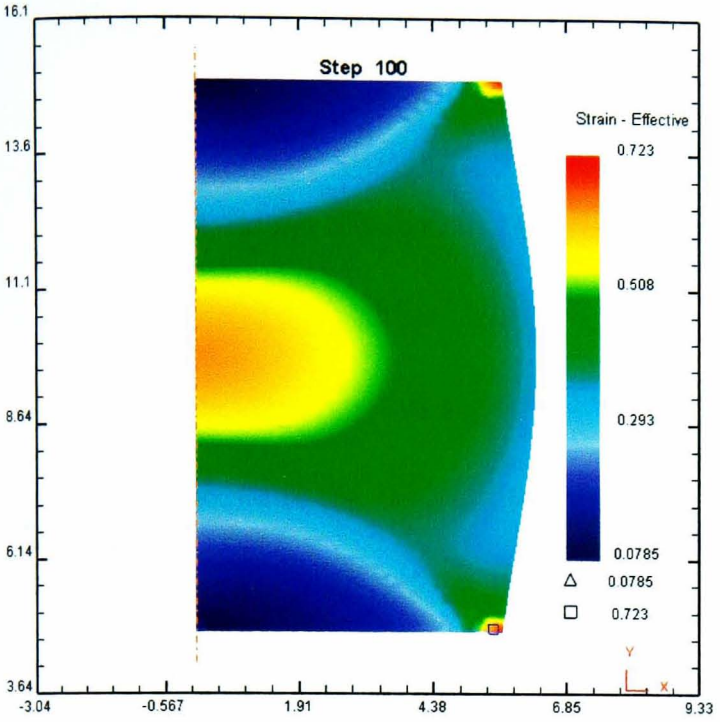

(a)

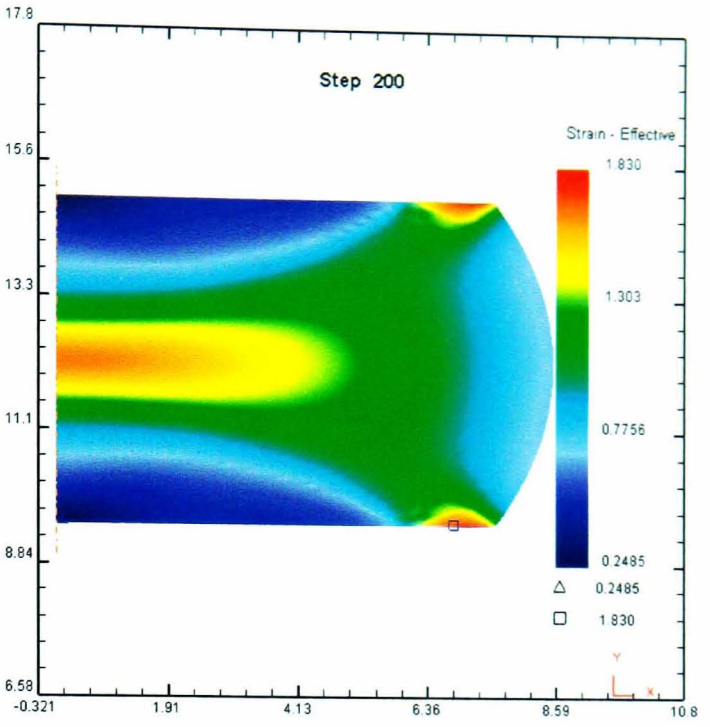

(b)

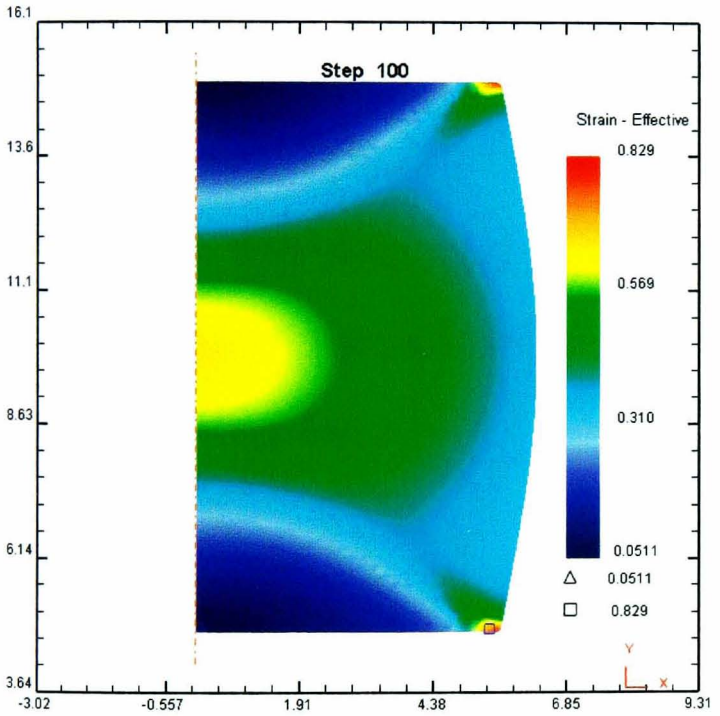

(c)

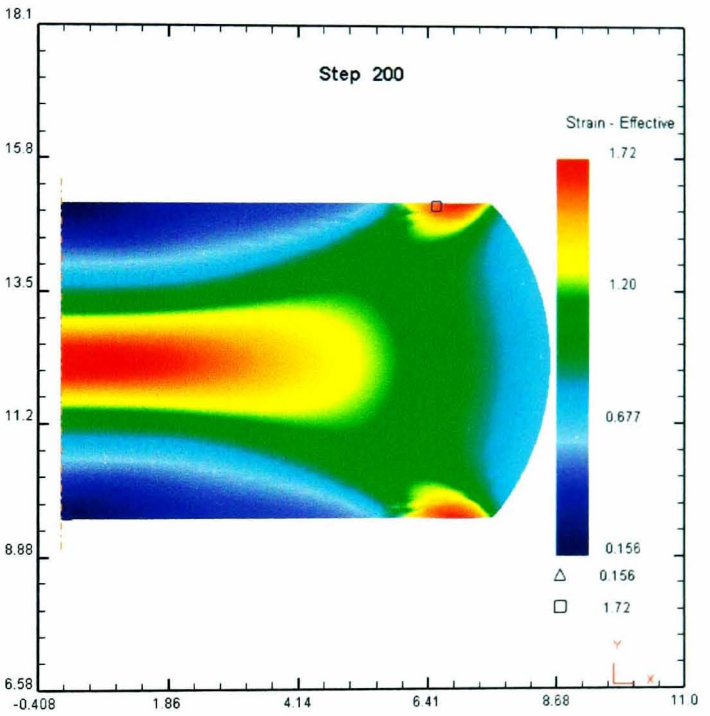

(d)

Figure 5.15: Comparison between distribution of local effective strain of cylindrical work-piece deformed at 950°C; 0.3/s; bulk strains of (a) 0.5; (b) 1 and 950°C;0.01/s; bulk strains of (c) 0.5; (d) 1.

5.4.2.2. Temperature profile

Figure 5.16.a-b illustrates the detailed temperature profile at bulk strains of 0.5 and 1.0 within a cylindrical work-piece deformed at 950°C and strain rates of 0.3 and 0.1/s. It is apparent that the degree of non-uniform temperature distribution increases with reduction in height. As the reduction in height reaches ~5mm from 15mm original height of the work-piece (step 100), it is found that the maximum local temperature occurs at the core of the work-piece, where the largest plastic strain occurred. The higher temperature here is due to the fact that most of the plastic work is converted into heat. However, the surface temperature is lower due to lower plastic deformation ('dead zone region') and rapid heat loss away from the work-piece to the dies. With progressing deformation, the temperature profile changes markedly. The region of maximum temperature tends to extend from the central region towards the barrelling edge.

On the other hand, the development of the temperature profile during slower strain rate testing, *i.e.*, 0.01/s, is shown in Figure 5.16.c-d. It can be seen that the temperature distribution is relatively uniform as deformation proceeds, compared to the temperature rise at a strain rate of 0.3/s.

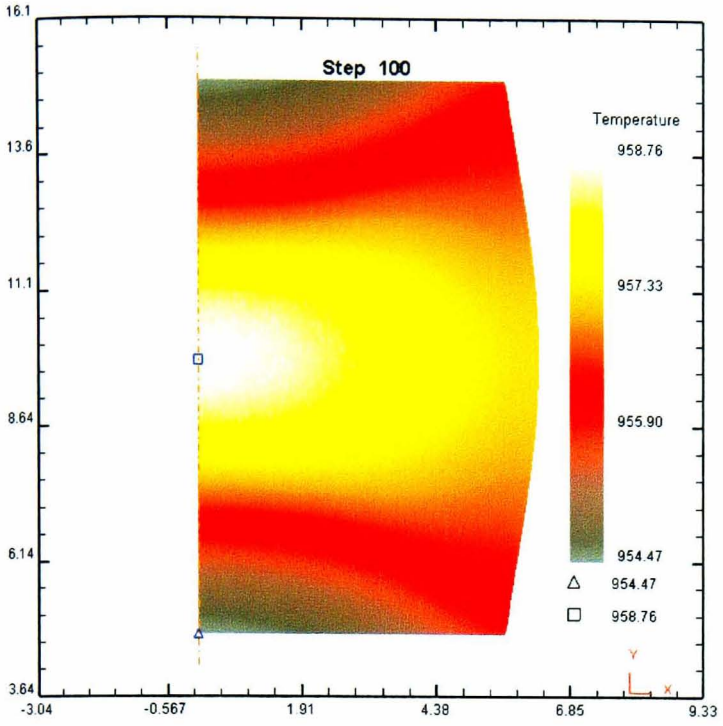

(a)

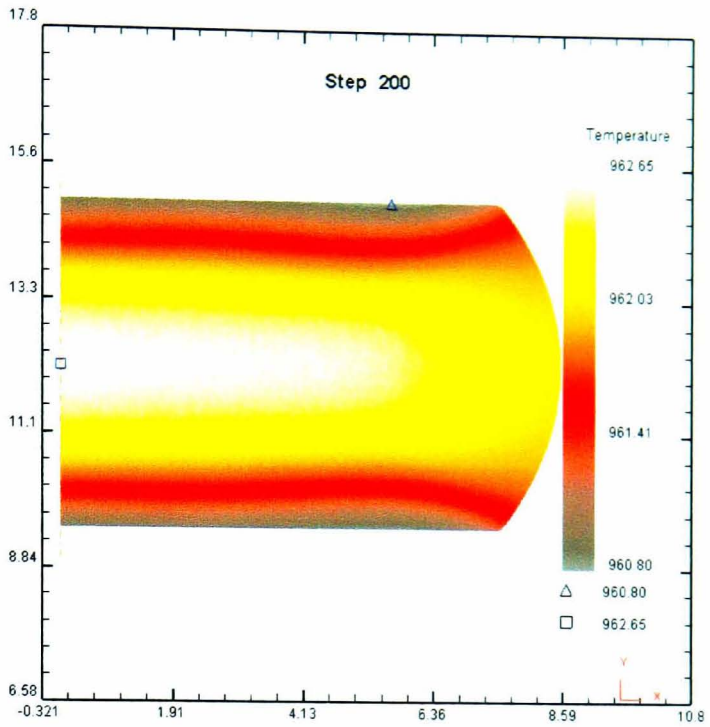

(b)

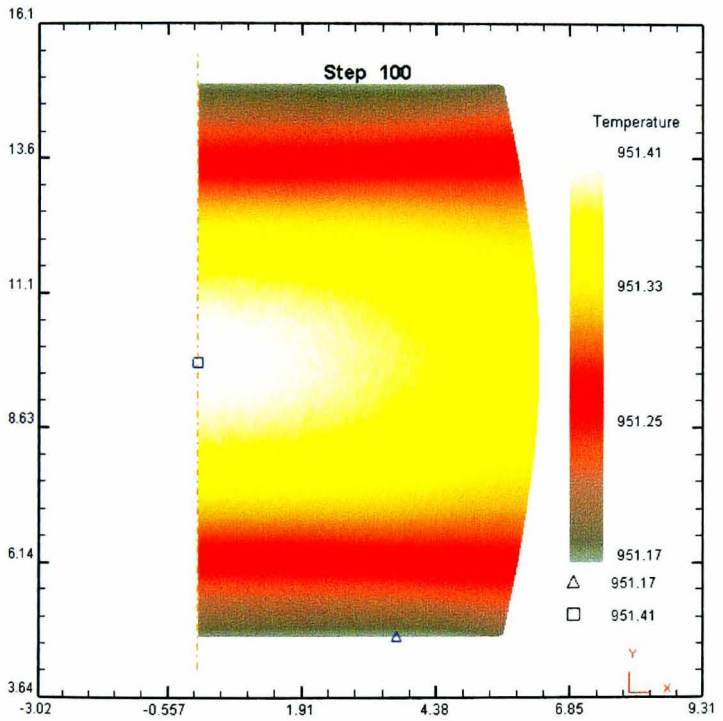

(c)

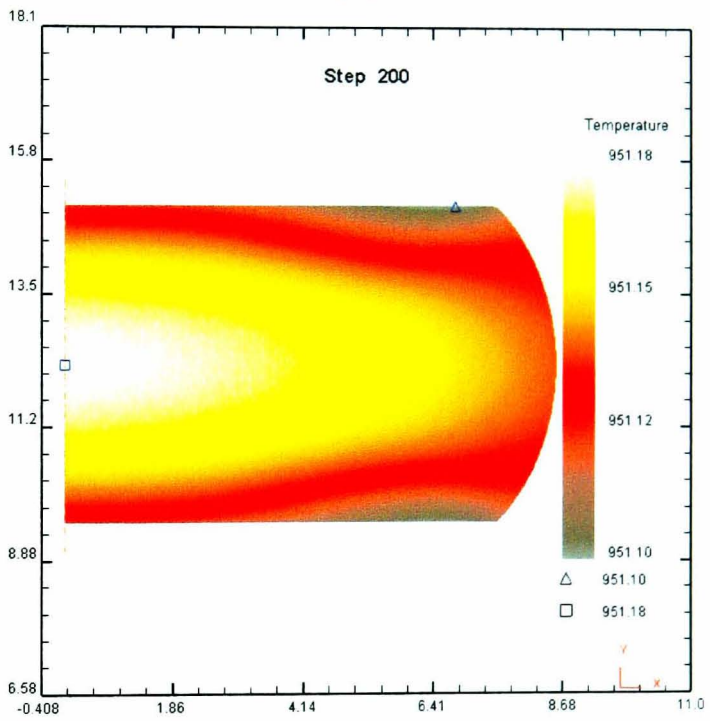

(d)

Figure 5.16: Temperature profile within cylindrical work-piece deformed at 950°C and 0.3/s; bulk strains of (a) 0.5; (b) 1 and 950°C;0.01/s; bulk strains of (c) 0.5; (d) 1.

Comparison of the axial and radial temperature distributions developed after a bulk strain of 1 within a work-piece deformed at 950°C and strain rates of 0.3 and 0.01/s are shown in Figure 5.17.

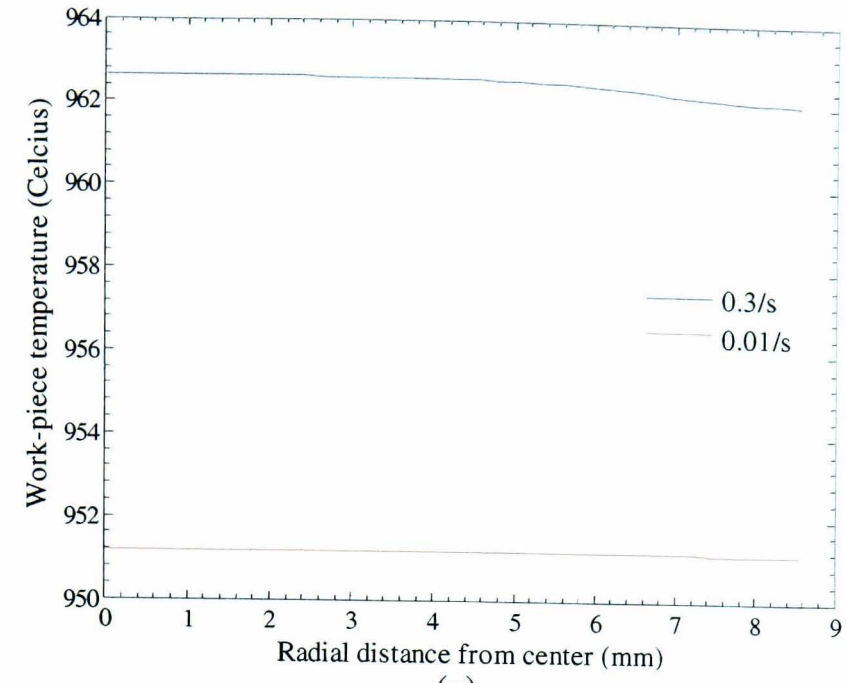

(a)

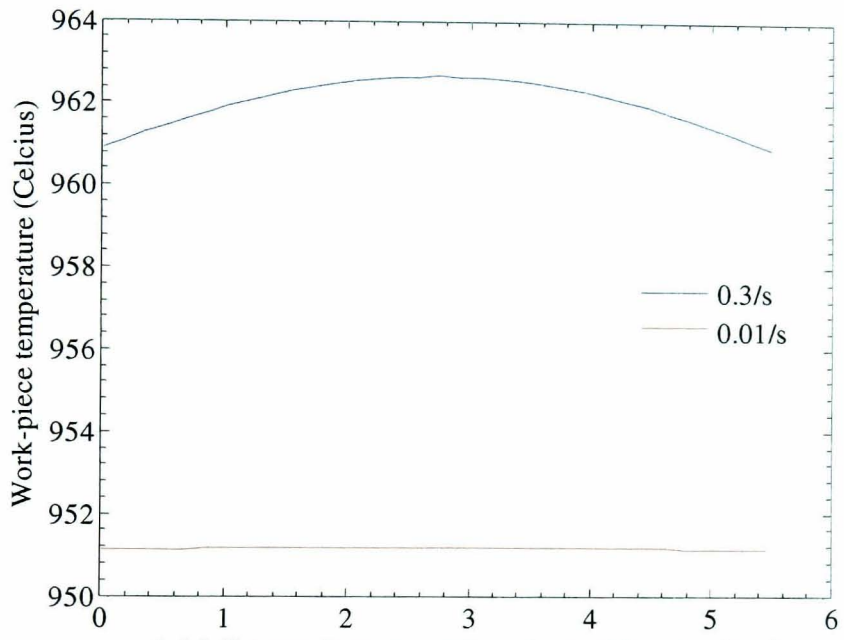

(b)

Figure 5.17: Comparison of temperature distribution developed after a bulk strain of 1 within work-piece deformed at 950°C in (a) radial and (b) axial direction.

The simulated maximum value of local temperature occurring at the centre of the work-piece was found to be 962.6°C during the final step for strain rate of 0.3/s, an increase of 12.6°C over the work-piece pre-test temperature (950°C). In contrast, the local temperature rise was only 1-2°C for deformation under the slower strain rate (0.01/s). These simulation results demonstrate that deformation performed at slower strain rate can maintain the isothermal condition because there is sufficient time to

achieve equilibrium where generation of deformation heat is balanced by heat transfer to surroundings (conduction to the dies and convection to environment).

5.4.2.3. Distribution of structural variable λ_{int}

Distribution of the λ_{int} values is used to predict the evolution of microstructure constituents within the work-piece during isothermal forging. A link between the λ_{int} values and any evolved microstructure parameters is described in detail in the next chapter.

Figure 5.18.a-d illustrates the evolution of structural variable λ_{int} at bulk strains of 0.5 and 1.0 within a cylindrical work-piece deformed at 950°C and strain rates of 0.3/s and 0.01/s. It should be noted that λ_{int} is equal to unity prior to forging. It can be seen that, at a bulk strain of 0.5, λ_{int} has decreased to between 0.894 and 0.553 along the axial mid-section of the cylinder. Greater values of λ_{int} are concentrated in areas where a lower degree deformation occurred such as near-surface areas ('dead zone region'). On the other hand, λ_{int} is smaller in the central region due to a higher degree of deformation and temperature. With progressing deformation, λ_{int} in the centre region is reduced more slowly (from 0.553 to 0.530 as strain is increased from 0.5 to 1.0) reflecting the attainment of a steady state value. A similar development of λ_{int} profile was also exhibited during isothermal forging performed at slower strain rate, *i.e*, 0.01/s (Figure 5.18.c-d). The primary difference is the λ_{int} values produced during slower strain rate are lower than those obtained under higher strain rate deformation.

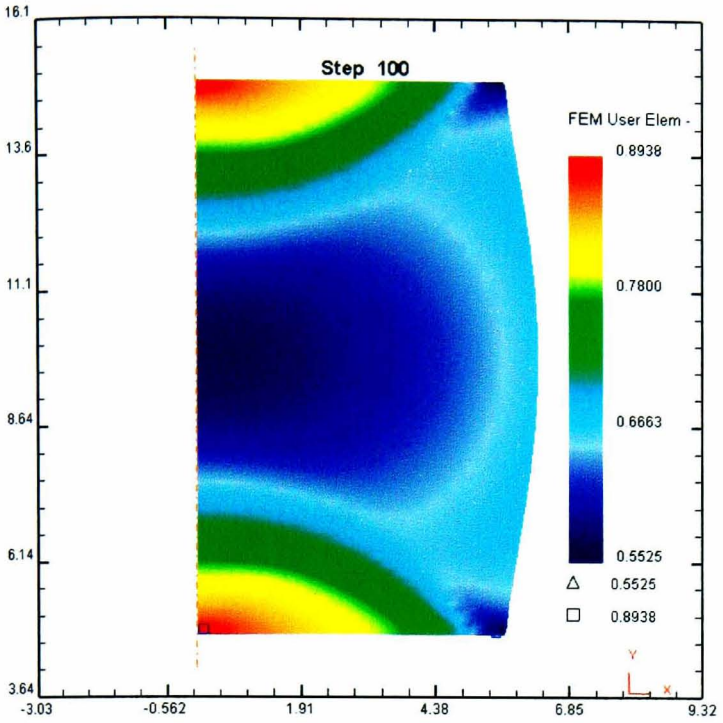

(a)

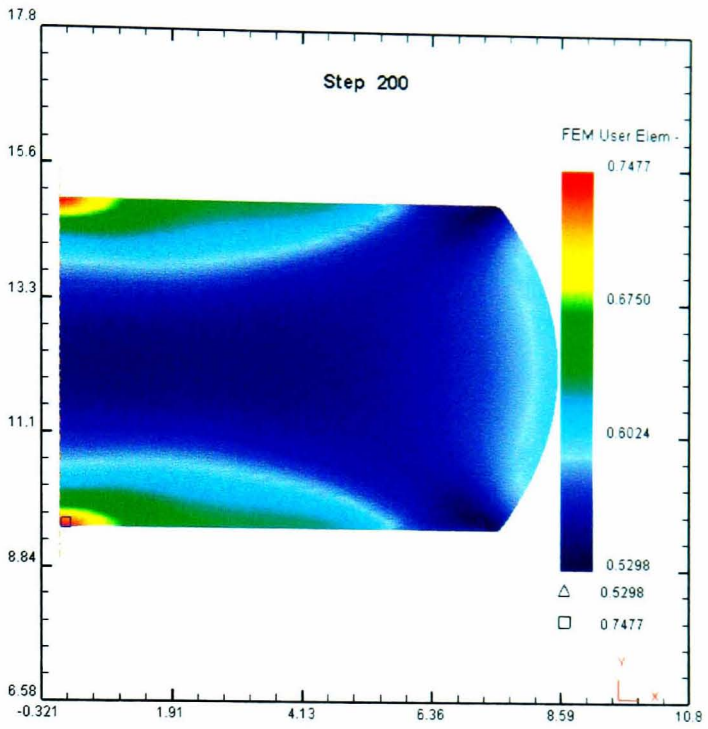

(b)

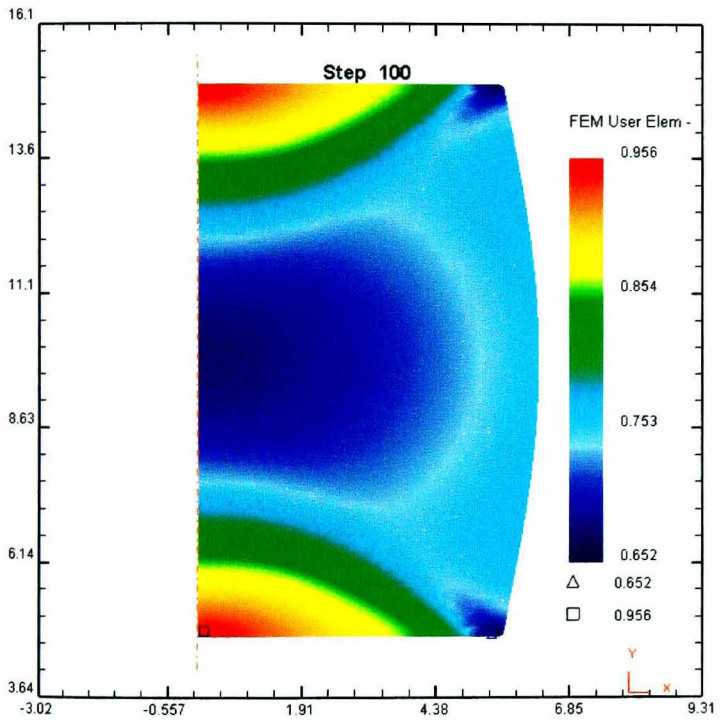

(c)

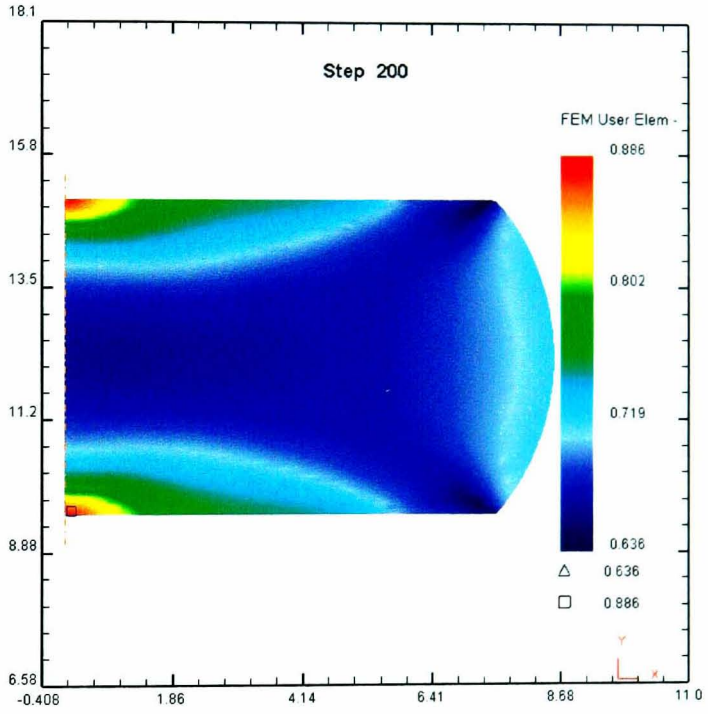

(d)

Figure 5.18: Comparison between distribution of structural variable λ_{int} within a cylindrical work-piece deformed at 950°C; 0.3/s; bulk strains of (a) 0.5; (b) 1.0 and 950°C;0.01/s; bulk strains of (c) 0.5; (d) 1.0.

For comparison, Figure 5.19 illustrates the distribution of λ_{int} values within a cylindrical work-piece deformed at 950°C and strain rates of 0.3 and 0.01/s. This result shows clearly the strain-rate dependence of the structural variable.

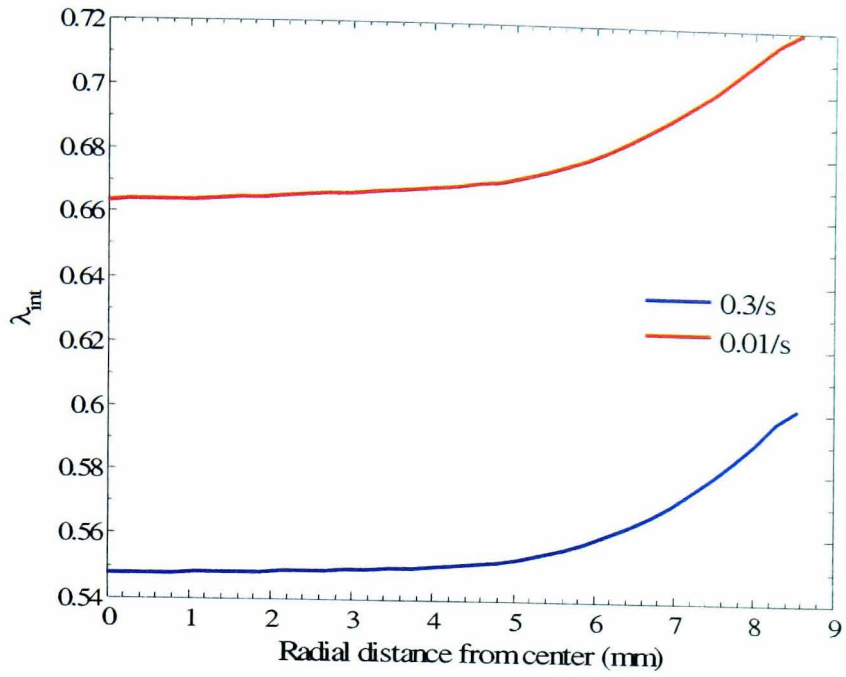

(a)

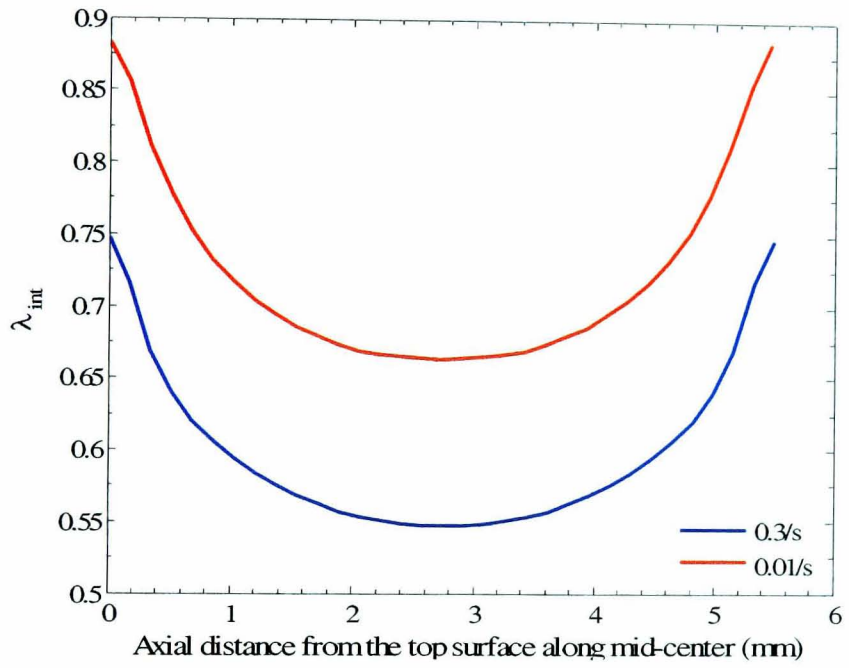

(b)

Figure 5.19: Comparison of λ_{int} distribution developed at final step (step 200) within work-piece deformed at 950°C along (a) radial and (b) axial (mid-centre).

5.4.3 Validation of Constitutive Model

To investigate the applicability of the constitutive model used (Eq. 5.3.3-6) in the case of complex-shape forging, an additional isothermal forging experiment and finite element simulation of a double-truncated cone were performed at 950°C and

0.01/s. Geometries of the specimen and dies used for this simulation are illustrated in Figure 5.20. The specimen FE mesh consisted of 5110 quadrilateral elements and 5254 nodes.

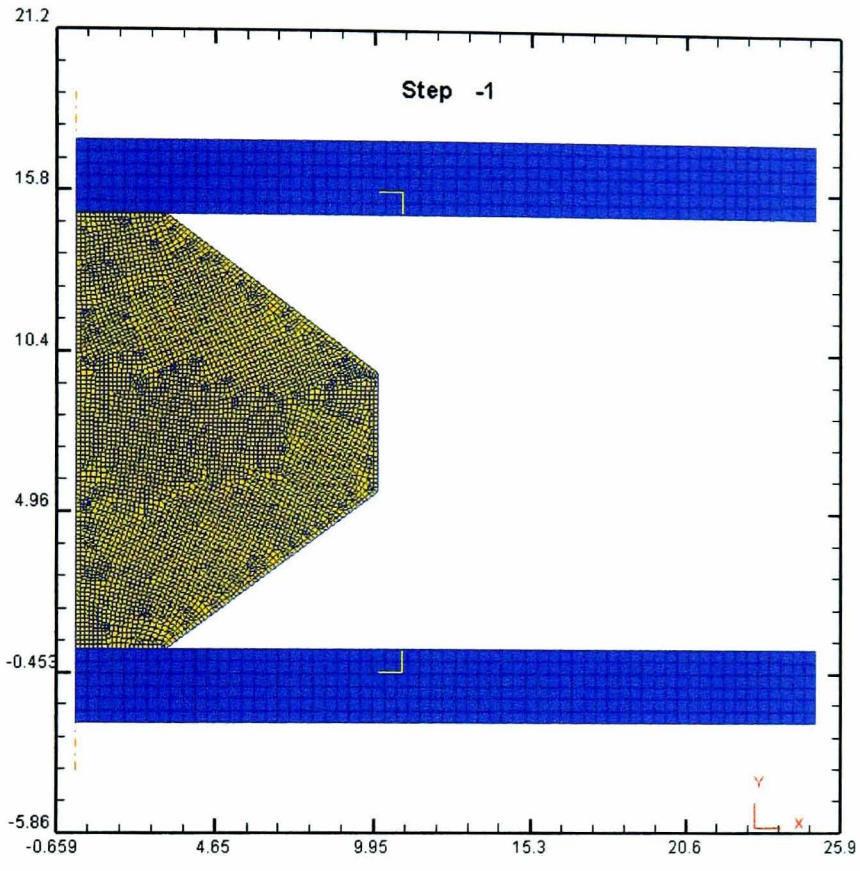

Figure 5.20: Initial geometry of axi-symmetrical double-truncated cone and dies.

Figure 5.21 shows a comparison of simulated load response and experimental load-displacement behaviour. It can be seen that the predicted curve is in excellent agreement with the measured load data. The sharp increase observed in the load values is captured accurately by the simulation. This demonstration verifies the predictive capability of the constitutive model developed (Eq. 5.3.3-6) in this study for modelling material properties employed within the finite element analysis.

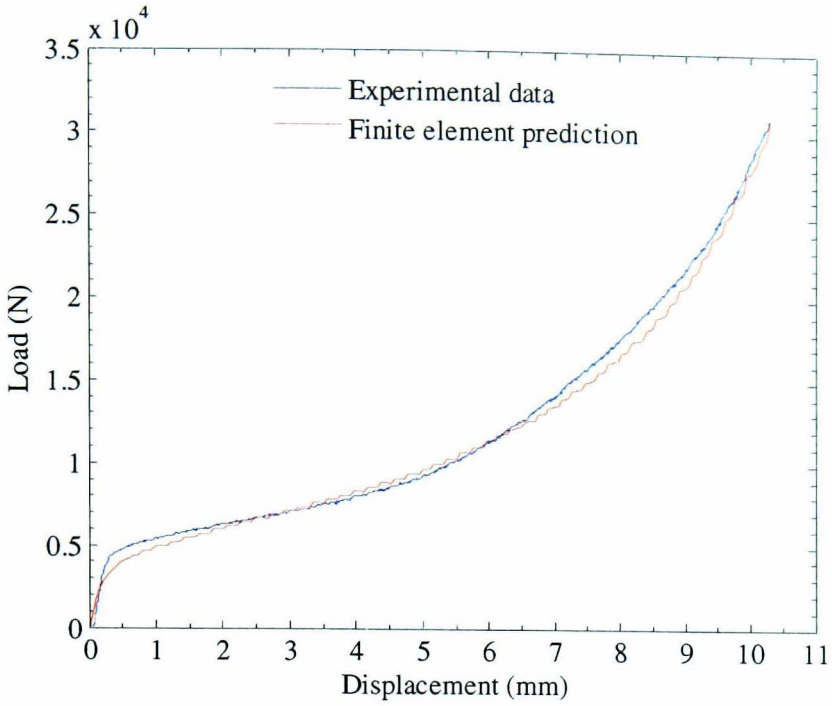

Figure 5.21: Comparison of the experimental deformation load with FE results for isothermal forging of double truncated cone at 950°C and 0.01/s.

The development of the strain profile within the work-piece is illustrated in Figure 5.22. It can be seen that there is a large variation in local plastic strain from 0.15 to 2.12. The maximum plastic strain occurs in the central region, further illustrated by the radial and axial distribution presented in Figure 5.23.

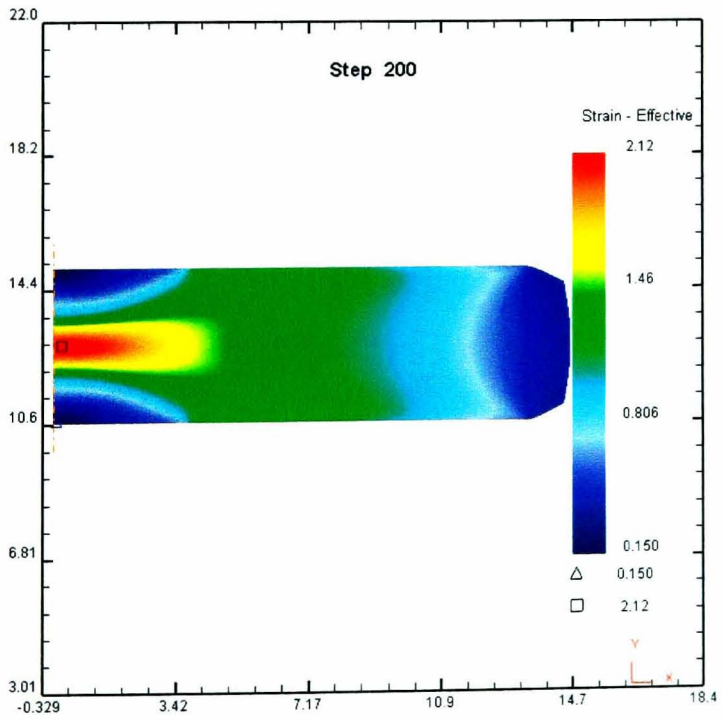

Figure 5.22: Distribution of local effective strain of a double truncated cone deformed at 950°C and 0.01/s.

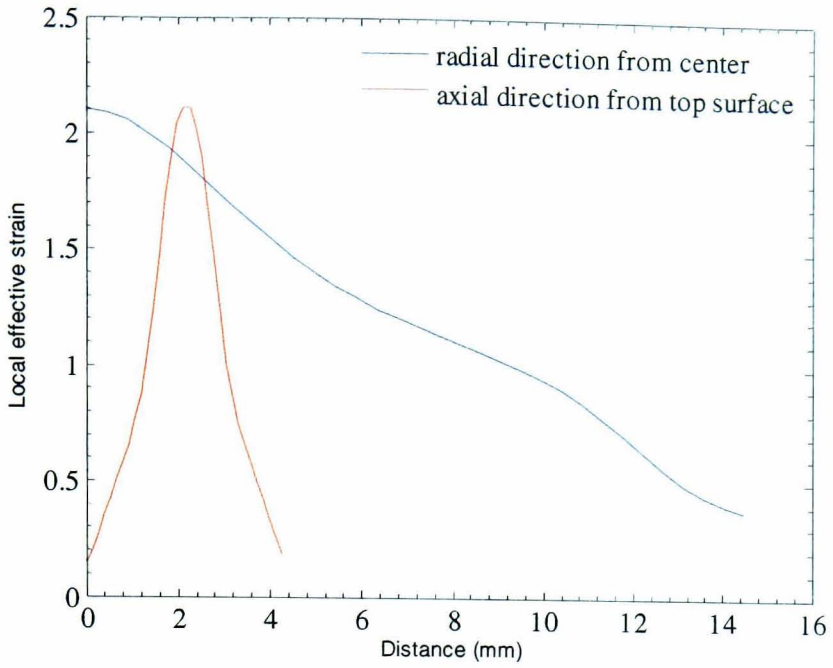

Figure 5.23: Local effective plastic strain distribution in the radial and axial direction within double-truncated cone deformed at 950°C and 0.01/s.

The distribution of λ_{int} obtained here is useful in predicting the microstructure evolution within a complex work-piece during isothermal forging. This is performed as a validation of the microstructure model derived from the isothermal forging of conventional cylindrical specimens. Figure 5.24 illustrates the evolution of structural variable λ_{int} within the double-truncated cone deformed at 950°C and 0.01/s. A direct correlation between λ_{int} and the degree of deformation is observed. Higher values of λ_{int} are concentrated in less deformed areas, such as the dead zone region and near the barrelling edge. In contrast, the smaller values were found in the more severe deformed areas, notably the centre.

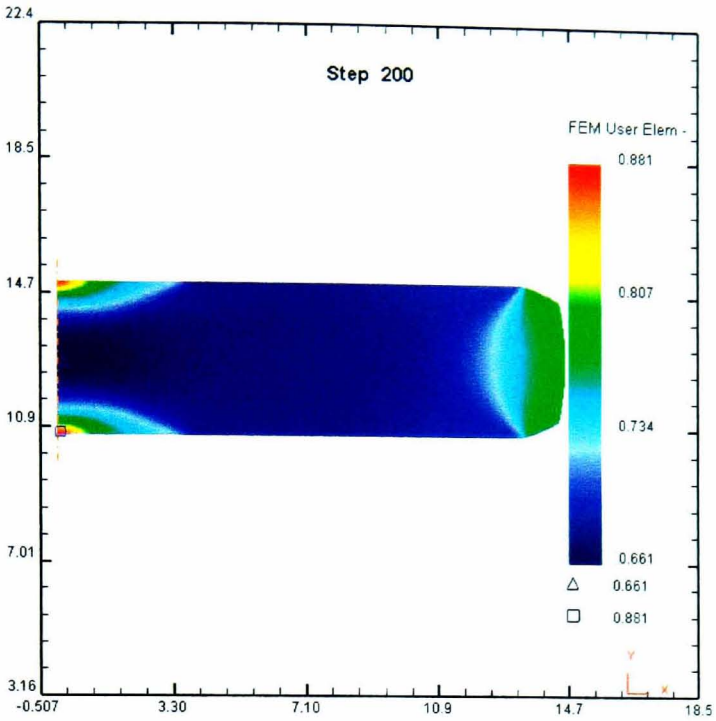

Figure 5.24: Final distribution of structural variable λ_{int} of double-truncated cone work-piece deformed at 950°C and 0.01/s.

In detail, the distribution of the structural variable λ_{int} within the final deformed double truncated cone specimen is illustrated in Figure 5.25. In the radial direction, the values vary from 0.663 at the centre to 0.781 at a location of 14.5mm from the centre. In the axial direction, λ_{int} falls from 0.88 in the dead zone region to a near steady-state value of 0.663 in the centre.

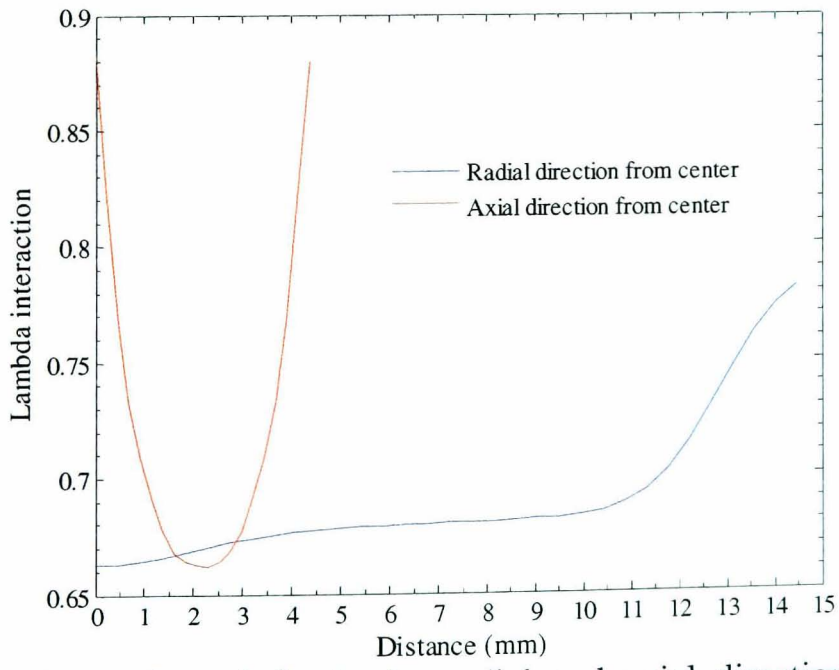

Figure 5.25: Distribution of λ_{int} in the radial and axial direction within double-truncated cone deformed at 950°C and 0.01/s.

5.5 Summary of results

A state variable model ('the λ-model'), which takes account of gross internal structural evolution, has been employed to model the flow stress behaviour of β-heat treated acicular Ti-6Al-4V during hot deformation at temperatures of 925-975°C and strain rates of 0.3-0.003/s.

Methods for parameter optimisation in the constitutive model for hot deformation have been compared. It was found that the Nelder-Mead simplex method shows the best performance as indicated by the final objective function value, and by the number of iterations and function evaluations required for optimisation. In addition, parameter confidence limits have been estimated for the first time in a multi-parameter nonlinear hot deformation constitutive model.

Although the λ-model prediction and the experimental data are in very good agreement, it is nevertheless important to establish a predictive model that can distinguish the deformation history of each phase constituent in order to take account of the two-phase nature of the deformation.

The iso-strain assumption (Taylor approach) has been employed to model the flow stress behaviour of β-heat-treated acicular Ti-6Al-4V. The strain within the individual phases (α and β) is assumed to be equal to that in the two-phase alloys. The flow stress of each phase is weighted by its temperature-dependent volume fraction in order to determine the total stress response of the bulk two-phase α+β Ti-6Al-4V. This assumption can estimate the peak stress of the alloy. However, the flow

softening is poorly predicted due to the absence of any post-peak interaction mechanisms embedded within the iso-strain equation.

In order to better predict the flow stress curves of heat-treated two-phase Ti-6Al-4V, a constitutive model has been developed by modifying the iso-strain approach to take account of gross interaction mechanisms between the individual phases. A structural variable λ_{int} has been introduced to represent the associated inter-phase strain accumulation and was effective in predicting post-peak flow softening.

The modified iso-strain model is able to follow the instantaneous change of imposed strain rate by capturing the trend of 'undershoot' and 'overshoot' during strain rate jump testing.

The constitutive model developed has been implemented as a user-routine within DEFORM-2D finite element software in order to simulate the isothermal forging of conventional cylindrical work-pieces. The FE model has been used to predict the distribution of local effective strain, temperature and structural variable at different bulk strains within deformed uniaxial cylindrical work-pieces. The FE and constitutive models have been validated using isothermal forging of a complex shape double-truncated cone specimen. The simulated forging load is in excellent agreement with the experimental load-displacement data.

Chapter 6

Microstructure Evolution of Ti-6Al-4V During Isothermal Forging

This chapter discusses the microstructure evolution of Ti-6Al-4V supplied as $\alpha + \beta$ hot-worked round bar in annealed condition. Prior to full investigation, the β-transus of the as-received material was determined experimentally by performing a series of heat treatments at various soak temperatures followed by water quenching. Volume fraction of the primary α phase was quantified using image analysis techniques. The effects of strain, strain rate and temperature on primary α morphology are described in order to provide an understanding of microstructural phase evolution during sub-transus isothermal forging.

Microstructure evolution was also investigated for Ti-6Al-4V with a transformed acicular initial microstructure, achieved by β-solution heat-treating the as-received material. The morphological changes of various microstructural parameters are again quantified using image analysis techniques.

6.1 Globular (as-received) microstructure

The microstructure of the as-received Ti-6Al-4V captured using backscattered electron imaging, as re-displayed in Figure 6.1., exhibits an α + β microstructure consisting of elongated primary α within a fine discontinuous β matrix. Nearly-equi-axed α grains are also observed in some regions.

Figure 6.1: As-received microstructure of Ti-6Al-4V consisting of elongated and nearly equi-axed primary α phase within discontinuous transformed β matrix.

This type of microstructure indicates that the material has received β hot-working which involves primary ingot breakdown in the single β-phase regime, followed by relatively slow cooling and further secondary hot working operations in the α + β phase field. The presence of some elongated primary α with a preferred orientation indicates that the material has undergone final hot rolling in the two-phase α + β

phase field. At higher magnification, a fine α phase structure was also observed within the β matrix as illustrated in Figure 6.2, possibly retained from break-up of coarse α during secondary operations.

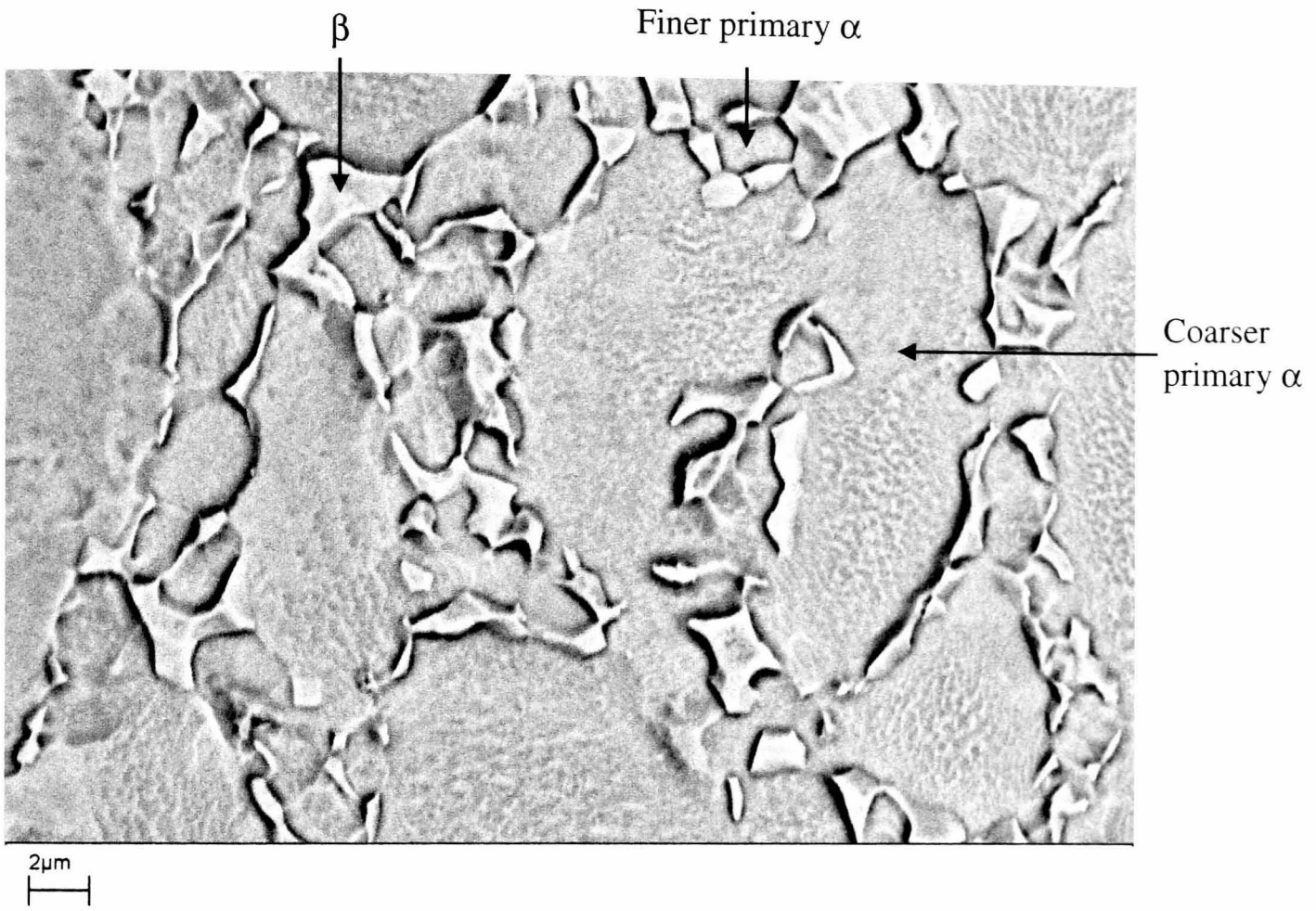

Figure 6.2: Micrograph of as-received Ti-6Al-4V illustrating finer α grains between coarser primary α phase within β matrix.

A series of heat treatments at various temperatures were carried out to determine the β-transus temperature. Figure 6.3 illustrates undeformed microstructures after soaking at temperatures of 850-1000°C for 1 hour and followed by water quenching. It can be seen that, with increasing temperature, most of the primary α has transformed to β phase, reducing the volume fraction of primary α. At 1000°C, the β phase is retained only in the form of secondary α indicating that 100% primary α has transformed into β phase. The morphology of secondary α can be easily recognised from its typical martensitic structure following rapid quenching, consisting of

misoriented colonies of needle-like α within prior β grains (Figure 6.3.f). Closer examination of the microstructures under higher magnification (Figure 6.4) reveals that the microstructure developed at 975°C exhibited a coarse needle-like secondary α phase, which is a typical morphology produced from β phase transformation upon rapid quenching, comparing to microstructures developed at lower temperatures. This indicates that a higher volume fraction of β-phase has been retained as temperature proceeds closer to β-transus.

Volume fractions of the α and β phases were measured, based on Figure 6.3, using quantitative metallography. The β-approach curve was derived by plotting quantified β volume fractions at different temperatures.

The curve obtained from the quantitative metallography is shown in Figure 6.5 and compared to measurements of Castro-Seraphin [110] and Semiatin *et al.* obtained using microprobe analysis [98]. The results obtained by the quantitative image analysis are in close agreement with the more rigorous microprobe measurements. The β-transus temperature was estimated to be 995°C.

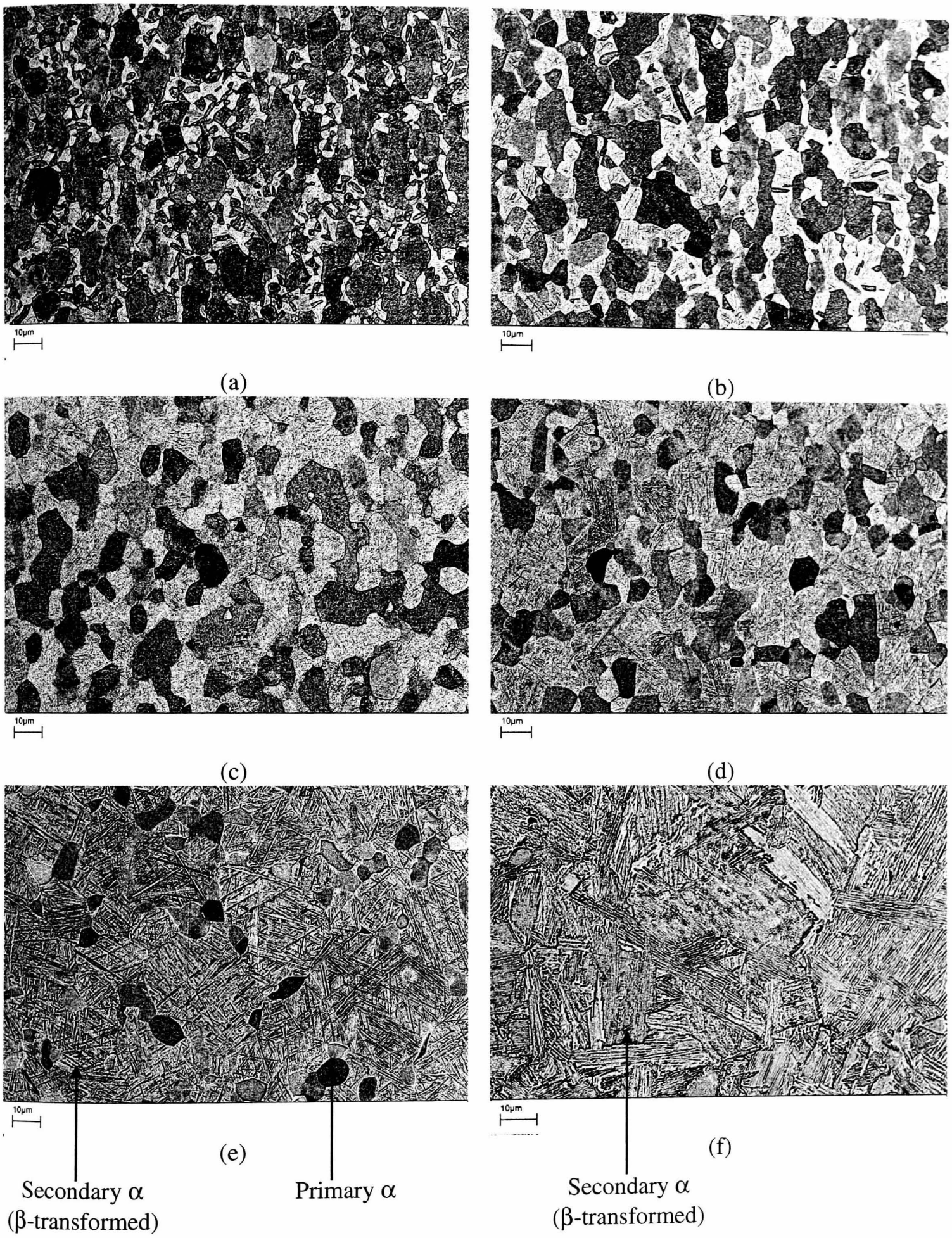

Figure 6.3: Microstructure evolution of as-received Ti-6Al-4V followed by water quenching after 1 hour soak at temperatures (a) 850, (b) 900, (c) 925, (d) 950, (e) 975 and (f) 1000°C.

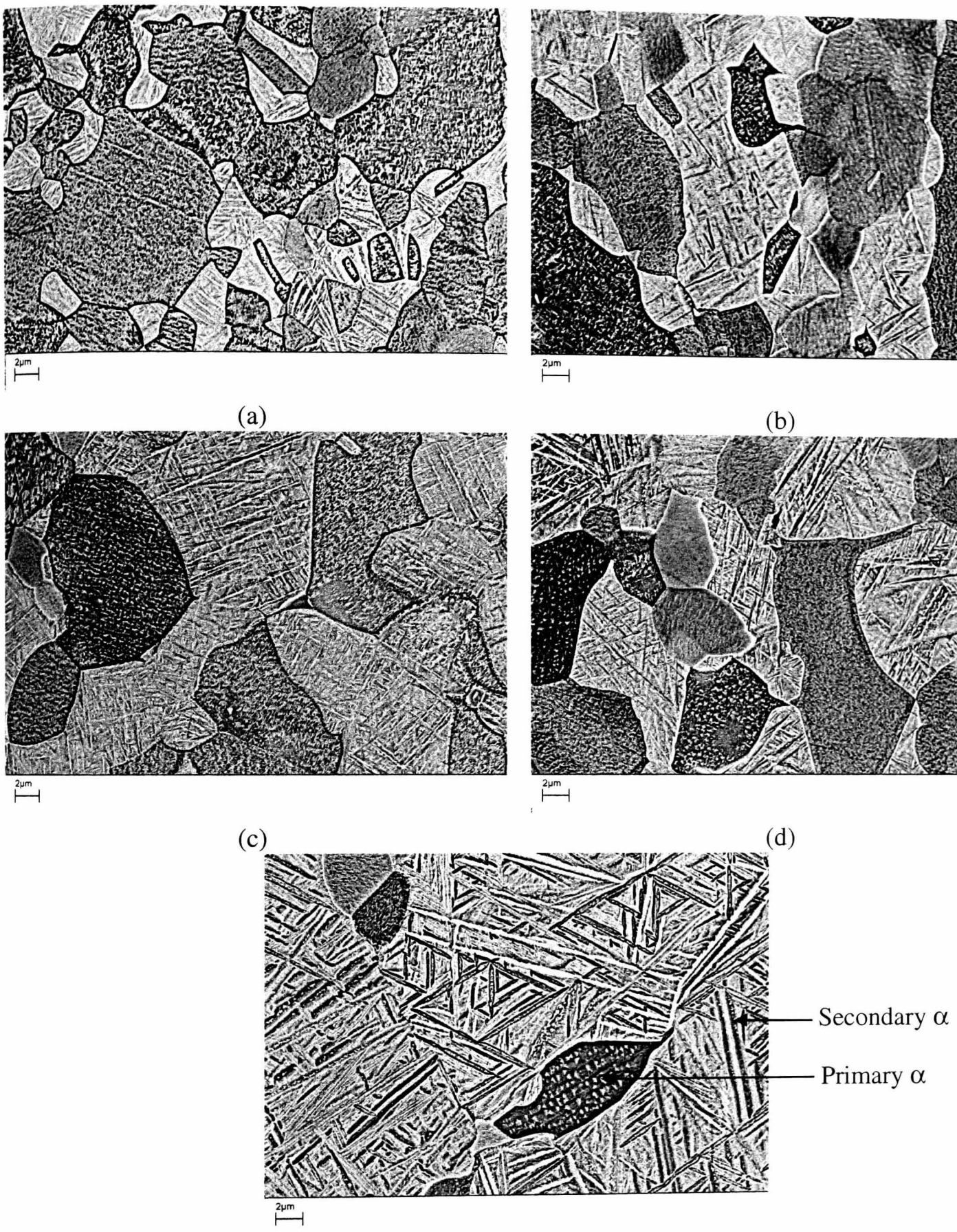

Figure 6.4: Micrographs with higher magnification illustrating a comparison of coarsening of secondary α at (a) 850, (b) 900, (c) 925, (d) 950 and (e) 975.

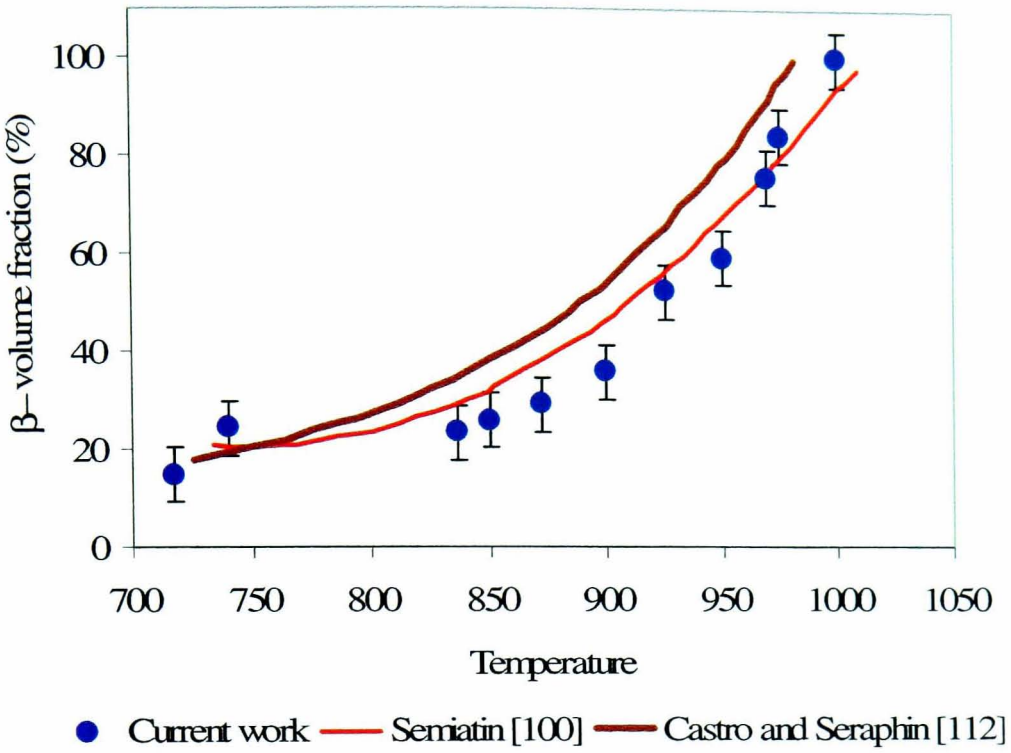

Figure 6.5: The β-approach curve of as-received Ti-6Al-4V.

6.1.1 Microstructure evolution during isothermal forging

In this subsection, the microstructure evolution of the as-received globular Ti-6Al-4V during hot isothermal forging is further discussed. The influence of forging parameters (strain, strain rate and temperature) on morphological changes in the primary α phase are investigated quantitatively. Microstructures developed prior to deformation are also shown for comparison purposes.

6.1.1.1. The effect of strain

An example of the microstructure developed during isothermal forging of the globular starting material at 950°C and 0.01/s is illustrated in Figure 6.6. A series of isothermal compression tests were performed and interrupted at strain levels of 0.03, 0.1, 0.5 and 1.0 in order to assess the effect of strain on microstructure evolution. Deformed specimens were water quenched immediately upon cessation of the tests. The effect of higher strain ($\varepsilon > 1$) on primary α morphology was also investigated by capturing additional micrographs in various regions. These were located along the central radial line of the deformed cylindrical specimens (at 0mm, 3mm and 6mm from the cylinder axis) and at a point on the axis one third of the final height from the top of the specimen. Micrographs were recorded by scanning electron microscopy under backscattered mode to give better contrast between the α and β phases.

Distribution of local strain within the specimen was estimated by using the large strain, rigid-viscoplastic finite element code DEFORM 2D. Input data included the specimen geometry, strain rates, and test temperatures, flow stress data corrected for adiabatic heating, thermo-physical properties of Ti-6Al-4V and the die material, and the value of the friction factor. The effective strain distribution within a cylindrical specimen deformed at 950°C and 0.01/s is shown in Figure 6.8. Local strains at pre-determined locations (one-third of final thickness (P1), centre (P2), 3mm (P3) and 6mm (P4) from centre) were found to be 1.06, 1.31, 1.26, and 1.12 respectively.

From Figure 6.6(a), the microstructure developed during pre-heating at 950°C prior to deformation, consists of a mixed structure of small numerous nearly globular α grains and some coarse elongated α grains. At lower strains (Figure 6.6.b-d), microstructures developed are still comparable to the pre-test microstructure. With increasing strain, the α grains exhibit a tendency to align in a direction perpendicular to the forging axis. At this stage, some of α grains have become deformed and reoriented (Figure 6.6.e). As strain proceeds further, it can be seen that most of the α grains have been flattened parallel to the direction of metal flow with a number of finer globular α grains evident in some regions (Figure 6.6.f). In more intensely deformed regions (Figure 6.7.a-c), there is a larger quantity of fine, nearly equi-axed primary α grains, characterised by well-defined grain boundaries interspersed between coarser grains and surrounded by the transformed β matrix.

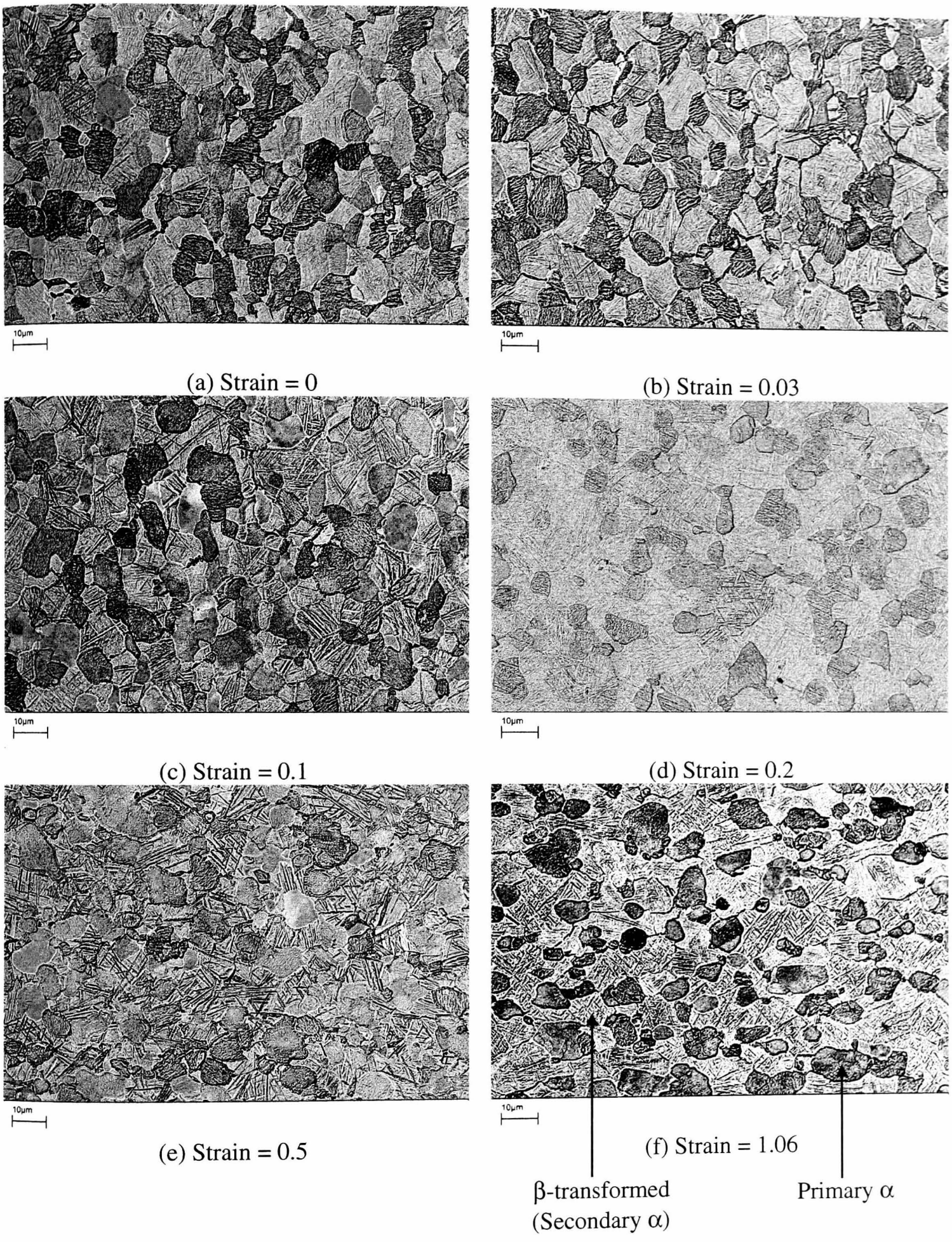

Figure 6.6: Microstructure development with strain during isothermal forging at 950°C and 0.01/s. Values of the total imposed strain were (a) 0 (pre-test/10 min soak at 950°C followed by water quenching); (b) 0.03; (c) 0.1; (d) 0.5; (e) 1.06. Forging axis is vertical direction.

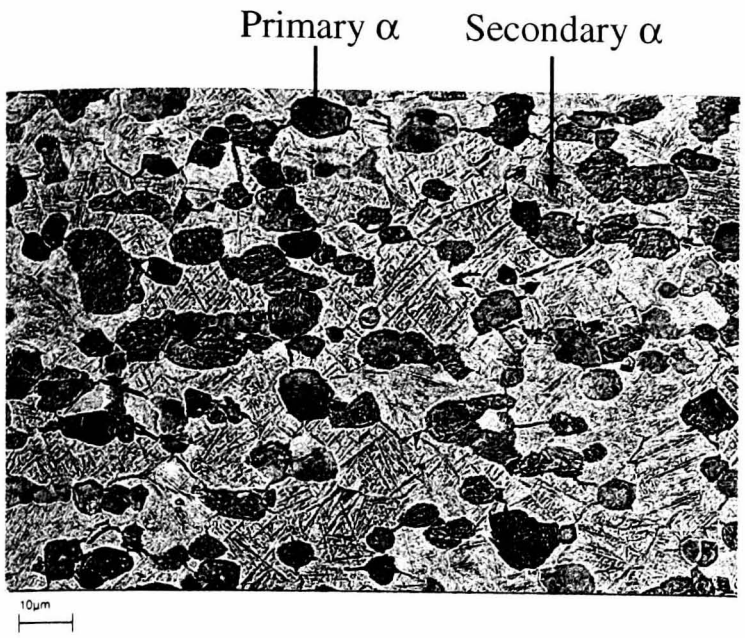

(a) Strain = 1.12

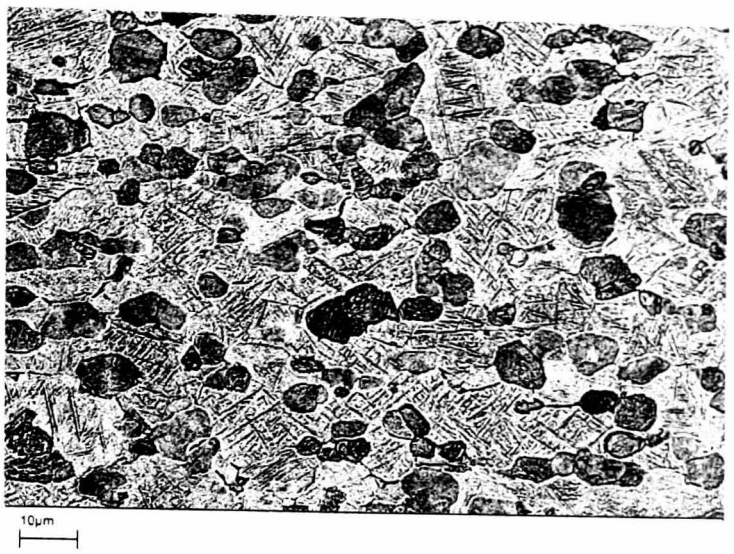

(b) Strain = 1.26

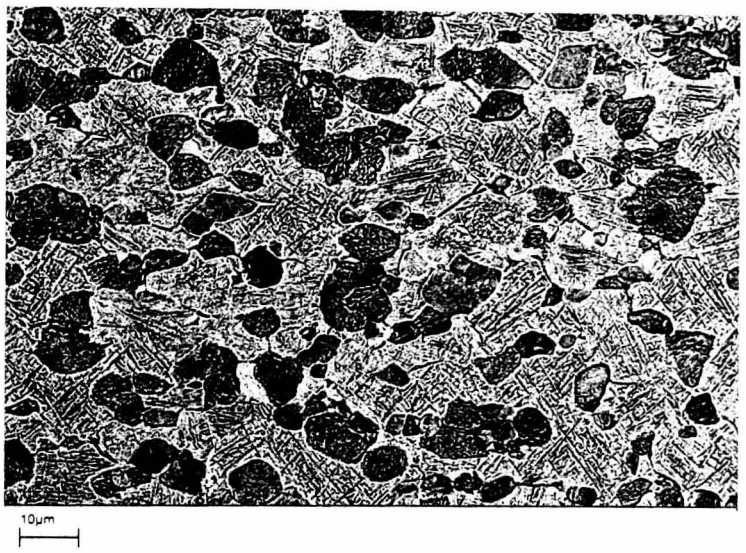

(c) Strain = 1.31

Figure 6.7: Microstructure development with strain during isothermal forging at 950°C and 0.01/s. Values of the total imposed strain were (a) 1.12 (6mm from centre); (b) 1.26 (3mm from centre); (c) 1.31 (centre). Forging axis is vertical.

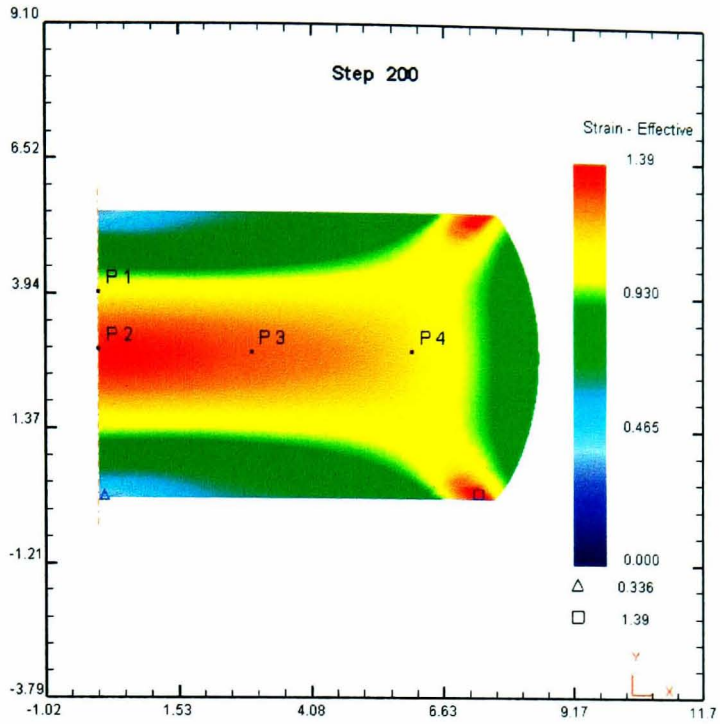

Figure 6.8: Effective strain distribution within cylindrical specimen deformed during isothermal forging at 950°C and 0.01/s.

The evolution of primary α grain size as a function of imposed strain is shown in Figure 6.9. It can be seen that, with increasing strain, the average grain size decreased significantly from 36.98μm^2 prior to deformation to 25.66μm^2 in the highest strain region, indicating that deformation has a refinement effect on the primary α phase.

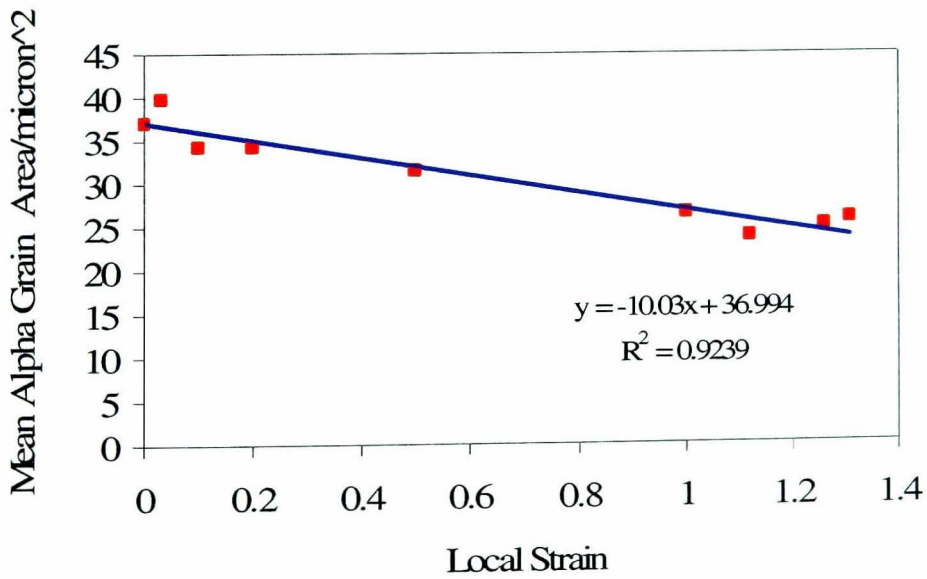

Figure 6.9: Grain size evolution as a function of strain during isothermal forging at 950°C and 0.01/s.

As can be seen from Figure 6.7.a-c, the elongated primary α structure may be 'pinched-off' during deformation, which leads the formation of finer and nearly equiaxed primary α structure. Closer examination of Figure 6.9 indicates that the grain size of the primary α phase may remain stable when the strain is greater than about 1. This may be attributed to the fact that the microstructure has reached a steady state condition, maintaining primary α grains size regardless of the imposed strain rate. There is a possibility that α grains undergo rotation beyond this point, behaving as hard inclusions rotated within a relatively soft β-phase matrix.

6.1.1.2. The effect of strain rate

The effect of strain rate on initially globular microstructures deformed to a strain of 1 was also investigated during isothermal forging at 950°C at various strain rates between 0.3-0.003/s as illustrated in Figure 6.10. The dependence of average α grain size on applied strain rate is shown in Figure 6.11. It appears that the effect of applied strain rate is negligibly small. With increasing strain rate, the mean grain sizes of primary α is statistically stable.

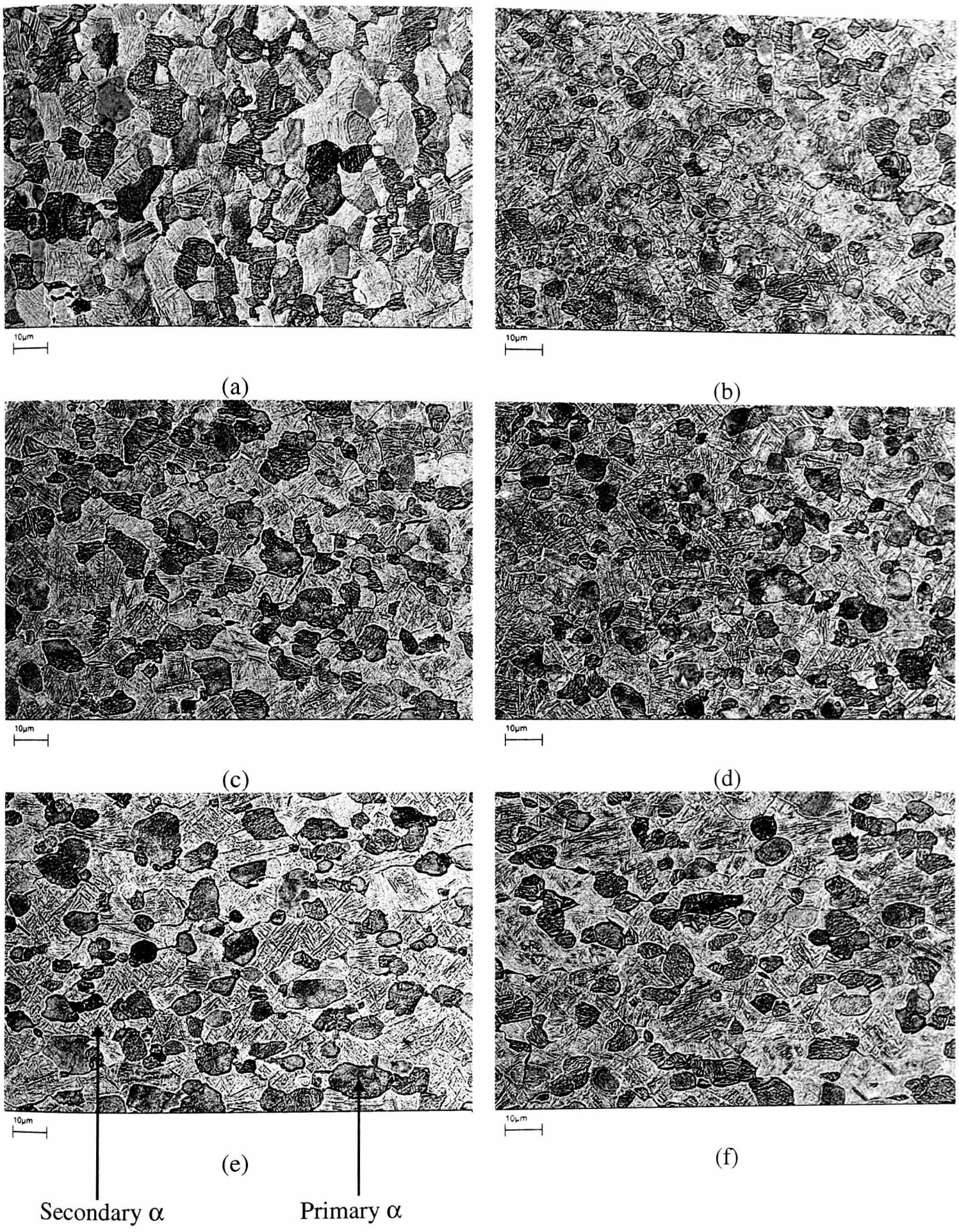

Figure 6.10: Microstructures of as-received Ti-6Al-4V followed by water quenching (a) after 10 min pre-test soak at 950°C and after isothermal forging at 950°C to a true strain of 1.0 for strain rates (b) 0.3/s; (c) 0.1/s; (d) 0.03/s; (e) 0.01/s and (f) 0.003/s. Forging axis is vertical direction.

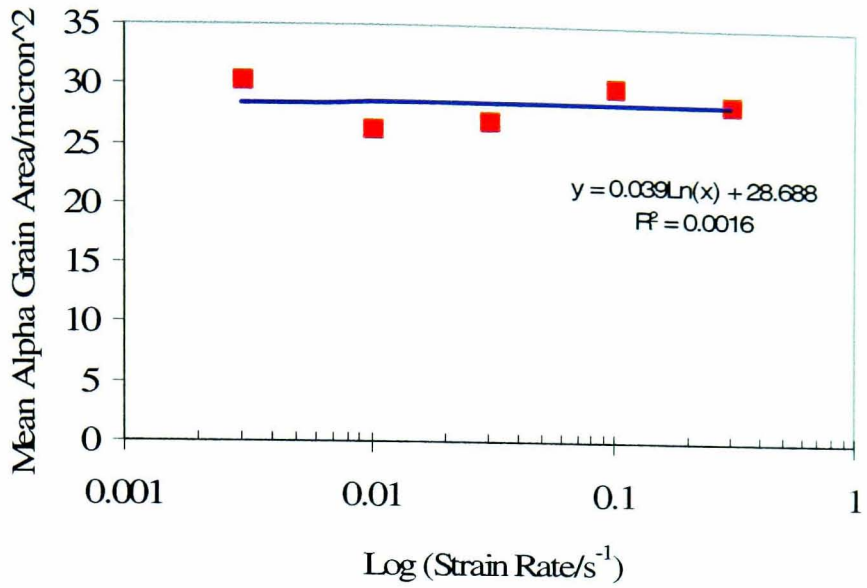

Figure 6.11: Variation of primary α grain size at various imposed strain rates during isothermal forging of Ti-6Al-4V with globular initial microstructure at 950°C and true strain of 1.

6.1.1.3. The effect of temperature

In order to characterise the microstructure development during isothermal forging, it is important to investigate the effects of temperature. Figure 6.12 show the microstructure changes of the as-received Ti-6Al-4V upon heating to sub-transus temperatures of 800, 900 and 950°C. Sections of the as-received materials were heat-treated at a rate 1°C/second to the temperatures then soaked for 10 minutes followed by water quenching. Microstructures developed by water quenching from 850°C and 900°C produced primary α phase within a discontinuous β matrix are illustrated in Figures 6.12.b and c. On the other hand, a duplex microstructure was produced upon water quenching from 950°C. The latter consists of a lower fraction of primary α embedded within a matrix of finer non-equilibrium supersaturated α (α′), produced by diffusionless transformation of the β phase.

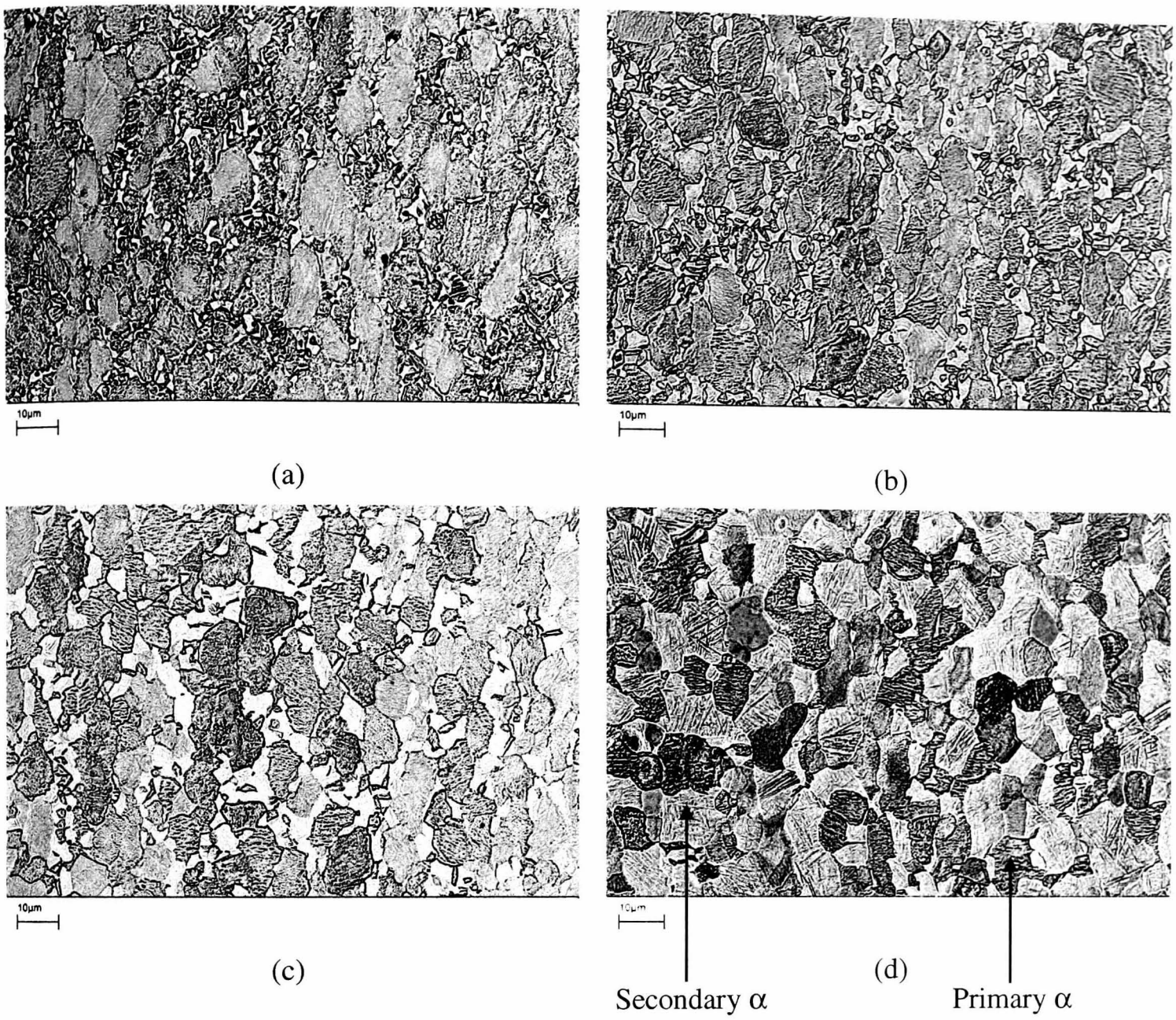

Figure 6.12: Illustration of microstructure changes of (a) as-received Ti-6Al-4V and after 10 minutes soak time followed by water quenching at temperatures (b) 850; (c) 900 and (d) 950°C.

The primary difference between microstructures at different temperatures is the volume fraction of primary α. From quantitative image analysis, the volume fraction of primary α decreases with increasing temperatures. The volume fraction of alpha was measured to be 73.1% at 850°C, 65.1% at 900°C and 49.2% at 950°C. The values of volume fraction derived in this way are comparable to those obtained during β transus determination, indicating that the microstructure has reached equilibrium after 10 minutes soak.

As temperature increases, more stored energy is available to drive diffusion and phase transformation thus decreasing the volume fraction of the α phase. The reduction in the amount of primary α also enables the β phase to grow as the temperature approaches the β-transus.

Figure 6.13 shows the influence of test temperatures on microstructure during isothermal forging at 0.01/s and strain of 1. From image analysis, the volume fraction of primary α decreases with increasing temperature being 72.5% at 850°C, 62.7% at 900°C and 47.2% at 950°C. It was found that there was no clear dependence of alpha grain size on temperature (Figure 6.14).

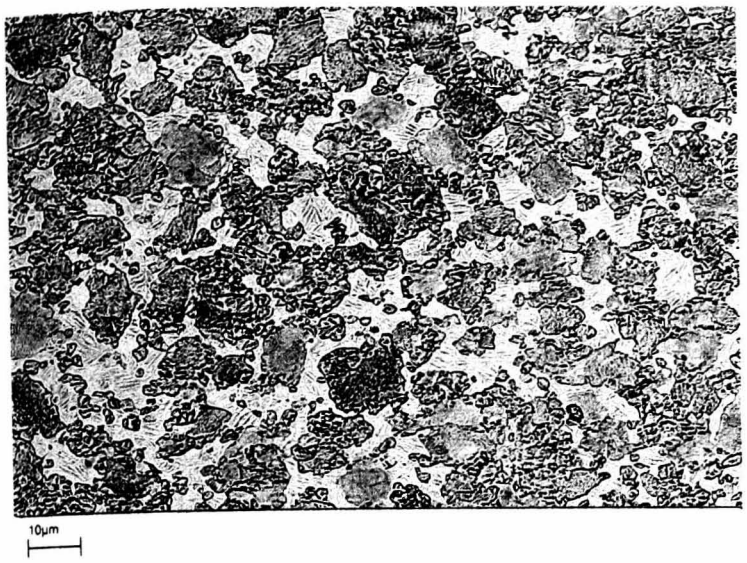

(a)

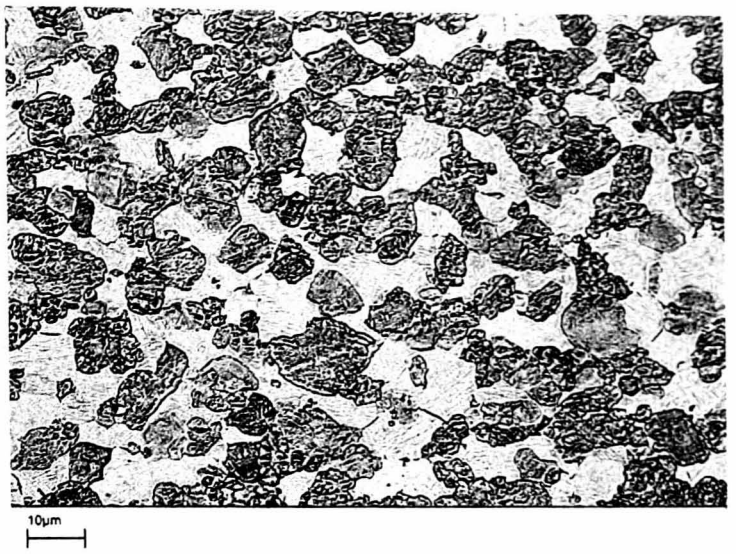

(b)

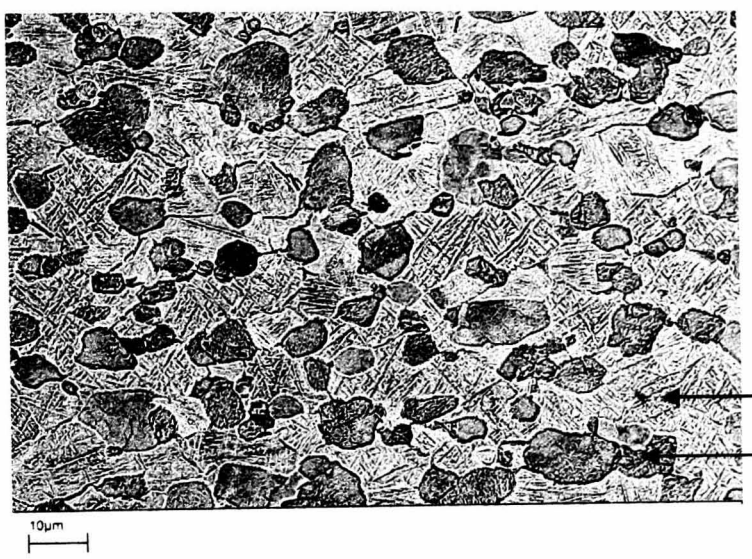

(c)

Figure 6.13: Microstructures of initially globular Ti-6Al-4V deformed to strain of 1 at strain rate 0.01/s and temperatures: (a) 850, (b) 900 and (c) 950°C. Forging axis is vertical.

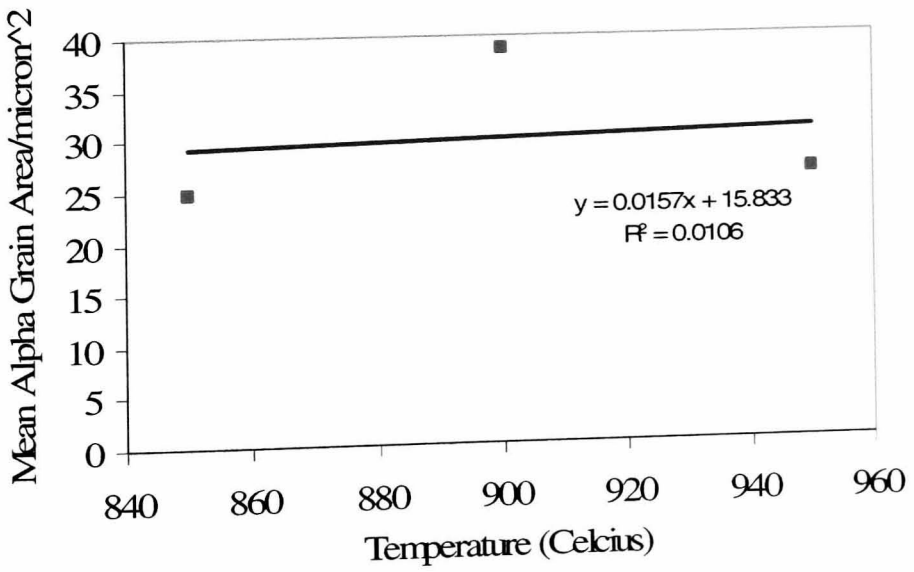

Figure 6.14: Variation of primary α grain size in Ti-6Al-4V with globular initial microstructure at various test temperatures during isothermal forging at 0.01/s to a true strain of 1.

6.2 Acicular initial microstructure

This section discusses the microstructure evolution of heat-treated Ti-6Al-4V. The as-received material was subjected to heat treatment involving sub-transus and supertransus solutioning in order to obtain a transformed acicular microstructure. The effects of strain, strain rate and temperature on the microstructure evolution are described in order to provide insight into the morphological transformations affected by processing parameters during isothermal forging.

6.2.1 Starting microstructure

Cylindrical specimens of the as-received Ti-6Al-4V bar stock were heat-treated at a rate of 1°C/s to a sub-transus temperature of 950°C and held for 10 minutes, then raised to a super-transus temperature of 1050°C for 2 minutes, followed by water quenching as schematically illustrated in Figure 6.15. This heat treatment produces a transformed microstructure as shown in Figure 6.16.a, consisting of colonies of acicular (needle-like) α phase (Figure 6.16.b) with approximately 0.25µm-thick laths within coarse prior-beta grains of 300-400µm.

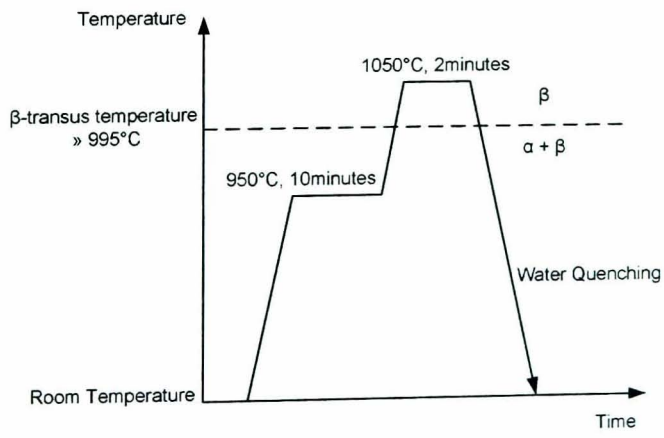

Figure 6.15: Schematic representation of the heat treatment used to obtain the transformed acicular microstructure.

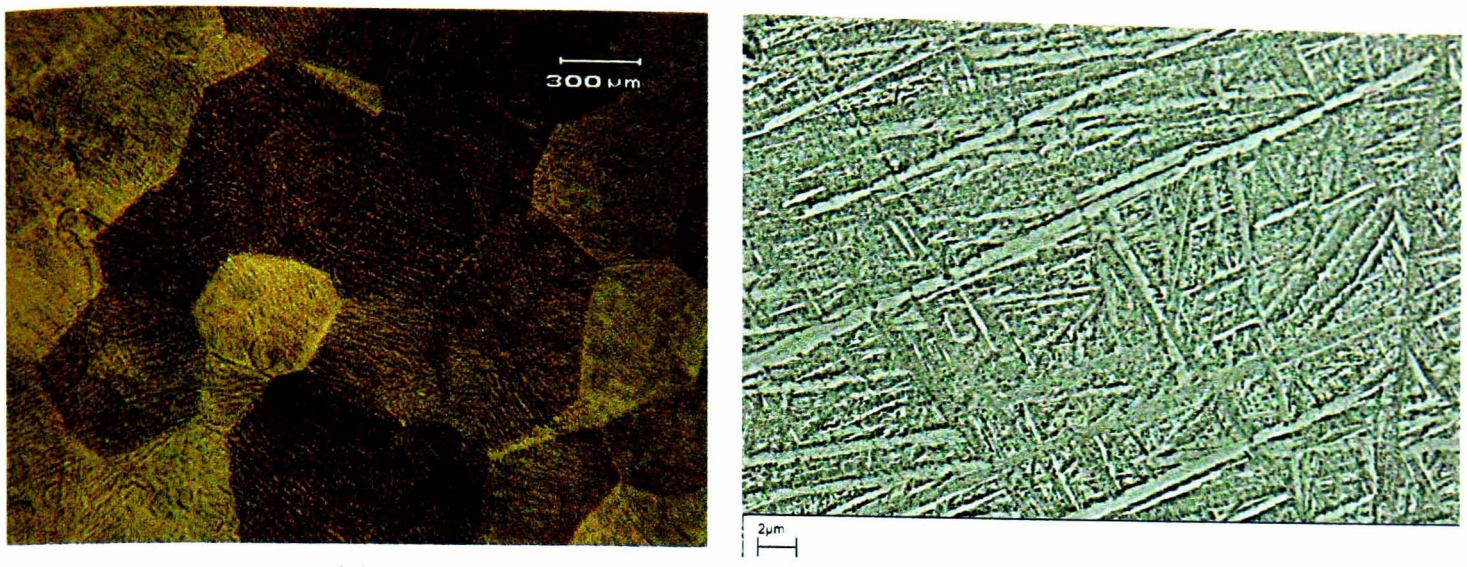

(a) (b)

Figure 6.16: Microstructures of as-received Ti-6Al-4V after heat treatment of 950°C/10min + 1050°C/2min followed by water quenching: (a) micrograph from optical microscopy; (b) backscattered SEM image.

6.2.2 Effect of soak temperature

Figure 6.17 illustrates the microstructural changes upon heating the initial acicular microstructure (Figure 6.17.a) from room temperature to test temperatures of 925, 950 and 975°C and soaking for 10 minutes. The heating rate applied was 1°C/s. Increasing the soaking temperature has a coarsening effect on the α laths. A lower aspect ratio of the α laths is also produced by a process of partial dissolution that becomes more dominant with increasing temperature. In addition, the spacing between the major axis of adjacent laths becomes larger to some extent. As soak temperature increases, more energy is stored as a driving force for the phase transformation, which leads to more dissolution of the α laths into the β phase. Hence, this eventually causes the reduction of α phase volume fraction.

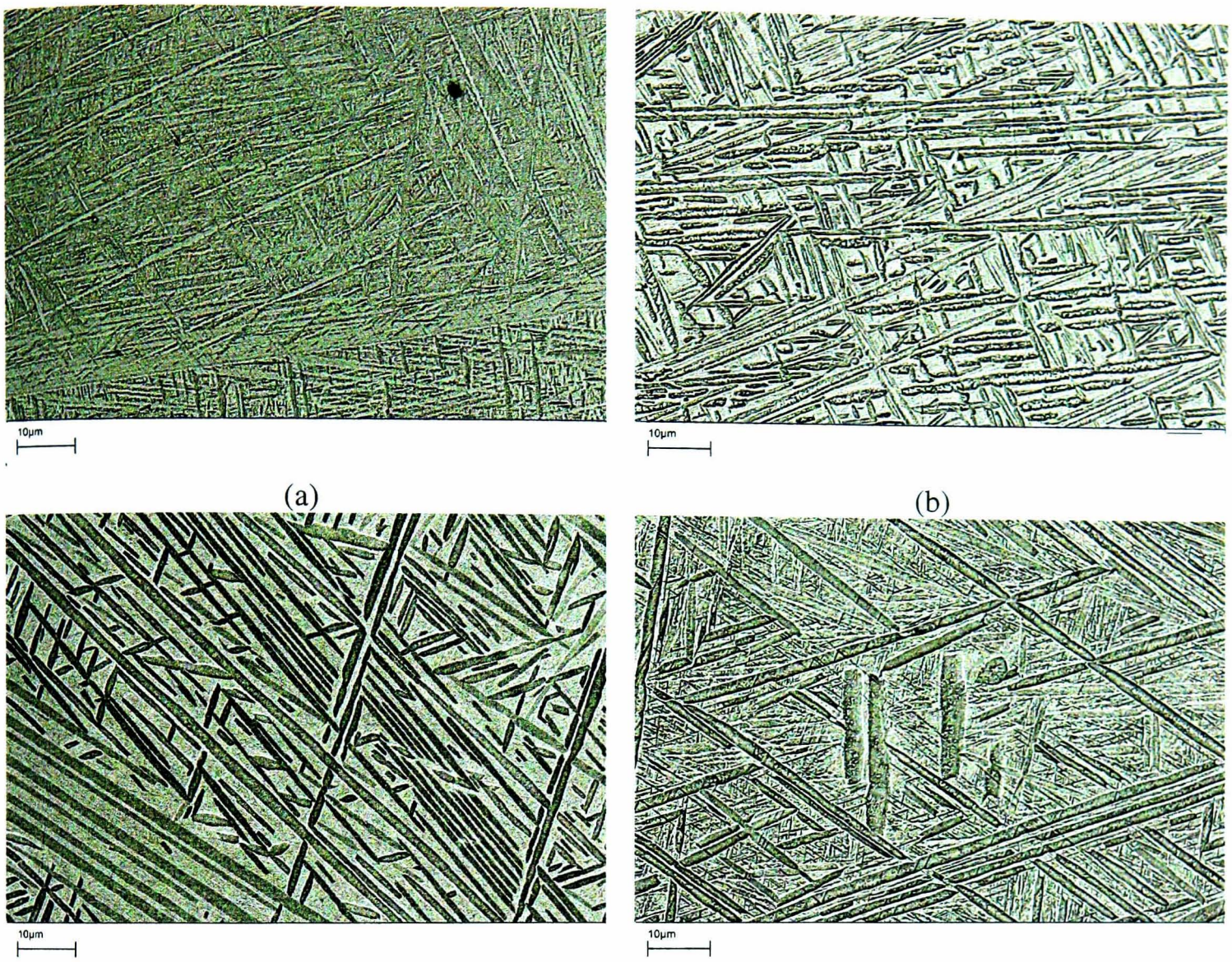

(a) (b)

(c) (d)

Figure 6.17: Illustration of microstructural changes of (a) starting microstructure and after 10 minutes soak time followed by water quenching at temperatures (b) 925; (c) 950; and (d) 975°C.

6.2.3 Microstructure evolution during isothermal forging at 950°C

In order to investigate the microstructure evolution during isothermal forging at 950°C, cylindrical samples were sectioned axially parallel to the forging axis and prepared by using standard metallographical procedures as outlined in Chapter 3. Micrographs were analysed using semi-automated image analysis software ImageTool [50] and ImageJ [49] for determination of microstructure (grain size, lath

width, aspect ratio) and volume fractions. From these measurements, plots of microstructure parameters versus effective strain predicted by finite element analysis were constructed.

6.2.3.1. The effect of strain

In this sub-section, the microstructure evolution during isothermal forging at 950°C was systematically studied with regard to its dependence on local strain. The microstructure observations showed that the break-up of the α lath structure occurred progressively with true strain. Microstructure evolution consisted of severe distortion, including bending and kinking of the laths and the formation of nearly globularised/equi-axed structure. The kinetics of these transformations depends on the deformation imposed and on the characteristics of the initial lath structure. As an example, microstructures illustrating the progress of the evolution of an α lath structure into a more globularised morphology at 950°C and 0.01/s are presented in Figure 6.18. Cylindrical specimens were forged to true strain values of 0.04, 0.1, 0.5 and 1.0. Additional observations of the microstructures were also recorded within various regions in the final deformed cylindrical specimen as a means of determining the microstructure developed at higher strain ($\varepsilon > 1$). The distribution of local strains and structural variable λ_{int} within these various locations were estimated by using finite element analysis, as illustrated in Figure 6.19. Local strains at pre-determined locations (one-third of final thickness (P1), centre (P2), 3mm (P3) and 6mm (P4) from centre) were 1.04, 1.69, 1.54, and 1.13 respectively. Backscattered scanning electron micrographs captured at these locations are shown in Figure 6.20.

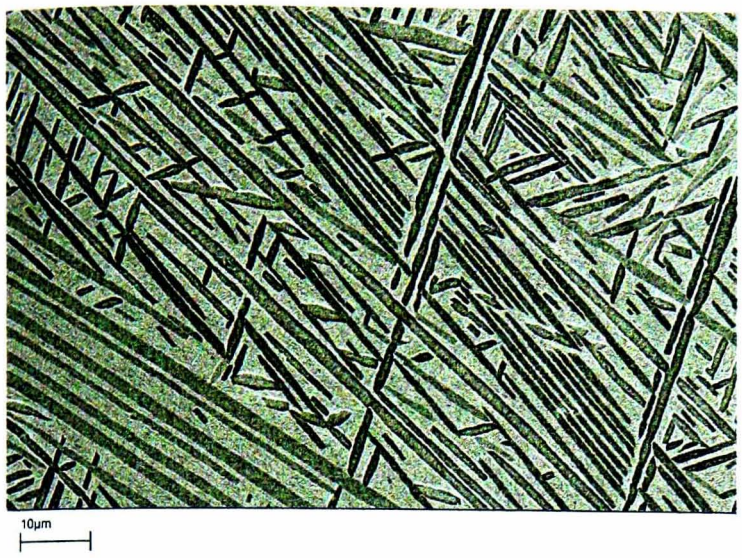

(a) Strain = 0

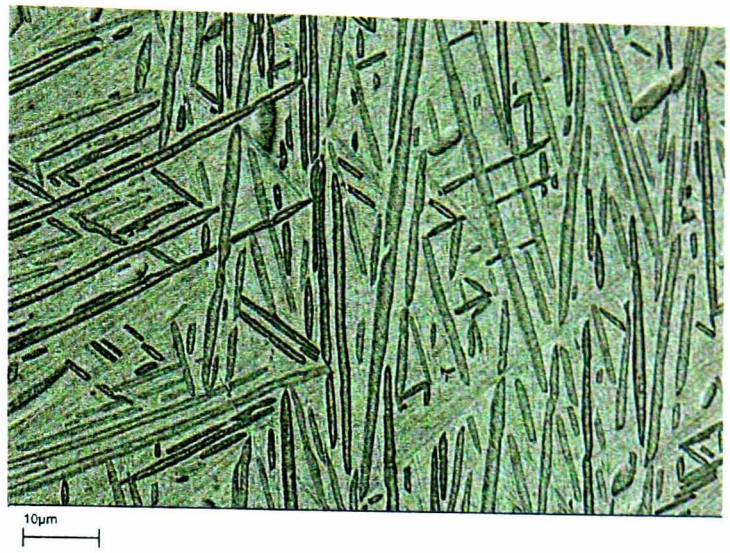

(b) Strain = 0.04

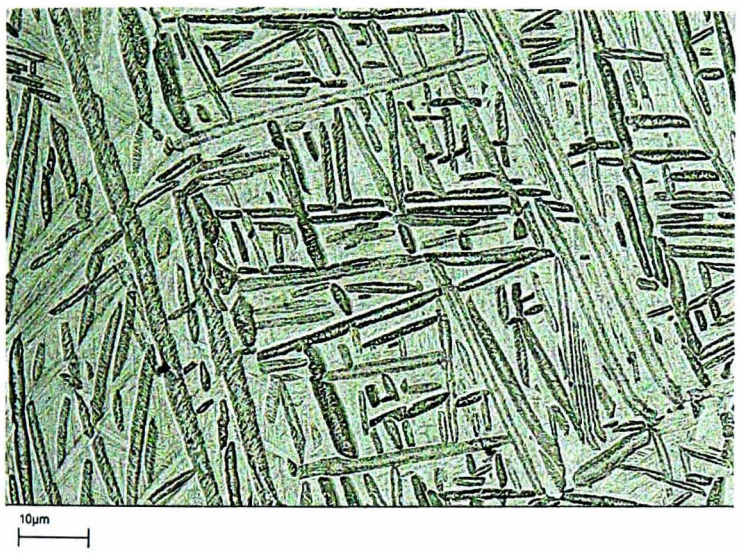

(c) Strain = 0.1

(d) Strain = 0.5

(e) Strain ≈ 1

Figure 6.18: Microstructure evolution with strain during isothermal forging of acicular Ti-6Al-4V at 950°C and 0.01/s. Values of the total imposed strain were (a) 0 (pre-test/10 min soak at 950°C followed by water quenching); (b) 0.04; (c) 0.1; (d) 0.5; (e) 1. Forging axis is vertical.

Figure 6.18(a) shows the microstructure prior to deformation, consisting of a mixture of low and high aspect ratio α-laths resulting from coarsening of the acicular α-phase during pre-heating. The α lath colonies appear to be oriented in a random manner throughout the prior β matrix. A significant number of α laths were noticed to be discontinuous or fragmented. Lath 'branching' was also observed in some regions. Overall, it is clear that the microstructure of deformed specimens exhibited significant changes in the α-phase morphology. At lower strain, the structure of the α phase already consists of a combination of undeformed and partially distorted laths with kinking and/or buckling occurring in some regions as shown in Figure 6.18 (d). At large strains, the α laths break up and transform the initial acicular morphology into a more globular, equi-axed structure (Figure 6.20.a-c).

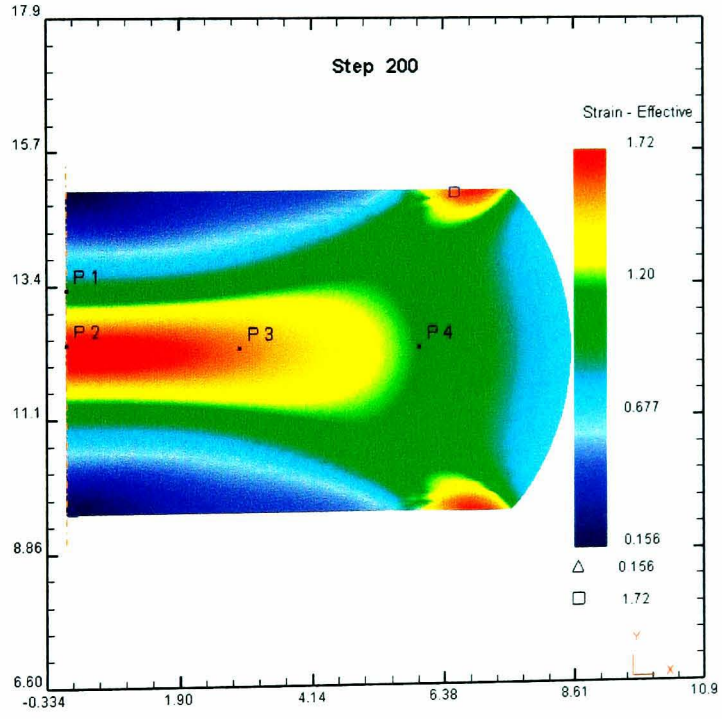

Figure 6.19: Local effective strain distribution within cylindrical specimen deformed during isothermal forging at 950°C and 0.01/s.

(a) Strain = 1.13

(b) Strain = 1.54

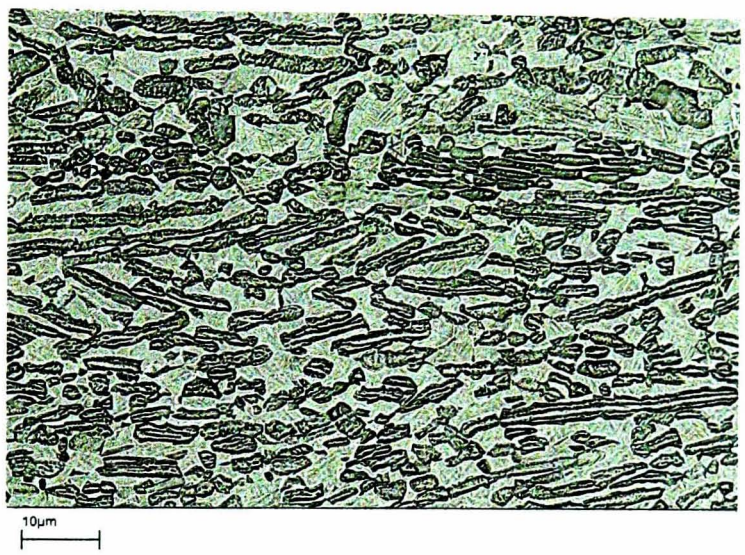

(c) Strain = 1.69

Figure 6.20: Microstructure development within cylindrical specimen of acicular Ti-6Al-4V after deformation at 950°C and 0.01/s. Values of the total imposed strain were (a) 1.13 (6mm from centre); (b) 1.54 (3mm from centre); (c) 1.69 (centre). Forging axis is vertical.

A possible mechanism for the break-up of α laths takes account of the fact that there are low and high angle boundaries between the various α laths with misorientation angles of varying magnitudes [111]. The β phase can penetrate into the α laths along the α/β interface or through the lath volume by diffusion of alloying elements such as aluminium and vanadium, the α and β stabilisers, respectively. If the α-lath width is small, separation of the laths can occur easily. Margolin and Cohen [112] have also proposed a model to describe the α globularisation process during hot working

or during heat treatment after hot working. The underlying mechanisms are schematically illustrated in Figure 6.21. The untransformed/unrecrystallised α laths (α_u) are shown in Figure 6.21.a. During the initial stage of globularisation (Figure 6.21.b), recrystallised α grains (α_R) grow across the α laths resulting in α/α boundaries which meet the β phase boundary. However, the existence of a 180° dihedral angle between α/α and β boundaries is inhibited due to surface tension requirements. Hence, the required dihedral angle is driven by the movement of some β phase into the α/β boundary simultaneously with the rotation of the α/β boundaries toward one another (Figure 6.21.c). This rotation induces an increased recrystallised grain size compared to the original lath width. This, in turn, permits the recrystallised grains to be in contact with the surrounding, unrecrystallised, α laths. Growth of these new grains continuous into the adjacent α, as shown in Figure 6.21.d.

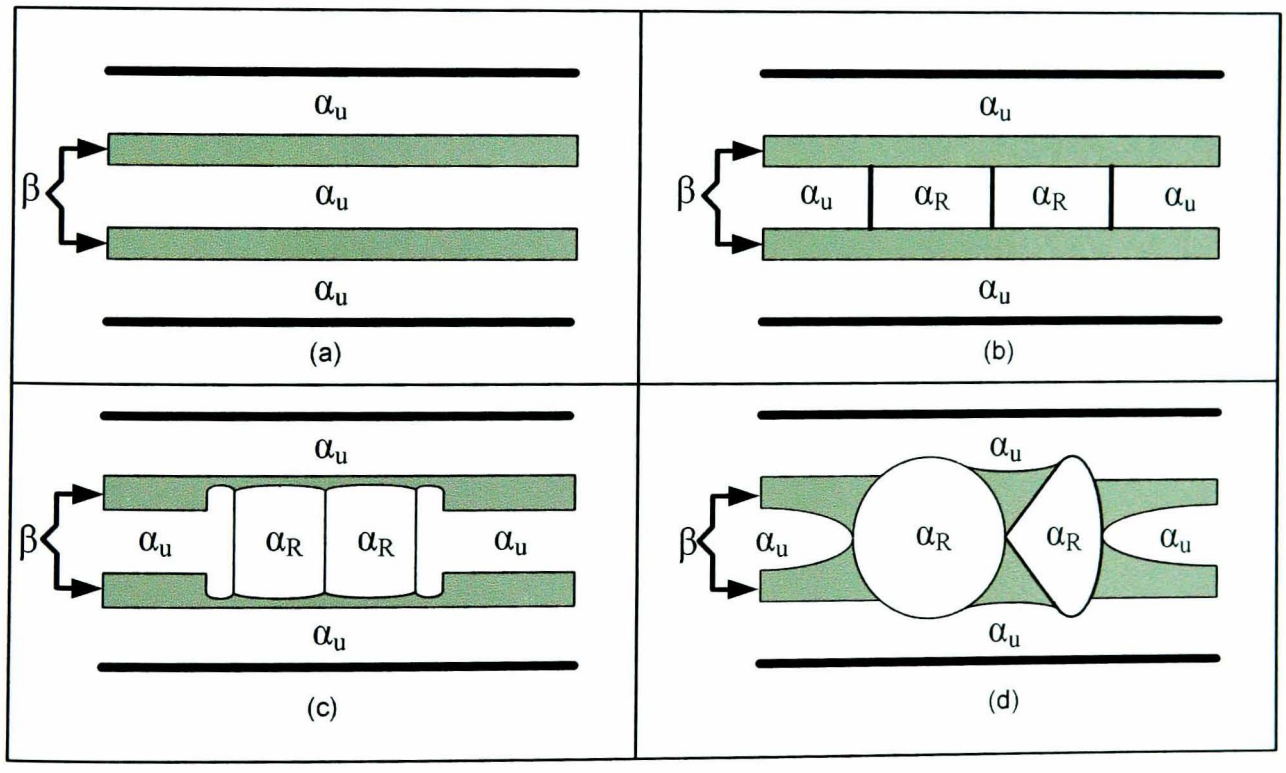

Figure 6.21: A schematic diagram of the mechanism of globularisation of α laths [112].

The nucleation sites and clearer appearance of the globularised α grains produced from the break-up process of α lamellae is shown in Figure 6.22. In certain regions it can be seen that the lath structures have become fragmented, transforming the lamellar structure into a nearly equi-axed morphology through the process of boundary splitting and edge spheroidisation. The diameter of the newly globularised structure is seen to be almost equal to the width of original laths. Stress concentration within certain regions might also speed up the globularisation process. Also non-uniform distribution of deformation exists, due to deformation incompatibilities between the colony of hard α laths within the surrounding soft β matrix.

(a) Strain = 1.11

(b) Strain = 1.53

(c) Strain = 1.7

Figure 6.22: Gobularisation of α laths during deformation at 950°C and 0.01/s.

The modified iso-strain approach employed within this thesis is intended to take account of interaction mechanisms, achieved using an internal state-variable which acts in parallel with the pure iso-strain approach (Eq. 5.3.3). This modification allows for possible additional strain, which might be induced due to boundary/interface sliding or deformation incompatibility occurring between the hard α and soft β-phases during hot deformation.

Transformation of α laths is also affected by their relative orientation with respect to the material flow and forging direction. The largest degree of deformation will be imposed on α laths that lie perpendicular to the material flow. Such laths can undergo bending, kinking and stretching along the flow direction. The α laths that are distributed parallel to the direction of metal flow develop a thinner, more elongated morphology. From image analysis, the orientation distribution of the α lath major axis with respect to the forging axis can be constructed quantitatively to clarify this observation. Here, the angle of the lath major axis is determined and plotted with respect to an axis *perpendicular* to the forging direction (0° is taken as parallel to the material flow and perpendicular to the forging direction; 90° is parallel to the forging direction). The frequency distribution of the α-lath orientation at various strain levels during isothermal forging at 950°C and 0.01/s is summarised in Figure 6.23. Prior to testing, the laths were distributed predominantly in a random orientation varying between -50° to 80° with respect to the nominal direction of metal flow. From Figure 6.23, the orientation of α laths displayed a positive skew distribution at low strains. As strain increases, the distribution of α laths shifts toward a nearly Gaussian distribution around 0° (Figure 6.23.c and d). At higher strain, it can be seen that most

of the α laths have become favourably orientated within a small angle of the nominal direction of material flow. In other words, the laths have become aligned perpendicular to the forging direction, suggesting that the lath structures may have undergone rigid-body rotation during deformation.

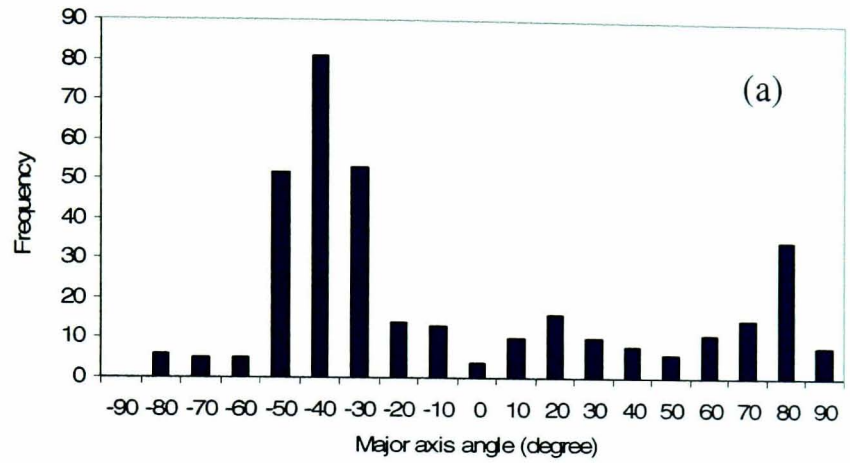

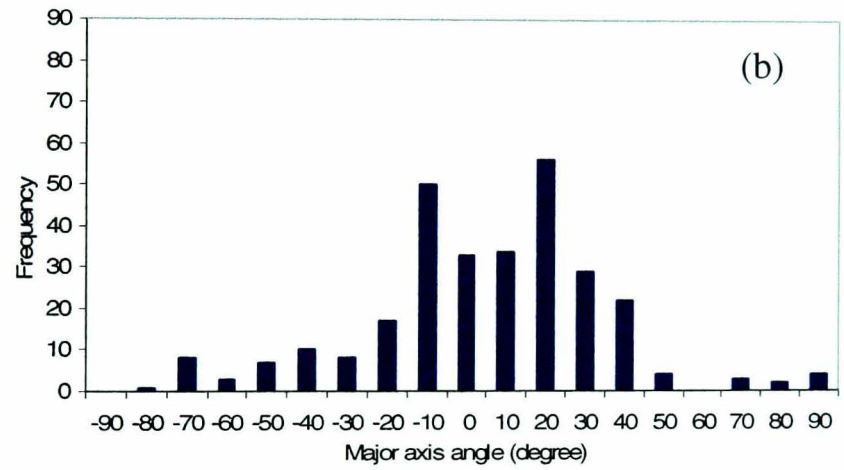

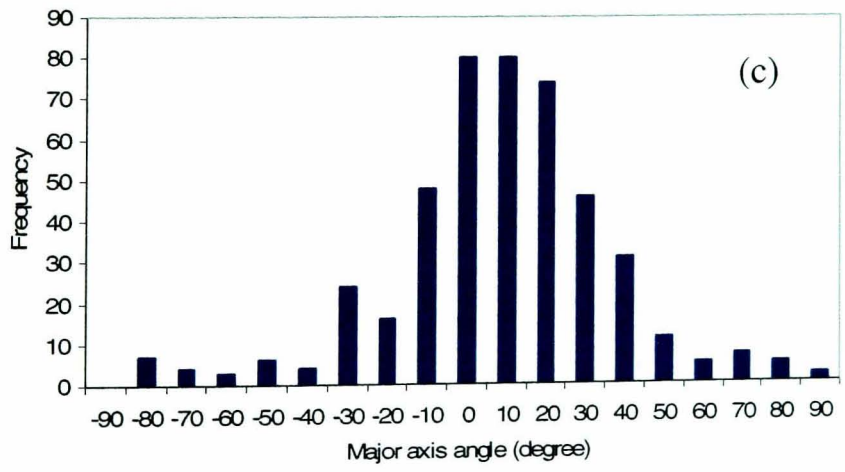

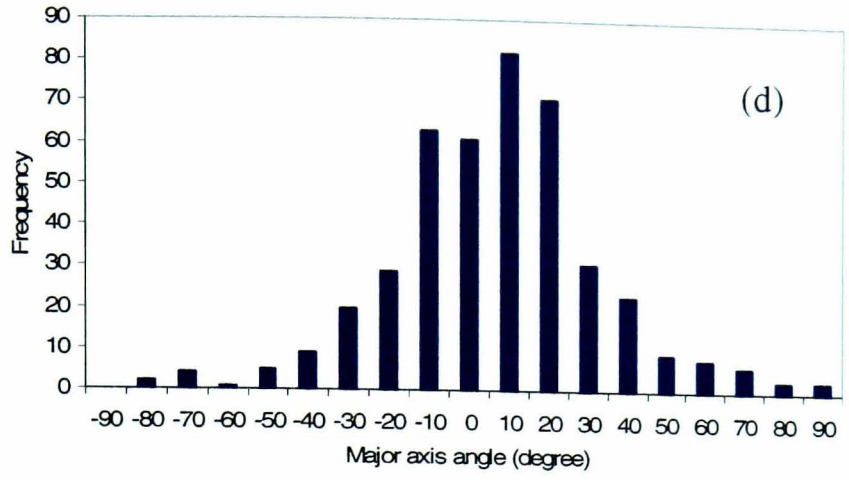

Figure 6.23: Distribution of α laths with respect to the axis perpendicular to the forging direction at 950°C and 0.01/s for strains of (a) 0, (b) 1.11, (c) 1.53, (d) 1.7.

Figure 6.24, 6.25 and 6.26 show other examples of microstructure evolution at 950°C for higher (0.3 and 0.03/s) and lower strain rates (0.003/s). For comparison purposes, the microstructure developed prior to deformation is re-displayed for each test condition. It can be seen that under all conditions the laths undergo significant distortion at some stage (Fig.6.24.b, 6.25.b, 6.26.b) involving bending, kinking and partial globularisation. A further increase in strain results in a significant change of their orientation with respect to the forging axis. In regions of highest local strain, most of α laths have become globularised and an almost complete transformation of the initial lamellar microstructure to an equi-axed one has taken place.

In order to describe the microstructure evolution quantitatively during isothermal forging at 950°C, comprehensive measurement of microstructure constituents were performed on microstructures (Figure 6.19,20 and 24-26) using quantitative image analysis. The results produced can be used to investigate the influence of local strain on the morphological changes in the α laths. Measured microstructure parameters included aspect ratio, area, and lath width. The aspect ratio of the α laths is one of the most important parameters influencing the mechanical properties of titanium

alloys [113-115]. Measurement of aspect ratio can provide insight into the degree of lath break-up, which in turn can usefully be used to quantify the degree of dynamic globularisation. In addition, microstructures consisting of predominantly of α-laths with a low aspect ratio exhibit increased ductility (at low temperatures), increased fatigue crack initiation resistance, and elevated temperature flow characteristics [111, 116]. The aspect ratio used here is defined as the ratio of the major axis (lath length) to the minor axis (lath width).

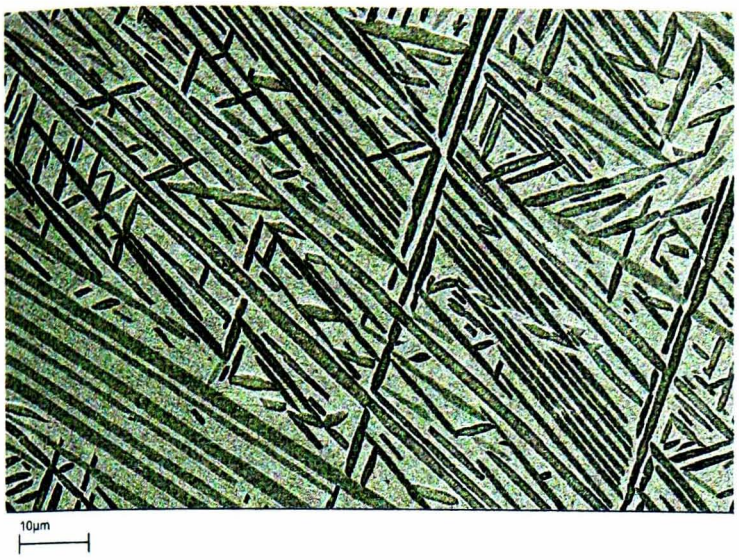

(a) Strain = 0

(b) Strain = 1.01

(c) Strain = 1.19

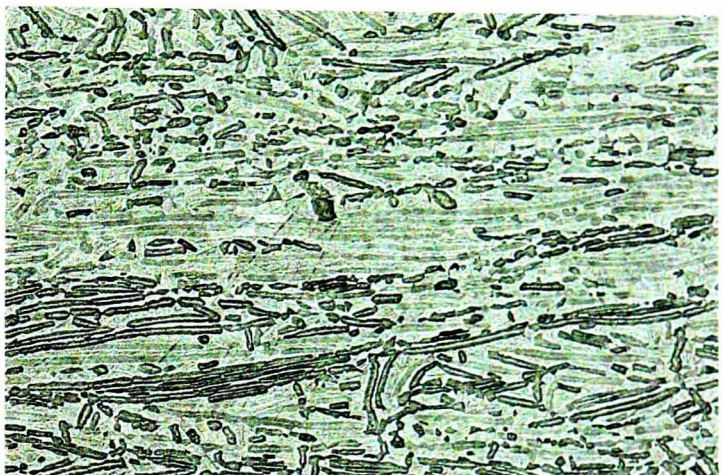

(d) Strain = 1.59

(e) Strain = 1.79

Figure 6.24: Microstructure evolution in acicular Ti-6Al-4V cylindrical specimens after (a) 10 min soak at 950°C followed by water quenching; and after isothermal forging at 0.3/s to (b) strain = 1.01 (one-third of final thickness); (c) strain = 1.19 (6mm from centre); (d) strain = 1.59 (3mm from centre); (e) strain = 1.79 (centre). Forging axis is vertical.

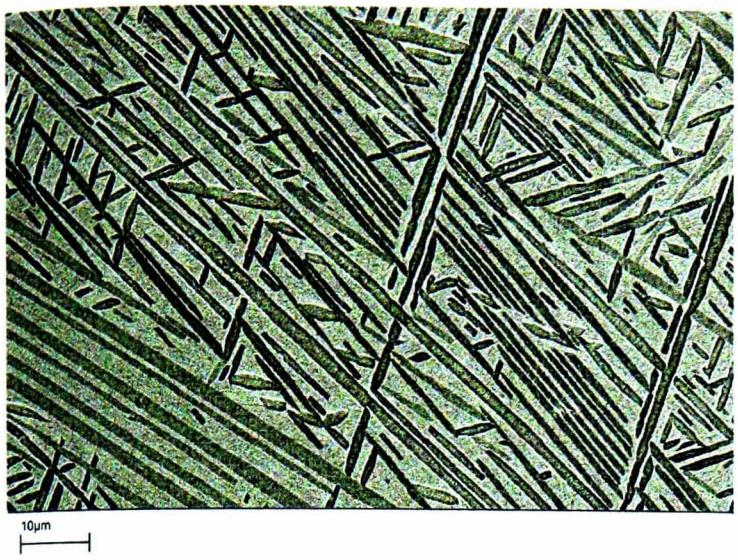

(a) Strain = 0

(b) Strain = 1.02

(c) Strain = 1.13

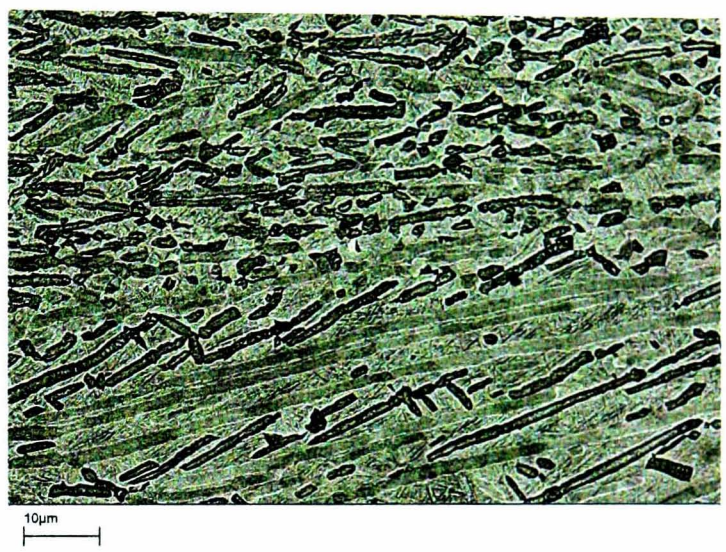

(d) Strain = 1.46

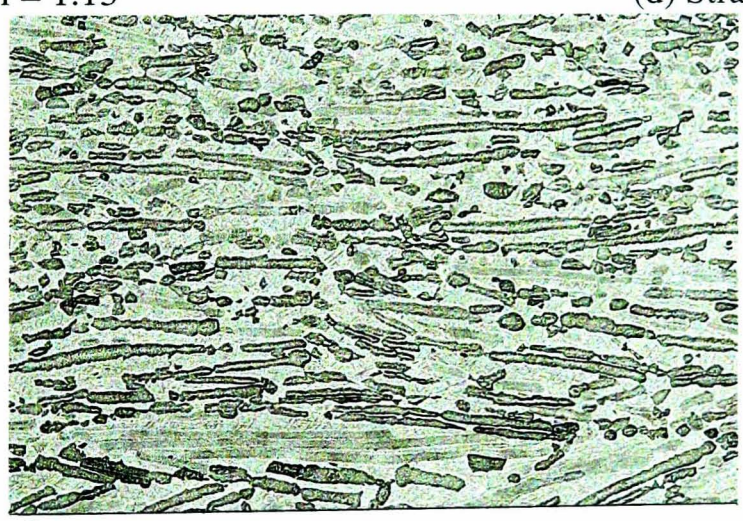

(e) Strain = 1.55

Figure 6.25: Microstructure evolution in acicular Ti-6Al-4V cylindrical specimens after (a) 10 min soak at 950°C followed by water quenching; and after isothermal forging at 0.03/s to (b) strain = 1.02 (one-third of final thickness); (c) strain = 1.13 (6mm from centre); (d) strain = 1.46 (3mm from centre); (e) strain = 1.55 (centre). Forging axis is vertical.

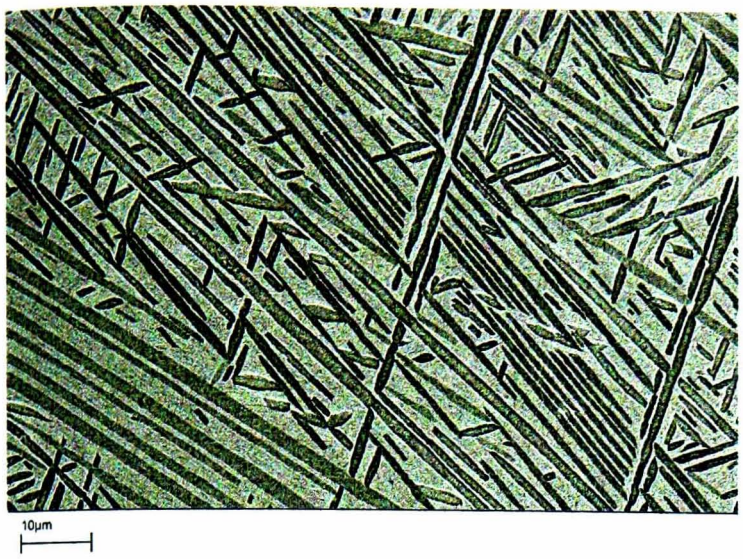

(a) Strain = 0

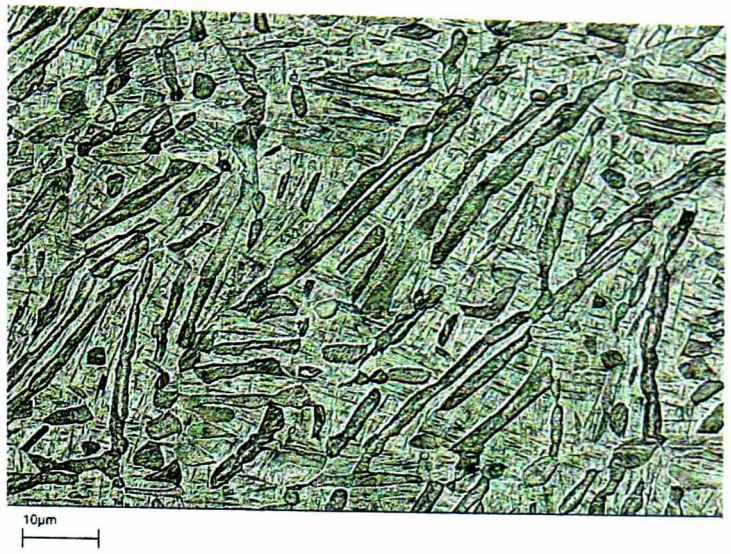

(b) Strain = 1.04

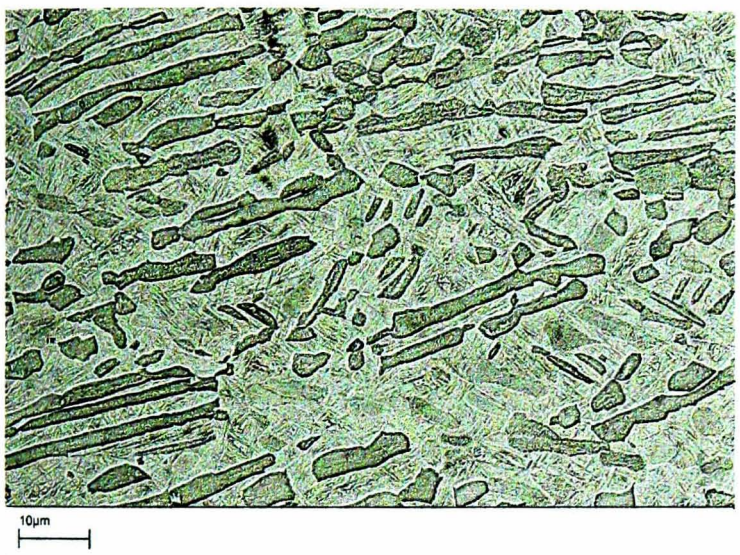

(c) Strain = 1.08

(d) Strain = 1.37

(e) Strain = 1.46

Figure 6.26: Microstructure evolution in acicular Ti-6Al-4V cylindrical specimens after (a) 10 min soak at 950°C followed by water quenching; and after isothermal forging at 0.003/s to (b) strain = 1.04 (one-third of final thickness); (c) strain = 1.08 (6mm from centre); (d) strain = 1.37 (3mm from centre); (e) strain = 1.46 (centre). Forging axis is vertical.

Another important microstructural parameter is the α-lath width. The lath width has a significant influence on mechanical properties of titanium alloys, including crack propagation resistance and toughness [117-119]. Hence, the effect of local strain on lath width was also measured during isothermal forging at 950°C. In addition, the lath perimeter was also quantified. Plots illustrating the effect of local strain on the evolution of the measured microstructure parameters during isothermal forging at 950°C at various strain rates are shown in Figure 6.27.

It is obvious that strain produces a refinement of the α-lath morphology. The average aspect ratio shows a gradual decrease from a value of about 6 prior to deformation to about 2.5 at the highest strain, reflecting the break-up of α laths as deformation proceeds.

Representative histograms showing the frequency distribution of the aspect ratio values of α laths measured pre-test (without deformation), at moderate strain (0.5), and at high strain (1.53 and 1.7) within cylindrical specimens deformed at 950°C and 0.01/s are presented in Figure 6.28. It can be seen that there is a shift from a positive skew-type distribution of aspect ratio values prior to deformation, towards a Gaussian distribution at the highest strain.

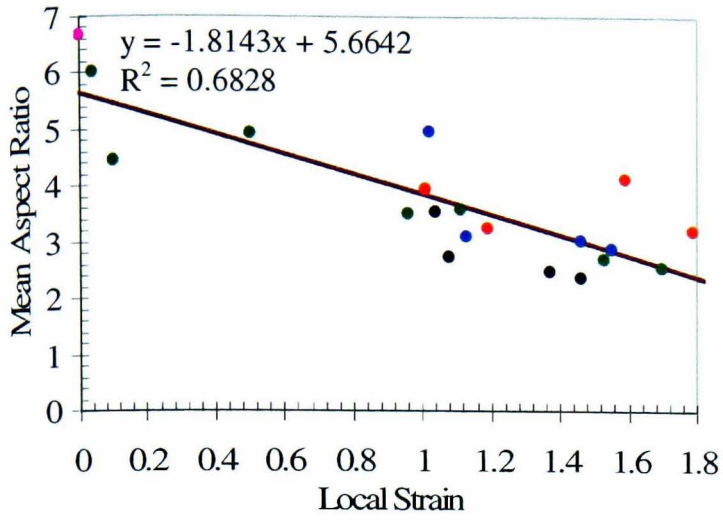

(a)

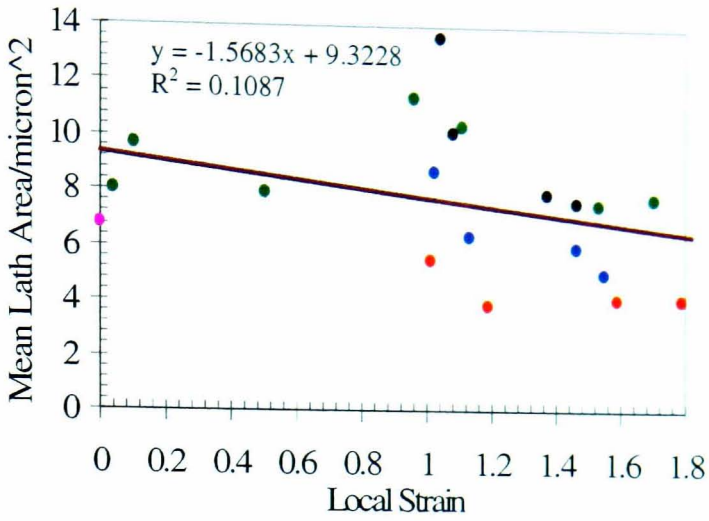

(b)

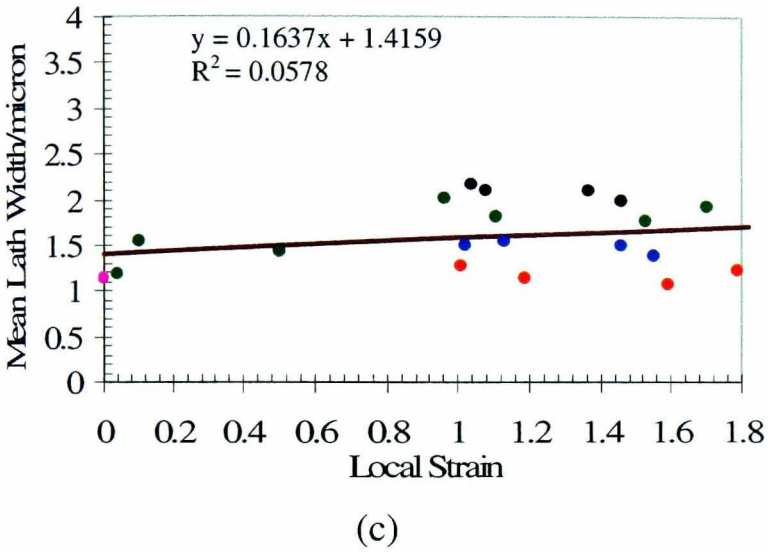

(c)

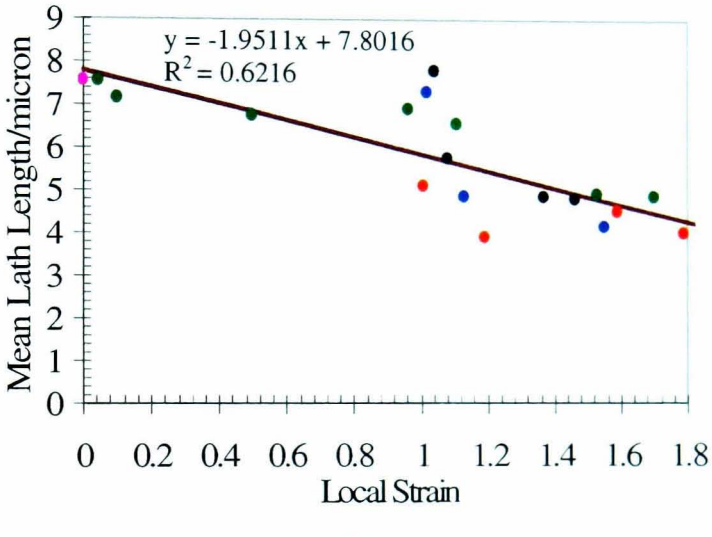

(d)

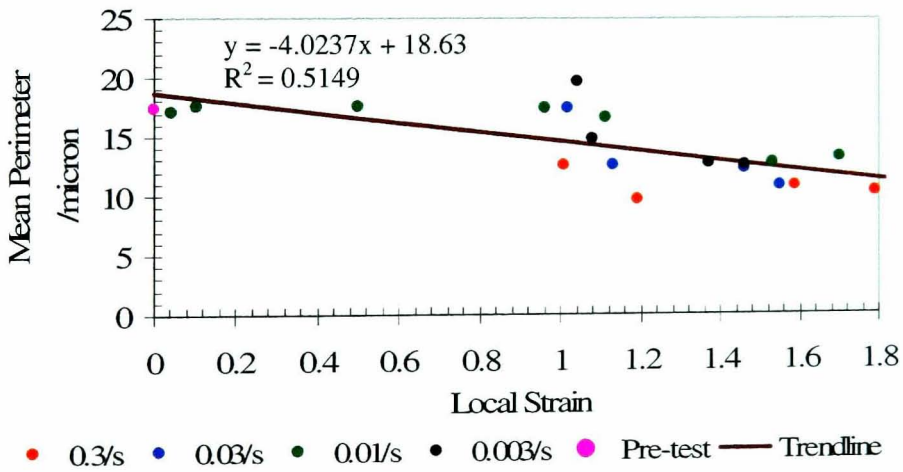

(e)

Figure 6.27: Plots of average values of a) aspect ratio, (b) lath area, (c) lath width, (d) lath length and (e) perimeter versus strain for isothermal forging of acicular Ti-6Al-4V at 950°C.

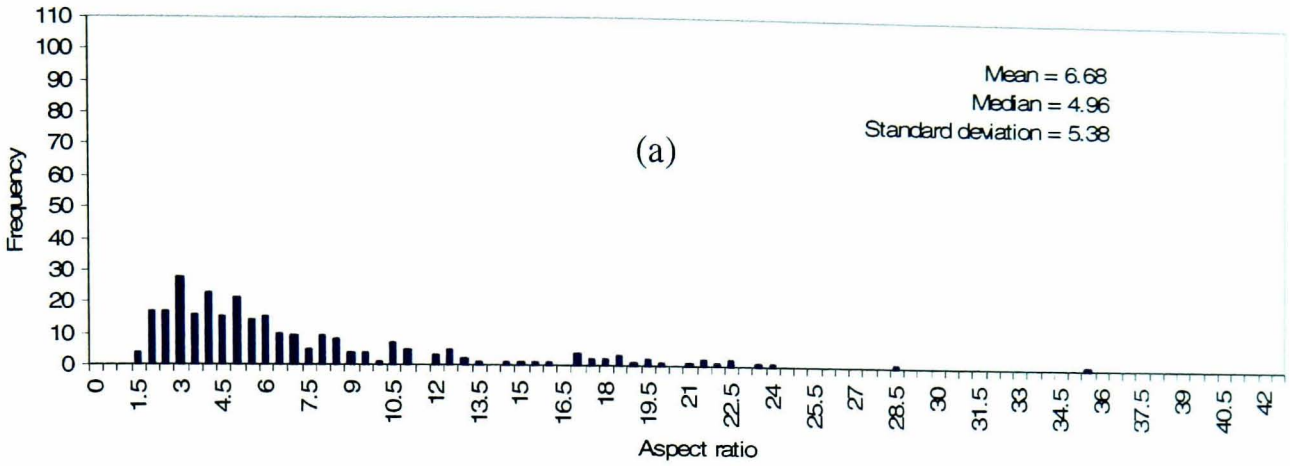

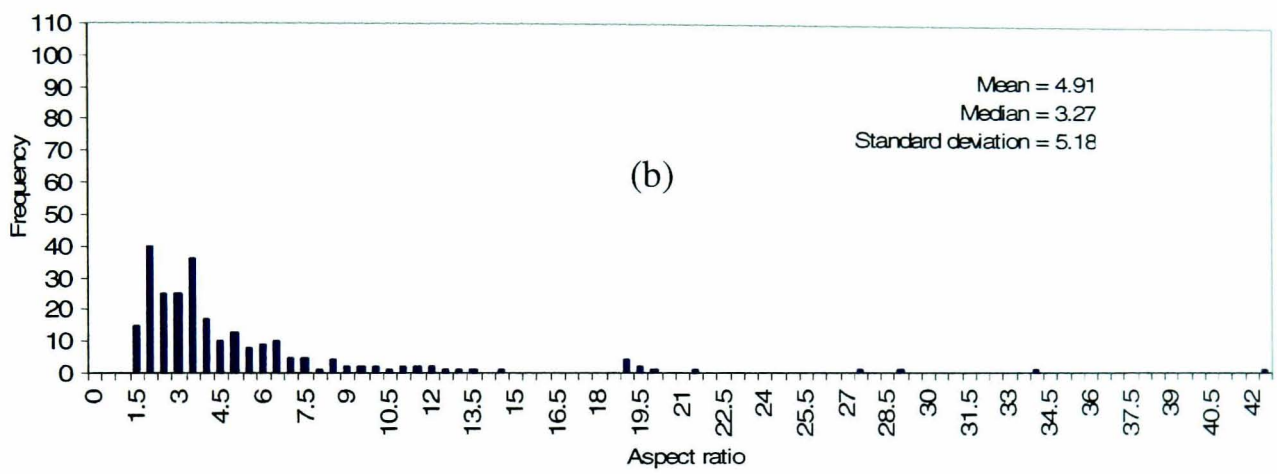

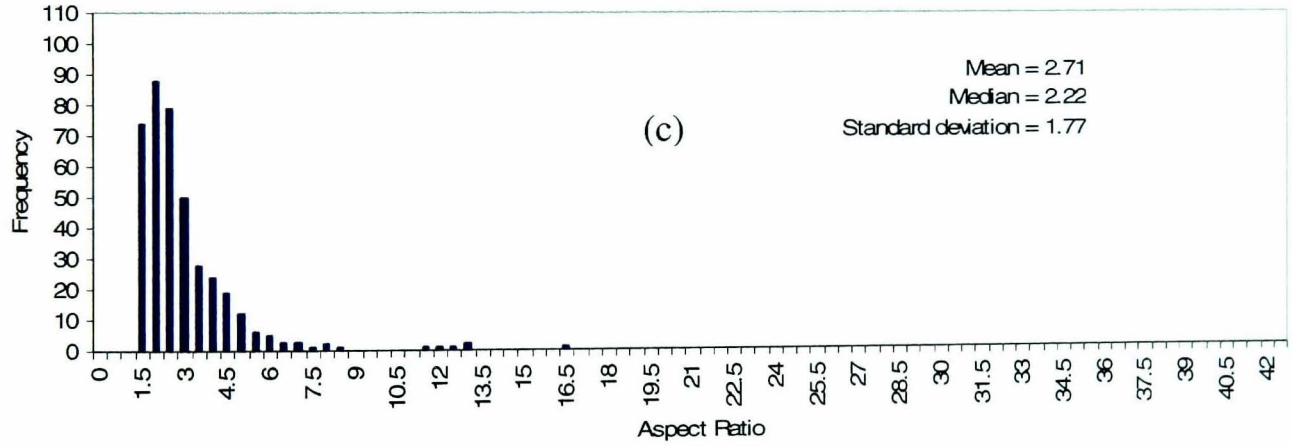

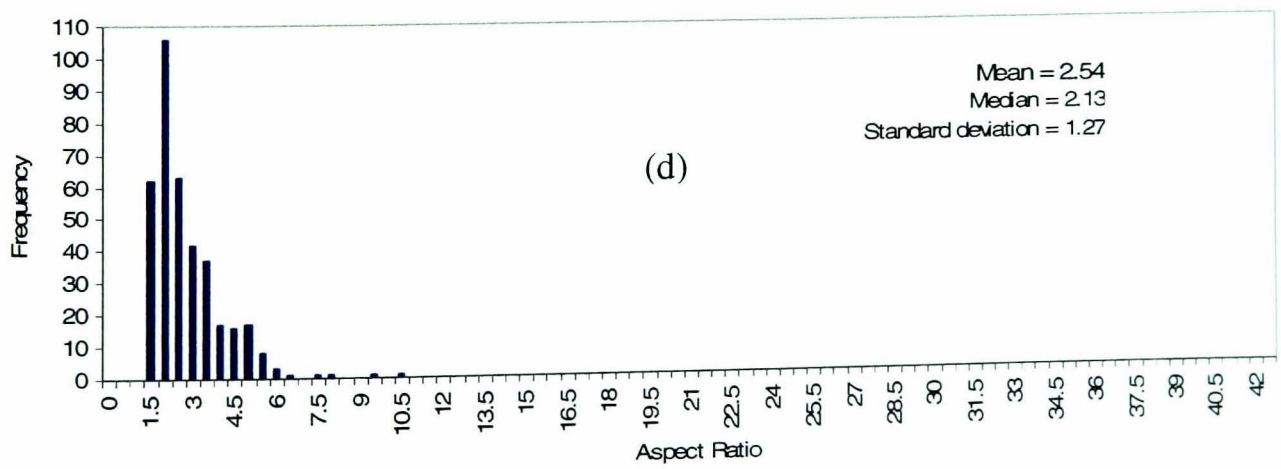

Figure 6.28: Frequency distribution of α laths aspect ratio during isothermal forging at 950°C and 0.01/s. (a) strain = 0; (b) strain = 0.5; (c) strain = 1.53; (d) strain = 1.7.

Measurement of aspect ratio also enables the degree of globularisation to be quantified. A globularised morphology was taken as that which has an alpha phase with an average aspect ratio of less than 2:1 [70]. For instance, the relationship between fraction globularised and local strain during isothermal forging at 950°C and 0.01/s is plotted in Figure 6.29. It can be seen that the volume fraction of globularised α phase increases with increasing strain. However, there is no evidence of significant globularisation occurring prior to the onset of the peak flow stress, or at a strain lower than 0.04.

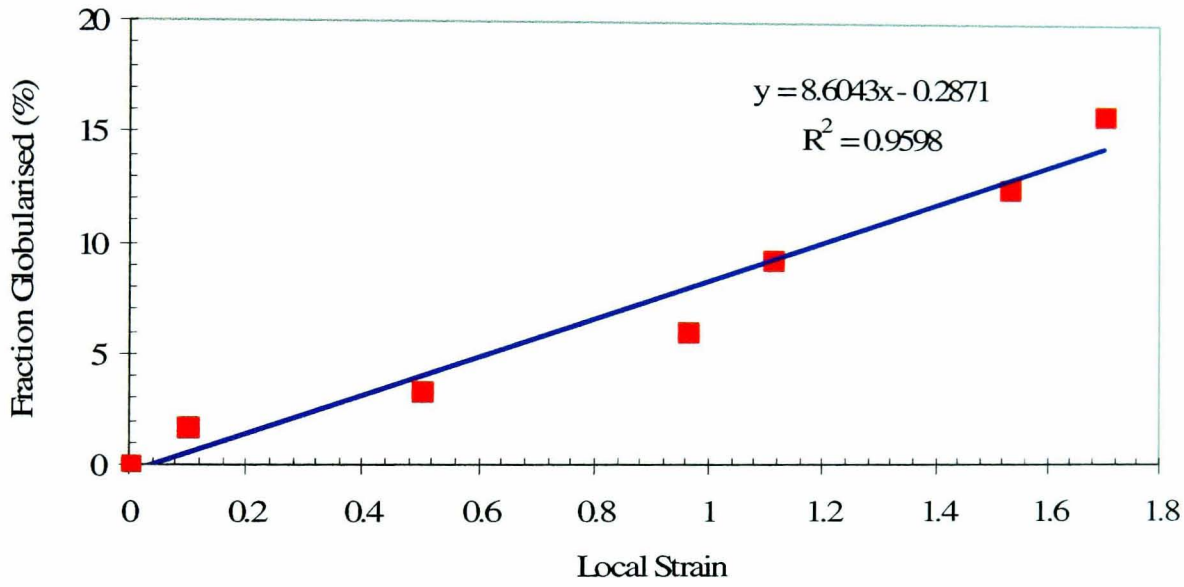

Figure 6.29: Dependence of the volume fraction of globularised α laths on local strain for isothermal forging at 950°C and 0.01/s

In addition, other lath parameters of area, length, and perimeter, also exhibited a tendency to decrease with increasing strain (Figure 6.27). In spite of the relatively weak strain-dependence of these measured microstructure parameters, the observations nevertheless provide a quantitative indication of the evolution of the initial lamellar structure into a globularised or lower aspect-ratio morphology. On the other hand, the average lath width, shown in Figure 6.27.c, appears to remain statistically stable for the whole range of strain rates investigated, although there is a

tendency towards a slight increase with strain. This may possibly be due to the complex relationship between the lath width and strain. According to R. Ding *et al*, the lath width is affected by various factors such as the initial size of the lath, local grain orientation, temperature, strain rate and even cross-section of the sample [78].

6.2.3.2. The effect of strain rate

Figure 6.30-6.32 illustrate the effect of strain rate on microstructure evolution at 925, 950 and 975°C. Backscattered electron images were captured at one-third of thickness of deformed cylindrical specimens, which represents an approximate local strain of 1. Strain rates imposed during isothermal forging were 0.3, 0.03 and 0.003/s. For comparison, the initial microstructure prior to deformation is also displayed for each temperature.

After deformation at the slowest strain rate (0.003/s) for all temperatures (925, 950 and 975°C) the volume fraction of the laths was reduced slightly, as compared to that at higher strain rates. This can be rationalised by considering that, at the slowest strain rate, there is more time for diffusion-controlled processes to take place, which leads to greater dissolution of the α phase in the β matrix. It also suggests that a degree of $\alpha \rightarrow \beta$ phase transformation can occur concurrently during hot deformation in the two-phase $\alpha + \beta$ phase regime. This tendency has also been observed previously [78, 120, 121].

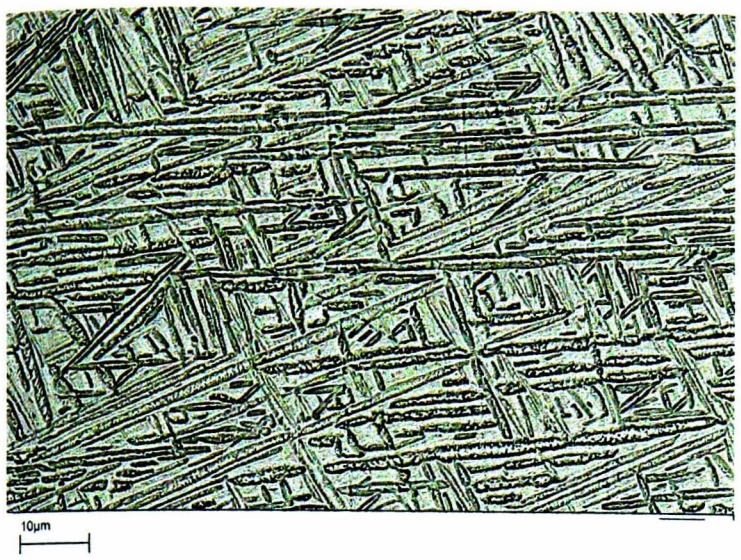

(a)

(b)

(c)

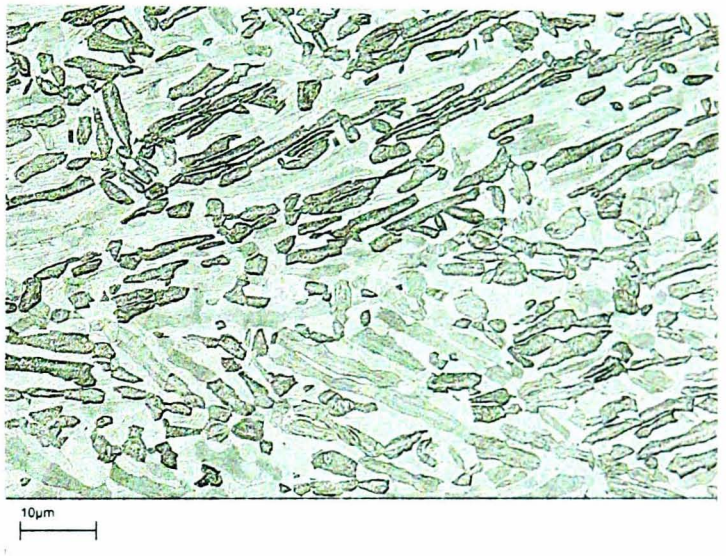

(d)

Figure 6.30: Microstructures of acicular Ti-6Al-4V (a) after 10 min pre-test soak at 925°C and after isothermal forging at 925°C to strain of 1.0 for strain rates (b) 0.3/s;(c) 0.03/s; and (d) 0.003/s. Forging axis is vertical.

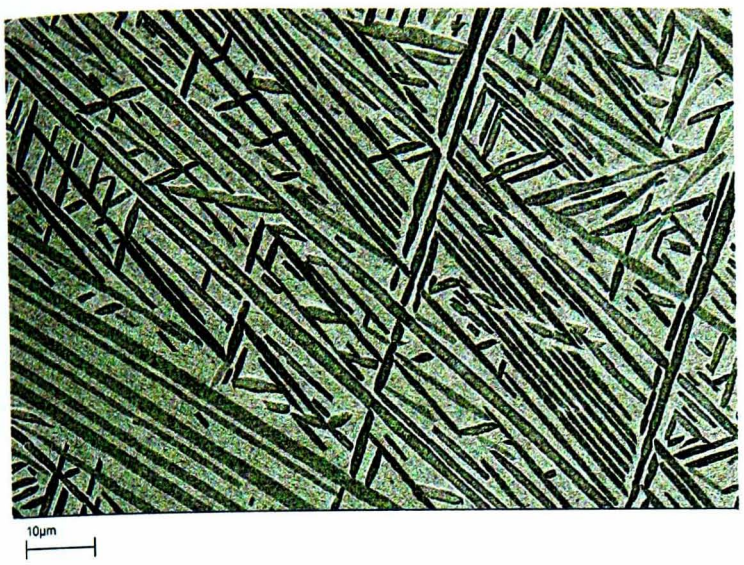

(a)

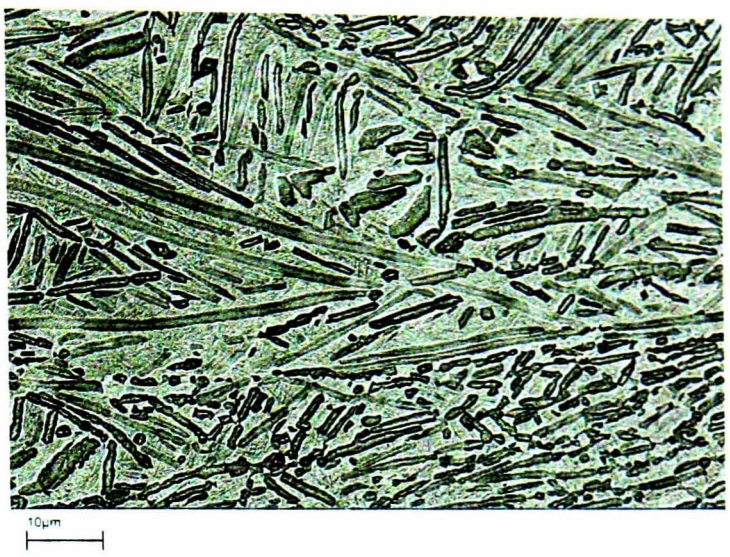

(b)

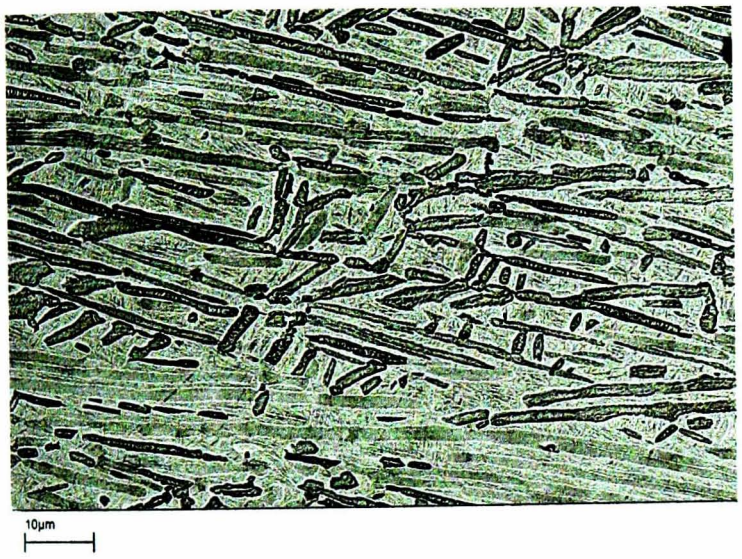

(c)

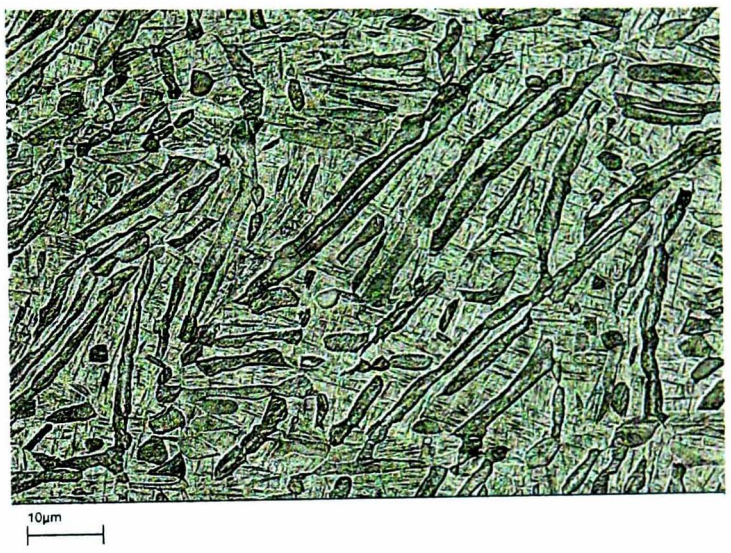

(d)

Figure 6.31: Microstructures of acicular Ti-6Al-4V (a) after 10 min pre-test soak at 950°C and after isothermal forging at 950°C to a true strain of 1.0 for strain rates (b) 0.3/s; (c) 0.03/s; and (d) 0.003/s. Forging axis is vertical direction.

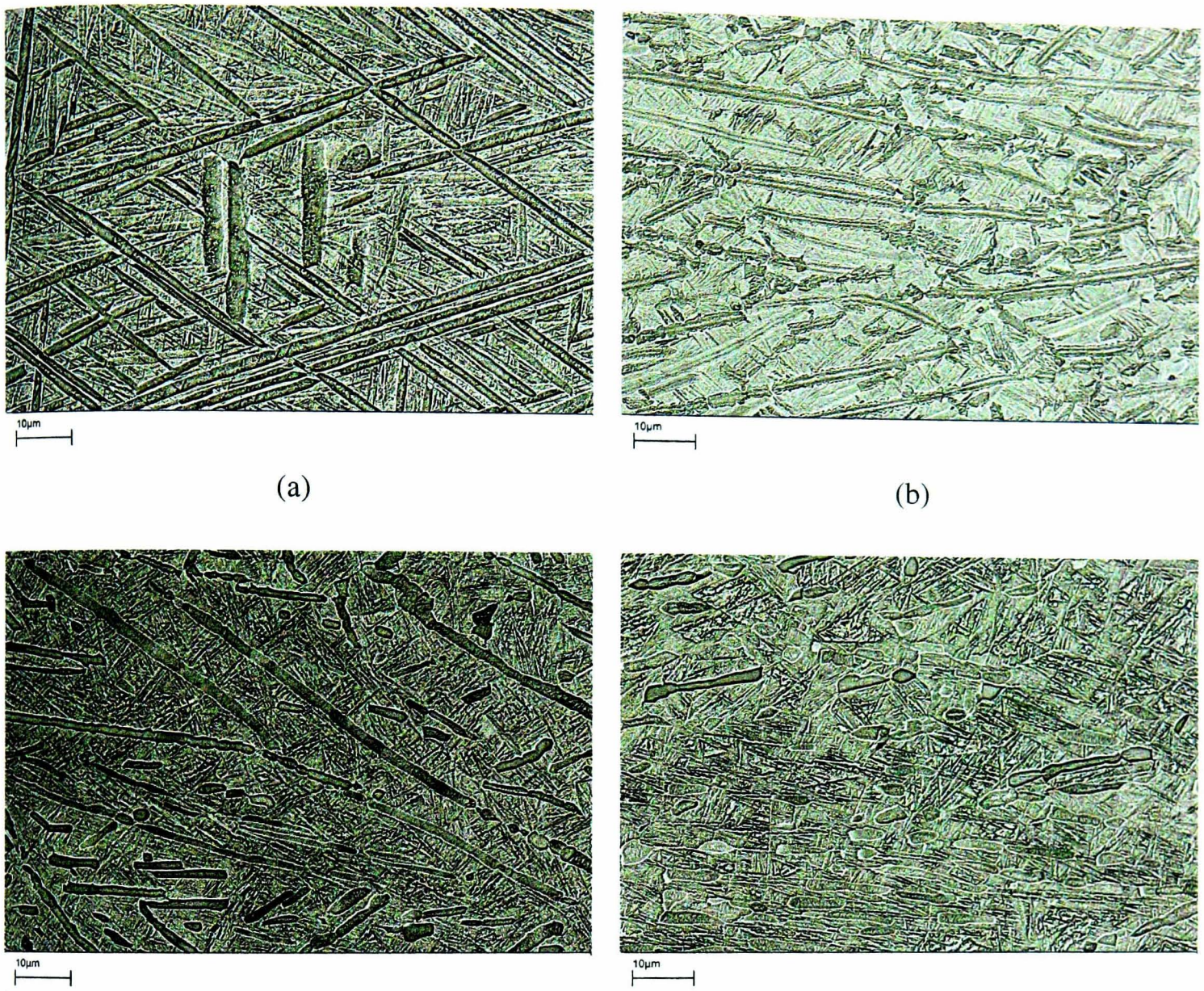

(a) (b)

(c) (d)

Figure 6.32: Microstructures of acicular Ti-6Al-4V (a) after 10 min pre-test soak at 975°C and after isothermal forging at 975°C to a true strain of 1.0 for strain rates (b) 0.3/s; (c) 0.03/s; and (d) 0.003/s. Forging axis is vertical.

The influence of strain rate on the microstructure evolution during isothermal forging at temperatures of 925, 950 and 975°C was investigated using quantitative image analysis. Plots of the evolved microstructural parameters versus imposed strain rates are presented in Figure 6.33.

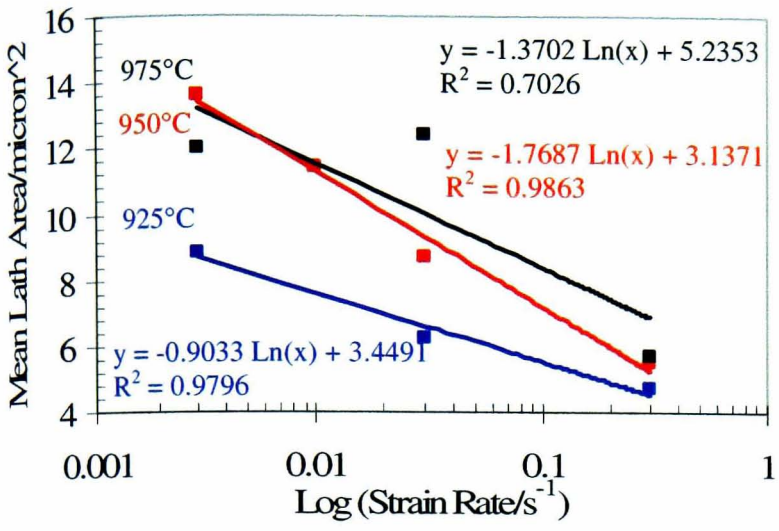

(a)

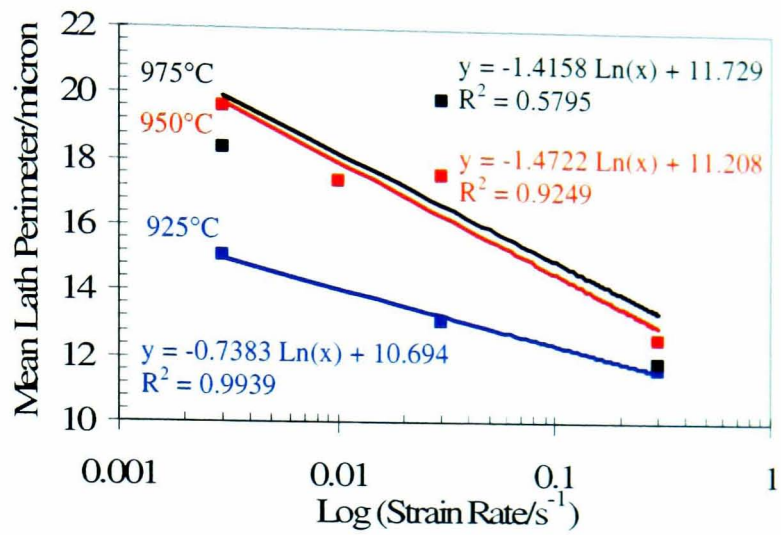

(b)

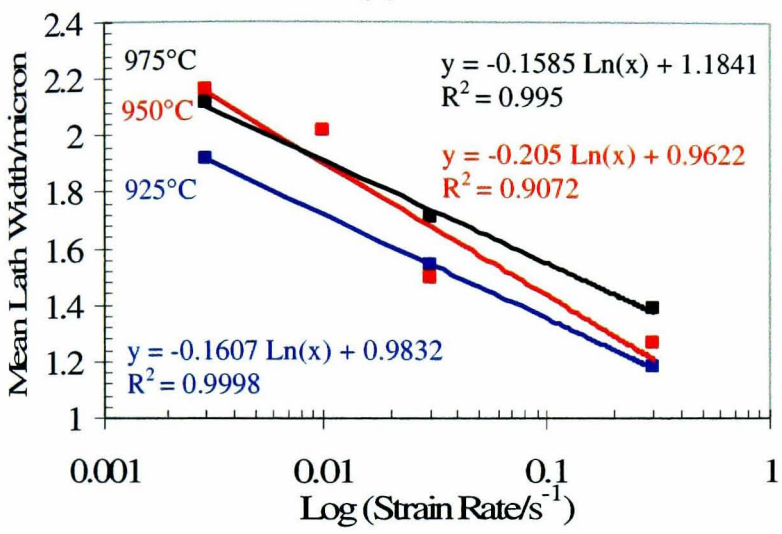

(c)

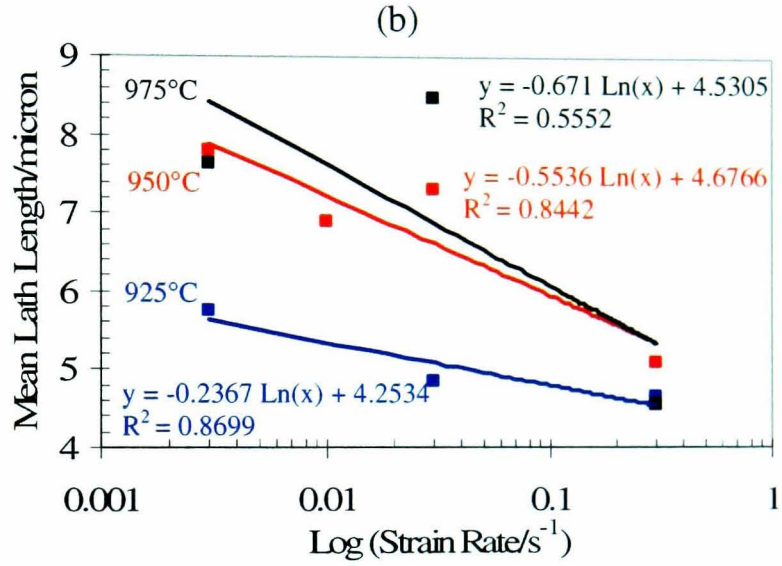

(d)

Figure 6.33: Plots of average values of (a) lath area, (b) lath perimeter, (c) lath width and (d) lath length versus strain rates for isothermal forging of acicular Ti-6Al-4V at 925, 950 and 975°C.

From the plots in Figure 6.33, it can be seen that there is a strong overall tendency with higher imposed strain rates to refine the α-lath shape. With increasing strain rate, a pronounced reduction in the mean area of the α-laths was observed for each test temperature. In addition, the average values of perimeter, width and length of the laths were also found to decrease with increasing strain rate.

6.2.3.3. The effect of temperature

Typical microstructures obtained at 925, 950 and 975°C for cylindrical specimens deformed at 0.03/s are shown in Figure 6.34(a-c), all of which exhibit a 'mixed' structure of undistorted, partially distorted and fully distorted (*i.e.* globularised) α-lath morphology. At lower temperature, it appears that the degree of globularisation is more intense, which results a higher fraction of globularised α phase. With increasing temperature, the volume fraction of α laths decreases substantially. Most of the α laths have dissolved and transformed into the β phase.

(a)

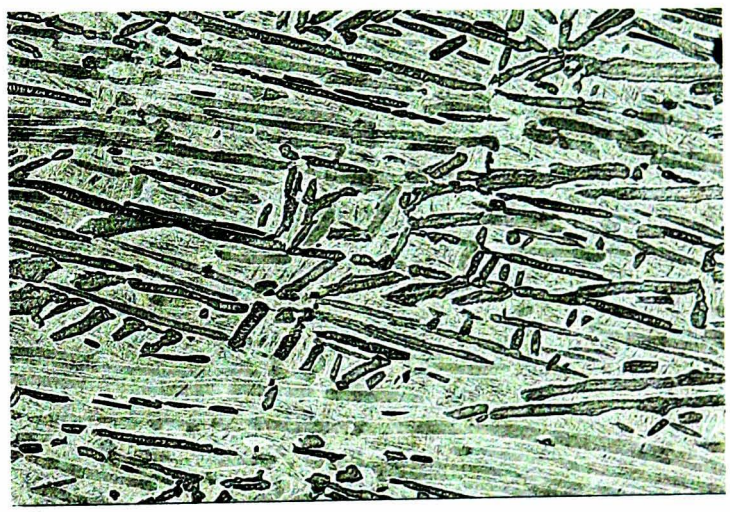

(b)

(c)

Figure 6.34: Microstructures of acicular Ti-6Al-4V deformed to strain of 1 at strain rate 0.03/s and temperatures: (a) 925, (b) 950 and (c) 975°C. Forging axis is vertical.

Figure 6.35 illustrates higher magnification backscattered micrographs of cylindrical specimens deformed to a true strain of 1 at a strain rate 0.03/s for temperatures 925, 950 and 975°C. It can be seen that the microstructure at 975°C (Figure 6.35.c) exhibits a high density of the secondary α-phase, which is produced from β phase upon water quenching. This indicates that, with increasing temperature, a higher percentage of α laths are transformed into β phase. The secondary α-phase is characterised by its unique appearance of very fine needle-like morphology with random orientation between retained untransformed larger primary α laths.

(a)

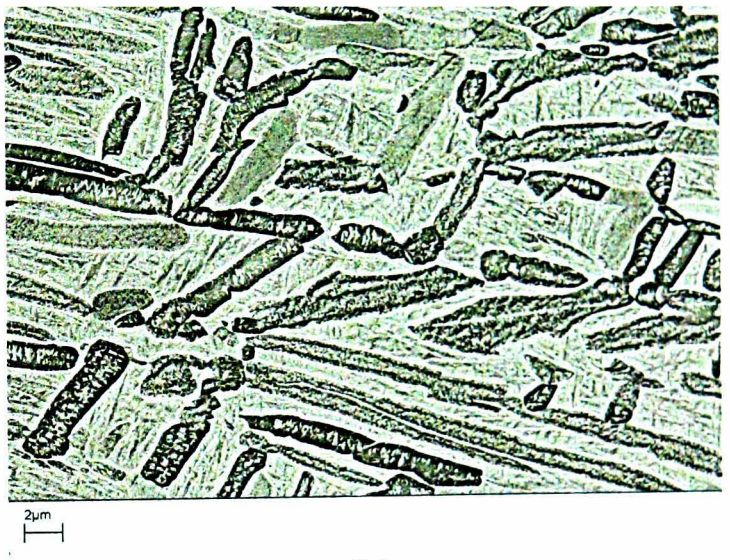

(b)

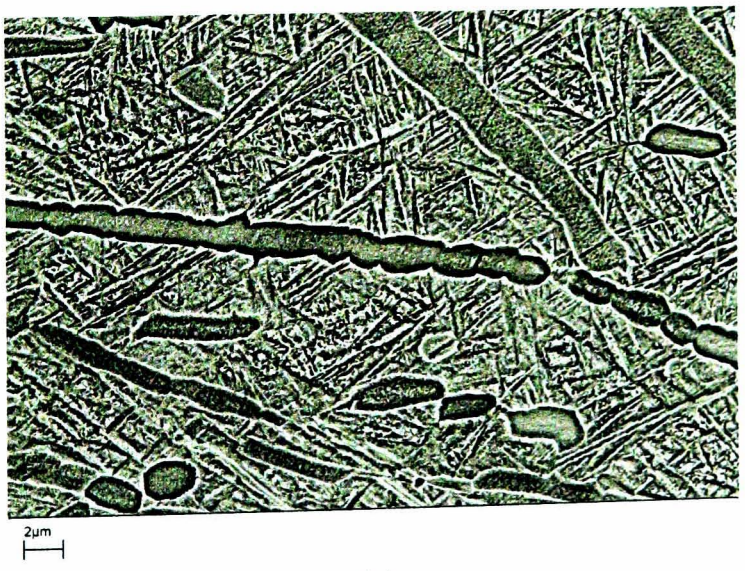

(c)

Figure 6.35: Microstructures illustrating the amount of secondary acicular α phase after deformation at a strain rate 0.03/s to true strain of 1, for different temperatures: (a) 925, (b) 950 and (c) 975°C. Forging axis is vertical direction.

The microstructure evolution was once again quantified using image analysis to examine the temperature dependence of microstructure parameters during isothermal forging at a strain rate 0.03/s. The results are plotted against test temperature in the range 925-975°C and displayed in Figure 6.36.

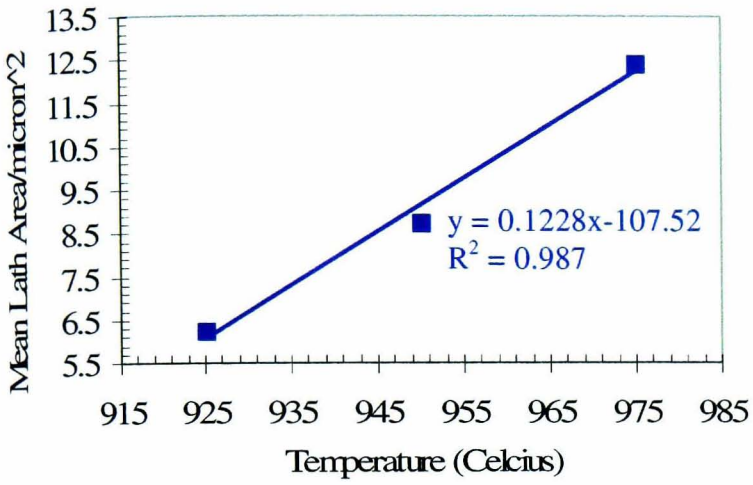

(a)

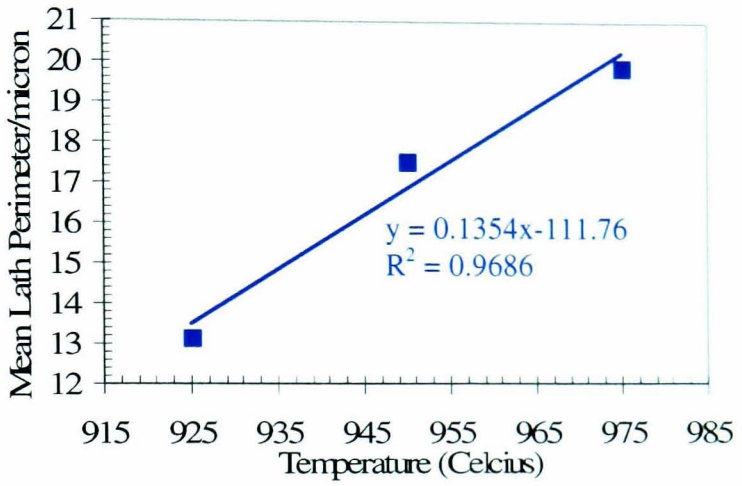

(b)

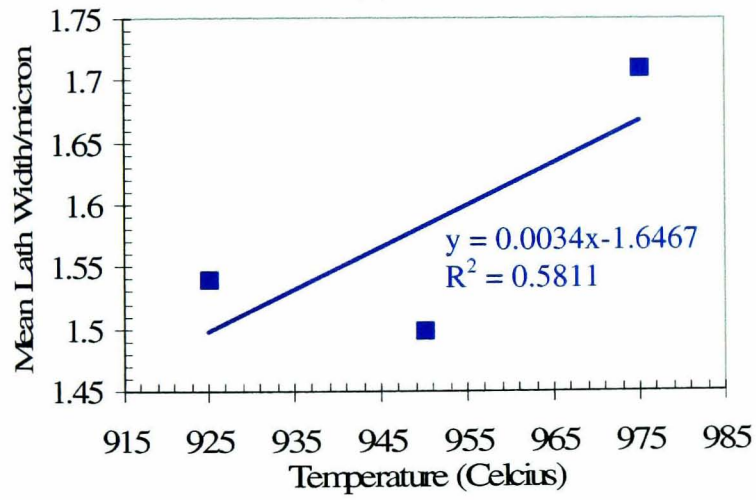

(c)

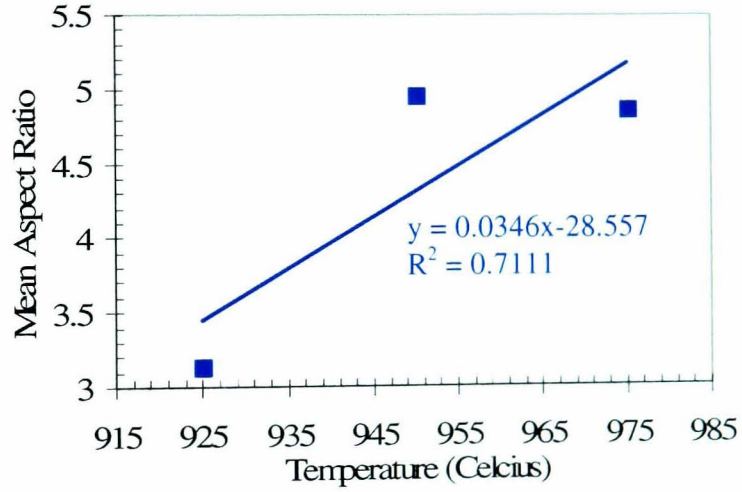

(d)

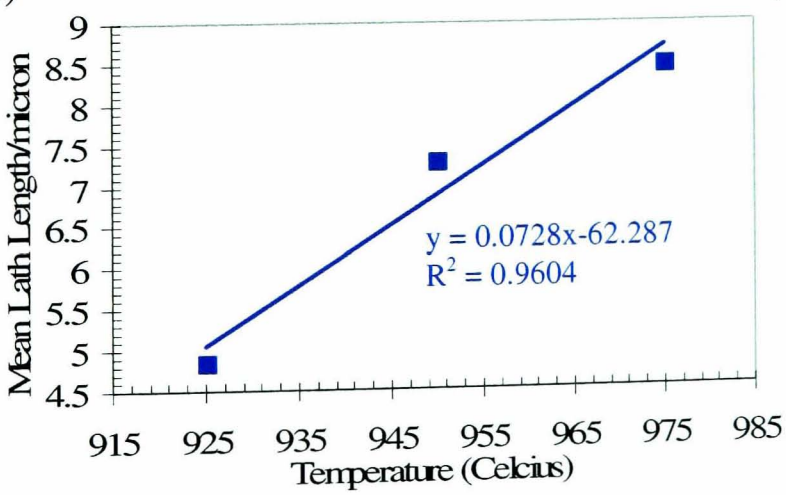

(e)

Figure 6.36: Plots of mean values of (a) area, (b) perimeter, (c) width, (d) aspect ratio and (e) length of α laths versus temperatures for isothermal forging of acicular Ti-6Al-4V at 925, 950 and 975°C.

The plots in Figure 6.36 reveal a strong temperature dependence of evolved α lath size during isothermal forging at 0.03/s. With increasing test temperature, the α laths undergo coarsening effects, as reflected by a tendency towards an increase in size (area, perimeter, length, width, and aspect ratio). The effect of lath coarsening is similarly observed during pre-heating prior to deformation, as shown in Figure 6.17. It suggests that higher temperature provides more stored energy as a driving force for thickening of α laths. In addition, the smaller α particles dissolve with increasing temperature, thus leaving the coarser laths remained.

6.3 Microstructure prediction for Ti-6Al-4V with acicular initial microstructure during isothermal forging at 950°C

The microstructure parameters within cylindrical work-pieces deformed during isothermal forging at 950°C and 0.01/s, as quantified in Section 6.2 were related to the structural parameter distribution, λ_{int} predicted using finite element analysis. This section describes the procedures used to build empirical relationships between λ_{int} and the measured microstructure parameters (aspect ratio, lath width and lath length). The microstructural relationships obtained were validated by using them to predict microstructural evolution within a complex-shape work-piece (*i.e.*, the double-truncated cone specimen), deformed at 950°C and 0.01/s.

6.3.1 Empirical relationships for microstructure prediction within cylindrical work-piece deformed at 950°C and 0.01/s

Figure 6.36 shows an example of the distribution of structural variable, λ_{int} predicted by finite element analysis, at pre-determined locations (one-third of final thickness (P1), centre (P2), 3mm (P3) and 6mm (P4) from centre) within a cylindrical work-piece deformed at 950°C and 0.01/s. Local λ_{int} values at the pre-determined locations P1, P2, P3 and P4 were found to be 0.678, 0.664, 0.667 and 0.681 respectively. Microstructural parameters were measured and then linked to the values of λ_{int} in order to establish a set of empirical relationships. The measurement results from quantitative image analysis of cylindrical specimens deformed at 950°C and 0.01/s are summarised in Table 6.1.

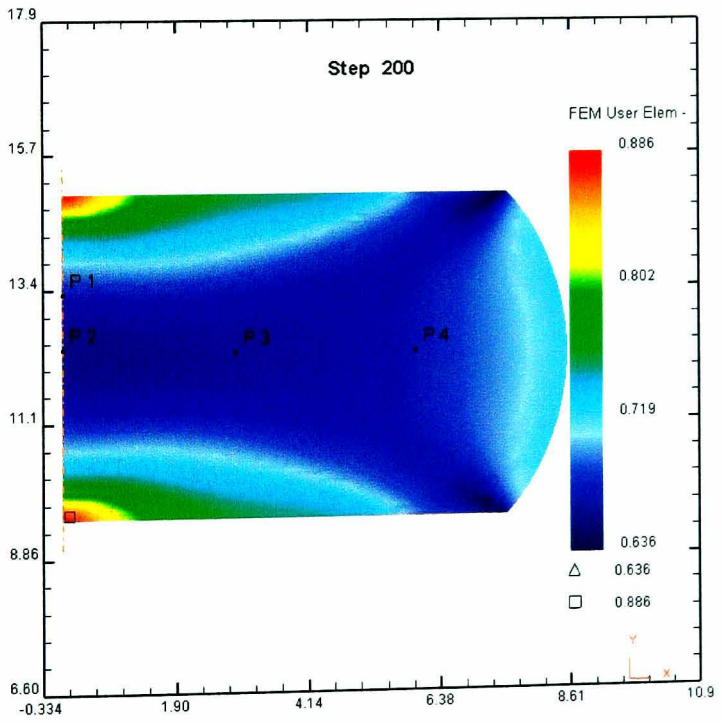

Figure 6.37: Distribution of structural variable λ_{int} within cylindrical specimen deformed during isothermal forging at 950°C and 0.01/s.

Table 6.1. **Measurement results of mean α-lath size obtained from quantitative image analysis within cylindrical work-piece of Ti-6Al-4V with acicular initial microstructure deformed at 950°C and 0.01/s.**

Strain rate (s^{-1})	0.01							
Strain (ε)	0	0.042	0.102	0.5	1.09	1.14	1.5	1.70
λ_{int}	1	0.95	0.889	0.723	0.676	0.679	0.667	0.664
Aspect ratio	6.68	6.03	4.46	4.91	3.51	3.56	2.71	2.54
Width (μm)	1.13	1.19	1.54	1.44	2.02	1.82	1.77	1.93
Length (μm)	7.55	7.53	7.13	6.73	6.89	6.54	4.89	4.83

A series of empirical microstructure models were derived based on the measurement results shown in Table 6.1. The models relate the microstructural features of the α-phase, *i.e.* aspect ratio, width and length, with structural variable λ_{int}. An exponential function for describing the evolution of α lath aspect ratio (AR) with λ_{int} was used such that:

$$AR = a_1 - a_2 \exp(-a_3 \lambda_{int}^{a_4}) \qquad \text{(Eq. 6.1.1)}$$

where a_1, a_2, a_3 and a_4 are structural constants. On the other hand, the dependence of evolved α-lath width (LW) with λ_{int} was well described using an exponential function, defined as:

$$LW = b_1 - b_2 \exp(b_3 \lambda_{int}^{b_4}) \qquad \text{(Eq. 6.1.2)}$$

where b_1, b_2, b_3 and b_4 are structural constants.

The dependence of α-lath length (LL) on the evolved structural variable λ_{int} was well-fitted by using a combination of power law and exponential functions:

$$\mathrm{LL}(\lambda_{int}) = c_1 \lambda_{\mathrm{int}}^{\ c_5} - c_2 \exp(-c_3 \lambda_{\mathrm{int}}^{\ c_4}) \qquad \text{(Eq. 6.1.3)}$$

where c_1, c_2, c_3 and c_4 are structural constants. The optimised structural constants were obtained by using the Nelder-Mead algorithm, and are listed in Table 6.2. Comparisons between the model fit (Eq.6.1.1-3) with the measured microstructure parameters are illustrated in Figure 6.38.

Table 6.2. **Optimised structural constants in the microstructure models for the evolution of (a) aspect ratio, (b) width and (c) length of α laths within Ti-6Al-4V with acicular initial microstructure deformed at 950°C and 0.01/s.**

(a)

a_1	a_2	a_3	a_4
-6.22995e4	-6.23052e4	1.31104e-7	-1.45448e1

(b)

b_1	b_2	b_3	b_4
-6.35281e4	-6.35292e4	3.71146e-7	-8.66459

(c)

c_1	c_2	c_3	c_4	c_5
-2.43374e4	-2.43449e4	2.64656e-21	-9.28626e1	-7.85472e-5

Hereafter, the derived microstructure models (Eq. 6.1.1-3) were employed to predict microstructure development across the centreline of a double truncated cone specimen deformed at 950°C and 0.01/s, as discussed in more detailed in the next section.

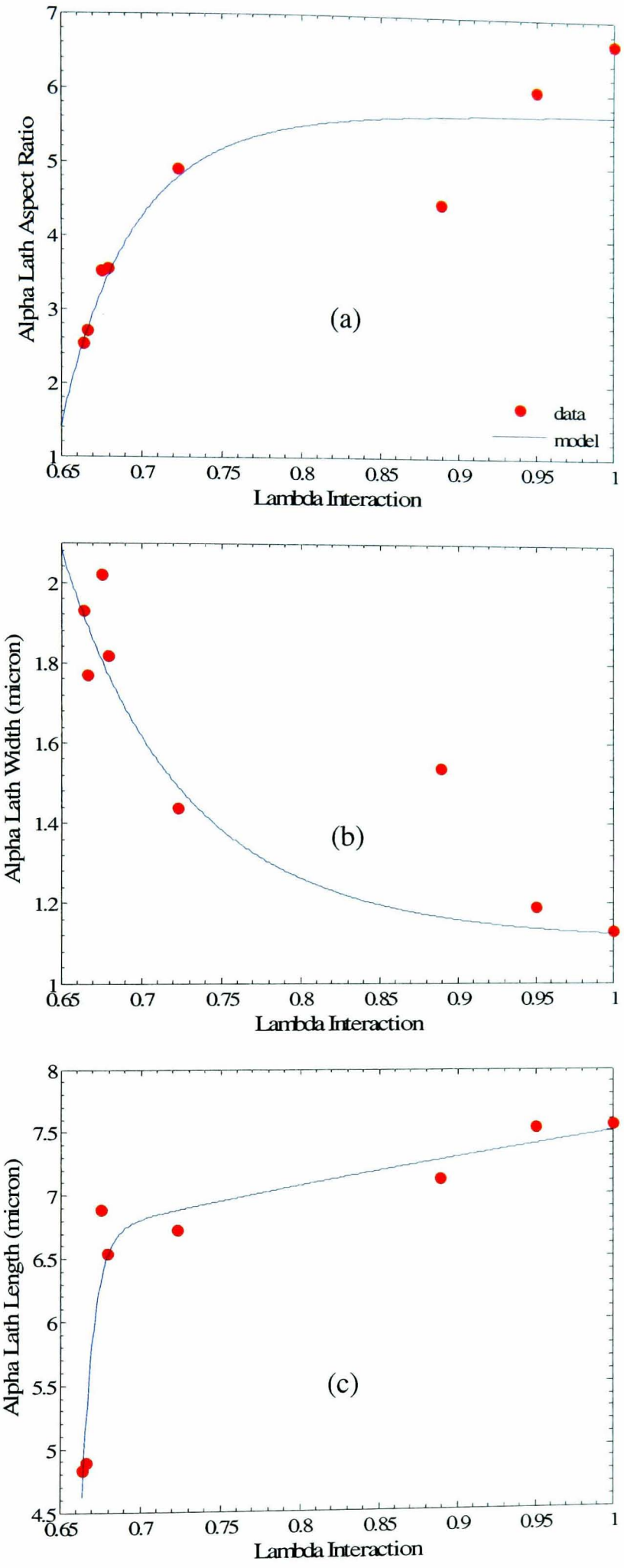

Figure 6.38: Comparison between model and measured data of (a) aspect ratio, (b) width and (c) length of α laths within cylindrical work-pieces of acicular Ti-6Al-4V deformed at 950 °C and 0.01/s.

6.3.2 Microstructure predictions for a double-truncated cone deformed at 950°C and 0.01/s

Figure 6.39 illustrates the progress of microstructure evolution within a double-truncated cone of acicular Ti-6Al-4V deformed at 950°C and 0.01/s. Backscattered scanning electron micrographs were recorded across the centre-line at different locations (centre and 2mm, 4mm, 6mm, 8mm, 10mm, 12mm and 14mm from the centre).

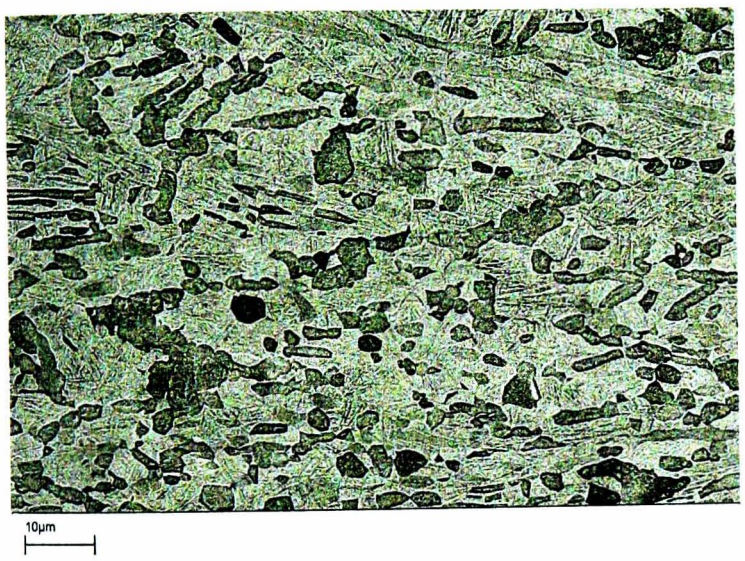

(a) Centre, strain = 2.10

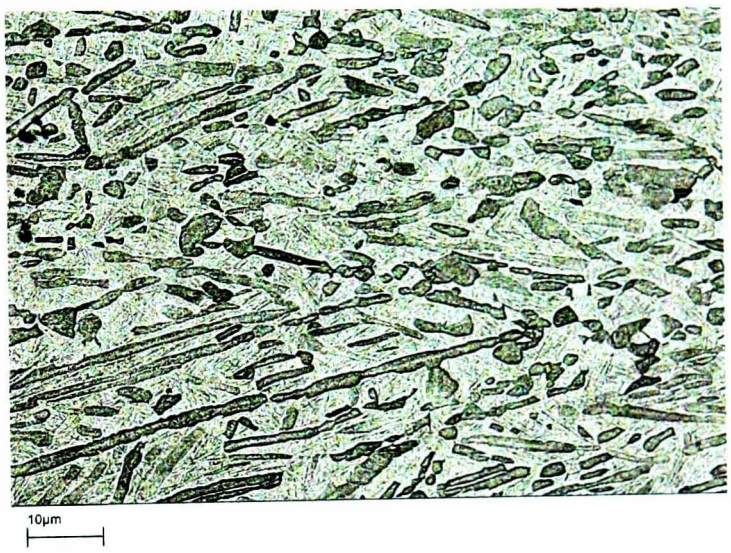

(b) 2mm from centre, strain = 1.90

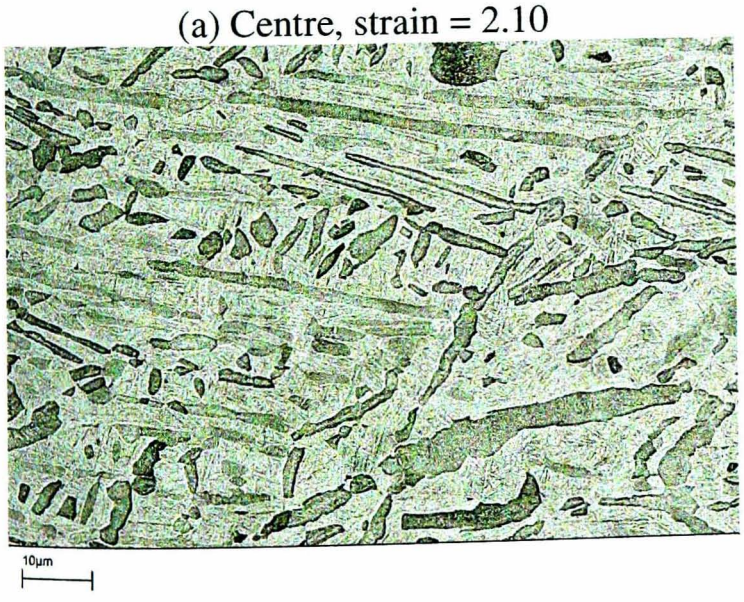

(c) 4mm from centre, strain = 1.54

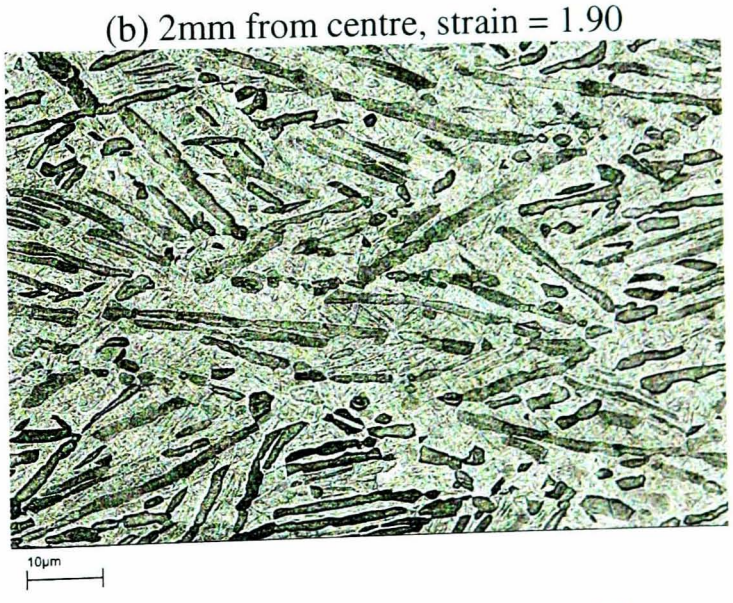

(d) 6mm from centre, strain = 1.28

(e) 8mm from centre, strain = 1.11

(f) 10mm from centre, strain = 0.94

(g) 12mm from centre, strain = 0.66

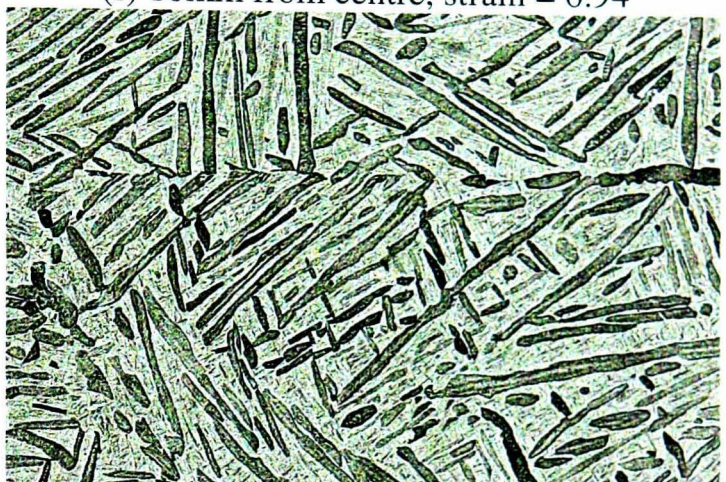

(h) 14mm from centre, strain = 0.40

Figure 6.39: Microstructure development across the centre-line of a double-truncated cone specimen of acicular Ti-6Al-4V deformed at 950°C and 0.01/s at locations of (a) centre and (b) 2mm, (c) 4mm, (d) 6mm, (e) 8mm, (f) 10mm, (g) 12mm and 14mm from the centre.

From Figure 6.39, it can be seen that there is a dramatic breakdown of the α-lath structure into an equi-axed morphology. Most of the lamellar α structures were broken-up and globularised in the most intensely deformed region (centre). On the other hand, at lower strain locations (e.g. in the circumferential region/14mm from centre), it appears that the lath structure was still maintained; here untransformed, partially transformed and bent laths can still be found within certain regions.

The empirical models (Eq.6.1.1-3) for microstructure modelling were then employed to provide instantaneous microstructural predictions, by substituting the values of structural variable, λ_{int} as predicted by finite element analysis, along the centre-line in the radial direction (Figure 5.24).

Figure 6.40 illustrates the comparison of measured results and model predictions for microstructure evolution along the centre line of the double truncated cone specimen deformed at 950°C and 0.01/s using model parameters summarised in Table 6.2. It can be seen that the internal structural variable λ_{int} correlated well with the evolved microstructure parameters within the double-truncated cone work-piece. There are slight discrepancies between the model predictions with the actual measurements, noteably at the circumferential regions in the case of the aspect ratio prediction. However, it can be seen that there is a reasonable degree of agreement between the model predictions and the measured data, showing the effectiveness of the models in handling the change of work-piece geometry and deformation paths.

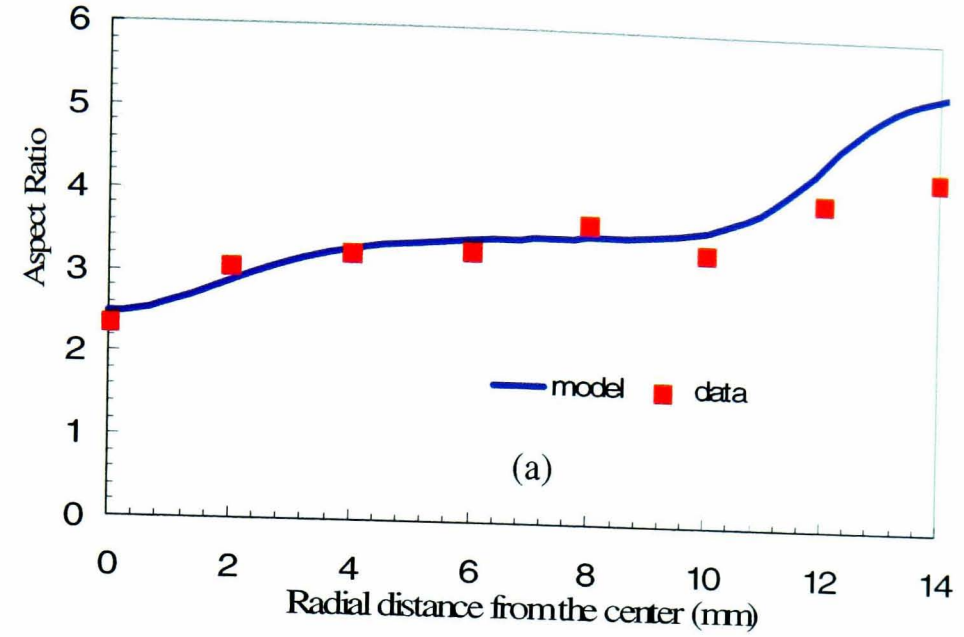

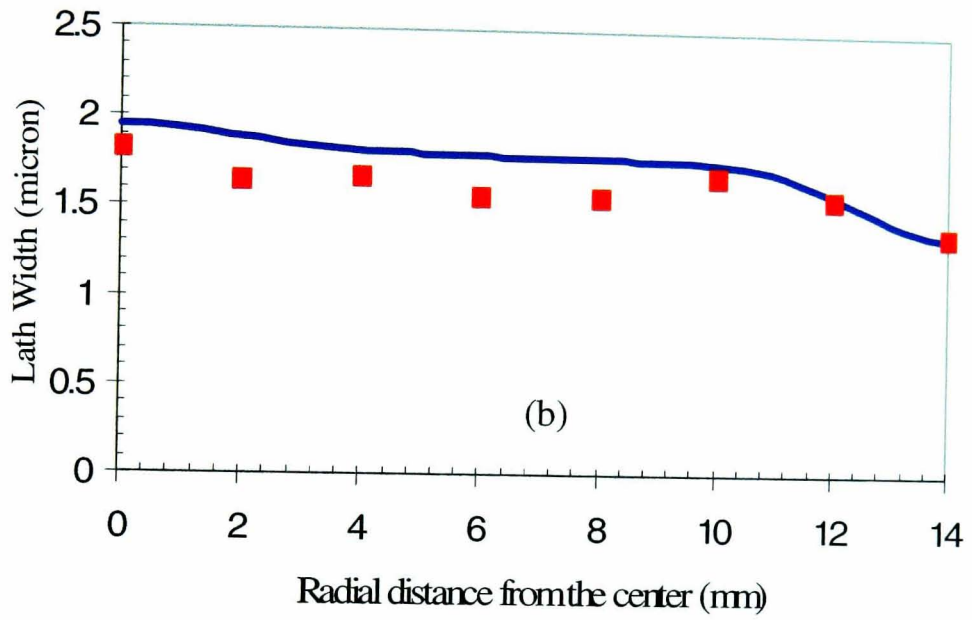

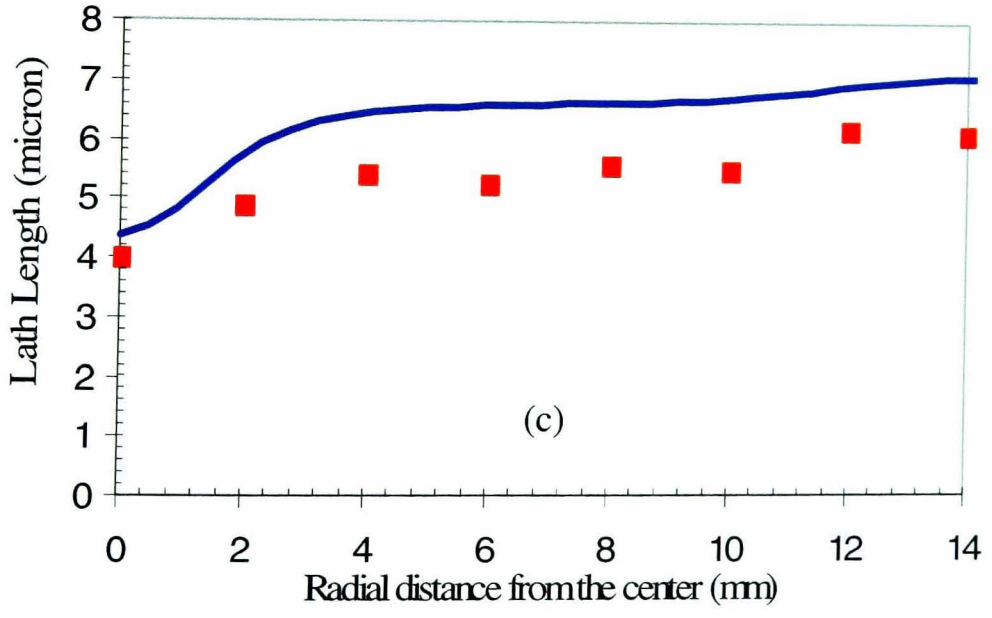

Figure 6.40: Comparison between model predictions and measurement data for (a) aspect ratio, (b) lath width and (c) length of α laths across the centre-line of a double-truncated cone specimen of acicular Ti-6Al-4V deformed at 950°C and 0.01/s.

Summary of results

Optical and backscattered scanning electron microscopy have been utilised in order to characterise the as-received and the β-heat treated microstructures of Ti-6Al-4V. The influence of forging parameters on the evolution of microstructural parameters during isothermal forging have also been analysed using quantitative metallography. According to the experimental findings, the following conclusions can be drawn for:

(a) As-received globular Ti-6Al-4V

- The microstructure of the as-received Ti-6Al-4V bar consisted of nearly equi-axed and elongated primary α within a fine discontinuous β matrix. This is a typical microstructure of a material which has been β-processed and subsequently α + β hot-worked.
- The volume fraction of primary α within the as-received Ti-6Al-4V decreased significantly as soaking temperature was increased from 850-1000°C. At temperatures closer to the β-transus temperature, higher volume fractions of the β-phase are retained. The β-transus temperature of the as-received material was estimated to be 995°C.
- It was found that, with increasing deformation, the primary α grains were deformed and flattened in a direction perpendicular to the forging axis. In the most severely deformed region, a finer globular structure of primary α with sharply-defined grain boundaries was observed, which was interspersed between coarser α grains within the β-phase matrix. The size

of the α grains underwent refinement up to a strain of 1, before reaching an apparent steady-state at larger strains. This equilibrated condition was possibly due to the occurrence of α-grain rotation within the soft β-phase matrix.

- The effect of imposed stain rate on morphology of the primary α grains was found to be negligible. The average grain size remains stable with increasing strain rate.
- It is apparent that the volume fraction of primary α varies with temperature. As temperature increases, the volume fraction of the α phase decreases considerably. On the other hand, the variation of α grain size with deformation temperature is relatively small, with a tendency towards a slight increase with increasing temperature.

(b) β-heat treated acicular Ti-6Al-4V

- The β-heat treated Ti-6Al-4V microstructure consisted of colonies of acicular/needle-like alpha phase within coarse prior β-grains. This is a typical microstructure produced from β-heat treatment followed by rapid quenching.
- It was found that soaking temperature strongly affects the α lath width. As temperature increases, the laths exhibit coarsening to some extent whilst higher aspect-ratio laths become partially dissolved and broken-up. Inter-spacing between adjacent laths also increased simultaneously. Consequently, the volume fraction of α laths decreased since there is sufficient driving force at elevated temperatures for dissolution of α phase

into the β matrix.

- It was found that at lower strains, the structure of the α phase consisted of a mixture of undeformed, partially distorted and fully distorted laths. As strain progressed, the α laths were broken-up and their aspect ratio decreased, forming a globularised structure due to severe distortion, bending and kinking within certain regions.
- Accumulated strain also affects the refinement of the α-lath morphology. The mean aspect ratio of α laths exhibited a gradual reduction as deformation proceeded. It was also found that the volume fraction of the globularised α phase increased with increasing strain. On the other hand, lath area, length and perimeter showed a tendency to decrease with increasing strain. These results are quantifiable evidence of α lath transformation. The mean lath width was found to be relatively stable within the range of imposed strain rates, with only a slight tendency to increase with increasing strain.
- A pronounced reduction of the mean size of α laths was observed for each test temperature with increasing imposed strain rate. A similar effect was also observed for mean values of perimeter, width and length.
- Volume fraction of the laths decreased slightly with decreasing strain rate. This suggests that at the slowest strain rate, there is sufficient time for diffusion-controlled processes to take place, which lead to dissolution of α phase into the β matrix. This observation demonstrated that some degree of phase transformation occurred concurrently with the mechanical deformation during α + β hot forging.

- At lower temperature, a higher degree of globularisation occurred as indicated by a higher fraction of globularised α grains. As temperature increases, most of the laths are dissolved into the β-matrix which in turn reduces the lath volume fraction. In addition, α laths undergo coarsening as indicated by a tendency towards increasing morphological size (aspect ratio, width, length, area, perimeter).

- The quantified microstructure constituents (aspect ratio, width and length of α laths) within deformed cylindrical work-pieces during isothermal forging at 950°C and 0.01/s have been linked to the distribution of the structural parameters λ_{int} as predicted using FE analysis, thus providing a basis for the establishment of a set of microstructure models. The evolution of aspect ratio and width of the α laths was well-described using an exponential function of λ_{int}. The dependency of α-lath length was also well-fitted by using a combination of power law and exponential functions of λ_{int}.

- The derived microstructure relationships were validated by using them to predict the microstructure development within a complex-shaped work-piece, *i.e.*, a double-truncated cone, deformed at 950°C and 0.01/s. It was found that the predicted λ_{int} correlated well with the measured microstructure parameters within the work-piece, demonstrating the effectiveness of the models in handling the change of work-piece geometry and deformation paths.

Chapter 7

General Discussion, Conclusions and Further Work

7.1 General Discussion

There have been several investigations into the flow stress behaviour of commercial Ti-6Al-4V under various hot deformation strain rates and temperatures, as summarised in Table 7.1.

Table 7.1. **Several previous investigations on hot deformation of commercial Ti-6Al-4V under various fixed strain rates and temperatures.**

Researchers	Testing methodology	Temperature range (°C)	Strain rate range (1/s)	Initial microstructure
Seshacharyulu [62]	Compression	750-1100	0.0003-100	Equiaxed
Seetharaman [58]	Compression	700-1000	0.0001-10	Equiaxed
Majorell [122]	Compression	377-1067	0.001-10	Equiaxed
Park [123]	Compression	850-1000	0.001-10	Equiaxed
Chen-Coyne [124]	Compression	816-982	0.0067-0.067	Equiaxed and acicular
Wagoner [125]	Compression	875	0.1-1000	Equiaxed and acicular
Barbosa [126]	Compression	800-950	0.1, 1, 3/s	Equiaxed
Sheppard-Norley [74]	Torsion	800-1100	0.05, 0.5, 15, 50	Equiaxed
Malcor [127]	Torsion	800-1200	0.005-5	Equiaxed and acicular

Surprisingly however, little published data is available with which to directly compare the results of the current study, emphasising the difficulty of acquiring high quality, reliable flow stress data. The flow stresses determined from some of these studies are compared with the current results, at the same level of strain, in Fig 7.1.

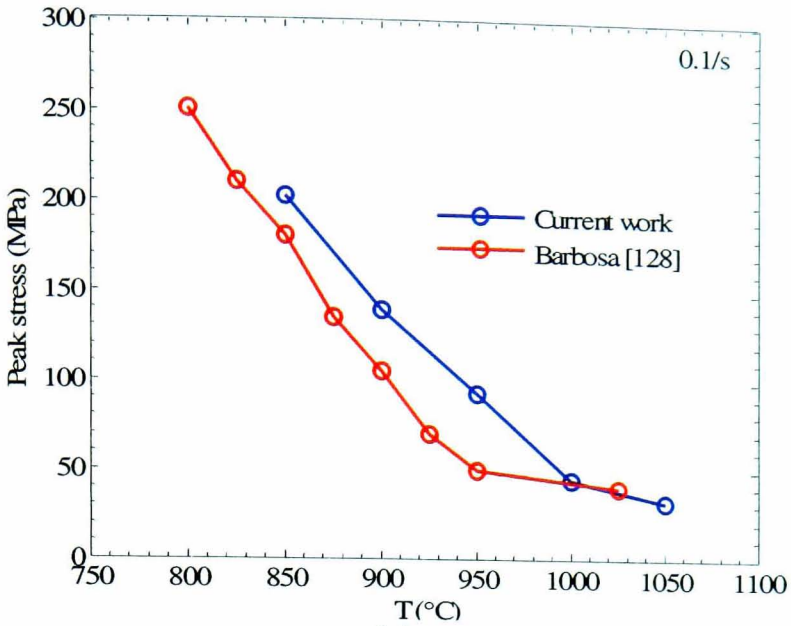
0.1/s
Current work
Barbosa [128]
Peak stress (MPa)
T(°C)

(a)

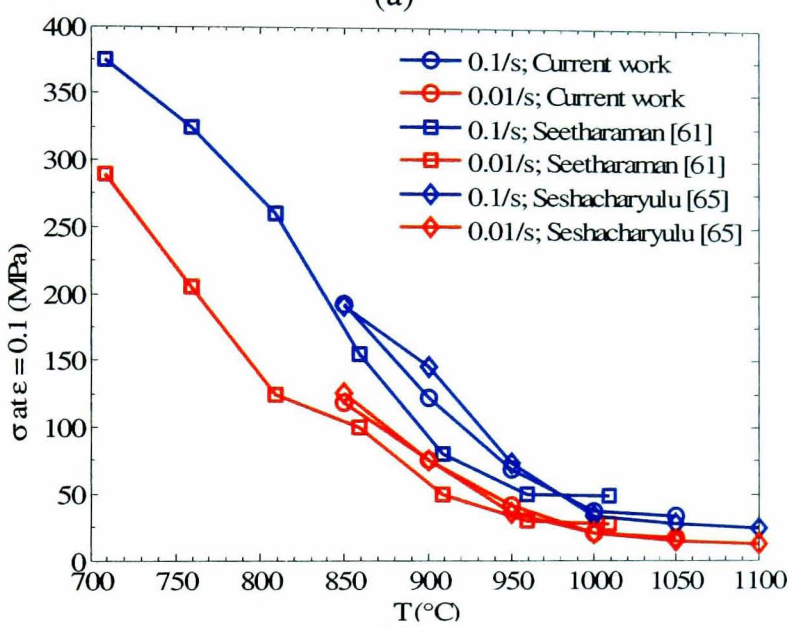
0.1/s; Current work
0.01/s; Current work
0.1/s; Seetharaman [61]
0.01/s; Seetharaman [61]
0.1/s; Seshacharyulu [65]
0.01/s; Seshacharyulu [65]
σ at ε = 0.1 (MPa)
T(°C)

(b)

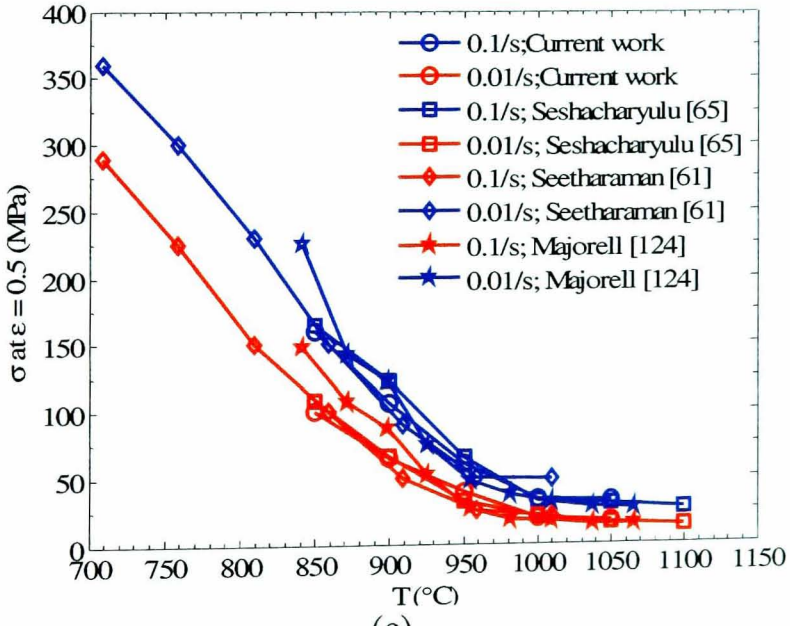
0.1/s;Current work
0.01/s;Current work
0.1/s; Seshacharyulu [65]
0.01/s; Seshacharyulu [65]
0.1/s; Seetharaman [61]
0.01/s; Seetharaman [61]
0.1/s; Majorell [124]
0.01/s; Majorell [124]
σ at ε = 0.5 (MPa)
T(°C)

(c)

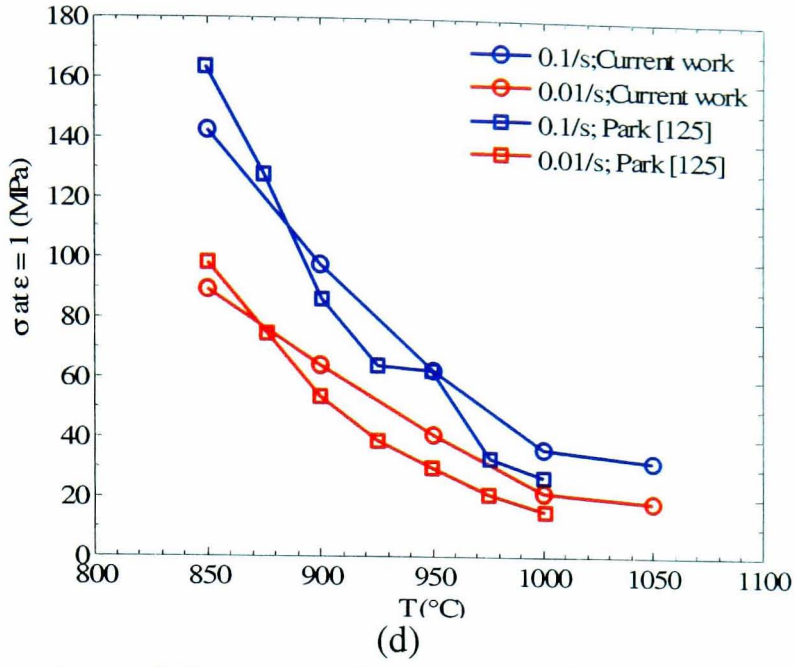

(d)

Figure 7.1: Comparison of flow stress between published results [58, 62, 122, 123, 126] and current work for globular Ti-6Al-4V for (a) peak stress; (b) $\varepsilon = 0.1$; (c) $\varepsilon = 0.5$; (d) $\varepsilon = 1$.

Although there is broad agreement between these studies there is nevertheless a degree of experimental scatter, requiring the issue of reproducibility and reliability of the measurement results to be addressed. The error in measuring flow stress during hot compression testing, for instance, may be attributed to several factors, i.e., temperature inhomogeneity/fluctuation during testing, interfacial friction condition and control of imposed strain rate [128-130]. Differences in flow stress results between the mentioned above studies (Table 7.1) may also be attributed to the difference of composition in alloying elements of the commercial Ti-6Al-4V, although this is likely to be a secondary factor.

In the current study, a strict experimental methodology has been developed for performing highly reliable hot compression tests to determine the flow stress of Ti-6Al-4V at elevated temperatures ranging from 850-1050°C and strain rates of 0.003-0.3/s, following recommended procedures laid down by the National Physics Laboratory, Teddington, UK [35]. The testing temperatures have been tightly

controlled by using a programmable temperature controller, in order to maintain temperatures within the range of ±1-3°C. In addition, thorough temperature calibration prior to testing has ensured higher accuracy of the nominal testing temperature (test setpoint) in order to eliminate one source of temperature uncertainty. Careful selection of the most appropriate lubrication system for high temperature deformation, i.e, Boron Nitride and Glass Deltaglaze, has also contributed in minimising errors due to friction effects, which in turn increases the quality and reliability level of measured flow stress. For example, the errors for flow stress measurement of globular Ti-6Al-4V deformed at 850°C and 0.1/s due to the effects of temperature, friction, and strain rate, based on upper and lower bounds, are summarised in Table 7.2.

Table 7.2. **Relative errors of flow stress measurement for globular Ti-6Al-4V deformed at 850°C and 0.1/s due to temperature, friction and strain rate effects.**

Effect	Lower Bound	Upper Bound	Error (%) in steady-state stress (σ_{ss})
Temperature (°C)	847	853	0.006-0.013
Friction coefficient at 850°C	0.035	0.06	0.916-1.663
Strain Rate (s^{-1})	0.093	0.102	0.077-0.297

The calculated standard deviation for repeated flow stress measurement of globular Ti-6Al-4V deformed at 850°C and 0.1/s is 1.6MPa for a peak stress average of 201.8MPa (an error in peak stress of 0.8%) and 2.5MPa for a steady-state flow stress average of 145.8MPa (an error in steady-state stress of 1.7%). It can be seen that the quantified errors are within an acceptable range, indicating a high confidence level of experimental results derived from tightly controlled testing conditions. To support this conclusion, Figure 7.2 illustrates experimental results from repeated tests for globular and acicular Ti-6Al-4V, and single α & β phase in Ti-6Al-4V. This figure clearly demonstrates the high reproducibility of measured flow stress during repeated

testing, reflecting the extent to which experimental errors have been minimised.

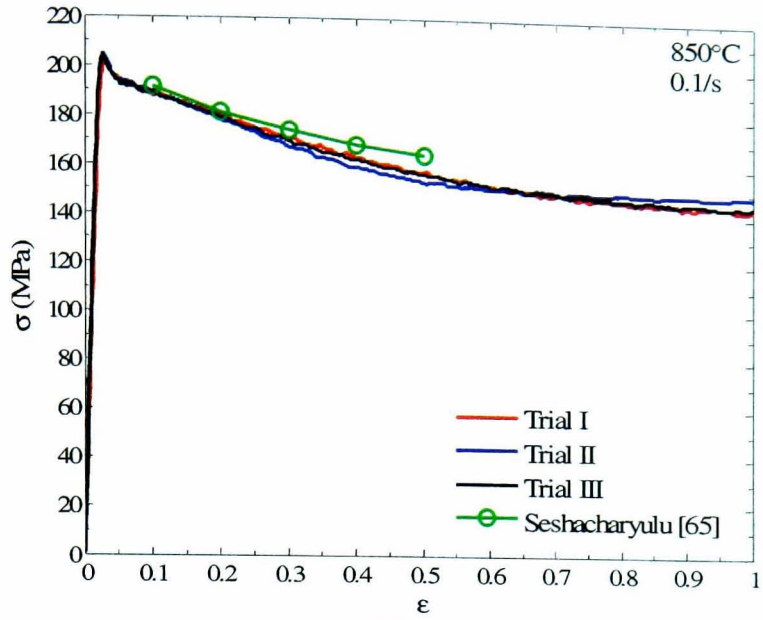

(a)

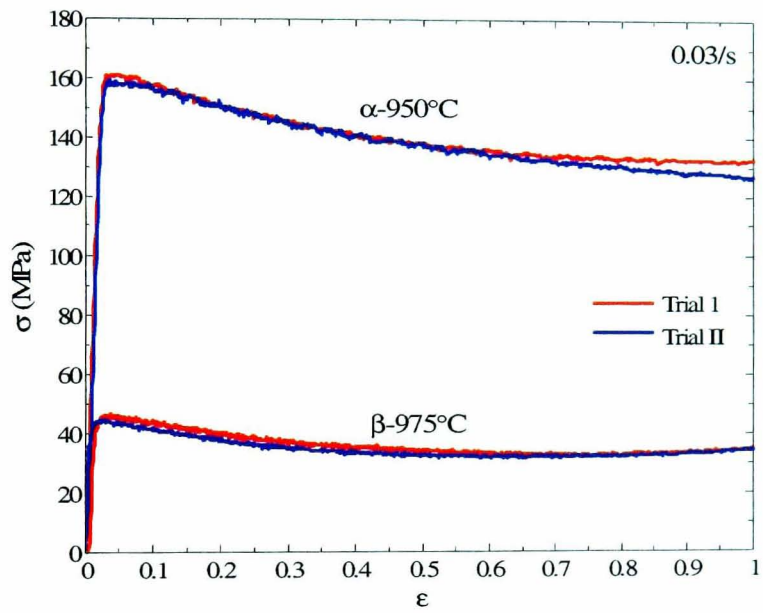

(b)

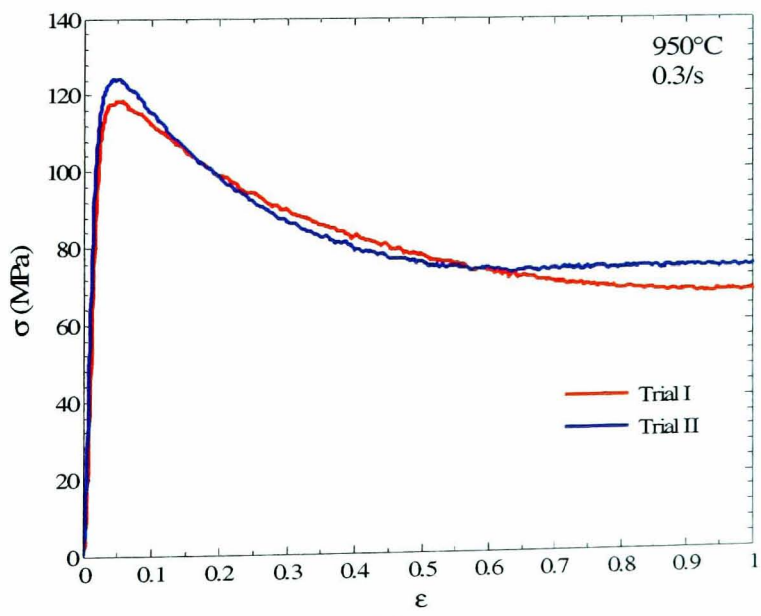

(c)

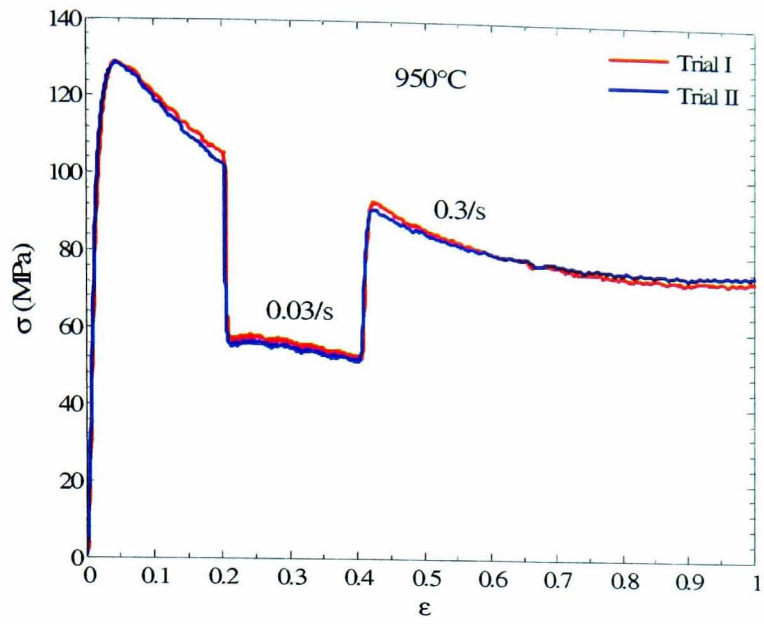

(d)

Figure 7.2: Experimental results from repeated hot compression tests of (a) globular Ti-6Al-4V at 850°C; 0.1/s, compared with data literature [62]; (b) Single α-950°C and β-975°C in Ti-6Al-4V at 0.03/s; (c) acicular Ti-6Al-4V at 950°C and 0.3/s and (d) strain rate jump tests for acicular Ti-6Al-4V at 950°C and 0.3/s → 0.03/s →0.3/s.

For comparison of full flow stress, the results of upset tests performed by Seshacharyulu *et al* [62], Shell *et al* [70] and data available from Kuhlman [131] are also plotted in Figure 7.3. It can be seen that there is good agreement between the experimental results obtained within this study compared with the data literature.

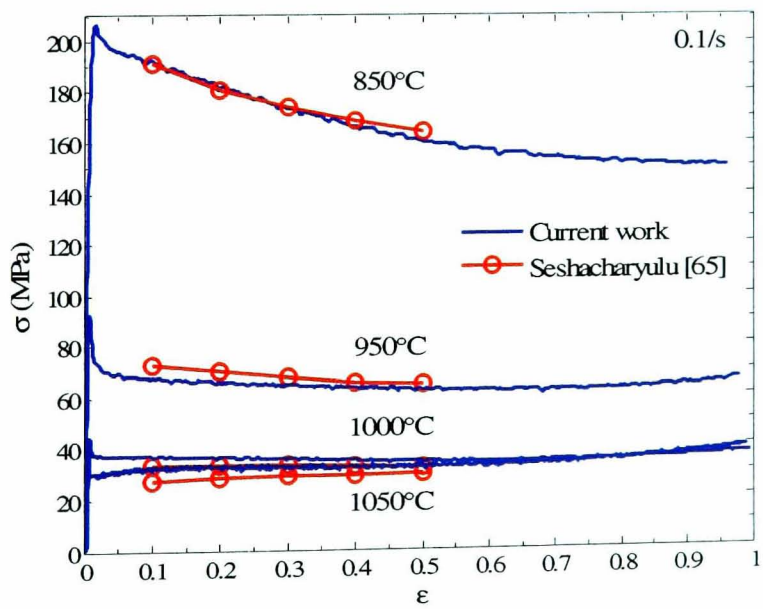

(a)

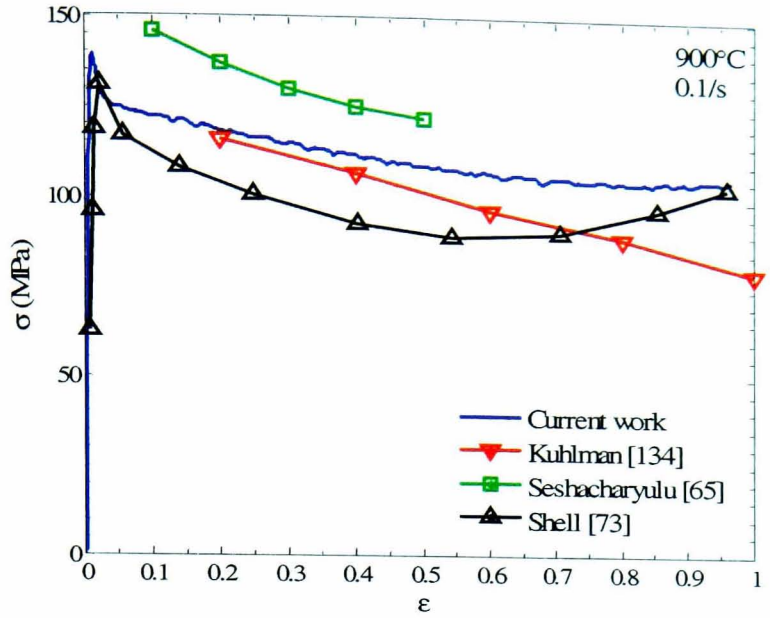

(b)

Figure 7.3: Comparison of full flow stress between published results and current work for globular Ti-6Al-4V at 0.1/s and (a) 850, 950, 1000 & 1050°C; (b) 900°C.

It is interesting to note that the flow stress behaviour of Ti-6Al-4V is highly influenced by its pre-form initial microstructure. As can be seen in Figure 7.4, the flow stress for the acicular microstructure exhibits higher peak stress at low strains followed by more pronounced flow softening than for the globular microstructure. As deformation proceeds, both acicular and globular microstructures approaches a comparable steady state-stress level.

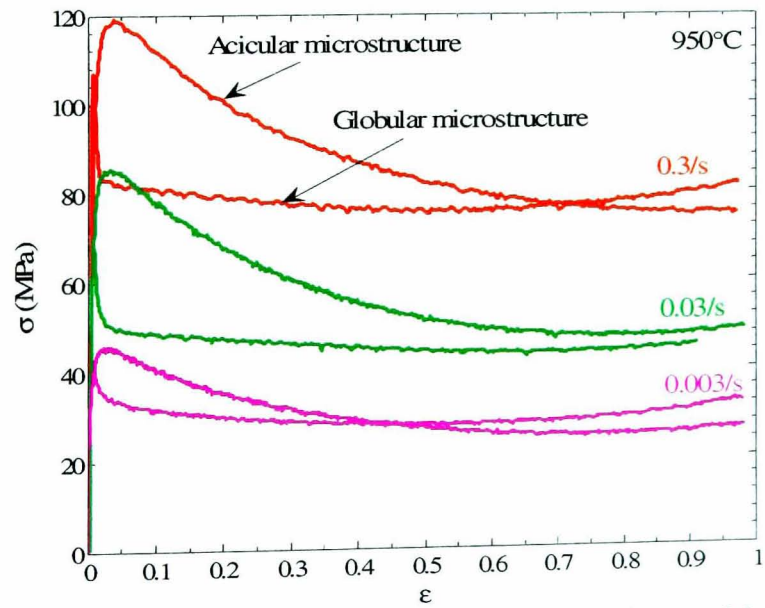

Figure 7.4: Comparison of flow stress for acicular with globular initial microstructure at 950°C.

The use of high quality, reproducible data for developing a constitutive model has the benefit of increasing the overall confidence of the industrial and research communities in the predictive capabilities of process modelling. This confidence is reinforced by proper estimation of the errors associated with derived constitutive parameters in model equations, as carried out in this study.

There have been several studies that have attempted to formulate a constitutive model for general deformation of Ti-6Al-4V at elevated temperatures (not limited to hot forging). For example, Barboza *et al* [132] developed a model to characterise the creep mechanisms and physical modelling of Ti-6Al-4V; Kim *et al* [133] determined high temperature deformation of Ti-6Al-4V within the framework of inelastic-deformation theory by considering grain matrix deformation and grain boundary sliding; Nemat-Naser, Seo and Lee-Lin [134-136] utilised models to investigate constitutive relations for Ti-6Al-4V under extremely high strain rates; Lin *et al* [137] studied the applicability of genetic algorithm techniques in optimising material constants of viscoplastic constitutive equations for characterising superplastic behaviour of Ti-6Al-4V. However, none of these works has attempted to determine the confidence limits of estimated parameters. In fact, it is believed that the current study is the first to determine the confidence limits of parameters used in any kind of hot forming analysis. The magnitude of confidence limits derived here are within an acceptable range, (see Table 5.2, 5.3 and 5.4 in Chapter 5), supporting the validity of the constitutive model adopted.

The two-phase model developed here has advantages of incorporating the deformation history of each phase constituent, temperature dependent volume fractions and interaction terms between two phases. Figure 7.5 illustrates a comparison of the two-phase and single-phase capability in modelling the gradual change of working temperature from 975°C ⇔ 925°C during isothermal compression of acicular Ti-6Al-4V. It can be seen that qualitatively, the two-phase model exhibits similar predictive capability to the single-phase model. However, there is a slight discrepancy in simulating the temperature change from 975 to 925°C (Figure 7.4.a), probably reflected by a slightly less good fit to the overall flow stress data when compared with the single phase model. Nevertheless, the two-phase model is more fundamentally based for the reasons mentioned above.

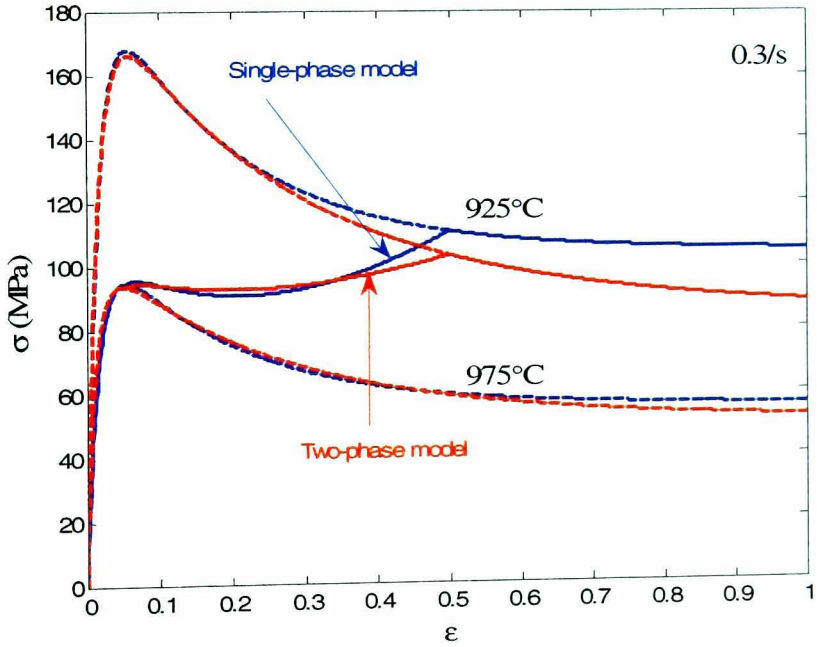

(a)

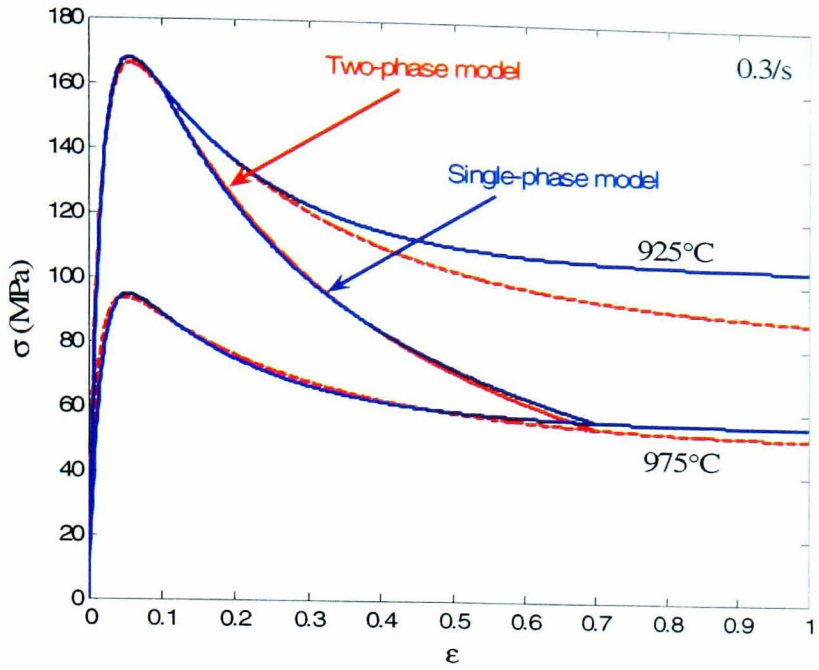

(b)

Figure 7.5: Comparison of two-phase with the single-phase constitutive model in predicting the gradual change of working temperature from (a) 975 to 925°C; (b) 925 to 975°C during isothermal compression of acicular Ti-6Al-4V at 0.3/s.

In this thesis, extensive work has been carried out in order to quantify microstructure evolution during hot forging of Ti-6Al-4V. Quantitative image analysis software has been used in order to characterise evolved microstructural parameters during isothermal forging. The evolved microstructural parameters have been related to processing conditions, i.e., strain, temperature and strain rates, including the value of structural variables within deformed cylindrical specimens. Shell *et al* [70] have also quantified evolved microstructures by focusing on the effect of initial microstructure on the plastic deformation and dynamic globularisation of acicular alpha phase during hot working of Ti-6Al-4V. The fraction of globularised alpha was quantified thoroughly and related to local strain as predicted by finite element analysis. In addition, the lath widths were quantified so as to determine the coarsening kinetics during static heat treatment. Seshacharyulu *et al* [71] have described microstructural evolution during hot working of acicular Ti-6Al-4V qualitatively. Ding *et al* [78] have investigated the influences of hot working parameters (temperature and strain

rate) on α lath widths. Although these earlier efforts have provided the quantitative insight into the microstructrural evolution of acicular α, modelling of microstructural development, particulary the morphology change of α laths during forging, has not been attempted by previous researchers. The microstructure model developed within this thesis is still currently empirical. However, in practice, physical dislocation-based constitutive models are often limited by many unknown variables, e.g, dislocation densities within engineering materials, which are extremely difficult to measure. The microstructure model has shown the capability to reasonably predict evolved aspect ratio and lath width of the α-phase, hence it warrants further industrial-scale implementation in order to characterise the degree of globularisation of primary α during secondary forge processing. By predicting these microstructural parameters, processing routes can be optimised in order to control microstructural development, which in turn dictates the mechanical properties of final product components. Further work is required to enhance and validate the model developed for industrial forging using larger scale non-axisymmetrical work-pieces.

7.2 Conclusions

The first goal of this thesis was to investigate the flow stress behaviour of two-phase Ti-6Al-4V and its individual α and β phases during isothermal forging at various temperatures and strain rates. The relationship between flow stress behaviour and initial pre-form microstructure of Ti-6Al-4V, which ranges from globular α to acicular α (β transformed), was investigated by heat-treating the as-received globular microstructures to produce an acicular β-transformed microstructure. Isothermal

forging tests were then performed at temperatures ranging from 850-1050°C under constant strain-rates of 0.3-0.003/s in order to characterise the flow stress behaviour of the as-received and β-heat treated bulk Ti-6Al-4V, and also its individual single α and β phases. The following concluding remarks concern the flow stress behaviour derived from isothermal forging tests:

a. For the as-received Ti-6Al-4V with globular initial microstructure:

- Flow stress curves of the as-received Ti-6Al-4V exhibited a strong dependence on working temperatures and imposed strain rates. With increasing temperature, flow stress decreases. In contrast, flow stress increases as the imposed strain rate increases.
- At strain rates higher than 0.01/s, flow stress curves derived during subtransus deformation (850-950°C) showed a peak stress followed by flow softening towards a steady-state stress. At strain rates lower than 0.01/s, predominantly steady-state flow behaviour was exhibited. For supertransus deformation (1000-1050°C) at strain rates of 0.003-0.3/s, the flow stress curves generally displayed a sharp yield drop followed by steady-state deformation.
- A pronounced discontinuous yielding phenomenon was exhibited, particularly during hot deformation at higher temperature (≥900°C) and higher strain rates (≥0.01/s).

b. For the β-heat treated Ti-6Al-4V with acicular initial microstructure:

- All flow stress curves reveal a broad peak stress level at low strains followed by moderate to extensive flow softening until a steady-state stress is reached. The flow stress curves exhibit strong temperature and strain-rate dependence for deformation at temperatures of 925-975°C and strain rates between 0.003-0.3/s.

c. For the single α and β-phases in Ti-6Al-4V:

- Flow stresses of the single α-phase material increased with increasing imposed strain rate and decreasing working temperature. At 925-950°C and 0.3/s, there is an indication of initial work hardening behaviour after the onset of plastic deformation at low strains. At 975°C, a pronounced flow softening is exhibited particularly at strain rates of 0.03-0.3/s.
- Flow stresses of the single β-phase material were found to be much lower than for the α-phase. In general, most of flow stress curves of β-phase are of the steady-state type with relatively little flow softening observed at strain rates of 0.03-0.3/s and 925-975°C. In contrast to the single α-phase, the steady state stress for the β-phase is relatively insensitive to temperature, particularly within the range 925-975°C.

The second goal of this thesis was to develop a semi-empirical, history-dependent constitutive model for prediction of the flow behaviour of Ti-6Al-4V during isothermal forging that incorporates the temperature-dependent volume fraction, the flow properties of the individual α and β phase in Ti-6Al-4V and an embedded structural-related variable for microstructure prediction. The aim was to implement the model within finite element subroutine (DEFORM-2D) in order to predict load response and microstructure development within a complex-shape geometry. In this study, a double truncated-cone specimen was used for this purpose. The major findings can be summarised as:

- A state variable model ('the λ-model') that takes account of gross internal structural evolution has been employed to model the flow stress behaviour of the bulk β-heat treated acicular Ti-6Al-4V during isothermal forging at

temperatures of 925-975°C and strain rates of 0.3-0.003/s.

- Several numerical optimisation methods were explored for parameter estimation in the λ-model. It was found that the Nelder-Mead Simplex method is the most computationally efficient because it shows the best performance, as indicated by the value of final objective function, number of iterations and function evaluations required to converge to the optimised solution. In addition, confidence limits have been estimated and presented for the first time in multi-parameter non-linear hot forming equations in order to assess the validity of the estimated parameters within the constitutive model.
- Although the λ-model prediction and the experimental data are in very good agreement, it is nevertheless important to establish a predictive model that distinguishes the deformation history of each phase constituent. The iso-strain assumption (Taylor approach) has been applied to model the total stress response of the bulk acicular Ti-6Al-4V by assuming the strain within the individual phases (α and β) is equal to that in the two-phase alloy and by weighting the flow stress of each phase with its individual temperature-dependent volume fraction. It was found that this assumption can only estimate the peak stress of the alloy whilst the flow softening is poorly predicted due to the absence of post-peak interaction mechanisms in the constitutive equations.
- In order to better predict the entire flow stress curves of β-heat-treated acicular Ti-6Al-4V, including post-peak softening behaviour, a constitutive model has been developed by modifying the iso-strain approach. A structural variable λ_{int} was introduced in order to represent the strain accumulation resulting from gross interaction mechanisms between each phase during deformation. It was found that the modified iso-strain can predict the post-peak flow softening,

indicating that the addition of λ_{int} is effective in accounting for the interaction between the α and β phases during deformation.

- The capability of the modified iso-strain model has been assessed in predicting the flow stress behaviour derived from a strain-rate jump test, which was performed at a temperature of 950°C with a sudden change in strain rate from 0.3 to 0.03/s at true strain of 0.2, and a further jump from 0.03 to 0.3/s at true strain of 0.4. It was found that the model was able to follow the instantaneous change of imposed strain rate by capturing the trend of 'undershoot' and 'overshoot' in the flow stress behaviour.
- The modified iso-strain model has been implemented into a user-routine in the DEFORM-2D finite element code in order to simulate hot forging of conventional cylindrical work-pieces. The FE model has been employed in order to predict the effect of forging variables on the distribution of local effective strain, temperature and structural variable λ_{int}. Non-uniform distribution of local plastic strain, temperature and structural variable λ_{int} were found to increase as deformation proceeds.
- The FE and constitutive model have been validated using an isothermal forging of a complex-shape double-truncated cone at 950°C and 0.01/s. The simulated forging load is in excellent agreement with the measured load-displacement data. This demonstrated that the combined approach of constitutive and FE modelling employed in this study has good general predictive capability for real-complex-shape isothermal forging, at least within the range of temperature (925-975°C) and strain rates (0.003-0.3/s) examined.

The third goal of this project was to investigate the microstructure evolution of Ti-6Al-4V under different processing conditions (temperature, strain and applied strain rate) and to employ the constitutive model developed for predicting microstructure development within a non-uniform deformed work-piece (the double-truncated cone specimen). The important conclusions that can be drawn from this work are as follows:

a. For the as-received Ti-6Al-4V

- The microstructure of the as-received Ti-6Al-4V bar consisted of nearly equi-axed and elongated primary α within a fine discontinuous β matrix. This is a typical microstructure produced within a material which has been β-processed before subsequent $\alpha + \beta$ hot working.
- The volume fraction of primary α within as-received Ti-6Al-4V decreased significantly as soaking temperature increased from 850-1000°C. As the β-transus temperature is approached, a higher volume fraction of β-phase is retained. The β-transus temperature of the as-received material was estimated to be 995°C.
- It was found that with increasing deformation, the primary α grains were deformed and flattened in a direction perpendicular to the forging axis. In the most severely deformed regions, a finer globular structure of primary α with sharp-defined grain boundaries interspersed between coarser α grains within β-phase matrix is observed. Refinement of the α grain size occurs up to strain of 1, and then a steady-state grain size appears to be attained. This equilibrium condition possibly reflects the occurrence of α grain rotation within the soft β-phase matrix.

- The effect of imposed strain rate on the morphology of primary α grains seems to be negligible. The average value of grain size remains stable upon increasing strain rate.
- It is apparent that volume fraction of primary α varies with temperature. As temperature decreases, volume fraction of the α-phase increases considerably. On the other hand, the variation of α grain size with temperature is relatively small, with a tendency towards a slight increase with increasing temperature.

b. For the β-heat treated Ti-6Al-4V

- The β-heat treated Ti-6Al-4V microstructure consisted of colonies of acicular or needle-like alpha phase within coarse prior-β grains. This is a typical microstructure produced from β heat-treatment followed by rapid quenching.
- It was found that soaking temperatures significantly affect the α lath width. As temperature increases, the laths exhibited coarsening to some extent whilst laths with higher aspect ratios became partially dissolved and broken-up. Inter-spacing between adjacent laths also increased simultaneously. Consequently, the volume fraction of α laths decreased since there is sufficient driving force at elevated temperatures for dissolution of the α phase into the β matrix.
- It was found that, at lower strains, the α laths consisted of undeformed, partially distorted and fully distorted (equi-axed) structures. As strain progressed, the α laths were further broken-up by distortion, bending and kinking. The mean aspect ratio of the α laths exhibited a gradual reduction with increasing strain. It was also found that the volume fraction of the globularised α-phase increased with increasing strain. On the other hand, lath area, length and perimeter showed a tendency to decrease with increasing strain. Such

measurements are useful in aiding a quantitative description of α lath transformations. The lath width remained relatively stable within the range of imposed strain rates, with a slight tendency to increase with increasing strain.

- A pronounced reduction in the mean size of the α laths was observed for each test temperature with increasing imposed strain rate. A similar effect was also noticed for mean values of perimeter, width and length.
- Volume fraction of the laths decreased slightly with decreasing strain rate. This suggests that at the slowest strain rate, there is sufficient time for diffusion-controlled process to take place, which leads to dissolution of α phase into the β matrix. This observation demonstrated that some degree of phase transformation occurred concurrently with the mechanical deformation during α + β hot forging.
- At lower temperature, a higher degree of globularisation occurred as indicated by the higher fraction of globularised α grains. As temperature increased, most of the laths become dissolved into the β-matrix which in turn reduces the lath volume fraction. In addition, α laths undergo coarsening as indicated by their tendency to increase their morphological size (aspect ratio, width, length, area, and perimeter).
- The quantified microstructure parameters (aspect ratio, width and length of α laths) within the deformed cylindrical work-piece during isothermal forging at 950°C and 0.01/s have been linked to the distribution of the structural parameter, λ_{int}, as predicted by finite element analysis in order to establish a set of microstructure models. The evolution of aspect ratio and width of the α laths was well-described by using an exponential function of λ_{int}. The dependency of

α-lath length was also well-fitted by using a combination of power law and exponential function of λ_{int}.

- The derived microstructure relationships were finally validated by predicting the microstructure development within a double-truncated cone deformed at 950°C and 0.01/s. It was found that λ_{int} correlated well with the measured microstructural parameters showing the effectiveness of the models in handling the change of work-piece geometry and deformation paths.

7.3 Further work

The research carried out in this thesis suggests a number of fruitful areas for further work, that is:

- The flow stress of the as-received Ti-6Al-4V with globular initial microstructure exhibited a sudden yield drop phenomenon. This behaviour may be attributed to dislocation pinning by solute atoms that may be breaking away from their locking points upon the imposition of a sufficiently high stress, which in turn generates a higher density of mobile dislocations and leads to a sudden stress drop. It is suggested that further investigation of this phenomenon could be performed by using transmission electron microscopy. Since it is extremely difficult to model the sudden yield drop phenomenon, it is expected that the TEM work can support the development of constitutive relations which can capture this behaviour, allowing the initial elastic part of the flow curve to be accounted for.
- The constitutive model developed here has shown a good capability in predicting the load response and microstructure development within a double-truncated cone specimen deformed at 950°C and 0.01/s. It would be interesting

to validate the constitutive model by predicting the load response and microstructural evolution for a case of larger-scale non-axisymmetrical hot forging by implementing the model into 3D-finite element software, for example DEFORM-3D. In addition, it would be useful to perform a series of interrupted tests at various temperatures and strain rates in order to improve the predictive capability of the microstructure model. By doing so, it is expected to enhance a microstructure data-base for refining the predictive capability of the model at lower strain.

- Another possible mechanism that may be responsible for flow softening observed during hot deformation of Ti-6Al-4V with acicular α initial microstructure is the evolution of crystallographic texture. It would be useful to incorporate the effect of texture within the developed two-phase constitutive model as the basis of a texture evolution model. A series of flow stress measurements on heavily textured materials can be performed in order to capture the orientation-dependence of flow stress.

References

1. Peter, M., Hemptenmacher, J., Kumpfert, J., Leyens, C., *Structure and Properties of Titanium and Titanium Alloys*, in *Titanium and Titanium Alloys: Fundamentals and Applications*, C.Leyens, Editor. 2003, Wiley-VCH GmbH & Co.KGaA: Germany. p. 1-36.
2. Lutjering, G., Williams, J.C, *Alpha + Beta Alloys*, in *Titanium*. 2003, Springer-Verlag: Heidelberg, Germany. p. 177-232.
3. Weiss, I., Semiatin, S.L, *Thermomechanical Processing of Alpha Titanium Alloys-An Overview*. Materials Science and Engineering, 1999. **A263**: p. 243-256.
4. Sellars, C.M., Zhu, Q., *Microstructural Modelling of Aluminium Alloys during Thermomechanical Processing*. Materials Science and Engineering, 2000. **A280**: p. 1-7.
5. Doherty, R.D., Hughes, D.A., *Current Issues in Recrystallization: A Review*. Materials Science and Engineering, 1997. **A238**: p. 219-274.
6. Terlinde, G., Witulski, T., Fischer, G., *Forging of Titanium*, in *Titanium and Titanium Alloys: Fundamentals and Applications*, C. Leyens, Editor. 2003, Wiley-VCH GmbH & Co.KGaA: Germany. p. 289-304.
7. Polmear, I.J., *Titanium Alloys*, in *Light Alloys: Metallurgy of the Light Metals*, R. Honeycombe, Editor. 1989, Edward Arnold: London, UK. p. 162-187.
8. Donachie Jr., M.J., *A Primer on Titanium and Its Alloys*, in *Titanium - A Technical Guide*. 2000, ASM International: Metals Park, OH. p. 1-3.
9. Lutjering, G., Williams, J.C, *Fundamental Aspects*, in *Titanium*. 2003, Springer-Verlag: Heidelberg, Germany. p. 13-50.
10. Kornilov, I.I., *Interaction of Titanium with Elements of The Periodic System*, in *The Science, Technology and Application of Titanium*, R.I. Jaffee, Editor. 1968, Pergamon Press: Oxford. p. 407-418.
11. Flower, H.M., *Microstructural Development in Relation to Hot Working of Titanium Alloys*. Materials Science and Technology, 1990. **6**: p. 1082-1092.
12. Donachie Jr., M.J., *Understanding The Metallurgy of Titanium*, in *Titanium - A Technical Guide*. 2000, ASM International: Metals Park, OH. p. 13-24.
13. Joshi, V.A., *Physical Metallurgy of Titanium Alloys*, in *Titanium Alloys: An Atlas of Structures and Fracture Features*. 2006, Taylor & Francis Group. p. 7-15.
14. Duerig, T.W., Middleton, R.M., Terlinde, G.T, Williams, J.C., *Stress Assisted Transformation in Ti-10V-2Fe-3AL*, in *Titanium'80:Science and Technology*, H.Kimura, Editor. 1980, TMS: Warrendale, PA. p. 1503-1512.
15. Weiss, I., Semiatin, S.L., *Thermomechanical Processing of Beta Titanium Alloys-An Overview*. Materials Science and Engineering, 1998. **A243**: p. 46-65.
16. Terlinde, G., Fischer, G., *Beta Titanium Alloys*, in *Titanium and Titanium Alloys: Fundamentals and Applications*, C.Leyens, Editor. 2003, Wiley-VCH GmbH & Co.KGaA: Germany. p. 37-57.
17. Duerig, T.W., Williams, J.C., *Overview:Microstructure and Properties of Beta Titanium Alloys*, in *Beta Titanium Alloys of the 1980's*, R.R.Boyer, Editor. 1984, TMS: Warrendale, PA, USA. p. 19.

18. Ankem, S., Seagle, S, *Heat Treatment of Metastable Beta Titanium Alloys*, in *Beta Titanium Alloys of the 1980's*, R.R.Boyer, Editor. 1984, TMS: Warrendale, PA, USA. p. 107.
19. www.timet.com, *www.timet.com*. January 2002.
20. Brick, R.M., Pense, A.W., Gordon, R.B, *Titanium and Zirconium; Titanium Alloys*, in *Structure and Properties of Engineering Materials*, M.B.Bever. Editor. 1977, McGraw-Hill. p. 233-253.
21. Donachie Jr., M.J., *Ingot Metallurgy and Mill Products*, in *Titanium - A Technical Guide*. 2000, ASM International: Metals Park, OH. p. 25-32.
22. Donachie Jr., M.J., *Forging and Forming*, in *Titanium - A Technical Guide*. 2000, ASM International: Metals Park, OH. p. 33-38.
23. *Design for Deformation Processes*, in *Handbook of Workability and Process Design*, G.E. Dieter, Editor. 2003, ASM International: Materials Park, OH 44073-0002. p. 139-171.
24. Altan, T., Oh, S., Gegel, H., *Recent Developments in Metal Forming Technology and Application of CAD/CAM*, in *Metal Forming: Fundamentals and Applications*. 2000, American Society for Metals: Metals Park, OH. p. 313-327.
25. Shen, G., Furrer, D, *Manufacturing of Aerospace Forgings*. Journal of Materials Processing Technology, 2000. **98**: p. 189-195.
26. Dieter, G.E., *Bulk Workability Testing*, in *Handbook of Workability and Process Design*, G.E. Dieter, Kuhn, H.A., Semiatin, S.L, Editor. 2003, ASM International: Materials Park, OH 44073-0002. p. 48-56.
27. Dieter, G.E., *Hot-Compression Testing*, in *Handbook of Workability and Process Design*, G.E. Dieter, Editor. 2003, ASM International: Materials Park, OH 44073-0002. p. 61-67.
28. McQueen, H.J., Jonas, J.J, *Recovery and Recrystallization during High Temperature Deformation*, in *Plastic Deformation of Materials, Treatise on Materials Science and Technology*, R.J. Arsenault, Editor. 1975, Academic Press: New York, NY. p. 393-493.
29. Rice, J.R., *Continuum Mechanics and Thermodynamics of Plasticity in Relation to Microscale Deformation Mechanisms*, in *Constitutive Equations in Plasticity*, A.S.Argon, Editor, MIT Press: Cambridge. p. 23.
30. Lee, C.H., Kobayashi, S., *New Solutions to Rigid Plastic Deformation Problems Using a Matrix Method.* Journal of Engineering for Industry-Transactions of ASME,, 1973. **95**: p. 865-873.
31. Kobayashi, S., *Rigid Plastic Finite Element Analysis of Axisymmetric Metal Forming Processes.* Numerical Modelling of Manufacturing Processes, ASME, PVP-PB-025, 1977: p. 49-68.
32. Oh, S.I., *Finite Elements Analysis of Metal Forming Problems with Arbitrarily Shaped Dies.* International Journal of Mechanical Science, 1982. **17**: p. 293.
33. Altan, T., Oh, S., Gegel, H., *Application of FEM to Simulation of Metal Forming Processes*, in *Metal Forming: Fundamentals and Applications*. 2000, American Society for Metals: Metals Park, OH. p. 329-340.
34. Wilson, A., *Private Communication*. 2006: TIMET UK, Birmingham.
35. Roebuck, B., Lord, J.D., Brooks, M., Loveday, M.S., Sellars, C.M, Evans, R.W, *Measurement Good Practice Guide:Measuring Flow Stress in Hot Axisymmetric Compression Tests*. 2002, The National Physical Laboratory: Teddington, United Kingdom.

36. Kuhn, H.A., *Workability Theory and Application in Bulk Forming Processes.* 9th ed. Metals Handbook. Vol. 14. 1988, Metals Park, OH: ASM. 388-404.
37. *Operating Instructions of 1100 C Radiant Furnace RHS1856A.* April 2005, Instron SFL.
38. *Operation Manual of Control Unit Model No:CU1856B.* April 2005, Instron SFL.
39. *Tribology in Metalworking*, in *Lubrication, Friction and Wear*, J.A. Schey, Editor. 1983, American Society for Metals: Metals Park, OH.
40. Male, A.T., *Variation in Friction Coefficients of Metals during Compressive Deformation.* Journal Institute of Metals, 1966. **94**: p. 121.
41. Douglas, J.R., Altan, T, *Flow Stress Determination for Metals at Forging Rates and Temperatures.* Journal of Engineering for Industry-Transactions of ASME, 1975: p. 66.
42. Lee, C.H., Altan, T, *Influence of Flow Stress and Friction Upon Metal Flow in Upset Forging of Rings and Cylinders.* Journal of Engineering for Industry-Transactions of ASME, 1972: p. 775.
43. Hawkyard, J.B., Johnson, W, *An Analysis of the Changes in Geometry of a Short Hollow Cylinder during Axial Compression.* International Journal of Mechanical Sciences, 1967. **9**: p. 163.
44. Male, A.T., Depierre, V, *The Validity of Mathematical Solutions for Determining Friction From the Ring Compression Test.* Journal of Lubrication Technology, November 1969. **69-WA/Lub-8**: p. 1-7.
45. Male, A.T., Cockroft, M.G, *A Method for the Determination of the Coefficient of Friction of Metals Under Conditions of Bulk Plastic Deformation.* Journal Institute of Metals, 1964-65. **93**: p. 38-46.
46. Dieter, G.E., *Mechanical Metallurgy.* 2nd ed. International Student Edition. 1989, Newyork, NY: McGraw-Hill. 563.
47. Taylor, B., Weidmann, E, *Metallographic Preparation of Titanium*, in *Application Notes*. 2002, Struers: Denmark.
48. www.struers.com.
49. http://rsb.info.nih.gov/ij/.
50. http://ddsdx.uthscsa.edu/dig/itdesc.html.
51. Long, M., Rack, H.J, *High Temperature Discontinuous Yielding in β–Phase Ti_3Al-(Nb,V,Mo) Alloys*, in *Titanium'95:Science and Technology*, P.A. Blenkinsop, Evans, W.J., Flower, H.M, Editor. 1996, Institute of Materials: London. p. 316-323.
52. Courtney, T.H., *Dislocations*, in *Mechanical Behaviour of Materials*. 2000, McGraw-Hill: New York, NY. p. 85-139.
53. Montheilet, F., Dajno, D., Come, N, *Hot Deformation of The High Strength BETACEZ Titanium Alloy*, in *Titanium '92:Science and Technology*, F.H. Froes, Editor. 1993, TMS: Warrendale, PA. p. 1347-1354.
54. Vijayshankar, M.N., Ankem, S., *High Temperature Tensile Deformation Behaviour of β-Ti Alloys.* Materials Science and Engineering, 1990. **A129**: p. 229-237.
55. Philippart, I., Rack, HJ, *High Temperature Dynamic Yielding in Metastable Ti-6.8Mo-4.5Fe-1.5Al.* Materials Science and Engineering, 1998. **A243**: p. 196-200.
56. Jonas, J.J., Heritier, B., Luton, M.J, *Anneal Hardening and Flow Softening in Beta Zirconium-Niobium Alloys.* Metallurgical Transactions, 1979. **10A**: p. 611-620.

57. Ankem, S., Shyue, J.G., Vijayshankar, M.N., Arsenault, R.J, *The Effect of Volume Per Cent of Phases on the High Temperature Tensile Deformation of Two-phase Ti-Mn Alloys.* Materials Science and Engineering, 1989. **A111**: p. 51-61.
58. Seetharaman, V., Boothe, L., Lombard, C.M, *Compressive Deformation Behaviour of a Ti-6Al-4V Alloy at High Temperatures and Strain Rates*, in *Microstructure/Property Relationships in Titanium Aluminides and Alloys*, Y.W.Kim, Editor. 1991. p. 605-622.
59. Sastry, D.H., Prasad, Y.V.R.K., Deevi, S.C, *Influence of Temperature and Strain Rate on The Flow Stress of an FeAl Alloy.* Materials Science and Engineering, 2001. **A299**: p. 157-163.
60. Semiatin, S.L., Lahoti, G.D, *The Occurence of Shear Bands in Isothermal Hot Forging.* Metallurgical Transactions, 1982. **13A**: p. 275-288.
61. Dieter, G.E., *Bulk Workability Testing*, in *Handbook of Workability and Process Design*, G.E. Dieter, Kuhn, H.A., Semiatin, S.L, Editor. 2003, ASM International: Materials Park, OH 44073-0002. p. 50.
62. Seshacharyulu, T., Medeiros, S.C., Frazier, W.G., Prasad, Y.V.R.K, *Hot Working of Commercial Ti-6Al-4V with an Equiaxed α–β Microstructure: Materials Modelling Considerations.* Materials Science and Engineering, 2000. **A284**: p. 184-194.
63. Wanjara, P.J., M., Monajati, H., Yue, S., Immarigeon, J.P, *Hot Working Behaviour of Near-α Alloy IMI834.* Materials Science and Engineering, 2005. **A 396**: p. 50-60.
64. Humpbreys, F.J., Hatherly, M, *Recrystallization and Related Annealing Phenomena.* 1995, New York: Pergamon Press. 8 & 373.
65. Dyment, F., Libanati, C.M, *Self-Diffusion of Ti, Zr, and Hf in their HCP Phases, and Diffusion of Nb in HCP Zr.* Journal of Materials Science, 1968. **3**: p. 349-359.
66. Jonas, J.J., Sellars, C.M, McG.Tegart, W.J, *Strength and Structure under Hot-Working Conditions.* Metallurgical Reviews, 1969. **14**: p. 1-24.
67. Bate, P.S., Blackwell, P.L., Brooks, J.W., *Thermo-Mechanical Processing of Titanium IMI 834*, in *Sixth World Conference on Titanium*, P.Lacombe, Editor. 1988: France. p. 287-292.
68. Briottet, L., Jonas, J.J., Montheillet, F, *A Mechanical Interpretation of the Activation Energy of High Temperature Deformation in Two Phase Materials.* Acta Materialia, 1996. **44**: p. 1665-1672.
69. Zener, C., Hollomon, J.H, *Effect of Strain Rate upon Plastic Flow of Steel.* Journal of Applied Physics, 1944. **15**: p. 22-32.
70. Shell, E.B., Semiatin, S.L, *Effect of Initial Microstructure and Plastic Flow and Dynamic Globularisation during Hot Working of Ti-6Al-4V.* Metallurgical and Materials Transactions, 1999. **30A**: p. 3219-3229.
71. Seshacharyulu, T., Medeiros, S.C., Frazier, W.G., Prasad, Y.V.R.K, *Microstructural Mechanisms during Hot Working of Commercial Grade Ti-6Al-4V with Lamellar Starting Structure.* Materials Science and Engineering, 2002. **A325**: p. 112-125.
72. Seetharaman, V., Semiatin, S.L, *Plastic-Flow and Microstructure Evolution During Hot Deformation of A Gamma Titanium Aluminide Alloy.* Metallurgical and Materials Transactions, 1997. **28A**: p. 2309-2321.
73. Argon, A.S., in *Physical Metallurgy*, R.W.Cahn, Editor. 1996: North-Holland, Amsterdam, 1996. p. 1957-2007.

74. Sheppard, T., Norley, J, *Deformation Characteristics of Ti-6Al-4V.* Materials Science and Technology, 1988. **4**: p. 903-908.
75. Seetharaman, V., Semiatin, S.L, *Influence of Temperature Transients on The Hot Workability of a Two-Phase Gamma Titanium Aluminide Alloy.* Metallurgical and Materials Transactions, 1996. **27A**: p. 1987-2004.
76. Semiatin, S.L., Seetharaman,V., Ghosh, A.K., *Plastic flow, microstructure evolution, and defect formation during primary hot working of titanium and titanium aluminide alloys with lamelar colony microstructures.* The Philosophical Transactions of The Royal Society of London A, 1999. **357**: p. 1487-1512.
77. Semiatin, S.L., Seetharaman, V. and Weiss, I.,, *Flow Behaviour and Globularization Kinetics during Hot Working of Ti-6Al-4V with a Colony Alpha Microstructure.* Materials Science and Engineering, 1999. **A263**: p. 257-271.
78. Ding, R., Guo, Z.X., Wilson, A, *Microstructural Evolution of a Ti-6Al-4V Alloy during Thermomechanical Processing.* Materials Science and Engineering, 2002. **A237**: p. 233-245.
79. Seetharaman, V., Semiatin, S.L, *Effect of the Lamellar Grain Size on Plastic Flow Behaviour and Microstructure Evolution during Hot Working of a Gamma Titanium Aluminide Alloy.* Metallurgical and Materials Transactions, 2002. **33A**: p. 3817-3830.
80. Jonas, J.J., Holt, R.A., Coleman, C.E, *Plastic Stability in Tension and Compression.* Acta Metallurgica, 1976. **24**: p. 911-918.
81. Semiatin, S.L., Bieler, T.R, *The Effect of Alpha Platelet Thickness on Plastic Flow during Hot Working of Ti-6Al-4V with a Transformed Microstructure.* Acta Materialia, 2001. **49**: p. 3565-3573.
82. Millet, J.C.F., Brooks, J.W., Jones, I.P, *Assessment and Modelling of Isothermal Forging of Intermetallic Compounds Part 1-TiAl.* Materials Science and Technology, 1999. **15**: p. 697-704.
83. Millet, J.C.F., Brooks, J.W., Jones, I.P, *Assessment and Modelling of Isothermal Forging of Intermetallic Compounds Part 2-Ti_3Al.* Materials Science and Technology, 2000. **16**: p. 617-624.
84. Millet, J.C.F., Brooks, J.W., Jones, I.P, *Assessment and Modelling of Isothermal Forging of Intermetallic Compounds Part 3-Ni_3Al.* Materials Science and Technology, 2000. **16**: p. 1041-1048.
85. Millet, J.C.F., Brooks, J.W., Jones, I.P, *Assessment and Modelling of Isothermal Forging of Intermetallic Compounds Part 4-NiAl.* Materials Science and Technology, 2001. **17**: p. 795-801.
86. Jackson, M., *Microstructural Evolution of Titanium Alloys during Isothermal Subtransus Forging*, in *PhD Thesis*. 2002, Department of Materials, Imperial College of Science, Technology and Medicine, University of London: London, UK.
87. Brown, S.B., Kim, K.H., Anand, L., *An Internal Variable Constitutive Model for Hot Working of Metals.* International Journal of Plasticity, 1989. **5**: p. 95-130.
88. Dieter, G.E., *Bulk Workability of Metals*, in *Handbook of Workability and Process Design*, G.E. Dieter, Kuhn, G.A., Semiatin, S.L, Editor. 2003, ASM International: Materials Park, OH 44073-0002. p. 23-34.

89. Garofalo, F., *An Empirical Relation Defining the Stress Dependence of Minimum Creep Rate in Metals.* Transactions of the Metallurgical Society of AIME, 1963. **227-355**: p. 351-355.
90. Sellars, C.M., Tegart, W.J.McG, Mem. Sci. Rev. Metall, 1966. **63**: p. 731.
91. Bate, P.S., *An Application of Computer Modelling to Isothermal Forging*, in *Conf. Proc. Aerospace Materials Process Modelling*. 1987, AGARD.426: Paris. p. 22.1-22.10.
92. Blackwell, P., Brooks, J.W., Bate, P.S., *Development of Microstructure in Isothermally Forged Nimonic Alloy AP1.* Materials Science and Technology, 1998. **14**: p. 1181-1188.
93. Rist, M.A., Reed, R.C, *Inverse Method for Parameter Optimisation in Superalloy Tertiary Creep Equations.* Materials Science and Technology, 2002. **18**: p. 179-186.
94. Nelder, J.A., Mead, R, *A Simplex Method for Function Minimization.* The Computer Journal, 1965. **7**: p. 308-313.
95. Press, W.H., Teukolsky, S.A., Vetterling, W.T, Flannery, B.P, *Minimization or Maximization of Functions*, in *Numerical Recipes in Fortran 77*. 1992, Cambridge University Press: Cambridge, UK. p. 402-406.
96. Press, W.H., Teukolsky, S.A., Vetterling, W.T, Flannery, B.P, *Modelling of Data*, in *Numerical Recipes in C*. 1992, Cambridge University Press: Cambridge, UK. p. 683-685.
97. *The Fortran 77 Library*, The Numerical Algorithms Group Ltd: Oxford, UK.
98. Semiatin, S.L., Montheillet, F., Shen, G., Jonas, J.J, *Self-Consistent Modelling of the Flow Behavior of Wrought Alpha/Beta Titanium Alloys under Isothermal and Nonisothermal Hot-Working Conditions.* Metallurgical and Materials Transactions A, 2002. **33A**: p. 2719-2727.
99. Suquet, P.M., *Overall Potentials and Extremal Surfaces of Power Law or Ideally Plastic Composites.* Journal of The Mechanics and Physics of Solids, 1993. **41**: p. 981-1002.
100. Vo, P., Jahazi, M., Yue, S., Bocher, P., *Flow Stress Prediction During Hot Working of Near-α Titanium Alloys.* Materials Science and Engineering, 2007. **A447**: p. 99-110.
101. www.deform.com.
102. Klocke, F., Raedt, H.W., Hoppe, S, *2D-FEM Simulation of The Orthogonal High Speed Cutting Process.* Machining Science and Technology, 2001. **5(3)**: p. 323-340.
103. Liu, Y., Baker, T.N, *A Comparison of Experimental and Computer Simulated Iso-thermal Upset Forging of IMI 685 Titanium Alloy.* Materials Science and Engineering A, 1996. **205**: p. 117-126.
104. www.absoft.com.
105. Brooks, J.W., Unpublished Internal Report, QinetiQ.
106. TIMET, *Timet Data Sheet of Ti-6Al-4V*. June 2007, www.timet.com.
107. Hu, Z.M., Brooks, J.W., Dean, T.A. *The Interfacial Heat Transfer Coefficient in Hot Die Forging of Titanium Alloy*. in *Proceeding of Institute of Mechanical Engineers*. 1998.
108. Coppa, P., Consorti, A, *Normal Emissivity of Samples Surrounded by Surfaces at Diverse Temperatures.* Measurement, 2005. **38**: p. 124-131.
109. Snape, R.G., Clift, S.E., Bramley, A.N, *Sensitivity of Finite Element Analysis of Forging to Input Parameters.* Journal of Materials Processing Technology, 1998. **82**: p. 21-26.

110. Castro, R., Seraphin, L, Mem. Sci. Rev. Metall, 1966. **63**: p. 1025-1058.
111. Weiss, I., Froes, F.H., Eylon, D., Welsch, G.E., *Modification of Alpha Morphology in Ti-6Al-4V by Thermomechanical Processing.* Metallurgical Transactions, 1986. **17A**: p. 1935-1947.
112. Margolin, H., Cohen, P., *Evolution of The Equiaxed Morphology of Phases in Ti-6Al-4V*, in *Titanium'80: Science and Technology.* 1980, TMS: Warrendale, PA. p. 1555-1561.
113. Semiatin, S.L., Lahoti, G.D, *Deformation and Unstable Flow in Hot Forging of Ti-6Al-2Sn-4Zr-2Mo-0.1Si.* Metallurgical Transactions, 1981. **12A**: p. 1705-1717.
114. Eylon, D., Pierce, C.M., *Effect of Microstructure on Notch Fatigue Properties of Ti-6Al-4V.* Metallurgical Transactions, 1976. **7A**: p. 111-121.
115. Froes, F.H., Highberger, W.T, *Synthesis of CORONA 5 (Ti-4.5Al-5Mo-1.5Cr).* Journal of Metals, 1980. **32**: p. 57-64.
116. Tiley, J., Searles, T., Lee, E., Kar, S., Banerjee, R., Russ, J.C., Fraser, H.L, *Quantification of Microstructural Features in α/β Titanium Alloys.* Materials Science Engineering A, 2004. **372**: p. 191-198.
117. Margolin, H., Farrar, P.A., Greenfield, M.A, *Thermo-mechanical Strengthening of High Strength Titanium Alloys*, in *The Science, Technology and Application of Titanium*, R.I.Jaffee, Editor. 1970, Pergamon Press: New York. p. 795-808.
118. Greenfield, M.A., Margolin, H., *The Interrelationship of Fracture Toughness and Microstructure in a Ti-5.25Al-5.5V-0.9Fe-0.5Cu Alloys.* Metallurgical Transactions, 1971. **2**: p. 841-847.
119. Greenfield, M.A., Margolin, H., *The Mechanism of Void Formation, Void Growth, and Tensile Fracture in an Alloy Consisting of Two Ductile Phases.* Metallurgical Transactions, 1972. **3**: p. 2649-2659.
120. Williams, J.C., Starke, E.A, *The Role of Thermomechanical Processing in Tailoring the Properties of Aluminium and Titanium Alloys*, in *Deformation Processing and Structure.* 1982, ASM: Ohio. p. 279-354.
121. Weiss, I., Srinivasan, R., Froes, F.H., *The Processing Window Concept for Beta Titanium Alloys*, in *Recrystallization'90*, T. Chandra, Editor. 1990, TMS: Ohio. p. 609-616.
122. Majorell A., S., S., Picu, R.C, *Mechanical Behavior of Ti-6Al-4V at High and Moderate Temperatures-Part I: Experimental Results.* Materials Science and Engineering, 2002. **A326**: p. 297-305.
123. Park, N.K., Yeom, J.T., Na, Y.S, *Characterization of Deformation Stability in Hot Forging of Conventional Ti-6Al-4V using Processing Maps.* Journal of Materials Processing Technology, 2002. **130-131**: p. 540-545.
124. Chen, C.C., Coyne, J.E, *Deformation Characteristics of Ti-6Al-4V Alloy Under Isothermal Forging Conditions.* Metallurgical Transactions, 1975. **7A**: p. 1931-1941.
125. Johnson, A.J.G., Bull, C.W., Kumar, K.S., Briant, C.I, *The Influence of Microstructure and Strain Rate on the Compressive Deformation Behavior of Ti-6Al-4V.* Metallurgical and Materials Transactions, 2003. **34A**: p. 295-306.
126. Barbosa, R.A.N.M., Braga, H.C., Breme, J. *Hot Strength of Ti and Ti Alloys Deformed in Axial Compression.* in *Titanium'92 Science and Technology.* 1992: The Minerals, Metals and Materials Society, 1993.

127. Malcor, J.G., Montheillet, F., Champin, B, *Mechanical and Microstructural Behavior of Ti-6Al-4V in the Hot Working Range*, in *Titanium: science and technology*, G.Luetjering, Editor. 1985: Oberursel, Germany. p. 1495-1502.
128. Evans, R.W., Scharning, P.J, *Axisymmetric Compression Test and Hot Working Properties of Alloys.* Materials Science and Technology, 2001. **17**: p. 995-1004.
129. Evans, R.W., Scharning, P.J, *Systematic Errors in Flow Stress Measurement for the Hot Plane Strain Compression Test.* Materials Science and Technology, 2004. **20**: p. 431-440.
130. Loveday, M.S., *Measurement Note (Draft for IAG) High Temperature Flow Stress Measurements: Quality & Traceability Issues*, NPL.
131. Kuhlman, G.W., *Forging of Titanium Alloys*, in *ASM Handbook: Forming and Forging*. 1988, ASM International. p. 267-287.
132. Barboza, M.J.R., Neto, C.M., Silva, C.R.M, *Creep Mechanisms and Physical Modelling for Ti-6Al-4V.* Materials Science and Engineering, 2004. **A369**: p. 201-209.
133. Kim, J.H., Semiatin, S.L., Lee, C.S, *Constitutive Analysis of The High Temperature Deformation of Ti-6Al-4V with a Transformed Microstructure.* Acta Materialia, 2003. **51**: p. 5613-5626.
134. Nemat-Nasser, S., Guo, W.G., Nesterenko, V.F, *Dynamic Response of Conventional and Hot Isostatically Pressed Ti-6Al-4V Alloys: Experiments and Modelling.* Mechanics of Materials, 2001. **33**: p. 425-439.
135. Seo, S., Min,. O, Yang, H, *Constitutive Equation for Ti-6Al-4V at High Temperatures Measured using the SHPB Techniques.* International of Journal of Impact Engineering, 2005. **31**: p. 735-754.
136. Lee, W.S., Lin, C.F, *Plastic Deformation and Fracture Behaviour of Ti-6Al-4V Alloy Loaded With High Strain Rate Under Various Temperatures.* Materials Science and Engineering, 1998. **A241**: p. 48-59.
137. Lin, J., Yang, J, *GA-based Multiple Objective Optimisation for Determining Viscoplastic Constitutive Equations for Superplastic Alloys.* International Journal of Plasticity, 1999: p. 1181-1196.